NASA Grant Report
GTRI Report A5004/2000-1

Active Control of Liner Impedance
by Varying Perforate Orifice Geometry

K. K. Ahuja and R. J. Gaeta, Jr.
Georgia Institute of Technology, GTRI/ATASL
Acoustics and Aerospace Technologies Branch
Atlanta, Georgia 30332-0844

Foreword/Acknowledgments

This report was prepared by the Acoustics and Aerospace Technologies Branch of the Aerospace, Transportation, and Advanced Systems Laboratory (ATASL) of Georgia Tech Research Institute (GTRI) for NASA Langley Research Center, Hampton, Virginia, under Grant NAG1-1734.

Mr. Mike Jones was the Project Manager for NASA Langley Research Center. GTRI's Project Director was Dr. K.K. Ahuja.

The work reported here also became the topic of the Doctoral dissertation of Mr. Richard. J. Gaeta. Jr., who received his Doctoral degree in January 1999 as the advisee of Dr. K. K. Ahuja. This report is in essence a reproduction of this dissertation with minor changes in the format, verbiage, and one of the Appendices. The authors would like to thank Mr. Tony Parrott and Mr. Mike Jones of NASA Langley Research Center for their support of this work.. They are also grateful to Mr. Steven Williams and Mr. Jeff Hsu of GTRI for their assistance in model fabrication and data acquisition.

Note that this report is one of five separate volumes prepared to document the work conducted by GTRI under NASA Grant NAG1-1734. The GTRI report numbers, authors, and titles of each report are listed in the table below:

GTRI Report Number	Authors	Title
A5004/2000-1	Ahuja, K. K. and Gaeta, R. J.	Active Control of Liner Impedance by Varying Perforate Orifice Geometry
A5004/2000-2	Ahuja, K. K., Munro, S. E. and Gaeta, R. J.	Flow Duct Data for Validation of Acoustic Liner Codes for Impedance Eduction
A5004/2000-3	Ahuja, K. K., Gaeta, R. J. and D'Agostino, M. S.	High Amplitude Acoustic Behavior of a Slit-Orifice backed by a Cavity
A5004/2000-4	Ahuja, K. K., Gaeta, R. J. and D'Agostino, M. S.	Acoustic Absorption Characteristics of an Orifice With a Mean Bias Flow
A5004/2000-5	Ahuja, K. K., Cataldi, P. and Gaeta, R. J.	Sound Absorption of a 2DOF Resonant Liner with Negative Bias Flow

TABLE OF CONTENTS

LIST OF TABLES

List of Figures

NOMENCLATURE

c   Speed of sound

C_D Discharge Coefficient

d   Orifice diameter

f   frequency

h   Perforate thickness

L   Honeycomb or cavity depth

k   Acoustic wave number $\dfrac{\omega}{c}$

$|k_s|$ Viscous Stokes wave number $\sqrt{\dfrac{\omega}{v}}$

J_0 Bessel function of zeroth order

J_1 Bessel function of first order

P   Acoustic pressure

R   Specific resistance

R_f Reflection Coefficient

r   Orifice radius

s   Spring stiffness constant

SPL   Sound Pressure Level

t   time

u   Particle velocity

W   Acoustic Power

VOP   Variable Orifice Perforate

Z   Specific impedance

α Absorption Coefficient

ε Eccentricity

χ Specific reactance

χ_m Specific mass reactance

λ Acoustic Wavelength

ρ Density of air

σ Porosity

ω Angular frequency

Subscripts:

1   Facing sheet or 1st liner layer property

2   Buried septum or 2nd liner layer property

NL   Nonlinear Quantity

rms   Root Mean Squared

o   Signifies orifice

i   Signifies incident acoustic wave

r   Signifies reflected acoustic wave

Executive Summary

The present work explored the feasibility of controlling the acoustic impedance of a resonant type acoustic liner. This was accomplished by translating one perforate over another of the same porosity creating a totally new perforate that had an intermediate porosity. This type of adjustable perforate created a variable orifice perforate, whose orifices were non-circular. The key objective of the present study was to quantify the degree of attenuation control that can be achieved by applying such a concept to the buried septum in a two-degree-of-freedom (2DOF) acoustic liner. An additional objective was to examine the adequacy of the existing impedance models to explain the behavior of the unique orifice shapes that result from the proposed sliding perforate concept. Different orifice shapes with equivalent area were also examined to determine if highly non-circular orifices had a significant impact on the impedance. This was primarily an experimental study and the objectives were met by conducting the following tests in the Aeroacoustics facilities at the Georgia Tech Research Institute Aerospace and Transportation Laboratory:

1) A 2DOF liner was fabricated with a variable orifice perforate as the buried septum porous layer and normal incidence impedance tests were conducted as a function of septum porosity.

2) Another 2DOF liner was fabricated to be used as partial wall treatment in a flow-duct. Insertion loss and transmission loss measurements were made as a function of septum

porosity and grazing flow velocity. Mean centerline velocities tested were 0, 100, 150, 200, and 250 ft/s.

3) The sliding, overlapping variable orifice perforate was "isolated" with a backing cavity and normal incidence impedance was measured as a function of perforate porosity and incident sound pressure level.

4) The normal incidence impedance of several orifice shapes (round, square, triangular, star-shaped) of the same equivalent area was measured for low and high incident sound pressure. Included in these different shapes is the stepped-oval orifice, which refers to the unique shape created by two overlapping circular orifices that are off-center. The resulting shape is somewhat oval or "eye-shaped".

5) Flow-visualization of several orifice shapes were acquired to examine the orifice "jetting" that results from the conversion of sound into vorticity.

Salient findings and conclusions are summarized below:

1) It was found that perforate translational movements on the order of the orifice diameter (1.6 mm) resulted in shifting of the primary resonance frequency approximately 14% (200 Hz) and the secondary frequency approximately 16% (800 Hz). As the buried septum porosity was reduced, the resonant frequencies were reduced. For grazing flow conditions in a flow-duct, similar translational movements in the buried septum of a 2DOF liner resulted in consistent trends with the impedance tube data. As

the septum porosity was reduced the peak resonant frequency was reduced and the magnitude of the liner's absorption was increased. Thus, it was concluded that absorption properties of a 2DOF liner could be controlled with a small amount of mechanical input.

2) The variable orifice perforate was found to produce a lower mass reactance as the porosity was reduced than would be predicted by using an equivalent porosity perforate consisting of elliptical holes and linear theory. The lower porosity configurations of the variable perforate also increased the nonlinearity of the perforate.

3) Normal incidence impedance measurements of an isolated stepped-oval orifice shape (produced by the overlapping of two circular orifices) resulted in approximately a 12% reduction in the attached mass of the orifice relative to a circular orifice. Flow-visualization of this uniquely shaped orifice revealed that the typical orifice jetting accompanying sound/orifice interactions was "vectored" or deflected off the orifice centerline axis.

4) Highly non-circular orifice shapes, such as star-shaped, resulted in higher resistance and thus higher absorption at lower incident sound pressure levels. However, at higher incident sound pressure levels, the highly non-circular orifice shapes did not show a significant difference in impedance.

SECTION I

Introduction

1.1 Motivation

Acoustic liners are common components of flow-ducts and fluid flow machines. The liner's purpose is to provide absorption of unwanted acoustic energy (i.e., noise). A particular class of fluid flow machine is the gas turbine engine or jet engine. One major problem concerning the design of these acoustic liners for jet engines is that the characteristic noise sources (e.g., fan, compressor, struts) and flowfield in the engine's duct vary widely over the operating range of the engine. For example, the amount of airflow through the engine is highest when in takeoff operation and typically lowest during landing/approach. Fan speeds and flow velocities are quite different for these cases resulting in different noise source characteristics, such as noise intensity and frequency. Another example of a changing noise source environment is the exhaust ducts of internal combustion engines. Different operating conditions produce different peak noise frequencies that result from the firing frequency of the combustion process. Ideally, the acoustic lining on the walls of the exhaust duct should be optimally matched for all engine power levels to obtain the most noise reduction. Designing an acoustic liner that can change its impedance properties with relatively small mechanical input could possibly lead to optimizing the amount of noise suppression in a flow-duct or any other environment where the noise source changes with time.

1.2 Resonant Acoustic Liners

Conventional acoustic liners that are used to suppress noise in a small bandwidth are referred to as resonant liners. They normally consist of a porous or perforated facing skin (forming the interior duct wall) overlaying a sound absorbing layer, that is comprised of a resonant airspace structure (e.g., honeycomb). Figure 1.1 shows a typical resonant acoustic liner construction for a jet engine flow-duct, taken from reference 1. Resonant liners, by design, absorb acoustic energy in a narrow frequency band. Their use is motivated by the fan (or compressor) noise source that is characterized by discrete tones. Figure 1.2 shows a typical noise spectrum of a large by-pass engine (from reference 1). The design of an acoustic liner, like the one shown in Figure 1.1, is a compromise between conflicting engine operating conditions. Thus, if the liner is optimum for the takeoff condition it will not be optimal for the landing/approach condition. This is because at the different operating conditions, fan speed and the speed of the flow over the liner are different, requiring different absorption performance from the liner. If the acoustic properties of the liner can be altered during the engine's operation, it is possible to increase noise suppression at "off design" conditions. One possible way to achieve variable acoustic properties of a liner is discussed below and is the backbone of this report.

Figure 1.3 illustrates a typical two-layered resonant acoustic liner along with the principal parameters that govern its performance. As mentioned earlier, the facing layer is typically made of a perforated metal sheet or a fine wire mesh. The air space behind this layer is partitioned by a honeycomb structure, providing cells or columns of air. Another airspace is partitioned in the same way beneath the first air space. It is separated from the first air space by another porous sheet (usually a perforate), normally referred to as the "buried

septum". The liner is terminated with a rigid back wall. The overall sound absorbing performance of this type of liner can be determined from knowledge of the acoustic impedance of its individual components. Thus. the total impedance of the liner is a function of the four impedances, Z_1, Z_2, Z_3, and Z_4 labeled in Figure 1.3. The facing layer offers a specific amount of hindrance to an incident sound wave. This hindrance is in essence the acoustic impedance of the facing layer. The impedance of the facing layer is a function of several parameters and is expressed as:

$$Z_{\text{face sheet}} = f\left(h, \sigma, d, u_i, V_{gr}, \omega, T\right)$$

where

h = thickness of perforate sheet

σ = porostiy of perforate sheet

d = Characteristic orifice opening dimension (e.g.. diameter)

u_i = Incident acoustic velocity on perforate sheet

V_{gr} = Grazing flow velocity

ω = Angular frequency of incident acoustic wave

T = Temperature at the facing sheet

The impedance of the air space partitioned by the honeycomb is chiefly determined by the length of the air gap and the temperature of the air in the gap. The buried septum layer has an impedance governed by the same parameters as the facing layer except that there is no grazing flow effect. Simply put. the facing layer governs how much sound reaches the first air gap and the septum governs how much sound reaches the second air gap. Since the septum is not exposed to the grazing flow, it has one less parameter governing its impedance.

This can be explained more clearly by examining two extreme cases. If the septum is acoustically transparent. i.e.. it allows the unhindered transmission of sound. then the air gap length is L_1 + L_2 (see Figure 1.3). If the septum is acoustically rigid. then the air gap length is just L_1 and it would behave as if the second air gap was non-existent. In practice. the impedance of the septum is somewhere between acoustically rigid and acoustically transparent. The degree to which this property of the septum can be controlled is the key to the control of the overall liner absorption. Intuitively. an ideal control parameter is the buried septum porosity, since it is the amount of open area which allows sound to pass through the layer.

1.3 The Variable Orifice Perforate Concept

Figure 1.4 shows how a variable "effective" perforate can be formed from two perforated sheets of identical orifice geometry and porosity. The hole patterns in Figure 1.4b was created by moving one perforated sheet (on top) relative to the other (on bottom). Both the porosity and orifice shape changes result in the change of the acoustic impedance of the perforate and hence the overall impedance of the liner. In this way, small translational movements in one perforate will produce a large change in the "effective" perforate porosity and orifice aperture shape.

A simple demonstration of the variable orifice perforate concept described was carried out in a commercially available impedance tube. An open cavity was coveredwith two perforates of

the identical porosity and orifice size. Figure 1.5 shows two random configurations of orifice hole shapes and porosities. Figure 1.6 shows the resulting absorption coefficient for the two cases as well as results with just one perforate. The absorption coefficient is a measure of the amount of acoustic energy absorbed by the perforate/cavity combination and is a function of the acoustic impedance. It is clear that the different porosity and possibly shape of the resultant perforate can impact the absorption performance of a resonant type material and hence contribute to the control of a multi-layered resonant liner. A study of the effectiveness of this concept is the main thrust of the research for this report.

A possible way of implementing this concept is shown in Figure 1.7. The buried septum in this case is replaced by two perforates, one that is stationary and one that is allowed to slide over the other. As with the sliding perforate concept shown in Figure 1.4. the impedance of the buried septum will change as the orifice pattern changes. Control of the buried septum impedance is expected to control the total impedance of the liner. The varying geometry perforate will be referred to as the "variable orifice perforate" (VOP) in the rest of this document.

1.4   Objective

The objective of the present study is to assess the degree of absorption control that can be achieved by a variable orifice buried septum perforate. An additional objective is to examine the adequacy of the existing impedance models to explain the behavior of the unique orifice shapes that result from the proposed sliding perforate concept.

1.5   Outline of Report

Section II presents previous research and current understanding in the area of orifice and perforate impedance along with some known liner impedance control concepts in the literature. Section III presents an experimental investigation of a two-degree-of-freedom resonant liner that utilizes a variable orifice buried septum to control its absorption performance. This is accomplished through normal incidence impedance measurements and absorption measurements in a flow-duct environment. Section IV describes the result of an experiment where the variable orifice perforate is measured in a normal incidence impedance tube and its absorption characteristics are examined for both low and high amplitude performance. Section V addresses the effect of orifice shape on the acoustic impedance. The impedance of several different orifice shapes are measured in an impedance tube for the same orifice area. The measured data are compared with existing models. Finally. the overall conclusions and suggestions for future work are presented in Section VI. Appendices are provided that detail measurement techniques used in this work as well as an uncertainty analysis used to assess the quality of the data presented.

PRIMARY EXHAUST

FAN (SECONDARY) EXHAUST

FAN DUCT

SPLITTER

CENTERBODY

CONCENTRIC RING

NOSE COWL INLET

HONEYCOMB CORE

SINGLE SANDWICH

ADHESIVE OR WELD

POROUS FACING SHEET

DOUBLE SANDWICH

OPTIONAL POROUS OR IMPERVIOUS FACING SHEETS
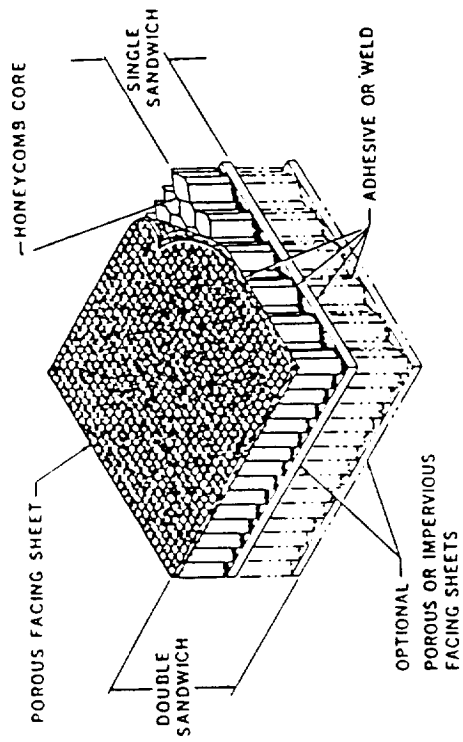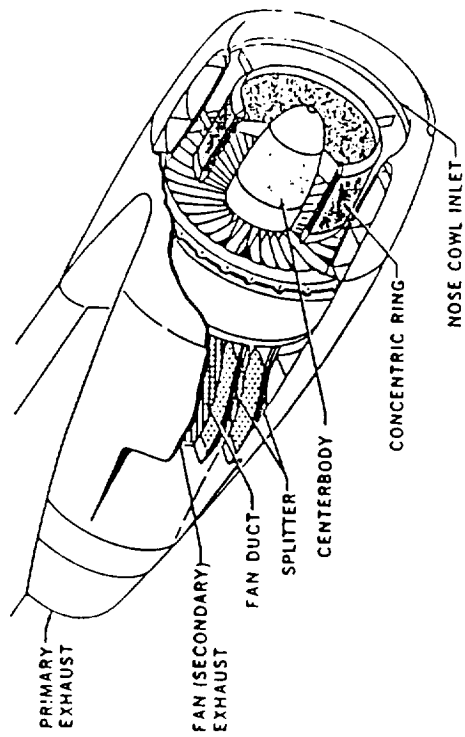
Figure 1.1 Typical construction of acoustic liner for jet engine application (from ref. 1.1).
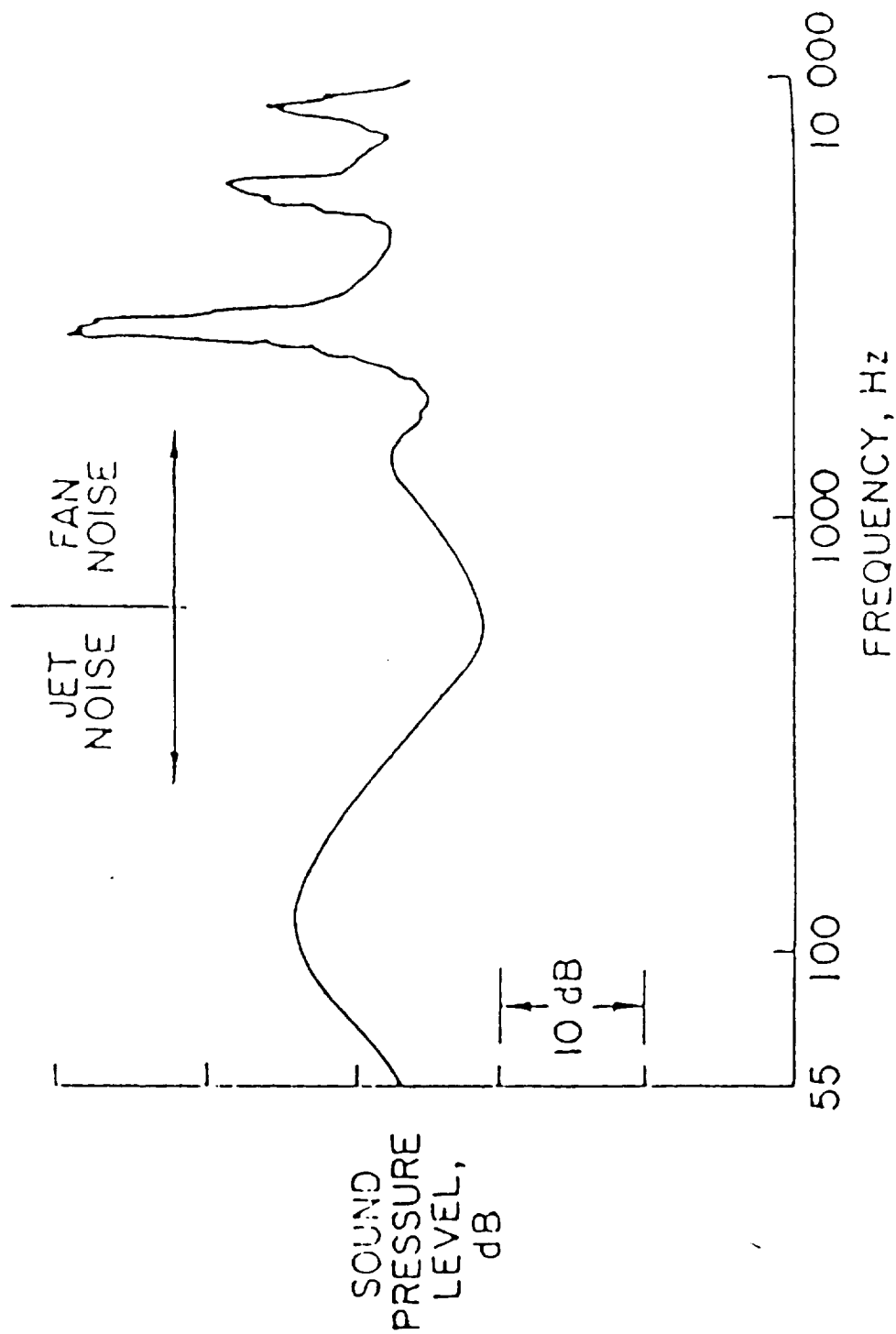
Figure 1.2 Typical jet engine inlet noise spectrum during landing/approach (from ref. 1.1).

Incident Sound
ω

Air gap partioned by honeycomb
$Z_2 = f(\omega, L_1, T)$

Air gap partioned by honeycomb
$Z_4 = f(\omega, L_2, T)$

L_1

L_2

V_{gr}

u_i

Acoustically Rigid Backing

Porous facing sheet (perforated metal)
$Z_1 = f(\sigma, t, r, u_i, V_{gr}, T)$

Buried septum (perforated metal)
$Z_3 = f(\sigma, t, r, u_i, T)$

$Z_{total} = f(Z_1, Z_2, Z_3, Z_4)$

$L = L_1 + L_2$

Z - acoustic impedance
σ - porosity
t - sheet thickness
r - characteristic orifice dimension (e.g. radius)
u_i - incident acoustic velocity
V_{gr} - grazing flow velocity
T - temperature
ω - frequency

Figure 1.3 Constituent parts of a resonant two-degree-of-freedom acoustic liner.

6
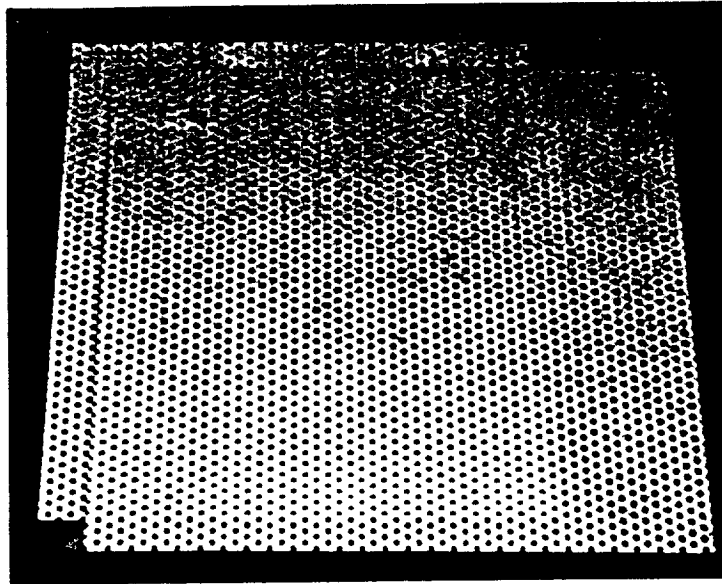
a. Two standard perforates with circular orifices
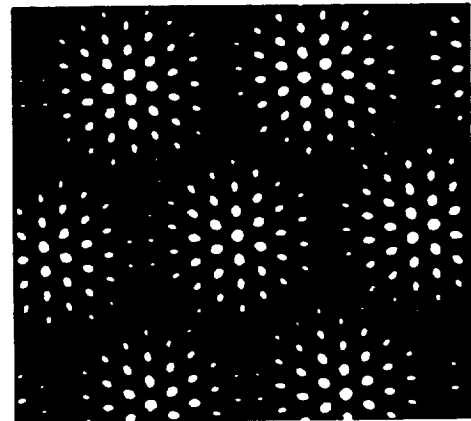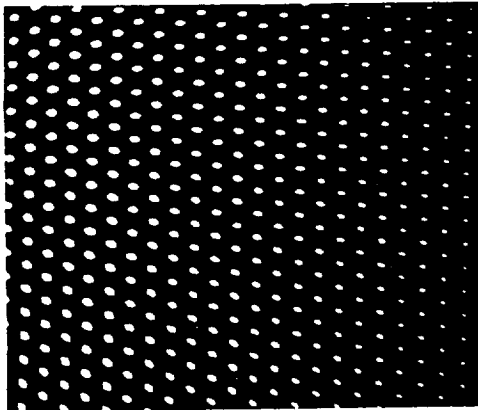
b. Examples of orifice patterns created by sliding one perforat over another

Figure 1.4 Variable orifice perforate concept: two standard circular orifice perforates creating an non-standard perforate.

7
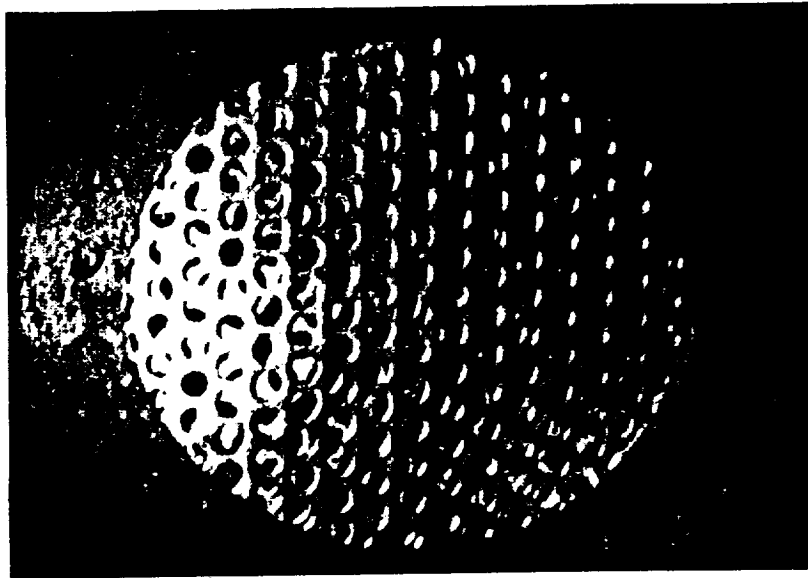
a. 2 Sheets of Perforate #2
Configuration B
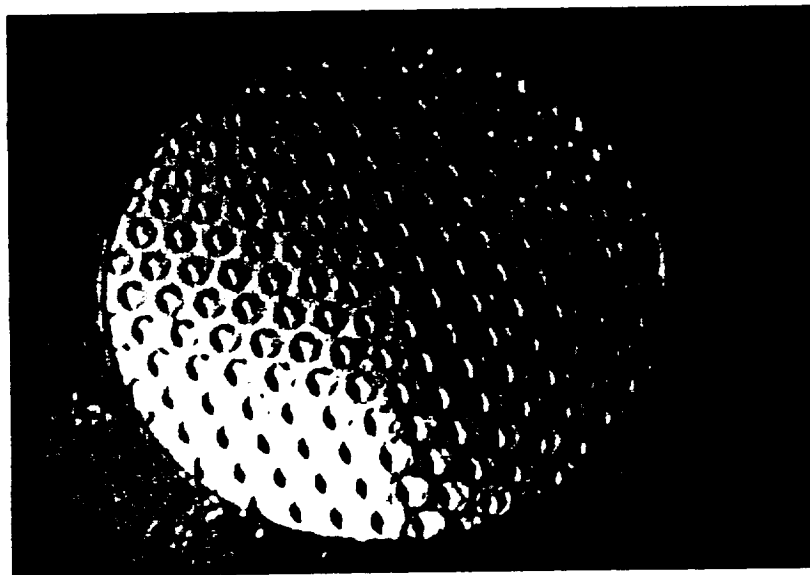
b. 2 Sheets of Perforate #2
Configuration D

Figure 1.5 Variable perforate concept impedance tube arrangement, perforate #2.
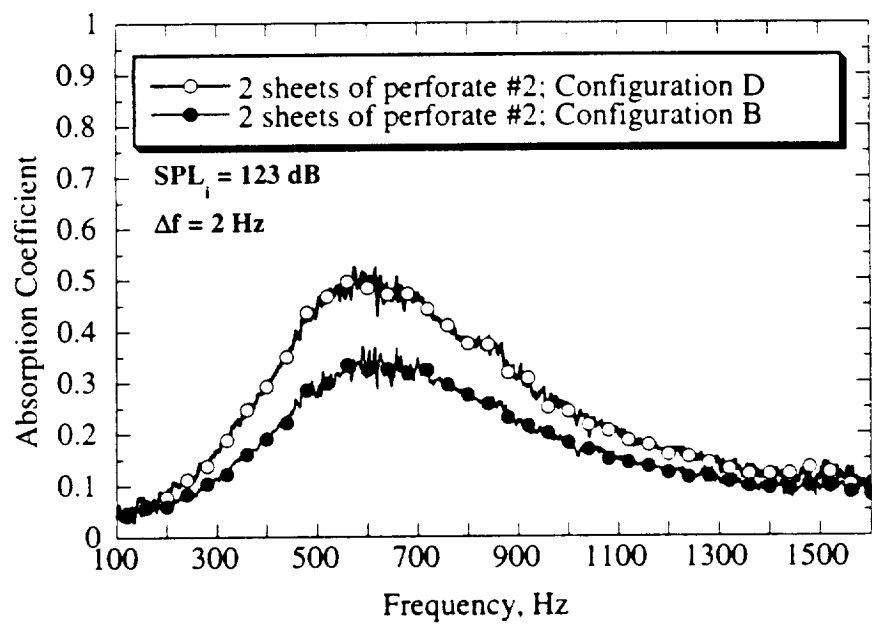
Figure 1.6 Impact of sliding perforates on absorption coefficient of a perforate/
cavity resonator.
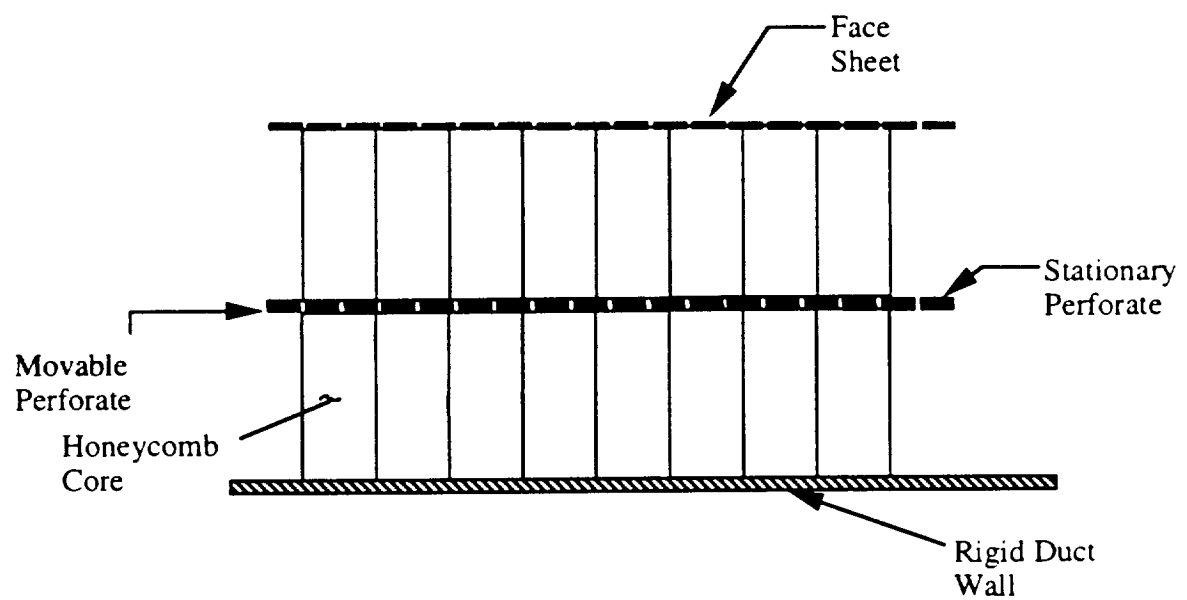
Figure 1.7 Application of variable orifice perforate in a two-degree-of-freedom liner.

10

SECTION II

Acoustic Behavior of Orifices:
Previous Research and Current Understanding

2.1   Introduction

The focus of the present research is the control of wall impedance with the use of a tunable resonant acoustic liner. Typical resonant liners are effective in a narrow frequency range. Controlling that frequency range is of interest when the liner is used in a changing noise spectrum environment. A common component of the resonant liner is a perforated metal sheet, usually referred to as a perforate. A perforate is a porous sheet that is distinguished from a fine wire mesh or other bulk-type material (e.g., fibermetal). Understanding of the sound wave interactions with a perforate or an orifice is critical to the present work because it is the both the size and the shape of these orifices that are deliberately being altered to bring about a change in the overall liner absorbing characteristic. It is from this perspective of the effect of orifice size and shapes on their sound absorbing properties that a discussion of the previous work is provided here.

This section starts in Section 2.2 with a brief description of the physical nature of the sound/orifice interactions. Section 2.3 includes a description of many of the impedance related terms like mass reactance, stiffness reactance, resistance and related equations that define them. Section 2.4 presents a linear model for the acoustic impedance of orifices and perforates. Section 2.5 addresses the effect of high amplitude incident sound on an orifice. Analytical impedance models that address the effect of grazing flow on orifices are presented in Section 2.6. Finally, Section 2.7 presents previous work that involves controlling the impedance of perforate-based acoustic liners.

2.2   The Interaction of Sound with an Orifice

Consider an acoustic wave that propagates along a waveguide tube and strikes an orifice connected to a backing cavity as shown in Figure 2.1. An acoustic wave generated at one end of the tube propagates along the tube and strikes the orifice at the other end of the tube. The resulting interaction is a complex phenomenon that involves the geometry of the tube and backing cavity, the geometry of the orifice and the fluid medium surrounding the orifice on each of its sides. Neglecting any energy loss in the tube, the energy in the acoustic wave is redirected, transformed, and dissipated in and around the orifice. The acoustic energy is partly redirected by sending a portion of the energy back towards the source. It is partly transformed by viscosity at the orifice edges and converted into vortical energy leading to its dissipation. Finally, the acoustic energy is partly transmitted and propagates on the other side of the orifice. The orifice's acoustic impedance is characterized by these conversions of energy.

The transformation of acoustic energy into fluid mechanical energy arises from the viscous interactions that can occur between sound and a solid boundary. Indeed, such interactions can lead to the formation of an oscillatory "jet" on either side of the orifice. Figures 2.2a-b show several views of the "downstream" side of an orifice whoseopposing side is subjected to varying

intensities of acoustic energy in a tube. In this case, the light is provided by a stroboscope. It is flashing at the same frequency as the acoustic wave is propagating in the tube. Thus, coherent structures are captured and "frozen" in space. It is clear that the acoustic energy is partially transformed into vortical energy to a greater extent as the acoustic intensity increases.

Current understanding of this phenomenon has been motivated by the common occurrence of orifices or groups of orifices in acoustic absorbers. This includes common sound absorbing treatment used in rocket motors, jet engines, internal combustion engines, and buildings. Connecting the physical picture described above to analytical formulations of sound absorption is the subject of this section.

2.3 Acoustic Impedance of a Resonant Absorber

Before presenting the impedance models for orifices and perforates, definitions of selected acoustic parameters is provided in a manner that will be useful for understanding the results presented later. In particular, terms like resonance and anti-resonance frequencies as well as the primary and secondary resonance frequencies for a two-degree-of-freedom liner will be defined in terms that will be consistent with the data presented in future sections. Furthermore, the concept of the absorption coefficient is presented.

Definition of Acoustic Impedance

In the context of materials used for acoustic liners, acoustic impedance can be defined as a measure of a material's ability to convert acoustic energy into other forms of energy. Or, in other words, it is a measure of how much a material impedes the flow of acoustic energy. It is mathematically defined as the ratio of acoustic pressure to the associated particle velocity at a point and is expressed as:

$$Z = \frac{P}{u} = R + i\chi \tag{2.1}$$

In general, the pressure and velocity are not in phase, thus the impedance is a complex quantity with a real and imaginary part. The real part is referred the acoustic *resistance* and the imaginary part is referred to as the acoustic *reactance*. The impedance is generally a function of frequency.

It is common practice to normalize the impedance of acoustic liners by the characteristic impedance of the medium through which sound travels before impinging upon the liner. This characteristic impedance of the medium is given by:

$$Z_{characteristic} = \rho c \tag{2.2}$$

Normalizing the impedance allows for the definition for the "perfect" absorption of sound. Since ρc is a real quantity, the impedance of an absorber that has a normalized resistance of unity and normalized reactance of zero results in an absorber that behaves like air. That is, sound will be transmitted through (and/or absorbed by) the absorber with no reflection back towards the source. This is an important concept because it is this impedance matching that determines the effectiveness of an absorber. The optimum acoustic impedance of a liner (no mean flow present) is that which equals the characteristic impedance of the medium in which the liner resides.

Impedance of Cavity Resonators

The development of an expression for impedance of a resonant absorber begins with the consideration of an open cavity of length L as shown in Figure 2.3a. The impedance of the cavity can be determined from standard transmission theory found in many acoustic textbooks. Neglecting viscous effects the normalized impedance at the opening of the cavity can be expressed as:

$$\frac{Z_o}{\rho c} = \frac{\frac{Z_L}{\rho c} + i\tan(kL)}{1 + i\frac{Z_L}{\rho c}\tan(kL)} \qquad (2.3)$$

If the back wall in the cavity is considered to be acoustically rigid, the impedance, Z_L, at L is infinite and equation 2.3 becomes:

$$\frac{Z_o}{\rho c} = -i\cot(kL) \qquad (2.4)$$

If the cavity is then covered with a plate of thickness h and an opening of area A_o (radius, r_o), as shown in Figure 2.3b, the physical picture changes. The fluid in and around the vicinity of the opening can be treated separately from the rest of the cavity. It possesses an impedance of its own and the total impedance of the cavity-backed opening can be expressed as the sum of these individual impedances. Thus, the normalized impedance can be written as[2,4]:

$$\frac{Z}{\rho c} = \frac{Z_{opening}}{\rho c} + \frac{Z_{cavity}}{\rho c} = \frac{Z_{opening}}{\rho c} - i\sigma\cot(kL) \qquad (2.5)$$

$$\text{where } \sigma = \frac{A_o}{A}$$

The Helmholtz Resonator

If the wavelength of the incident sound is much larger than the opening dimensions or the cavity dimensions (e.g., $\lambda \gg r_o$, L), then the physical picture can be represented mechanically as shown in Figure 2.3c. The fluid in and around the opening can be seen as a mass, the fluid in the backing cavity can be treated as a spring, and the viscous forces can be treated a dashpot-damper. Thus, given the condition of very long wavelength compared to the physical dimensions, the resonator can be viewed as a harmonic oscillator with one degree of freedom. This is also referred to as a *lumped acoustic element* model. In essence, the mass oscillates as a bulk mass. The resonator under the conditions stipulated above is referred to as a *Helmholtz* resonator. Two methods will be presented on deriving the expression for impedance of a Helmholtz resonator: 1) A classical development from mechanical vibration theory and 2) A simplification of the more general formulation embodied in equation 2.5.

The Harmonic Oscillator Model

Given the physical model shown in Figure 2.3c, the equation of motion describing the displacement of the mass is well established. It is a linear, ordinary differential equation given by:

$$m \frac{d^2x}{dt^2} + R_{mech} \frac{dx}{dt} + sx = f(t) \qquad (2.6$$

where R_{mech} is defined as the mechanical resistance and s is the spring constant. For the steady-state solution to equation 2.6 the driving force is assumed to be complex of the form:

$$f(t) = Fe^{i\omega t} \qquad (2.7)$$

The solution of the differential equation is then of the form:

$$x = Ae^{i\omega t} \qquad (2.8)$$

where A is in general complex. Substituting equation 2.8 into equation 2.6 and solving for A in terms of the driving force yields an expression for the displacement:

$$x = \frac{Fe^{i\omega t}}{i\omega \left[R_{mech} + i\left(\omega m - \frac{s}{\omega} \right) \right]} \qquad (2.9)$$

Differentiating equation 2.9 yields the complex speed:

$$u = \frac{Fe^{i\omega t}}{\left[R_{mech} + i\left(\omega m - \frac{s}{\omega} \right) \right]} \qquad (2.10)$$

The complex mechanical impedance is defined as the ratio of the driving complex force to the resultant complex speed at the point where the force is applied. Thus from equation 2.10, this ratio is:

$$Z_{mech} = \frac{Fe^{i\omega t}}{u} = R_{mech} + iX_{mech}$$

$$= R_{mech} + i\left[\underbrace{\omega m}_{\substack{\text{Mechanical} \\ \text{Mass Reactance}}} - \underbrace{\frac{s}{\omega}}_{\substack{\text{Mechanical} \\ \text{Stiffness Reactance}}} \right] \qquad (2.11)$$

Note that the mechanical reactance of the system can be separated into two parts: the *mechanical mass reactance* and the *mechanical stiffness reactance*. The mechanical mass reactance is the inertial contribution from the mass of air in the orifice. By analogy, the stiffness reactance is that part of the acoustic reactance that results from the air contained in the backing cavity. Thus, the cavity provides the "spring" for the system. In general, the total reactance acts as a mechanism that can store and release energy provided by the driving force, just like the spring and mass in the spring-mass system.

The acoustic impedance results from normalizing the mechanical impedance by the orifice area. The normalized acoustic impedance then becomes:

$$\frac{Z}{\rho c} = \frac{Z_{mech}}{A_o \rho c} = \frac{R_{mech}}{A_o \rho c} + i \left[\underbrace{\frac{\omega m}{A_o \rho c}}_{\substack{\text{Acoustic} \\ \text{Mass Reactance}}} - \underbrace{\frac{s}{\omega A_o \rho c}}_{\substack{\text{Acoustic} \\ \text{Stiffness} \\ \text{Reactance}}} \right] = \frac{R}{\rho c} + i \frac{\chi}{\rho c} \qquad (2.12)$$

The first term in brackets in equation 2.12 is referred to as the *normalized mass reactance* which is the reactance associated with the opening of the resonator. The second term in brackets is referred to as the stiffness reactance. A description of the stiffness constant, s, can now be expressed in terms of thermodynamic and geometric parameters.

The stiffness constant is analogous to the spring constant that obeys Hooke's law where the force applied is the acoustic pressure multiplied by the resonator opening area and x is the distance needed for the "spring" to maintain this force:

$$Force = pA_o = sx \qquad (2.13)$$

The volume change due to the mass pushing the air in the resonator cavity is:

$$\Delta V = -A_o x \qquad (2.14)$$

The acoustic pressure can be written in terms of the change in volume using the equation of state:

$$p = \rho c^2 \left(\frac{\Delta \rho}{\rho} \right) \qquad (2.15)$$

The change in instantaneous density can be written as:

$$\frac{\Delta \rho}{\rho} = \frac{\Delta V}{V} \qquad (2.16)$$

Using equations 2.14 - 2.16, the stiffness constant can be expressed as:

$$s = \rho c^2 \frac{A_o^2}{V} \qquad (2.17)$$

15

Now the impedance of the Helmholtz resonator using equation 2.17 and 2.12 can be expressed as:

$$\frac{Z}{\rho c} = \frac{R}{\rho c} + i\left[\frac{\omega m}{A_o \rho c} - \frac{cA_o}{\omega V}\right] \qquad (2.18)$$

For a cavity that is cylindrical with area A and length L, equation 2.18 can be rewritten as:

$$\frac{Z}{\rho c} = \frac{R}{\rho c} + i\left[\frac{\omega m}{A_o \rho c} - \frac{cA_o}{\omega AL}\right] \qquad (2.19)$$

$$= \frac{R}{\rho c} + i\left[\frac{\omega m}{A_o \rho c} - \frac{\sigma c}{\omega L}\right]$$

Simplification of the General Cavity Model

The expression for the Helmholtz resonator impedance can also be found from a more general expression beginning with equation 2.5. Comparing equation 2.5 with equation 2.19, the impedance of a cavity-backed opening can be expressed as:

$$\frac{Z}{\rho c} = \frac{R}{\rho c} + i\left[\frac{\omega m}{A_o \rho c} - \sigma \cot(kL)\right] \qquad (2.20)$$

Equation 2.20 is more general than equation 2.19 because it can be applied for conditions when the incident acoustic wavelength is large or small compared to the dimensions of the resonator. This can be seen by replacing the cotangent function with its equivalent series expansion[25]:

$$\frac{Z}{\rho c} = \frac{R}{\rho c} + i\left[\frac{\omega m}{A_o \rho c} - \sigma\left(\frac{1}{kL} - \frac{kL}{3} - \frac{kL^3}{45} + H.O.T.\right)\right] \qquad (2.21)$$

In order to consider the resonator a Helmholtz resonator, the wavelength must be small compared to the resonator dimensions. This corresponds to kL >> 1 and equation 2.21 becomes:

$$\frac{Z}{\rho c} = \frac{R}{\rho c} + i\left[\frac{\omega m}{A_o \rho c} - \frac{\sigma}{kL}\right]$$

$$= \frac{R}{\rho c} + i\left[\frac{\omega m}{A_o \rho c} - \frac{\sigma c}{\omega L}\right] \qquad (2.22)$$

Equation 2.22 is equivalent to the result derived from the harmonic oscillator model given by equation 2.19.

Resonance and Anti-Resonance

An important aspect of an acoustic resonator is its resonance frequency. Acoustic resonance and anti-resonance are defined as follows[23]:

Resonance: Occurs when the liner resistance is *small* and the reactance vanishes.
Anti-Resonance: Occurs when the liner resistance is *large* and the reactance vanishes.

Thus when resonance occurs, the imaginary part of impedance is zero providing that the resistance is relatively small. The resonance frequency of a Helmholtz resonator can be

determined by finding the frequency at which the imaginary part of equation 2.19 becomes zero. This yields:

$$\omega_{res}^{2} = \frac{c^{2}A_{o}\rho}{mL} \qquad (2.23)$$

The mass can be expressed from the density of the fluid and geometry of the opening as:

$$m = \rho A_{o} h' \qquad (2.24)$$

$h' \equiv$ thickness of covering plate + some additional length

This mass will be referred to as the *acoustic mass*, as it is the mass that contributes to the acoustic impedance. The additional length is referred to the mass or inertial end correction to the plate thickness, h, and will be discussed further in the next section. Substituting equation 2.24 into equation 2.23 results in the well known equation for the resonance frequency of a Helmholtz resonator:

$$\omega_{res} = c\sqrt{\frac{A_{o}}{Vh'}} \qquad (2.25)$$

$V \equiv$ Resonator Volume

The resonance frequency can also be determined from the more general expression in equation 2.20. Equating the normalized reactance to zero yields a transcendental equation whose roots are the resonance frequencies of the resonator.

$$\omega_{res} - \frac{\sigma c}{h'} \cot(\frac{\omega_{res} L}{c}) = 0 \qquad (2.26)$$

For large wavelengths, the first root to equation 2.26 will be equivalent to that obtained from equation 2.25. The higher multiple roots result from standing waves in the cavity and are not harmonically related to the smallest root. In Sections IV and V, the resonance frequencies of a cavity-backed perforate or orifice will be referred to as the 1st, 2nd, 3rd, etc. resonance frequencies corresponding to the lowest to highest roots to equation 2.26.

Primary and Secondary Resonance of 2DOF Liner

If two-cavities are connected by an opening similar to that shown in Figure 2.3b, then the resulting model is considered to be a two-degree-of-freedom (2DOF) system if the incident wavelength is much greater than the cavity and opening dimensions. The 2DOF liner resonance frequency can be determined from a more complicated expression for a double Helmholtz resonator (see Blevins[26]) that results in two resonance frequencies.

These resonance frequencies can also be determined from an expression for the combined liner impedance. In the next section, an expression is developed for the impedance of an orifice and a perforate which are typical coverings for the two cavities making up the 2DOF liner. The combined 2DOF liner impedance model will be presented in Section III. The frequencies at which the normalized reactance of this combined system is zero and the normalized resistance is relatively small are the resonance frequencies. The corresponding frequency at which the normalized resistance is very large while the reactance vanishes is the anti-resonance frequency.

17

The lowest frequency that corresponds to resonance will be referred to as the *primary* resonance frequency. Likewise, the next highest frequency corresponding to resonance will be referred to as the *secondary* resonance frequency. This terms will be used for the 2DOF liner study presented in Section III.

Absorption Coefficient

A common and useful quantity that can be computed from the impedance is the absorption coefficient. It is a measure of the amount of incident acoustic energy that is absorbed by a given material. For the condition of no mean flow and normal incidence, the absorption coefficient is defined as:

$$\alpha = 1 - |R_f|^2 \tag{2.27}$$

Where R_f is the normal incidence reflection coefficient. The reflection coefficient represents the fraction of incident acoustic pressure that is reflected back towards the source and is defined as:

Where P_r and P_i are the incident and reflected acoustic pressures, respectively. For plane waves

$$R_f = \frac{P_r}{P_i} \tag{2.28}$$

where

$$P_i = Ae^{i(\omega t - kx)}$$

$$P_r = Be^{i(\omega t + kx)}$$

and normal incidence, the impedance at the surface of a material is expressed as the ratio of the acoustic pressure to the particle velocity at the surface. This derives from the mechanical analogy mentioned above where the impedance was defined as the ratio of the driving force to the speed of the mass. At the surface of a material exposed to normal incidence planar acoustic waves, the complex impedance (Z_s) can be expressed in terms of incident and reflected quantities as:

$$Z_s = \frac{P_i + P_r}{u_i + u_r} \tag{2.29}$$

For plane waves, the particle velocity can be written in terms of the wave impedance of the propagating medium. With air as the propagating medium, u_i and u_r are expressed as:

$$u_i = \frac{P_i}{\rho c}; \quad u_r = -\frac{P_r}{\rho c} \tag{2.30a,b}$$

Using the definition of incident and reflected acoustic pressure from equation 2.28 along with equation 2.29, the surface (x = 0) impedance can be expressed as:

$$Z_s = \rho c \frac{A + B}{A - B} \tag{2.31}$$

18

Now the square of the reflection coefficient amplitude can be expressed in terms of the incident and reflected pressure amplitudes:

$$|R_f|^2 = \frac{|P_r|^2}{|P_i|^2} = \frac{B^2}{A^2} \qquad (2.32)$$

Solving for the reflected amplitude. B. in terms of the incident amplitude. A from equation 2.31 and substituting into equation 2.32 yields:

$$|R_f|^2 = \frac{\left|\left(\dfrac{Z_s}{\rho c} - 1\right)\right|^2}{\left|\left(\dfrac{Z_s}{\rho c} + 1\right)\right|^2} \qquad (2.33)$$

From equation 2.33 and 2.27 the absorption coefficient becomes:

$$\alpha = 1 - \frac{\left|\left(\dfrac{Z_s}{\rho c} - 1\right)\right|^2}{\left|\left(\dfrac{Z_s}{\rho c} + 1\right)\right|^2} \qquad (2.34)$$

Finally. the absorption coefficient can be written in terms of resistance and reactance. Substituting the complex impedance components into equation 2.34 and after some manipulation, the absorption coefficient can be expressed as:

$$\alpha = \frac{4\left(\dfrac{R_s}{\rho c}\right)}{\left(\dfrac{R_s}{\rho c} + 1\right)^2 + \left(\dfrac{X_s}{\rho c}\right)^2} \qquad (2.35)$$

Equation 2.35 is used to compute the absorption coefficient from measured impedance in a normal incidence. plane wave environment.

2.4   Linear Model for Impedance of Orifices

By far the most common orifice geometry is circular and therefore the bulk of the literature deals with circular orifices. When noncircular orifice shapes are discussed in the literature. square or rectangular shapes are normally addressed. The orifice shapes that will be studied in the present work will be much more deviant from circular or even rectangular. The development of an analytical expression for the impedance of an orifice under linear assumptions is now presented. The term "linear" in the present context is defined as the impedance of the orifice behaving independent of incident sound pressure level. Conversely. the term "nonlinear" implies that the orifice impedance is a function of the incident sound pressure level.

Impedance Within Narrow Tubes

If the orifice is treated as a narrow tube. as shown in Figure 2.4. then by balancing the viscous and inertial forces the acoustic impedance can be expressed by [25]:

$$-\frac{\partial p}{\partial x} = \left[i\omega\rho - \frac{\mu}{r}\frac{\partial}{\partial r}\left(r\frac{\partial}{\partial r} \right) \right] u \qquad (2.36)$$

Equation 2.36 can be re-written as:

$$-\frac{1}{\mu}\frac{\partial p}{\partial x} = \left[\frac{\partial^2}{\partial r^2} + \frac{1}{r}\frac{\partial}{\partial r} + k_s^2 \right] u \qquad (2.37)$$

$$\text{where} \quad k_s^2 = -\frac{i\omega\rho}{\mu}$$

Equation 2.37 can now be solved using Bessel Functions. Taking the ratio of the pressure to the velocity. the acoustic impedance of the narrow tube is:

$$Z_{tube} = \frac{i\omega\rho h}{\left[1 - \frac{2J_1(k_s r_o)}{k_s r_o J_0(k_s r_o)} \right]} \qquad (2.38)$$

where

J_0 . J_1 are zeroth and first order Bessel functions of the first kind

The quantity. k_s. is the wave number associated with the viscous Stokes wave. Equation 2.38 can be approximated and assumes that all of the forces are linear. that is. the viscous and inertial forces are independent of the acoustic driving force. After normalizing with respect to the characteristic impedance of air. ρc, equation 2.38 can be approximated depending on the value of $|k_s r_o|$:

$$\frac{Z_{tube}}{\rho c} = \frac{h\sqrt{2\omega v}}{c r_o} + i\frac{h}{c}\left[\frac{\sqrt{2\omega v}}{r_o} + \omega \right] \qquad \text{for } |k_s r_o| > 10 \qquad (2.39)$$

$$\frac{Z_{tube}}{\rho c} = \frac{8vh}{c r_o^2} + i\frac{4}{3}\frac{\omega h}{c} \qquad \text{for } |k_s r_o| < 1 \qquad (2.40)$$

$$\frac{Z_{tube}}{\rho c} = \frac{8vh}{c r_o^2}\sqrt{1 + \frac{|k_s r_o|^2}{32}} + i\frac{\omega h}{c}\left[1 + \frac{1}{\sqrt{9 + \frac{|k_s r_o|^2}{2}}} \right] \qquad \text{for } 1 < |k_s r_o| < 10 \qquad (2.41)$$

20

The real portion of equation 2.39 was first determined by Helmholtz[ ]. The real part of equation 2.40 is known as Poiseuille's law of resistance for laminar flow in narrow tubes. For most orifices and perforates in acoustic liners, equation 2.39 is applicable. When $1 < |r_o k_s| < 10$, Maa[ ] offers the approximation in equation 2.41. Equations 2.38 - 2.41 are expressions for the impedance of a viscous medium set in motion inside a tube of length, h.

Definition of the End Correction

The impedance expressed in the equation 2.38 does not address the contribution of the air just outside the orifice on each side. Consider a single circular orifice in an infinite plane as shown in Figure 2.5. When the orifice is exposed to incident sound, the air inside the orifice oscillates in some relationship with the driving acoustic force. That is, the air in the orifice behaves as a piston of air. The vibrating mass of air in the orifice "pushes" portions of the surrounding air on either side of the orifice, labeled as attached mass in Figure 2.5. This leads to the so-called "end-correction."[ ] The additional impedance that is associated with the attached mass is constructed from the radiation impedance of the orifice.

Radiation Impedance

If the orifice is analyzed as a thin circular piston of air in an infinite baffle, then under acoustic excitation, the piston will radiate sound back towards the source direction. The resulting impedance can be expressed as[ ]:

$$Z_{rad} = A_o \rho c (R_{rad} + i X_{rad}) \qquad (2.42a)$$

where

$$R_{rad} = 1 - \frac{J_1(2kr_o)}{2kr_o} = \frac{(2kr_o)^2}{2^2 \bullet 1 \bullet 2!} - \frac{(2kr_o)^4}{2^4 \bullet 2! \bullet 3!} + \cdots \qquad (2.42b)$$

$$X_{rad} = \frac{4}{\pi} \left[\frac{2kr_o}{3} - \frac{(2kr_o)^3}{3^2 \bullet 5} + \frac{(2kr_o)^5}{3^2 \bullet 5^2 \bullet 7} - \cdots \right] \qquad (2.42c)$$

When $kr_o \ll 1$, or when the acoustic wavelength is much greater than the orifice radius, the normalized radiation impedance simplifies to:

$$\frac{R_{rad}}{\rho c} \cong \frac{1}{2}(kr_o)^2 = \frac{1}{2}\left(\frac{\omega}{c}r_o\right)^2 \qquad (2.43a)$$

$$\frac{X_{rad}}{\rho c} \cong \frac{8}{3\pi}(kr_o) = \frac{8}{3\pi}r_o\frac{\omega}{c} \qquad (2.43b)$$

Note that the radiation reactance in equation 2.43b is of the same form as the reactive (imaginary) part of equations 2.39 - 2.41, namely, the inertial contribution. Similarly, the

resistive (real) part of equation 2.43a can be grouped with the real part of equations 2.39 - 2.41. The radiation impedance forms the basis for the end-correction to the core orifice impedance.

Mass Inertial End Correction

Recall from Section 2.3, that the acoustic impedance of a cavity resonator is analogous to driven mass-spring oscillator. As the mass oscillates, it alternatively accepts and re-distributes acoustic energy. From Figure 2.5 the mass reactance can be broken up into regions within the orifice and external to the orifice. The imaginary part of equation 2.38 represent the reactance of the orifice *within* the orifice, denoted by χ_{mi} below. It is common to ignore the viscous component of the imaginary part of equation 2.38 since it is usually very much smaller than the impedance of air[24]. The *external* contribution (denoted by χ_{me}) comes from the radiation impedance. Classically[2,10] the radiation reactance was assumed to be acting on both sides of the orifice. Thus by combining the imaginary part of equation 2.38 (ignoring the viscous component) and twice equation 2.43b, the total mass reactance of the orifice is:

The term δ_m in the parenthesis of equation 2.44 is considered the effective length that should be

$$\frac{\chi_m}{\rho c} = \frac{\chi_{mi}}{\rho c} + \frac{\chi_{me}}{\rho c}$$

$$= \frac{\omega}{c}\left(h + 2 \underbrace{\frac{8}{3\pi} r_0}_{\delta_m} \right) \qquad (2.44)$$

added to the orifice thickness, *h*, for determination of the mass reactance. Therefore the classical inertial mass end correction is given by:

$$\delta_m = 2\left(\frac{8}{3\pi} r_o \right) \qquad (2.45)$$

Radiation Impedance Revisited

The end correction expressed in equation 2.45 was developed in the context of a circular orifice radiating in an infinite baffle. The radiation impedance of a noncircular orifice is more complex and was first addressed by Ingard[2] and more recently by Chanaud[27]. Ingard examined corrections for orifices that were rectangular as well as circular and that were backed on one side with a rectangular or a circular cavity. He computed the correction due to a "noncircular" baffled piston radiating to a circular or rectangular tube. His key result germane to the current work is his analytical approximation for orifices of area A_o radiating into cylindrical tubes. For orifice radius to tube radius ratios less than 0.4, his approximate mass end-correction was:

$$\delta_{mi} \cong 0.48 * \sqrt{A_o}(1 - 1.25\xi) \qquad (2.46)$$

$$\text{where } \xi = \frac{r_o}{R}$$

22

$$\delta_{m-facing\ cavity} = \frac{L}{A_o A_c} \sum_{m=0}^{\infty} \sum_{n=0}^{\infty} \upsilon_{mn} I_{mn}^2 \frac{\coth(k_x L)}{k_x L} \qquad (2.47)$$

where

L Cavity Depth

A_o Orifice Area

A_c Cavity Cross Sectional Area

$\upsilon_{oo} = 1$

$\upsilon_{m0} = \upsilon_{0n} = 2$, for all m and n

$\upsilon_{mn} = 4$, for all m and n

$$I_{mn} = \oiint_{orifice} \cos\left(\frac{m\pi y}{a}\right)\cos\left(\frac{n\pi z}{b}\right) dy dz$$

Here, R is the cylindrical tube radius. Equation 2.46 holds for circular and square orifices backed by a cylindrical tube. If the orifice has the same cylindrical cavity on both sides, then the total mass end correction is twice that found from equation 2.46.

Chanaud also examined rectangular orifices as well as orifices made up of two rectangular shapes placed perpendicular to each other (referred to as "cross-orifices"). Figure 2.6 shows the orifice shapes Chanaud examined. For the side of the orifice that faces away from the cavity. Chanaud found that no closed form solution for a rectangular radiating piston existed; so he restricted his analysis to wavelengths much larger than the longest dimension of the orifice. This is equivalent to $kr_o << 1$. Chanaud then computed an equivalent round orifice radius that had the same area as the non-circular orifice. The equivalent radius was then used as one part of the mass inertial end correction.

For the side of the orifice facing the inside of the cavity, Chanaud followed Ingard's formulation for an orifice backed by a rectangular cavity and this part of the mass internal end correction resulted in the expression:

The integral in equation 2.47 depends on the geometry of the orifice. In general, this more complicated end correction becomes important when the dimensions of the cavity become extreme, i.e., shallow and wide cavities or deep and narrow cavities. Under the assumption of the incident wavelength being much larger than the orifice dimensions, Chanaud concluded that orifice shape does not significantly affect the resonance frequency of a resonator even though the interior mass end corrections he computed by equation 2.47 were between 50 and 70 percent of that predicted by the classical formula (see equation 2.45). These conclusions were based on orifice areas that were 12.6% of the resonator face area and they suggest that the contribution from the orifice shape to the end correction does not impact the total resonance of the system significantly. Chanaud did not examine the effects of high amplitude sound impinging on non-circular orifice shapes.

Mass End Correction for an Elliptical Orifice

The present study deals with orifice shapes that, in some cases, can be close to elliptical in shapes. An analytical expression for the mass end correction for an elliptical orifice is now presented.

The mass end correction for an orifice of area A_o can be expressed as[2][13]:

$$\delta_m = \frac{A_o}{K} \qquad (2.48)$$

The term K is referred to as the orifice conductivity. Rayleigh[2][14] derived an analytical expression for the conductivity of an ellipse which is:

$$K = \left(2\sqrt{\frac{A_o}{\pi}}\right)\left[1 + \frac{\varepsilon^4}{64} + \frac{\varepsilon^4}{64} + \ldots\ldots\right] \qquad (2.49)$$

where $\varepsilon \equiv$ eccentricity

The eccentricity of the ellipse is defined as:

$$\varepsilon = \frac{\sqrt{a^2 - b^2}}{a} \qquad (2.50)$$

where $a \equiv$ semi-major axis

$b \equiv$ semi-minor axis

Substituting equation 2.49 into 2.48 yields:

$$\delta_m = \frac{\dfrac{\sqrt{\pi A_o}}{2}}{\left[1 + \dfrac{\varepsilon^4}{64} + \dfrac{\varepsilon^4}{64} + \ldots\ldots\right]} \qquad (2.51)$$

Thus, for a circular orifice (eccentricity = 0), the end correction is consistent with twice the end correction expressed in equation 2.46.

Viscous End Correction

The attached mass present outside of the orifice also has an effect on the resistance of the orifice. In a sense, the additional "tube length" represented by the attached mass end correction will increase the viscous resistance. Sivian[2] recognized the need for this correction and he assumed that this added length was the same as the inertial end correction, namely, that expressed in equation 2.45. Ingard[2][11] found from his experiments that the viscous end correction was closer to a value of $2r_0$. This latter correction has been generally accepted and is used in most perforate impedance models[2][7]. The resistive contribution from the radiation impedance is usually neglected because its magnitude is much smaller than the internal viscous impedance. The viscous end correction can be applied directly to equation 2.38 (or equation 2.39 - 2.41) as an addition to the orifice thickness.

The increased orifice resistance due to conversion of acoustic energy into vortical energy is treated as a fluid dynamic loss that can be expressed as a function of the mean (root mean squared) velocity through the orifice. This effect, which is substantial, is treated in the next section.

Accounting for Interactions between Multiple Orifices

As multiple orifices exist in a perforate, they can interact with each other and affect the overall perforate impedance depending upon how close the orifices are spaced. This is determined by the porosity of the perforate which is a ratio of the open-area to the total area exposed to incident sound. Recall the physical picture presented in Figure 2.5 of the so-called attached mass of an orifice. The extra "length" of the orifice was idealized as a cylindrical extension of the orifice. Melling[2] suggests that the actual attached mass distribution is more like that shown in Figure 2.7. As the spacing of the a perforate is reduced, the attached mass for each orifice can interact with each other. This interaction reduces the amount of mass outside of the hole region that can be affected by the oscillatory motion of the air inside of each orifice. Thus, the mass reactance of the total perforate will be reduced. Since the spacing is a function of the perforate's porosity, the inertial end correction and hence the mass reactance will be reduced as the porosity is increased.

Ingard[2] considered the interactions of two orifices and concluded that (combining the effect on both sides of the orifice) a modified inertial end correction should be:

$$\delta_m = 2\left(\frac{8}{3\pi} r_o\right)\left(1 - \sqrt{\frac{\sigma}{2}}\right) \tag{2.52}$$

where σ is the porosity of the perforate and is defined as the ratio of open area of the perforate to the total area it encompasses. This interaction effect has been generally adopted for impedance models of perforates.

Summary of Linear Impedance Model

We can now write down an expression for the normalized impedance of an orifice by using equation 2.38 and the concept of end corrections:

$$\frac{Z_o}{\rho c} = \frac{R_o}{\rho c} + i\frac{\chi_o}{\rho c} \qquad (2.53)$$

$$= \text{Real}\left\{\frac{i\omega\, h_{vis}'}{\left[1 - \frac{2J_1(k_s r_o)}{k_s r_o \text{Jo}(k_s r_o)}\right]}\right\} + \text{Imag}\left\{\frac{i\omega\, h_m'}{\left[1 - \frac{2J_1(k_s r_o)}{k_s r_o \text{Jo}(k_s r_o)}\right]}\right\}$$

where

$$h_{vis}' = h + \delta_{vis}$$

$$h_m' = h + \delta_m$$

For circular orifices and most applications, the accepted values of the end corrections are:

$$\delta_{vis} = 2r_o \qquad (2.54a)$$

$$\delta_m = 2\left(\frac{8}{3\pi}r_o\right) \qquad (2.54b)$$

Equation 2.54b can be corrected for an elliptical orifice using equation 2.51. For a perforate of porosity σ equation 2.53 is multiplied by $1/\sigma$ and the inertial end correction is modified using equation 2.52. The multiplication of the inverse of the porosity is to account for the correct particle velocity in each orifice by enforcing continuity. That is, the particle velocity in each hole is expressed from continuity as:

$$u_n = \sigma u_o \qquad (2.55)$$

where $u_n \equiv$ Incident particle velocity

$u_o \equiv$ Particle velocity in orifice

The perforate impedance then becomes:

$$\frac{Z_{perf}}{\rho c} = \frac{Z_o}{\sigma \rho c} \qquad (2.56)$$

with

$$h_m' = h + \left[2\left(\frac{8}{3\pi}\right)\right]\left[1 - \sqrt{\frac{\sigma}{2}}\right]$$

26

2.5   Nonlinear Effects Part I: Orifice Impedance at High Sound Amplitudes

It is generally acknowledged that Sivian[21], in 1935, was the first to observe the phenomenon of increasing acoustic resistance (thus, impedance) with a corresponding increase of the orifice particle velocity. This observed behavior has many far-reaching implications in the design of resonant absorbers that rely on perforates and/or single orifices, including classical Helmholtz resonators. Since the theories discussed in the previous section do not reflect this behavior, a description is needed to account for the rapid increase in orifice impedance with orifice velocity. A failure to account for this in the design of resonators can lead to large errors in the prediction of impedance at high incident sound pressure levels. Furthermore, the present research is concerned with the effect of orifice shape on this high velocity phenomenon and as such, attention needs to be paid to how the shape will impact any analytical treatment. To the author's knowledge, the previous work dealing with the nonlinear aspects of orifice impedance has dealt almost exclusively with circular orifices, most notably by Sivian[10], Ingard and LaBate[2], Ingard[11], Ingard and Ising[16], Zinn[17], Melling[9], Hersh and Rogers[18], Cummings[5], and Salikuddin and Brown[20]. In selected cases where the nonlinear response of a non-circular orifice has been studied, the shape has been rectangular [Sivian]. An exception is the work reported by Prasad[22]. He looked at the nonlinear behavior of what he referred to as louver orifices for automobile muffler use.

The effects of high amplitude incident sound on the impedance of an orifice can be summed up with two simple statements: 1) The acoustic resistance increases as a function of the sound amplitude and 2) the acoustic reactance stays relatively constant but starts to decreases after a certain sound intensity is reached. The physical reasons for these effects and how they can be incorporated into impedance modeling will be discussed in terms of resistance and reactance separately.

Acoustic Resistance

When Sivian[10] observed the marked increase in resistance with a corresponding increase in particle velocity in the orifice, he at first speculated that the resistance increase was mainly due to the turbulence within the orifice. However, his calculations of Reynolds number was much lower than what has been typically assumed for turbulent flow, i.e., below 1400. For all of the orifices he tested, the increase in resistance for all orifices had a remarkably similar trend, namely, a relatively constant resistance below orifice velocities of 0.5 m/s followed by a rapid rise that appeared to be linearly proportional to the velocity. Figure 2.8 shows this trend. At orifice velocities below 0.5 m/s, the resistance was observed to be independent of the orifice velocity. This corresponded to the linear viscous resistance that can be predicted by equation 2.53. Above a particle velocity of about 1 m/s, the resistance increased in proportion to the orifice velocity. This formed the nonlinear region of acoustic resistance of an orifice. Since the flow in the orifice was thought to be in the laminar regime, Sivian theorizes that the increased resistance is an effect of the increased kinetic energy within the orifice. In other words, the acoustic resistance at high particle velocities can be thought of as a steady flow pressure loss. This pressure difference across the orifice is the kinetic energy as expressed in Bernoulli's equation. This acoustic pressure then becomes directly proportional to the square of the particle velocity. When expressed in terms of impedance the resistance can be approximated as:

$$R \approx R_o + \frac{1}{2}\frac{\rho |U|}{A_o}$$

(2.57)

27

Where R_o is the resistance associated with the "low orifice velocity" case and $|U|$ recognizes that the flow in the orifice aperture is alternating. Plotting equation 2.57 with his data, he found that it followed the trends reasonably well. Sivian observed the behavior of the resistance at high orifice velocities, the so-called nonlinear behavior, and concluded that it can be explained partially on the basis of the pressure loss across the orifice due to particle velocity acceleration, i.e. an increase in kinetic energy. He speculated that turbulence can be a factor, but need not be the sole cause.

In an important article, Ingard and Labate[21] undertook a detailed study of acoustic incident sound on an orifice by examining the flow patterns resulting from the sound-orifice interaction. By visualizing the flow patterns in and around 25 circular orifices of different thickness and diameters exposed to an incident sound wave, they distinguish four distinct regions of flow as the particle velocity in the orifice is increased. They developed a phase diagram from their data and showed that the acoustic impedance is closely connected to the flow regimes identified separately. Ingard and Labate referred to the various flow patterns as manifestations of what they call circulation. In the context of their work, they used the word "circulation" to describe the resulting vorticity in and around the orifice resulting from incident sound. In modern terms, this can be described as the conversion of sound into vorticity that is generated at the orifice edges. A typical phase diagram from their work is shown in Figure 2.9. The four regions of the diagram are described as follows[21]:

Region I: Low sound intensity, where the flow is directed *out* along the axis of the orifice and the circulation is stationary.

Region II: Flow is directed *in* along the axis of the orifice, where conditions are reverse of region I.

Region III:Medium sound intensity where pulsatory effects are superimposed on a stationary circulation.

Region IV:High intensity sound where pulsatory effects are dominant, resulting in the formation of jets and vortex rings synchronized with the sound

The terms *out* and *in* used above are defined as movement away from the sound source and towards the source, respectively. As noted above, Region IV is characterized by a distinct jet. Recall Figure 2.2 shows evidence of the strong jetting representative of region IV described above. It was found that for thicker orifices, it required more sound intensity to produce the jet in region IV. Relatively thin perforates with orifice diameters less than 0.2 cm are more commonly used in applications for acoustic liners. For such orifices the incident frequencies are such that it is possible for that a jump from region I to region IV can occur as shown in the lower frequency region of Figure 2.9. Thus, intense jetting of the fluid in and out of the orifice with its attendant vortices is expected for these perforates. This will have an important effect on the impedance of the orifice. The circulation effects refer to these vortices and the other aspects of jet dynamics. Since a typical orifice thickness is small, the viscous effects within the orifice are likely to be negligible. Ingard and LaBate observed that the really large increases in the acoustic impedance corresponded to the region IV flow regime. They suggested that the acoustic energy is transformed into the kinetic energy of the jet and vortical energy of the jet. They did mention that the "acoustic mass" or the reactance was found to be reduced relative to that at very low

orifice velocities. The reduction was most evident when the "jetting" was evident from region IV. No reason was given for this effect.

In his paper on the theory and design of resonators, Ingard[211] accounted for the nonlinear effect with an additional resistance end correction. Using the terminology presented earlier, this additional end correction is expressed as:

$$\delta_{vis} = \underbrace{\delta_{Lin}}_{\text{equation 2.54a}} + \delta_{NL} \qquad (2.58)$$

From measured data on circular orifices, Ingard expressed the empirical non-dimensional nonlinear end correction as:

$$\frac{\Delta_{NL}}{d} \approx 0.7\left(\frac{U}{100}\right)^{1.7} \qquad (2.59)$$

The constant 0.7 outside the parenthesis and the exponent of 1.7 were determined from Ingard's measured data. The quantity U is the root mean square particle velocity in the orifice. Note that Ingard found that the resistance is not linearly proportional to the velocity, however, his empirical relationship was based on orifice velocities less than 0.6 m/s and the linear relationship was believed to become more prominent at much higher orifice velocities.

Fluid Mechanical Approach to Nonlinear Orifice Impedance

A resurgence of interest in the nonlinearity of orifices occurred in the 1960's. This stemmed from the fact that acoustic liners in the form of arrays of resonators and perforated sheets were becoming common on high by-pass jet engines and rocket motors. These liners were subjected to high amplitude acoustic pressures. Bies and Wilson[22] measured the orifice impedance for even higher orifice velocities up to 50 m/s, which were higher than those used by Sivian or Ingard and, like Sivian, found a similar linear dependence of resistance with orifice velocity (like that of equation 2.57). Even experiments in liquids showed the same nonlinearity of an orifice exposed to intense sound pressures[23].

Except for the case where liquid was used, all prior impedance measurements were made with a standing wave tube. In 1967, Ingard and Ising[16] published an important article on the nonlinearity of an orifice. They made measurements with a hot wire in the aperture of an orifice exposed to high intensity sound. Again, only circular orifices were studied. Particle velocities up to 50 m/s were generated in the orifice. Figure 2.10, taken from reference 2.16, shows their experimental set-up. At orifice velocities above 10 m/s, it was found that the acoustic resistance was linearly proportional to the velocity. This dependence is consistent with the findings of others[27,216] and established a firm relationship between acoustic resistance of circular orifices and high orifice velocity. Indeed, at these high velocity amplitudes, Ingard and Ising showed that the resistance is much greater than the reactance and the magnitude of the orifice impedance can be approximated solely by the resistance. The relationship for the normalized acoustic impedance for very high incident sound pressure levels is consistent with Sivian's expression:

29

$$\frac{R_{NL}}{\rho c} \approx \frac{K|U_o|}{c} \tag{2.60}$$

where U_o is the orifice particle velocity magnitude and the constant K is dependent on the fluid mechanical behavior of the orifice in a "jetting" condition. The fluid mechanical approach to describing orifice impedance at high incident sound amplitudes was subsequently pursued by several researchers.

Zinn[2][17] developed a theoretical model that was based on the fluid mechanical behavior of induced particle motion in and around an orifice. This approach was motivated by the "jetting" observed by Ingard and LaBate (corresponding to their Region IV). Using the appropriate conservation equations for the inlet side of the resonator and the cavity side, Zinn formulated the differential equations describing the first and second order effects. From his analysis, he attributed the energy losses at high amplitude SPLs to the dissipation of the kinetic energy of the "jetting" in the orifice. Zinn essentially assumed that at the exit (or cavity side) of the orifice, the amplitude of the particle oscillation is very large compared to the orifice thickness, thus the flow encompassing the formed jet can be considered quasi-steady. The resulting second order momentum equation contained the jet velocity that would be observed in the absence of friction forces and contraction effects. Zinn recognized this by incorporating an empirical relationship between the orifice velocity and the real jet velocity:

$$u_j = \frac{u_o}{C_c C_v} = \frac{u_o}{C_D} \tag{2.61}$$

where C_D = Discharge Coefficient

The definition of the discharge coefficient can be found in standard flow-meter literature[22] and is expressed as the product of the velocity coefficient (C_v) and the contraction coefficient (C_c). Thus:

$$C_D = C_v C_c \tag{2.62}$$

The term C_v is referred to as the velocity coefficient and is a measure of how much the actual velocity differs from the ideal velocity through the orifice and is defined as:

$$C_v = \frac{u_{ideal}}{u_{actual}} \tag{2.63}$$

The contraction coefficient, C_c, is defined as the ratio between the area associated with a *vena contracta* (A_{vc}) and the physical orifice area, (A_o) and is expressed as:

$$C_c = \frac{A_{vc}}{A_o} \tag{2.64}$$

In the literature, sometimes the distinction between the contraction coefficient and discharge coefficient is blurred because the velocity coefficient is usually ignored. For incompressible

flow, the discharge coefficient has been found to be a function of Reynolds number and orifice to duct area ratio as well as orifice geometry. Using the large database of steady flow orifice data (for circular orifices), Zinn used a discharge coefficient of 0.61. This represented an approximate value for the orifice type and Reynolds number of interest. He derived the following expression for the nonlinear resistance of an orifice:

$$\frac{R_{NL}}{\rho c} \cong \frac{4}{3\pi} \frac{u_o}{c C_D^2} \tag{2.65}$$

Equation 2.65 was used, with $C_D = 0.61$, to predict the data of Ingard and Ising[19] and Bies and Wilson[22]. The predicted nonlinear resistance was in reasonable agreement with the data. The importance of the discharge coefficient is evident from equation 2.65. For steady flow, it is known to be a function of orifice Reynolds number and porosity when circular orifices are considered[24,25].

The fluid mechanical approach of Zinn was extended by Hersh and Rogers[18]. The main difference is that Hersh and Rogers assumed spherical inflow whereas Zinn assumed a one-dimensional inflow. Figure 2.11 shows a schematic of this spherical inflow. Hersh and Rogers modeled the acoustic velocity in the vicinity of an orifice, in the first approximation, as an unsteady, incompressible flow. This fluid mechanical model was semi-empirical and predicted the orifice impedance in both the linear regime (low incident sound pressures) and nonlinear regime (high incident sound pressure). Like Zinn, Hersh and Rogers used the concept of the discharge coefficient to model the acoustic flow through the orifice. However, they defined the discharge coefficient as essentially the velocity coefficient, as expressed in equation 2.63. Their main result for the nonlinear regime was:

By comparing equation 2.66 with the experimental data from Ingard and Ising and Thurston, et

$$\frac{R_{NL}}{\rho c} \cong \frac{0.64}{C_D^2} \left[1 - 1.06 \left(\frac{C_D \omega (d+h)}{u_i} \right)^2 \right] \left[\frac{u_i}{c} \right] \tag{2.66}$$

al., Hersh and Rogers determined that the best fit was achieved with a discharge coefficient of about 0.8. Note that equation 2.66 is expressed in terms of the orifice ideal velocity, u_i, and not the maximum velocity, u_{max}, as labeled in Figure 2.11.

Accounting for Orifice Interactions and Porosity

Melling[7] developed a fluid mechanical expression for the nonlinear resistance that accounted for an array of orifices (i.e., a perforate) or a single orifice enclosed duct with a given porosity. This is accomplished by using the porosity parameter to effectively reduce the resistance as the porosity is increased as shown below:

$$\frac{R_{NL}}{\rho c} \cong \frac{0.6}{C_D^2} \left(\frac{1 - \sigma^2}{\sigma} \right) \frac{|u_{o-rms}|}{c} \tag{2.67}$$

Equation 2.67 is very similar to equation 2.66 and compared reasonably with Melling's experimental data for perforates with circular orifices. Melling also recognized the importance of the discharge coefficient. He compared discharge coefficients inferred from his data with

steady flow determined discharge coefficients with reasonable success. Melling found that the discharge coefficients that fit his data were approximately 0.89 and 0.96 for perforates with porosites of 7.5% and 22.5%, respectively.

Acoustic Energy Loss due to Vortex Shedding at an Orifice

It has been established that as the driving acoustic force increases in amplitude, the acoustic resistance of an orifice increases. This has been explained as a conversion of acoustic energy into vortical energy. Specifically, as sound interacts with an orifice, vorticity is shed at its edge and convects downstream. Several researchers have studied this interaction in the context of acoustic power losses of nozzle terminations with a steady mean flow superimposed on an acoustic field. Notably, Bechert[21] and Howe[22] formulated theories for the absorption of sound due to vorticity shedding in the presence of a mean flow. These models accounted for the convection of the shed vorticity in the mean jet flow. When a steady flow is present, sound is also absorbed in the jet turbulence that issues from orifices or groups of orifices[26].

Experiments measuring the acoustic power loss from nozzle exits[22] have instigated theoretical models that account for the shedding of vorticity from various nozzle terminations, including nozzles terminating in orifice plates and perforates. Figure 2.12 shows photographic evidence of vorticity shedding from some tested nozzle terminations in reference 2.27.

In an effort to understand acoustic power losses of pipes terminated with an orifice in the presence or absence of mean flow, Cummings and Eversman[28] and Cummings[19] developed a theoretical expression for the acoustic resistance based on a fluid mechanical description of the acoustic flow through an orifice in the vein of Zinn and Hersh and Rogers. Cummings and Eversman's work was developed to help explain the experimental data of Salikuddin and Ahuja[27]. Figure 2.13 shows the experimental set-up. They began their analysis by using the unsteady Bernoulli's equation. By discarding the time-dependent terms (a steady flow assumption) and writing the velocity in terms of an average value plus a perturbation, they arrived at an expression for the impedance at the exit of the nozzle. The nonlinear resistive contribution to the impedance was expressed as:

$$\frac{R_{NL}}{\rho c} = \frac{0.57}{C_c^2} \frac{\left[1 - \sigma C_c^2\right]}{\sigma} \frac{|u_{o-rms}|}{c}$$

(2.68)

Here, the use of the contraction coefficient, C_c, is employed. Equation 2.68, in conjunction with a radiation impedance term and reactive term, was used with success to predict power absorption and power transmission of experimental data using a contraction coefficient of 0.61. Figure 2.14 shows the general result of the net acoustic power loss for a nozzle with an orifice termination. A significant amount of loss is experienced at the lower frequencies. This was explained as the large conversion of acoustic energy into vorticity that was first explained by Ingard and Labate. Recall that at lower frequencies, significant turbulent jetting was observed from an orifice under intense incident acoustic energy. This corresponded to increased acoustic resistance and hence acoustic energy absorption.

32

Acoustic Mass Reactance

The effect of high amplitude sound on the acoustic mass reactance of an orifice has been addressed by several researchers and a general consensus has been reached on the end result[211, 216, 222, 229]: *Intense sound produces high amplitude fluctuating velocity within the orifice which in turn tends to reduce the attached mass in the near field of the orifice.* It is not quite clear as to *why* this high velocity reduces the attached mass, however, most agree that the turbulent jet produced by the intense sound "breaks apart" the oscillating slug of mass in and around the near field or the orifice. Figure 2.15 shows the general behavior of the orifice reactance as a function of orifice velocity observed by previously cited researchers. The reactance has a linear region where the orifice reactance is independent of the orifice velocity. This is followed by a more or less linear decrease in reactance to some minimum value that approaches one-half of the linear value. Most of all the researchers cited in the discussion on the nonlinear resistance model in the previous section have found that a reduction in mass reactance also accompanies the increased orifice velocity due to high incident sound pressure levels. More specifically, the reactance is reduced by almost half at the extremes of orifice velocities considered, namely 30 m/s.

Ingard[216] made quantitative measurements of the mass reactance and showed that the mass end correction at first stayed relatively independent of the orifice velocity until the onset of strong jetting (recall his region IV defined earlier) in the orifice. The lower level circulation effects, regions I, II, and III, didn't seem to affect the attached mass of the orifice. The conditions that support the strong jet in the orifice coincided with a decrease in the mass end correction and thus a decrease in the reactance. Ingard observed that this phenomenon was more prevalent in thinner orifices (such as those commonly used for perforates) where the attached mass contributes greatly to the overall reactance of the orifice. Ingard qualitatively explained the mechanism that causes the decrease in mass reactance. He suggested that the kinetic energy of the sound in and around the orifice is transferred into turbulent motion that "breaks away" from the orifice. Thus, part of the reactance is lost and soon dissipated by viscosity. He then suggested that the nonlinear resistance and reactance are related in that the decreased reactance shows up as an increase in resistance. The data presented by Ingard shows that large diameter orifices have less attached mass for a given orifice thickness. It should be noted that only circular orifices were tested for nonlinear effects.

The same nonlinear model that Hersh and Rogers[214] used to develop an expression for acoustic resistance produce an expression for acoustic reactance of an orifice, shown below:

$$\frac{\chi_{NL}}{\rho c} \cong \frac{-0.33}{C_D^2}\frac{\omega(2r_o+h)}{c}\left\{1+2.48\left[\frac{C_D\omega(2r_o+h)}{u_i}\right]^{\frac{1}{3}}\right\}\left\{1-1.06\left[\frac{C_D\omega(2r_o+h)}{u_i}\right]^2\right\} \quad (2.69)$$

This model showed that the nonlinear reactance and resistance were coupled through the discharge coefficient, which seems intuitive based on the dependence of Reynolds number of the velocity in the orifice.

Summary of Nonlinear Orifice Impedance Models

It appears from the literature reviewed above that considerable progress has been made in establishing the basic physical mechanisms that govern the impedance of sound impinging on an

orifice. The bulk of the literature deals with circular orifice geometry. The key finding is that at high orifice velocity, the acoustic pressure is proportional to the square of the particle velocity. This leads to a description of the orifice impedance as a "Bernoulli loss" or an association of the pressure drop through the orifice with kinetic energy conversion. The introduction of the discharge coefficient to account for viscous losses across the orifice provides a parameter to which these losses can be "lumped." This loss coefficient is especially critical in the high amplitude behavior of orifice impedance. Discharge coefficients of approximately 0.6 have been used by several researchers[2,18,219] to compare their models with measured data of single orifices, with reasonable success. However, more recent semi-empirical correlations[2,3] suggest that values of discharge coefficients close to 0.4 fit experimental acoustic data at these higher levels well. Since acoustic pressures are unsteady, this suggests that the direct application of steady flow discharge coefficients may not be completely accurate. If this discharge coefficient can be used universally, i.e., for circular and non-circular orifices alike, then it should be able to predict the impedance of the eye-shaped orifices of the sliding perforate used in the present work.

In general, the acoustic impedance of an orifice subjected to high amplitude sound can be represented by the nonlinear acoustic resistance. This is because the magnitude of the reactance is reduced and is small relative the orifice resistance. At very high orifice velocities, corresponding to high incident sound pressure amplitudes, the orifice resistance is several orders of magnitude larger than the orifice reactance. Therefore, a good approximation of the high amplitude orifice impedance is:

$$\frac{Z_0}{\rho c} \approx \frac{R_{NL}}{\rho c}; \qquad \frac{R_{NL}}{\rho c} >> \frac{X_{NL}}{\rho c} \qquad (2.70)$$

The expression in terms of rms orifice velocity developed by Hersh and Rogers (equation 2.66), Melling (equation 2.67) and Cummings (equation 2.68) are consistent in their general form. Therefore, an expression for normalized orifice impedance at high amplitudes and accounting for porosity is given by:

$$\frac{Z_{NL}}{\rho c} \approx \frac{R_{NL}}{\rho c} \approx \frac{0.6}{C_D^2}\left(\frac{1-\sigma^2}{\sigma^2}\right)\frac{|u_{o-rms}|}{c} \qquad (2.71)$$

2.6   Nonlinear Effects Part II: Grazing Flow Effects on Orifice Impedance

For acoustic absorbers made of perforated sheets or resonators with small openings that line ducts carrying fluid, an additional physical mechanism contributes to the orifice impedance. Tangential flow over orifices is commonly referred to as grazing flow. Orifices or perforates exposed to grazing flow represent another facet of their nonlinearity with respect to their acoustic impedance. In this case, the term "nonlinear" refers to the changing impedance with changing magnitude of the grazing flow. The effects of grazing flow on the acoustic impedance of orifices became more important as more experimental observations began to show discrepancies between the predictions and measurements of liner impedance[2,31]. This, of course, had an impact on liners used in jet engines because in some cases, grazing flow velocities reached 130 m/s. It thus became important to incorporate these effects in the impedance models. For the present study,

34

the impact of grazing flow is not of primary concern because the orifice/perforate of interest is located in the buried septum of a two-degree-of-freedom liner and hence it is not exposed to grazing flow. Hence, details are spared and only a general description of the physical picture is presented in this section.

Interaction Between Grazing Mean Flow and the Oscillating Orifice Flow

Beginning with the work of Meyer, et al.[ ], and later that of Feder and Dean[ ], and Dean[ ], it was observed that the acoustic resistance of an orifice backed by a cavity increased with the magnitude of the grazing flow over the orifice.

Baumeister and Rice[ ] performed detailed flow visualization of the interaction of grazing flow over an orifice backed by a cavity (i.e., a Helmholtz resonator). They found that the steady grazing flow and the oscillating orifice flow interacted mainly at the downstream lip of the orifice. Figure 2.16 shows the physical picture of this phenomenon. It was speculated that this interaction reduced the effective orifice open area. This picture was used to form the basis for a semi-empirical model for the orifice impedance.

Effect of Grazing Flow on Orifice Impedance

Rogers and Hersh[ ], building on their fluid mechanical model of acoustic resistance discussed earlier, correlated steady-state resistance measurements of single orifices exposed to grazing flow in terms of an effective discharge coefficient. In their work, Rogers and Hersh provided a physical mechanism that explained the increased resistance with grazing flow. The interaction between the grazing flow and the orifice "flow" into and out of the orifice causes the "orifice flow to be constricted in its passage through the orifice." These inflow and outflow conditions of the orifice took on what was called the "Inviscid Interaction model," or the "Lid" model, where the orifice was seen to behave as if a hinged lid covered the aperture. Figure 2.17 shows the basic features of this model. During the outflow cycle, the lid tends to block emerging flow and during the inflow, edge separation causes further restriction of the orifice flow. This physical picture was observed in a water tunnel. Wind tunnel tests were also performed with grazing flow speeds up to 84 m/s. The interaction model correlated the grazing flow with orifice resistance and found that a different correlation existed between the inflow cycle and the outflow cycle of the orifice flow. In both cases, the resistance was proportional to a discharge coefficient which in turn was a function of the orifice velocity and the grazing flow velocity.

For low grazing flow speeds typical of internal combustion muffler systems, Rao and Munjal[ ] correlated perforate impedance as a function of grazing flow velocity, perforate thickness, and perforate diameter. Their experiments examined the impedance of a perforate with a maximum grazing flow Mach number of 0.2. Rao and Munjal provided curve fits of their impedance data which showed that the resistance of the perforate increased linearly with grazing flow velocity, while the reactance remained relatively constant.

More recently, Hersh and Walker[ ] further built on the earlier work of Rogers and Hersh. They developed a one-dimensional fluid mechanical/lumped element hybrid model for predicting the impedance of a Helmholtz resonator with grazing flow over the orifice aperture. They found that the principal effects of grazing flow are to increase the resistance and decrease the reactance of the resonator. They also found that resonator impedance becomes linear (independent of

35

sound pressure amplitude) at high grazing flow speeds on the order of $\omega_o d_o$ which is the resonance frequency times the effective orifice diameter. Comparing with experimental data. Hersh and Walker were able to correlate impedance with several characteristic velocities. They concluded that at sufficiently high grazing flow speeds on the order of 150 m/s, the mass end corrections "virtually vanishes." This is explained as the fluid associated with the mass end correction being swept away by the grazing flow.

2.7 Previous Work Related to Controlling Liner Impedance

Large turbofan jet engine with their characteristic tonal noise signature led to the development of acoustic wall treatments of the resonant type. As mentioned in Section 1.2, the honeycomb-type resonant liner has inherently good structural characteristics as well as high attenuation over a small frequency band. It provides excellent attenuation for a single design condition, but when conditions in the jet engine duct change (i.e., lower or higher engine power setting, grazing flow Mach number changes) the single-point treatment design becomes non-optimum or "de-tuned." This was recognized early in the development of such treatments and several techniques have been put forth to address this problem.

Variable wall impedance can be achieved via passive or active methods. Passive is defined here as a system which requires no adjusting or moving parts. Active systems are those which control or vary the wall impedance by some mechanical or electronic means once installed. Truly actively-controlled systems can be realized by incorporating the mechanical or electronic devices into a feedback loop to automatically adjust liner impedance.

Passive Control Methods

Several methods have been put forth with the aim of controlling the wall impedance passively. In general, most of these concepts revolve around spatially varying geometric parameters with the result of varying the local surface impedance. The concept of a segmented liner (i.e., a liner which consists of sections, each with a different impedance) is somewhat of a "brute-force" way of controlling the overall acoustic attenuation in a duct. Usually, to accommodate the required attenuation, the length of a segmented liner is large[2,38].

A more efficient approach is the variable-depth honeycomb liner concept. Figure 2.18 shows the features of this type of liner. This method uses the sandwiched honeycomb resonant type liner configuration that has a variable backing depth with axial distance. The varying depth means that each honeycomb cell has a unique resonant frequency, hence as the depth changes, so does the liner impedance. While maximum attenuation is not quite as good as a constant-depth honeycomb liner, it attenuates over a broader frequency range[2,39]. Figure 2.19 shows a comparison of transmission loss between a typical constant-depth liner and a variable-depth liner taken from reference 2.39.

Figures 2.20-2.23 show several other different liner concepts, all based on a passive control methods. Arcas and Parente[2,40] proposed a unique variable depth liner which uses the circumference of a jet engine nacelle to form a "sine wave" variable depth honeycomb liner which is shown in Figure 2.20. A novel approach to this concept was proposed and studied by Wirt[2,41], see Figure 2.21. Placing a permeable oblique (to the incident sound wave) obstruction

in a honeycomb or other waveguide, produces attenuation results which are comparable to some bulk absorbing material.

Shenoda[2,42] discussed a liner that has spatially varying cell volume and shapes. This provided a wide-band attenuation in tests conducted in a flow-duct. Spatially varying the facing sheet porosity (in a preset, fixed manner) can also vary the surface impedance. Shenoda, et al[2,43] examined a so-called "variable-slit" liner which varies the amount of face sheet area along the flow direction of a duct. Figure 2.22 shows this liner concept with reflection coefficient and transmission loss results. Their results show a significant attenuation over a wide frequency range.

Snyder[2,44] disclosed a multi-layered (up to 7 layers) laminate installation in a jet engine nacelle for improved sound attenuation, that is shown in Figure 2.23. By incorporating protective layers (e.g., moisture barriers) this concept also fulfills structural design objectives. Use of hollow rivets was suggested to act as a further conduit of sound to some of the intermediate layers. The series of layers or laminate separated by air gaps make this liner non-locally reactive to grazing incident sound.

Active Control Methods

Many ideas for new acoustic liners relating to jet engines have been proposed over the last 30 years. Few studies involving the active control of wall impedance in a jet engine environment seem to have been pursued with research in the open literature, with a few notable exceptions. Active control of wall impedance in a free-field application has been demonstrated recently by Marc, et al[2,45]. This research involves what the authors call "actively enhanced porous layers" whereby the impedance of porous layers is directly controlled by using a control acoustic driver on one side of the layer to alter the other side's impedance. The acoustic pressure on one side of the layer is driven to zero at a single microphone located very close to the porous layer. This concept is shown in Figure 2.24a. Microphones on the other side of the layer are used to compute the reflection coefficient (and hence the absorption coefficient). A Least Mean Square (LMS) computer algorithm is used to automatically adjust the control speaker for a given source input. Figure 2.24b shows that high attenuation can be achieved. This concept is an extension of Guicking and colleagues[2,46, 2,47] work who successfully demonstrated this technique in an impedance tube.

Of particular interest to the present study is previous work on changing wall impedance through the manipulations of the impedance of resistive layers in a multi-degree-of-freedom resonant liner. The concept of introducing a steady flow through a resonant type liner in hopes of controlling the resistance of the liner facing sheet has been postulated by Green and Feder[2,48]. Such a system involves pumping a steady flow through the liner cells, which varies the liner impedance, exploiting the nonlinearity of the perforates. Simply put, if the facing sheet resistance can be varied, the total acoustic impedance of the liner as a whole can be varied. The desired result is to adjust the peak attenuation frequency as dictated by the engine operating condition. Figure 2.25a, taken from Green and Feder[2,48] shows a schematic of their concept.

Dean and Tester[2,49] implemented a liner concept similar to Green and Feder's idea. Dean and Tester were able to show that the peak attenuation of a resonant liner can be controlled by

forcing air through the liner and allowing it to spill into the flow-duct. They showed that both the normal and the grazing incident impedance can be altered significantly. Where Green and Feder's patent spoke only of a single degree-of-freedom (SDOF) liner, Dean and Tester applied the "bias flow", as they termed the steady liner through-flow, to a two degree-of-freedom (2DOF) liner. Figure 2.25b, taken from reference 2.49, shows this bias flow concept. This had a distinct advantage: it allowed the main controlling resistance to be that of the septum sheet separating the two honeycomb cores. This septum is a low porosity perforated metal sheet which, by design, has a highly nonlinear characteristic with regard to orifice flow. The facing sheet (i.e., the perforated sheet exposed to the flow-duct) is typically of high porosity and not as susceptible to the bias flow due to the grazing flow effect. Green and Feder did not claim a reverse flow scenario in their patent and Dean did not test this possibility in his work. In recent work at the Georgia Tech Research Institute[2,50] under the direction of Dr. K. K. Ahuja, it was demonstrated that reverse bias flow or "suction" bias flow can be extremely effective in controlling the liner impedance.

Finally, an interesting and potentially powerful concept for controlling wall impedance was put forth by Harvey[2,51]. In a patent, Harvey, describes a movable perforate sheet on top of another perforate sheet (forming either the facing sheet, the septum, or both). This has the desired effect of changing the porosity of the combined sheets, which act as a single impediment to incident sound. The porosity of the perforate sheet is a fundamental parameter that governs the impedance of the sheet. This is the concept that is explored in the present work. While the author has found this concept only in the patent filed by Harvey, implementation of this idea has not been found in the open literature to date.
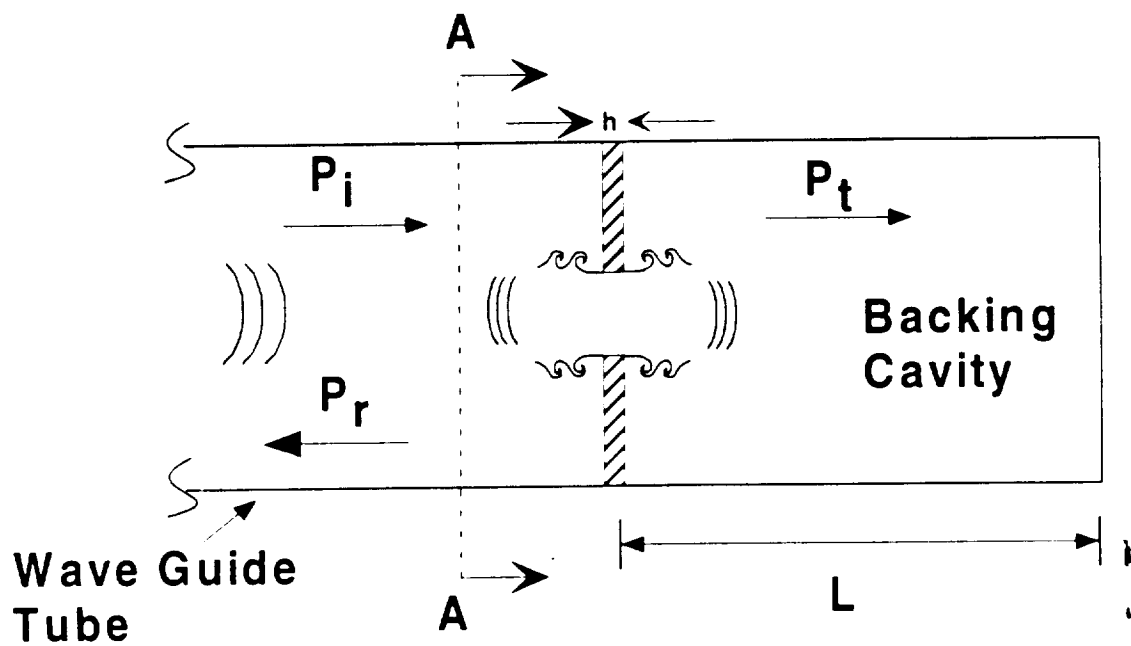
L = Cavity length
h = Orifice thickness
r_o = Orifice radius
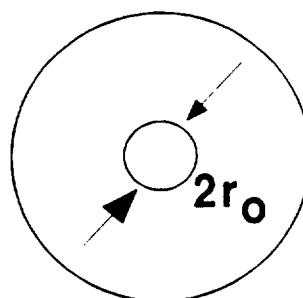
A - A

Figure 2.1 Physical schematic of sound interaction with an orifice.
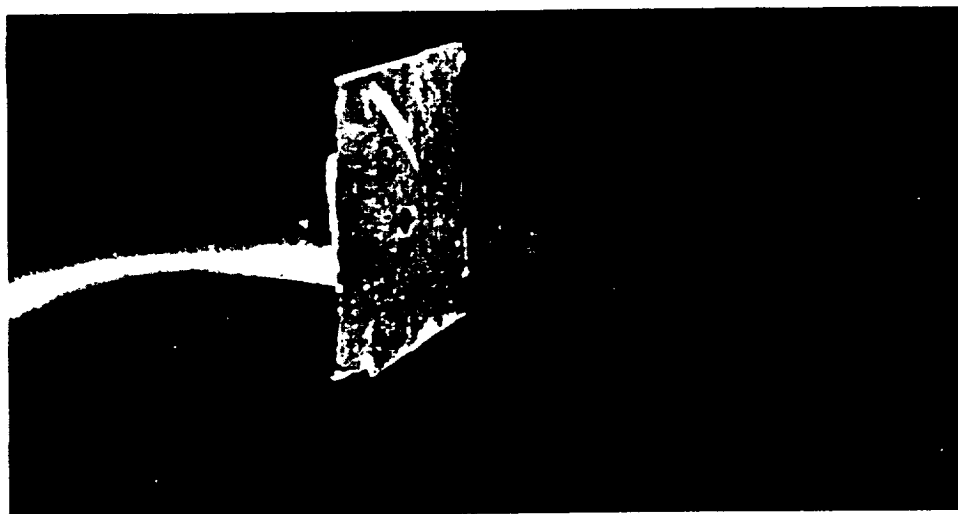
a. f ~ 130 Hz
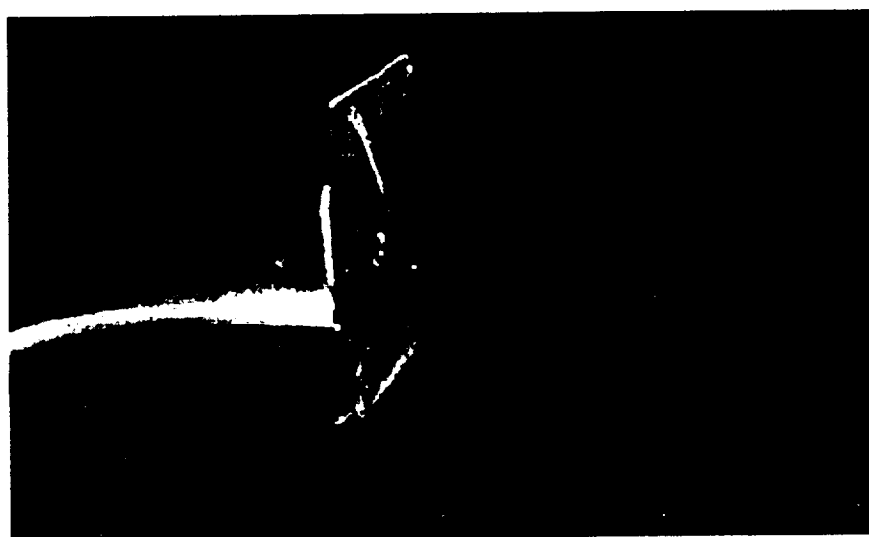
b. f ~ 800 Hz

Figure 2.2 Photographic evidence of orifice "jetting" when subjected to sound.
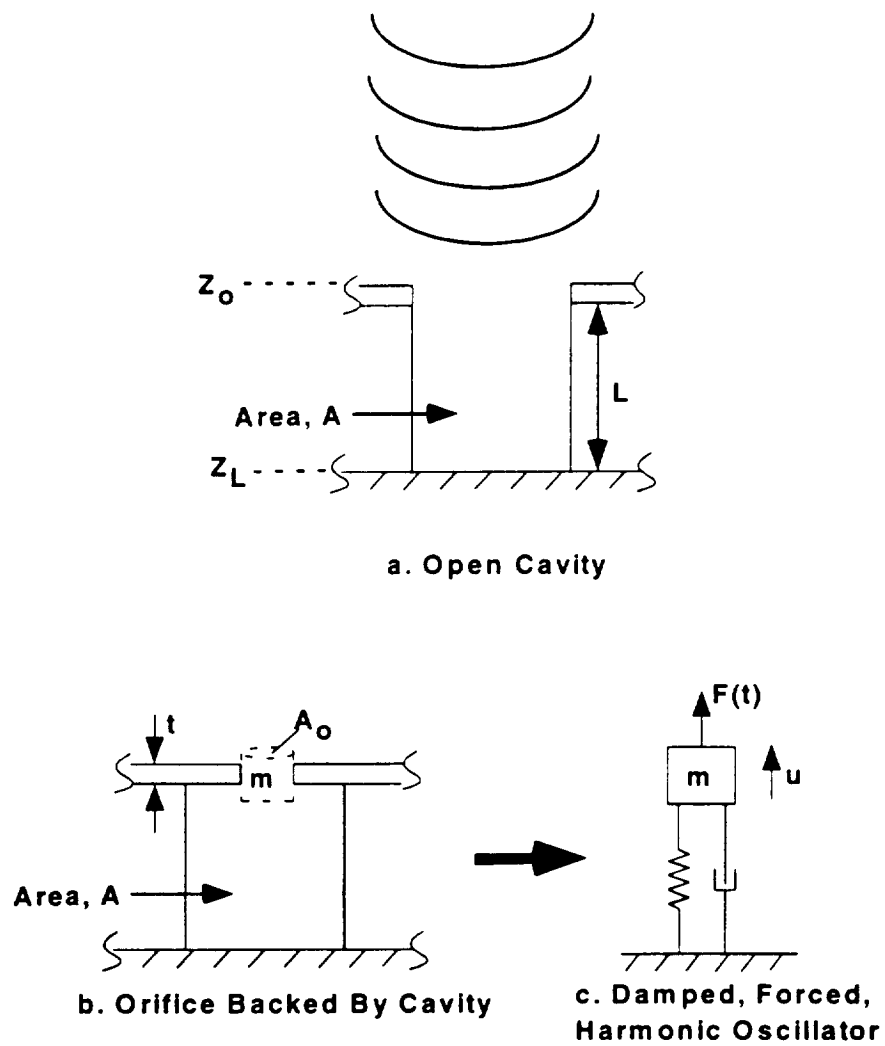
Figure 2.3 Mechanical vibration - acoustic analogy used for acoustic
impedance modeling of a cavity resonator.
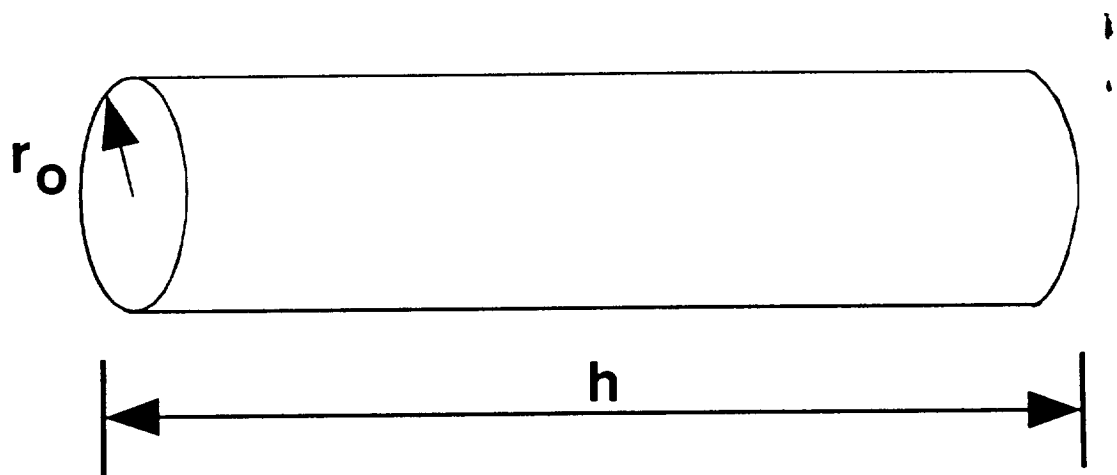
Figure 2.4 Narrow tube model used for internal impdance of an orifice.
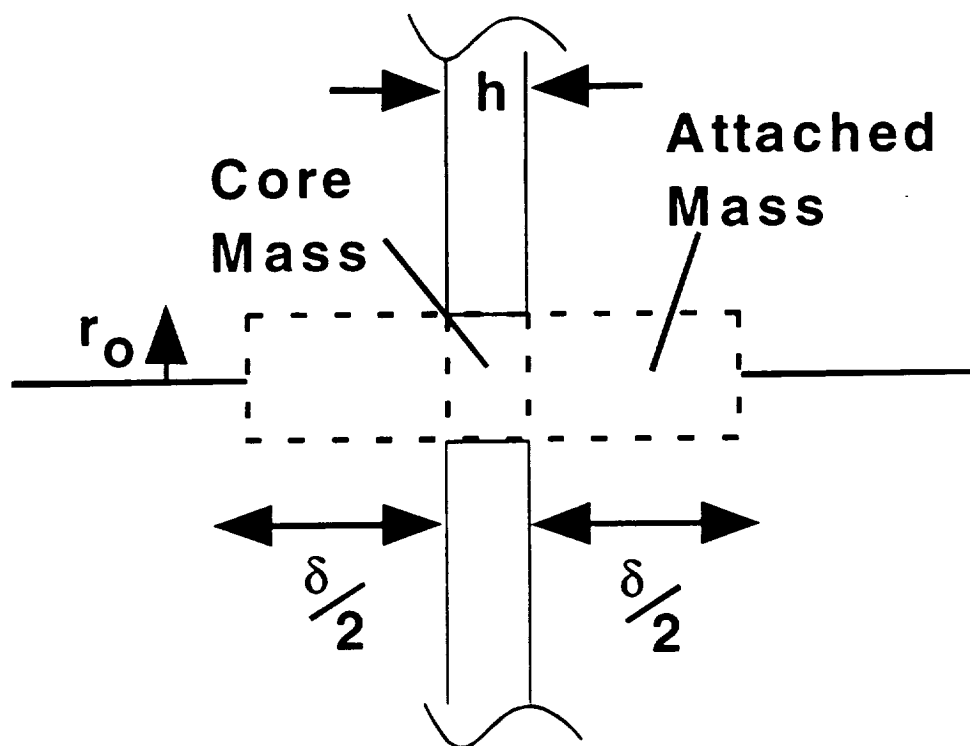
Figure 2.5 Attached mass of an orifice subjected to incident sound.
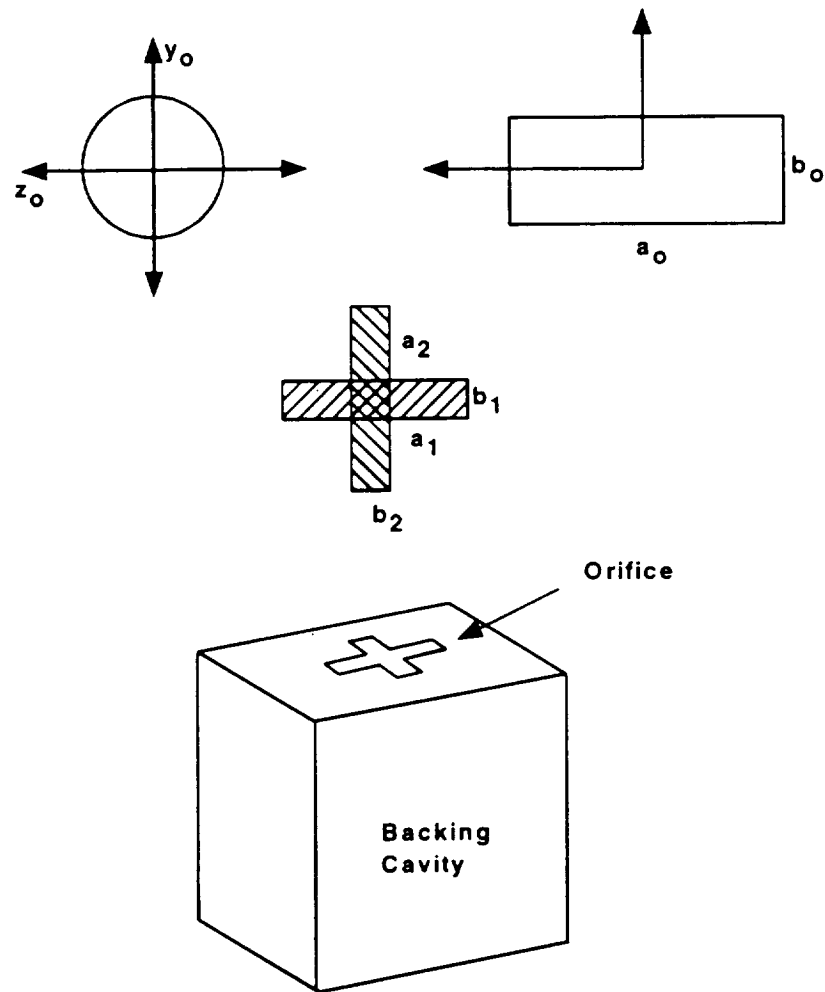
Figure 2.6 Non-circular orifice geometry used by Chanaud [ref. 2.12] to compute radiation impedance.
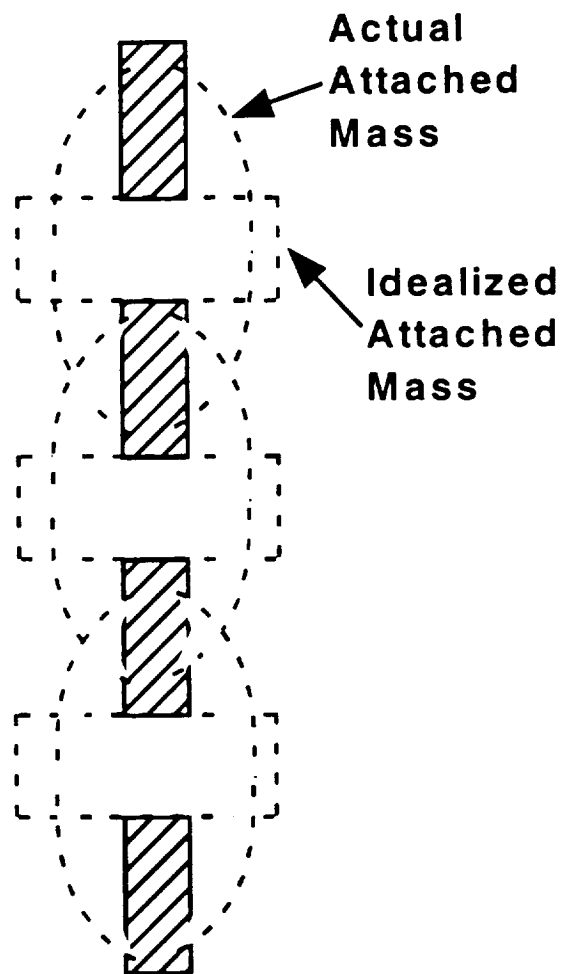
Figure 2.7 Orifice end-correction interaction as suggested by Melling [ref. 2.7].
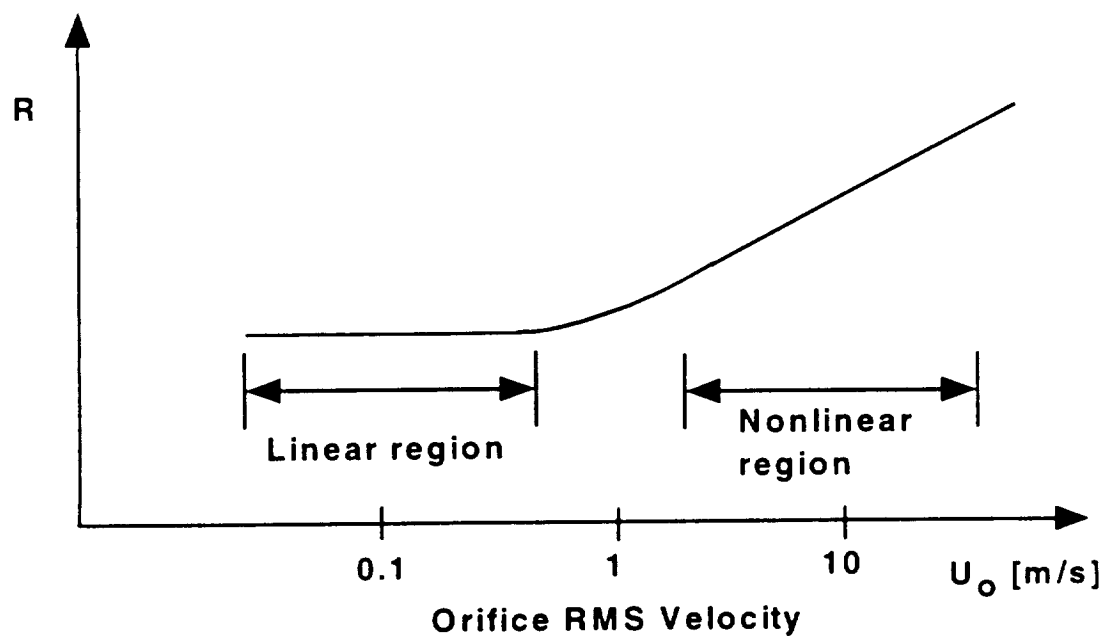
Figure 2.8 Increasing orifice acoustic resistance as orifice velocity is increased.
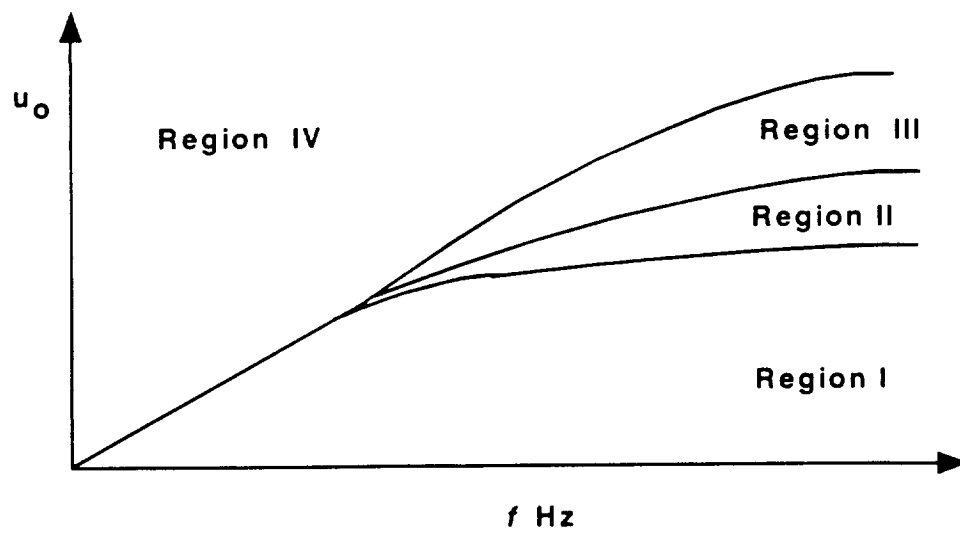
Figure 2.9 Phase diagram of flow regime regions associated with oscillatory flow through an orifice from Labate and Ingard [ref. 2.15].
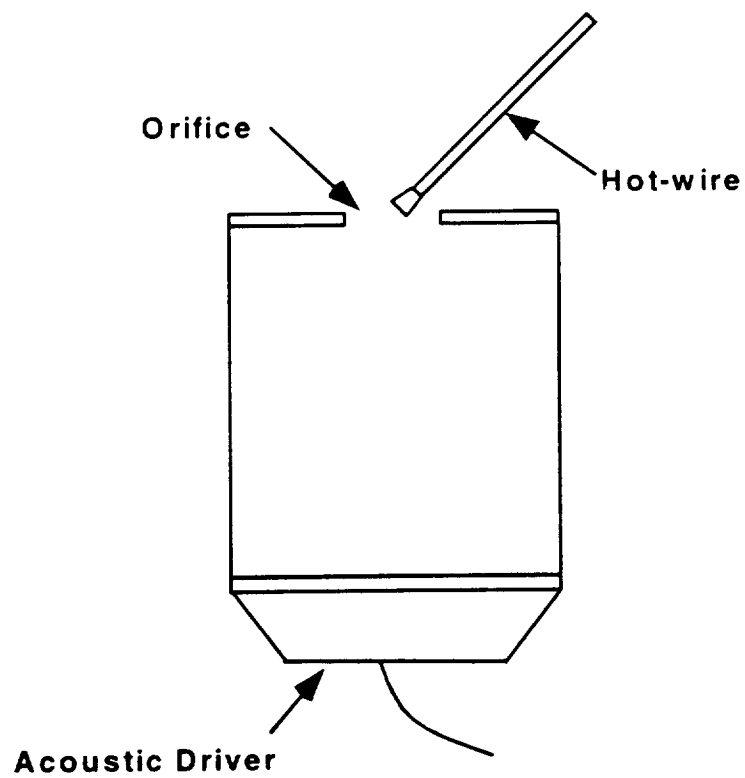
Figure 2.10 Experimental arrangement for the measurement of orifice velocity as a function of incident sound amplitude from Ingard and Ising [ref. 2.16].
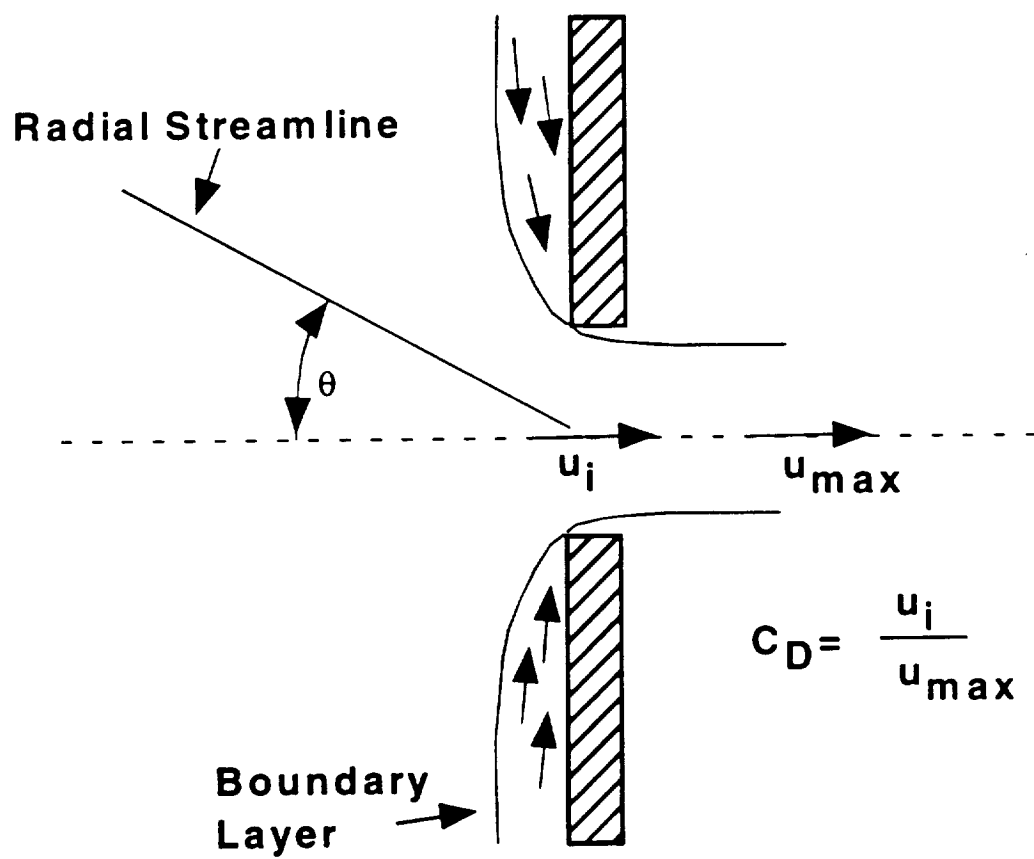
Figure 2.11 Instantaneous flowfield near orifice for fluid-mechanical model of Hersh & Rogers [2.18].

(a)	(b)
Circular Nozzle Exit	Suppressor Nozzle Exit
(c)	(d)
Single Orifice Plate at Nozzle Exit	Perforated Plate at Nozzle Exit
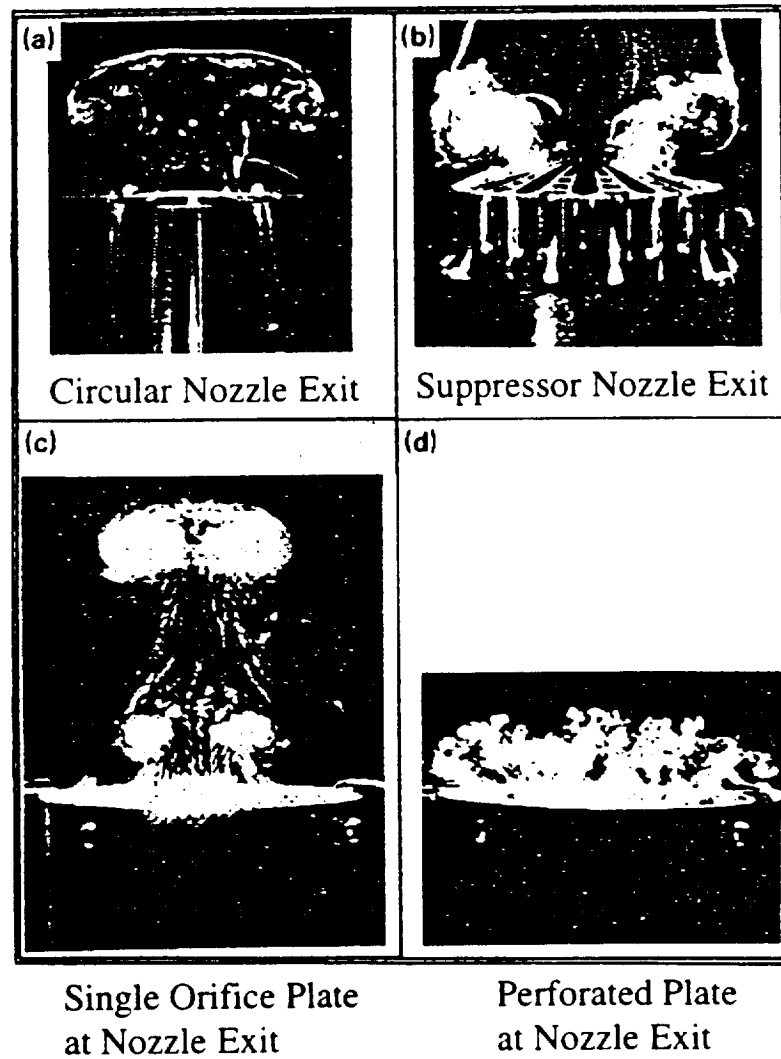
Figure 2.12 Vorticity formation at exit of nozzle with various termination geometry configurations; No mean flow present (ref. 2.27).
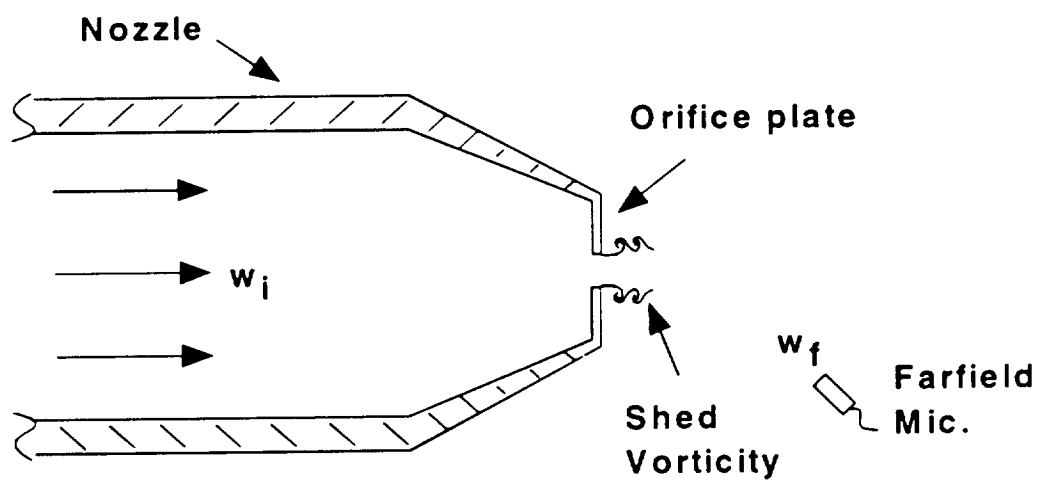
Net Acoustic Power Loss = 10 log [w_i / w_f]

Figure 2.13 Experimental arrangement for quantifying net acoustic power loss at nozzle exit [ref. 2.27].
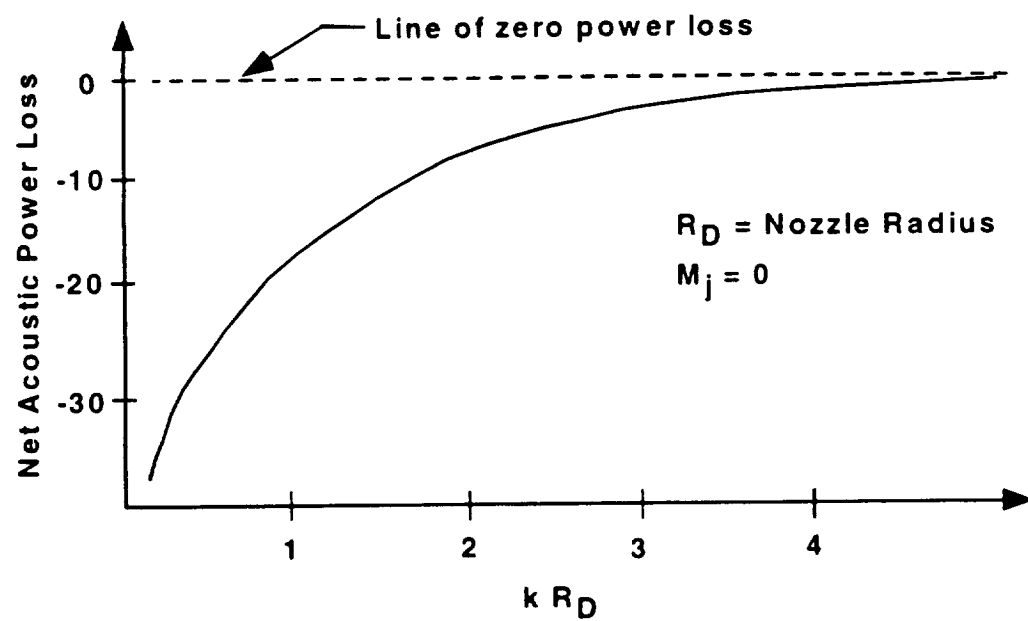
Figure 2.14 General result of net acoustic power loss of an orifice-terminated nozzle [ref. 2.27].
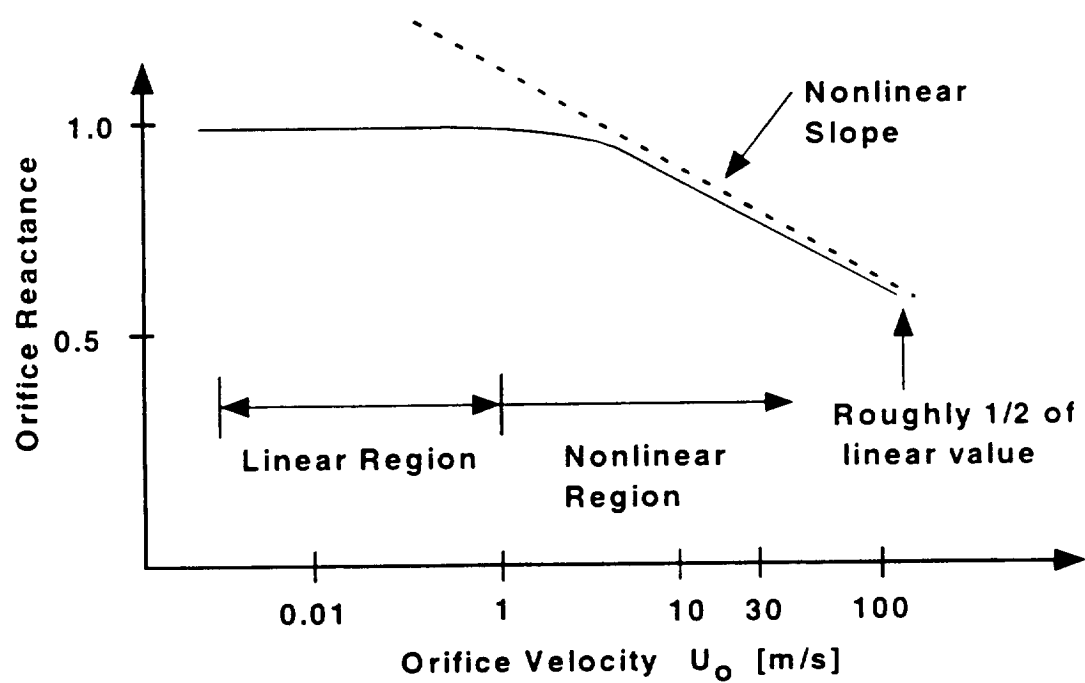
Figure 2.15 General observed trend in orifice reactance with increasing orifice velocity
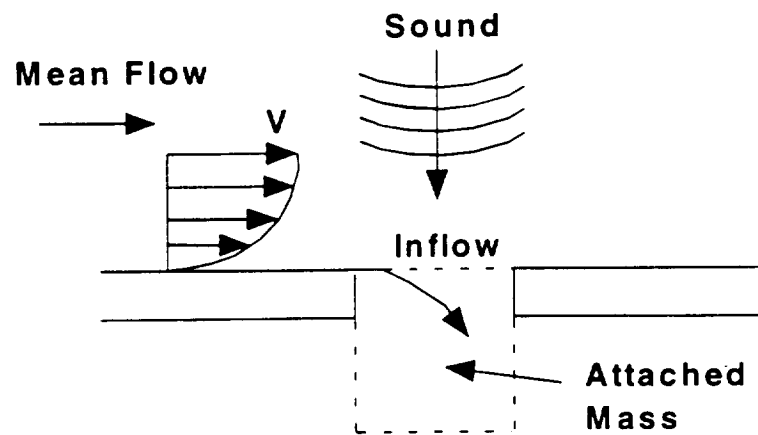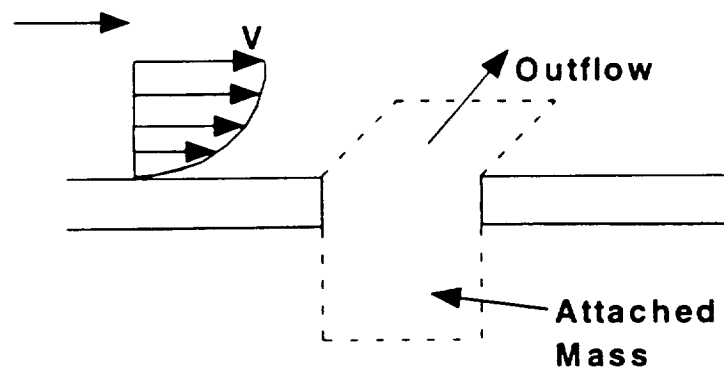
Figure 2.16 Interaction of grazing flow with an orifice under acoustic excitation.
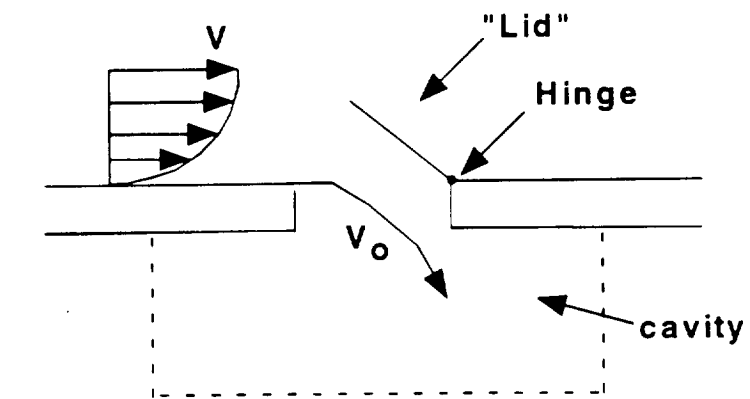
a. Inflow
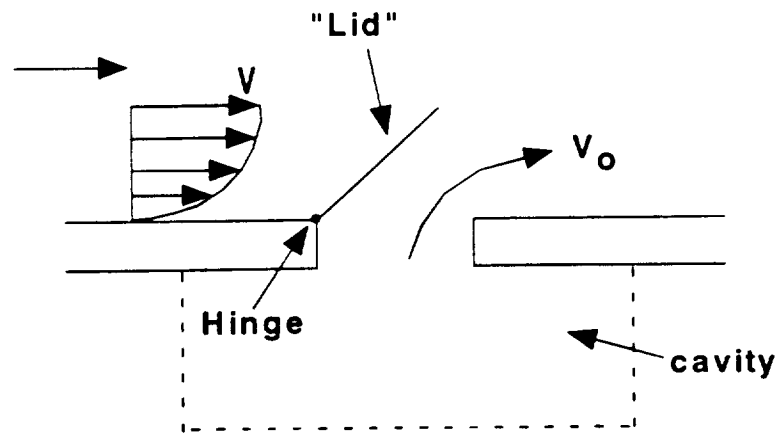
b. Outflow

Figure 2.17 The "Lid" model of Rogers and Hersh [ref. 2.35].
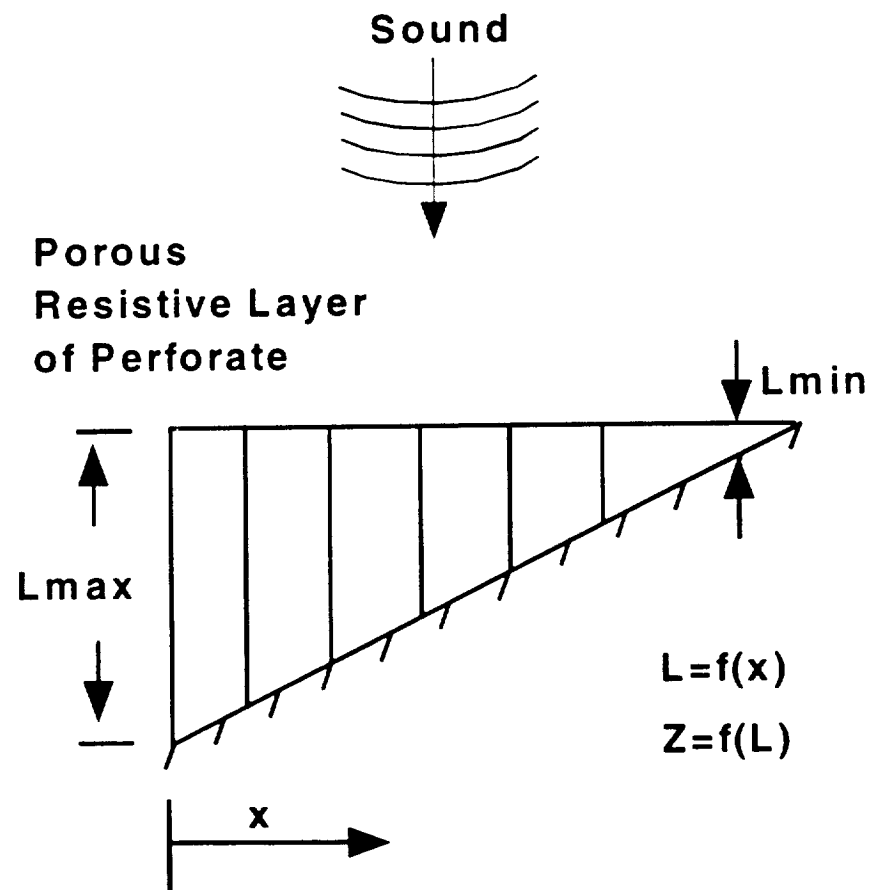
Figure 2.18 Variable-depth honeycomb resonant liner concept [ref. 2.39].

4-cycle Variable
Depth Liner
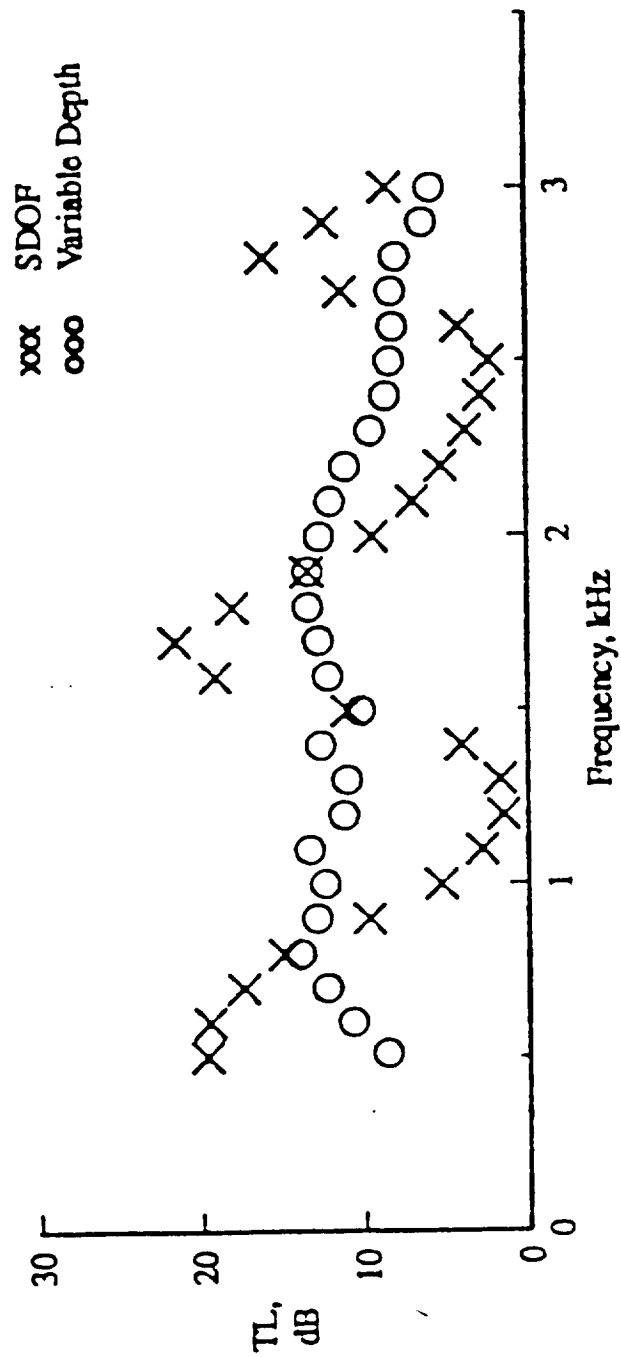
Figure 2.19 Comparison of variable-depth honeycomb liner transmission loss with single-depth liner transmission loss (ref. 2.39).
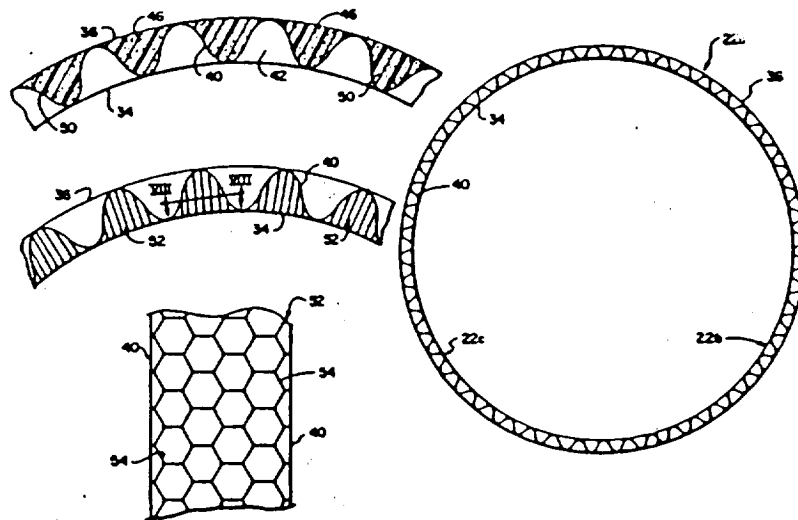
Figure 2.20 Variable-depth honeycomb liner concept from Arcas and Parente (ref. 2.40).
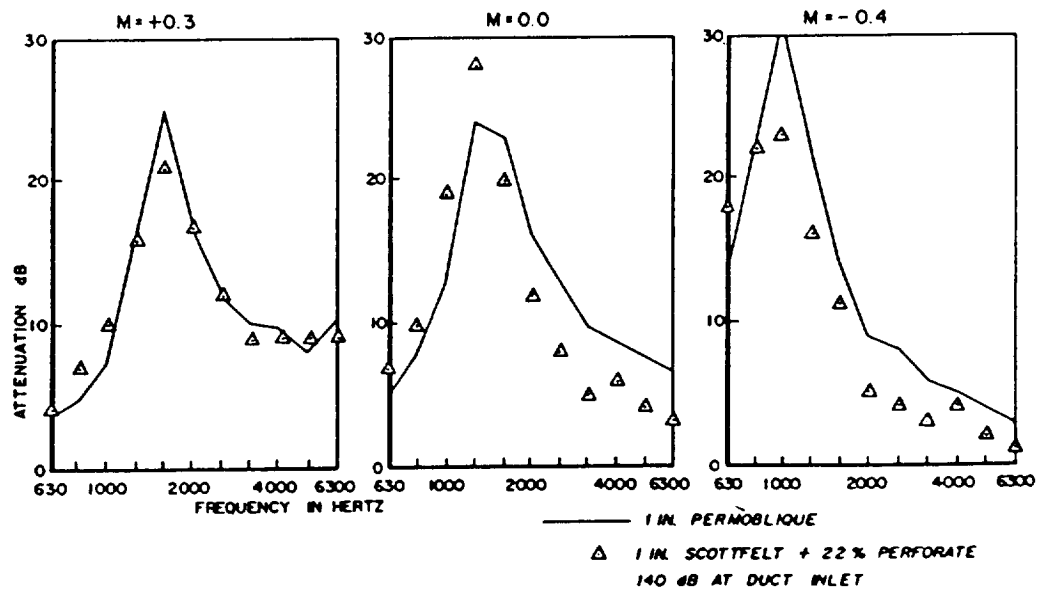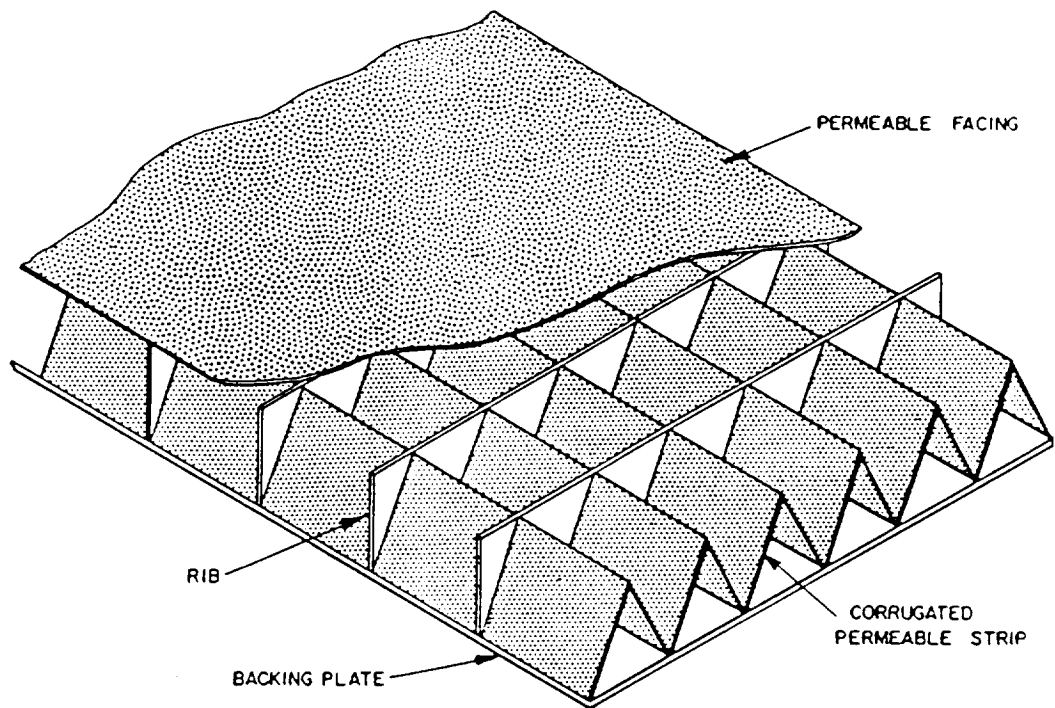
Figure 2.21 Permoblique liner concept of Wirt (ref. 2.41).
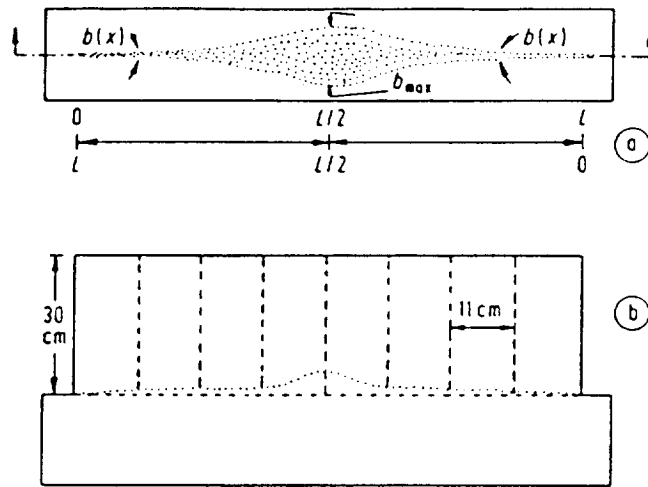
a) A variable slit along the silencer length (replaced by a
perforated area of more than 35% perforation ratio),

b) Silencer with an outside chamber of constant depth
(30 cm).
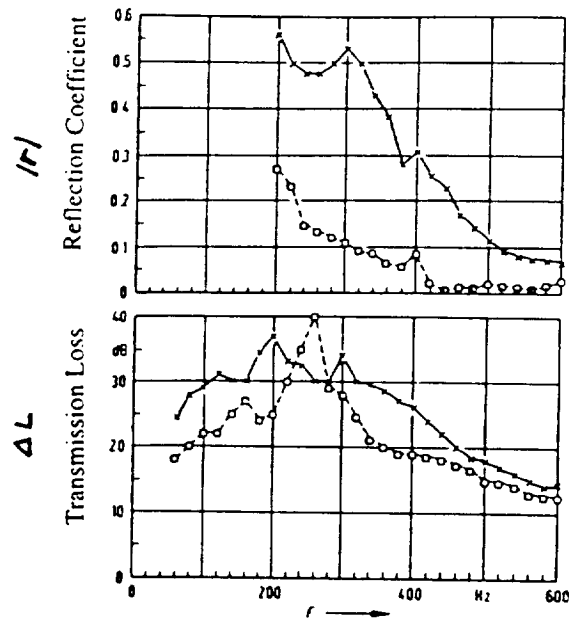
Comparison between the measured $|r|$ and ΔL
against F for the proposed silencer and those of a silencer
of constant slit width. Constant width slit with $b = 5$ cm
and $L = 100$ cm (x——x); parabolic slit with $b_{max} = 5$ cm
and $L = 100$ cm (□---□).

Figure 2.22 Variable slit liner concept of Shenoda, et al. (ref. 2.42).

60
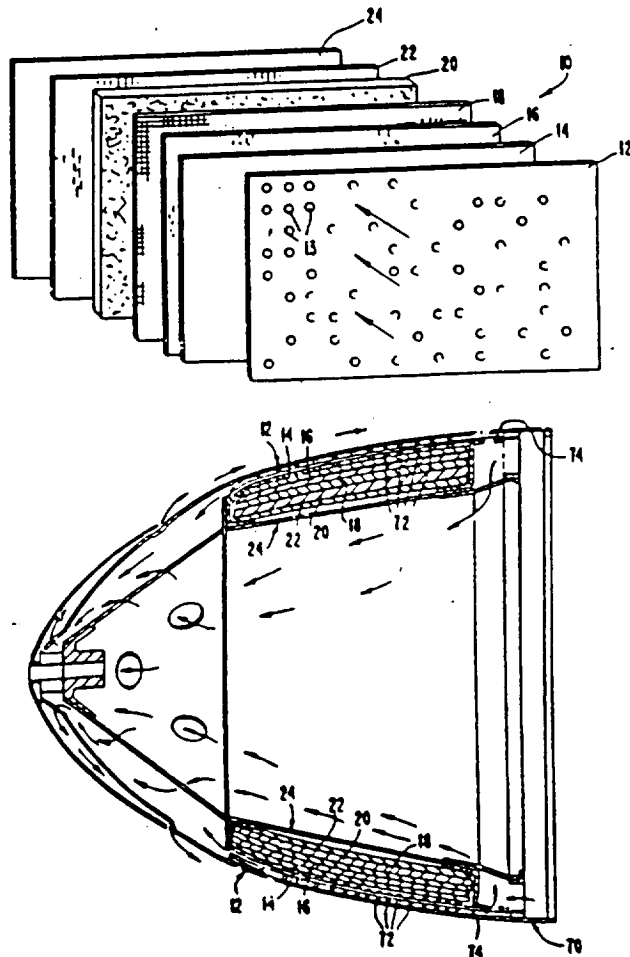
Figure 2.23 Multi-layer perforate liner concept of Snyder (ref. 2.44).
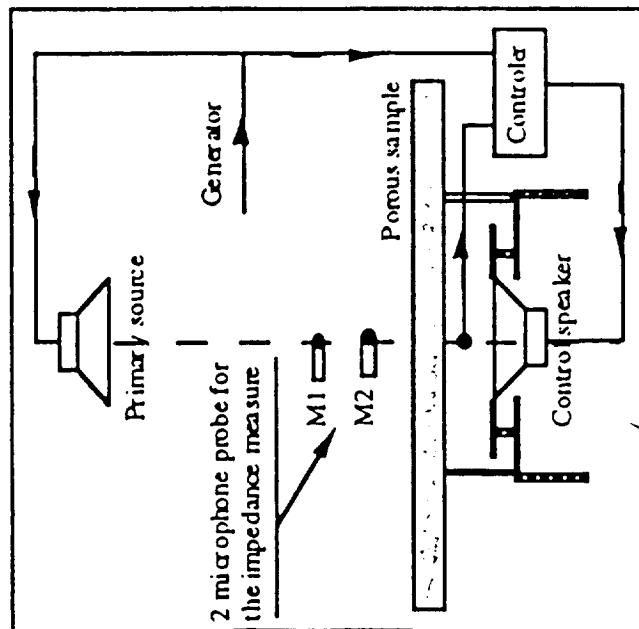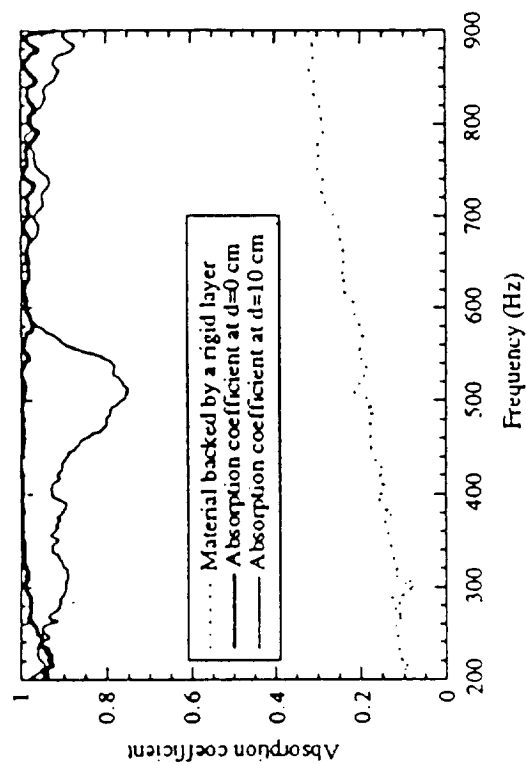
Absorption Coefficient

Figure 2.24 Actively controlled porous layer concept of Marc, et al. (ref. 2.45).

Experimental Set-Up
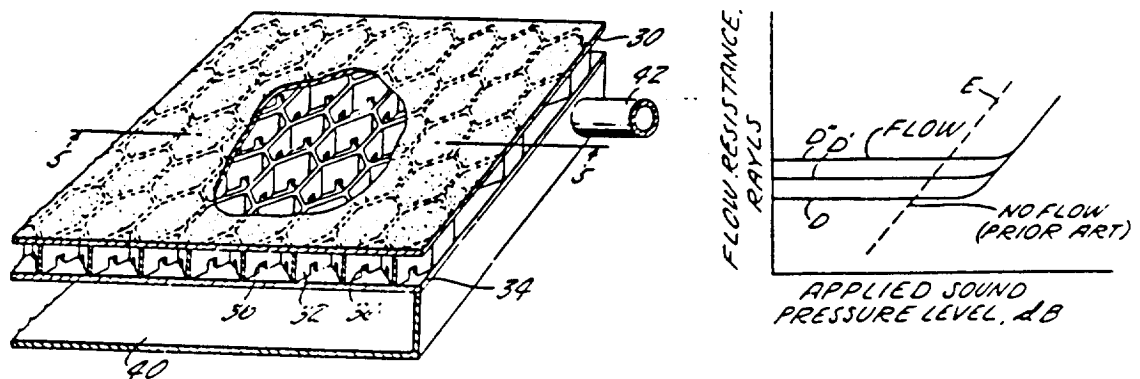
a. Bias flow concept of Green and Feder (ref. 2.48)
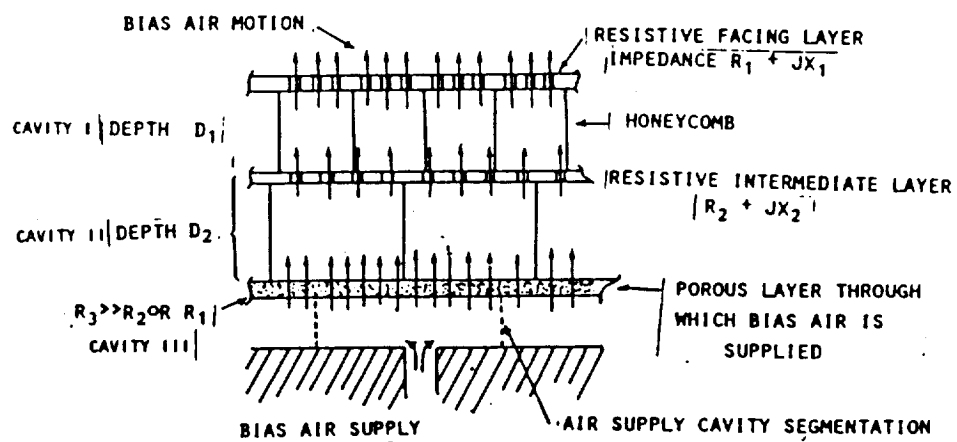
b. Bias flow concept of Dean and Tester (ref. 2.49)

Figure 2.25 Bias flow concepts for actively controlled liner absorption.

SECTION III

Absorption Control of a 2DOF Liner
with a Controllable Buried Septum

3.1 Introduction

This section examines the application of the variable orifice perforate concept introduced in Section I as a component in a two-degree-of-freedom acoustic liner. Experiments were conducted that characterize the liner's performance and the effectiveness of the variable liner impedance concept.

Objective

The objective of this Section is to quantify the degree of absorption control that can be achieved by using a variable porosity and variable geometry perforate as the buried septum in a two-degree-of-freedom liner that is similar to liners used in turbofan engines as acoustic treatment.

Outline of Section

This section will describe two main types of experiments: 1) Normal incidence impedance measurements and 2) Liner absorption measurements in a flow-duct with a specified noise source upstream. A description of the experimental approach of these experiments, prediction of the liner resonance frequencies, and the facilities and data processing used will be discussed before the presentation of the results.

3.2 Experimental Approach

Two-Degree-of-Freedom Liner

Using commercially available stock honeycomb and perforate, a 2DOF liner was built that could be used as flow-duct wall treatment and another was built that could be used in a normal incidence impedance tube. These liners had a buried septum that consisted of two perforated sheets with the ability of one of the sheets to slide over the other. This dual-layer liner was chosen for testing for two reasons: 1) it is a common liner type used in the aircraft engine industry and 2) the effects of the sliding buried septum are not complicated by grazing flow. Changing the septum porosity, and thus orifice shape, was believed to alter the tuned resonant frequencies of the liner. Characterizing the acoustic impedance and absorption as a function of this change in buried septum was accomplished by examining the normal incidence behavior in an impedance tube. Attenuation characteristics were then examined by measuring transmission loss and insertion loss of the liner in a flow-duct.

Normal Incidence Behavior

The acoustic behavior of the tunable-septum liner, particularly the resonant frequency behavior, was first examined in a normal incidence impedance tube. A 2DOF liner with a variable buried septum was constructed that was approximately 4.5 inches square in surface area.

The primary objective was to determine how much the primary and secondary resonant frequencies can be shifted with a very small amount of mechanical movement of the septum. Recall from Section II that the primary and secondary resonance frequencies refer to the first and second frequencies in the impedance spectrum where the normalized reactance vanishes and the normalized resistance is relatively small.

Flow-duct Behavior

The acoustic behavior of a tunable-septum liner was also quantified in a grazing incidence and grazing flow environment. This was accomplished in a flow-duct where acoustic energy was superimposed on a mean flowfield. The liner performance was quantified with two experiments outlined below.

Transmission Loss

A section of one side of the flow-duct downstream of an acoustic source, was treated with the tunable-septum liner. Sound pressure levels along the centerline of the duct were acquired so that the transmission loss could be calculated as a function of liner septum configuration. Figure 3.1a shows the basic set-up for this experiment. The transmission loss is defined as the amount of incident acoustic energy that is lost. presumably, to a liner on the wall of a duct. The difference between the incident acoustic energy upstream of the liner and the incident energy after passing the liner is referred to as the transmission loss. Figure 3.1b shows schematically incident acoustic energy in the context of a non-anechoic duct termination. Once the incident power (W_i) is computed. the transmission loss is calculated as follows:

$$TL = 10 \log \left[\frac{W_i \text{ - upstream of liner}}{W_i \text{ - downstream of liner}} \right] \qquad (3.1)$$

Calculation of the transmission loss from measurements was accomplished using a two-microphone method developed by Chung & Blaser[1]. Details of this methodology can be found in Appendix B . These data will help quantify the effect of the variable septum on the sound absorption in a grazing mean flow and grazing incident acoustic field. This data could also be used to extract the wall impedance using a NASA Langley code. currently being developed by Dr. Watson[2]. The methodology used to compute the transmission loss limited the analysis to frequencies below 2000 Hz. This is because the method relies on the assumption of plane wave propagation and the flow-duct used in the present study has higher order duct modes present above this frequency. The behavior of the liner at higher frequencies was quantified with the computation of insertion loss.

Insertion Loss

The insertion loss measures the effect that the acoustic liner has on sound transmitted from the exit of the flow-duct. This was accomplished by first replacing the liner with a rigid wall. Sound was introduced into the flow-duct and the mean velocity in the duct was varied. Acoustic measurements were made outside of the flow-duct on a radius of 2 feet from the center of the duct exit plane at polar angles of 30. 60 and 90 degrees. Figure 3.2a shows the experimental set-up for this experiment. Then the liner was installed on a portion of one side of the flow-duct. The difference between the measured sound pressure levels with the rigid wall and the liner constitute the effect that the liner had in attenuating the acoustic energy in the duct. see Figure

3.2b. Since all of the acoustic energy exiting the duct is not measured, insertion loss in the strictest sense is not computed. However, using selective measurements outside of the flow-duct does provide a good representation of the general absorption qualities of a particular liner. The acoustic input was a frequency sweep from 500 Hz to 6400 Hz produced by a function generator in a 1 second length of time. The sweep allowed for higher levels to be reached across the frequency range in one measurement. This greatly reduced the number of experimental runs needed and allowed examination of data at many frequencies.

3.3 Prediction of 2DOF Liner Resonance Frequency Shift

The amount of primary and secondary resonance frequency shift of a 2DOF liner can be predicted using analytical methods outlined in Section II. Using expressions for the perforate impedance developed in Section II along with the impedance of a backing cavity, an overall liner impedance can be obtained. Impedance modeling of a 2DOF liner based on this approach is given by :

$$
\frac{Z}{\rho c} = \frac{Z_1}{\rho c} + \frac{\dfrac{Z_2}{\rho c}\dfrac{\cos(kL_4)\sin(kL_2)}{\sin(kL)} - i\cot(kL)}{1 + i\dfrac{Z_2}{\rho c}\dfrac{\sin(kL_4)\sin(kL_2)}{\sin(kL)}}
\tag{3.2}
$$

The dimensions L_1, L_2, and L are defined in Figure 1.3. The impedances Z_1 and Z_2 are the impedance of the face sheet and the buried septum, respectively, and are further defined as:

$$
\frac{Z_1}{\rho c} = \frac{R_1}{\rho c} + i\frac{\chi_{m1}}{\rho c}
\tag{3.3a}
$$

$$
\frac{Z_2}{\rho c} = \frac{R_2}{\rho c} + i\frac{\chi_{m2}}{\rho c}
\tag{3.3b}
$$

If the face sheet and buried septum are perforates and only linear effects are taken into account, then the applicable analytical expression from Section II is

$$
\frac{Z_{j(j=1,2)}}{\rho c} = -i\frac{\omega(h + h_{vis})}{c\sigma}\left[\frac{2J_1(k_s r)}{k_s r J_0(k_s r)} - 1\right]^{-1} + i\frac{\omega}{\sigma c}2\left(\frac{8r_o}{3\pi}\right)\left[1 - \sqrt{\frac{\sigma}{2}}\right]
\tag{3.4}
$$

The subscripts 1 and 2 refer to the face sheet and buried septum respectively. The geometric parameters of the baseline 2DOF liner used in this study are given below:

Face Sheet

$h = 0.032$ inches

$r = 0.03125$ inches

$\sigma = 0.196$ accounting for honeycomb cell blockage

66

Septum

$h = 0.064$ inches

$r = 0.03125$ inches

$\sigma = 0.196$ accounting for honeycomb cell blockage

Honeycomb Layers

1st Layer depth. $L_1 = 0.5$ inches

2nd layer depth: $L_2 = 1.25$ inches

Note that the septum thickness is twice as large as the face sheet thickness. This is to account for the perforate-on-perforate concept that was used to vary the septum porosity.

With these parameters and using equations 3.2 - 3.4, the normal incidence impedance was computed and is shown in Figure 3.3. Note that there are *three* frequencies at which the normalized reactance is zero, however, only two of these frequencies correspond to small normalized resistances (see Figure 3.3a and 3.3b). These two frequencies are referred to as the primary and secondary frequency, respectively. From Figure 3.3b, the primary frequency is 1570 Hz and the secondary frequency is 5330 Hz. The frequency at which the normalized reactance crosses zero and corresponds to a very large normalized resistance is approximately 3400 Hz. This is the *anti-resonance* frequency of the liner.

One objective of this current study is to affect changes in the normalized reactance with very small mechanical changes of a given liner. Fundamentally, this will require changing the mass reactance of the perforates since the cavity reactance will remain essentially unchanged. The resistance will also be altered which will contribute to the overall magnitude of the absorption. An estimate to how much reactance change can be achieved with the tunable-septum liner was made by changing the buried septum porosity from a nominal 19.6% to a very small values of 1% and 0%. The latter case assumes that the liner behaves like a single-degree-of-freedom liner. Figure 3.4a compares the predicted reactance spectrum for a septum porosity of 19.6% and 1.0%. Figure 3.4b compares the predicted reactance for 19.6% septum porosity and 0.0% porosity. Note that a large amount of resonant frequency change is predicted for the primary frequency, from 1570 Hz to 960 Hz.

When the septum porosity is zero, the primary frequency effectively vanishes and the resonant frequency moves to 5130 Hz from the baseline of 5330 Hz. Thus theoretically, the liner changes from a 2DOF liner to 1DOF liner, shifting from two resonance frequencies (1570 Hz and 5330 Hz) to a single resonance frequency (5130 Hz).

It is important to note that the prediction of the septum impedance from equation 3.3 includes two important assumptions: 1) Linearity, 2) The orifice geometry is circular. The experimental liner uses a variable buried septum that varies the orifice shape from circular to highly non-circular shapes.

67

3.4   Liner Design and Fabrication

Variable Porosity Buried Septum Layer

The implementation of a variable porosity buried septum as part of a 2DOF resonant liner was achieved by using two 22.5% porosity perforates that were readily available "off-the-shelf." This baseline perforate consisted of round orifices with 0.0625-inch diameters and were spaced 0.125 inches on staggered centers. The thickness of this perforate was 0.032 inches. Figure 3.5 shows the orifice pattern of this perforate. When one of these perforates is placed on another and the orifices are aligned, the resulting perforate has the same properties except that the thickness is now doubled to 0.064 inches.

When one of the perforates is translated over the other perforate, the resulting orifice pattern is changed such that the porosity is reduced. Furthermore, the shapes of the orifice become non-circular. Figure 3.5 shows various porosites and shapes that can be generated with the movement of one perforate over another. The spacing and diameter of the orifices are such that a translation of one perforate 0.0625 inches would result in a completely closed metal sheet. Accounting for the blockage from the honeycomb, the porosity of the resulting two-perforate layer can be changed from 19.6% to 0%.

Liner Construction – Normal Incidence Liner

A two-layer (2DOF) liner was fabricated for testing an impedance tube for purposes of establishing the normal incidence response of this type of liner. Figure 3.6 shows the basic features of this liner and its movable septum mechanism. The exposed liner area was 4.5-inch square. The liner consisted of two layers of commercially available honeycomb. The honeycomb cell lateral dimension is approximately 0.5 inches. The first layer was made to be 0.5 inches thick. It was sandwiched between two perforated metal sheets that had a nominal specifications of the type described above. The second liner layer consisted of the same honeycomb dimensions used in the first layer, except that the layer was 1.25 inches thick. These honeycomb layers were framed in nominal 0.75-inch thick, cabinet-grade plywood. The two layers were constructed such that the honeycomb cells of the first layer were aligned with the cells of the second layer. The second layer terminated with a 1.5inch thick layer of Plexiglas. This simulated a rigid wall backing and had the added advantage of allowing sight of the buried septum and was helpful in quantifying the amount of translational movement implemented. A distributed force along the edge of the perforate was applied, allowing precise translation with a turn of a screw A machine screw with 20 threads-per-inch was used for translational movement. Thus, each revolution of the screw translated the septum 0.05 inches.

Liner Construction – Flow-Duct Liner

Another liner was fabricated for measurements in a flow-duct. This two-layer (2DOF) liner was fabricated for testing an acoustic treatment on one side of a flow-duct. The liner duct-facing area was approximately 4.7 inches wide by 10.5 inches long. The liner consisted of two layers of commercially available honeycomb. The honeycomb cell lateral dimension is approximately 0.5 inches. The components of this liner is shown in Figure 3.7. The construction of the layers was similar to that of the normal incidence liner. One difference, however, was the method by which with the movable perforate in the buried septum was translated. The perforate movement in the flow-duct liner was accomplished with an "off-line" application of force, approximately 4 inches

above the translational plane of the perforate. As with the normal incidence liner construction, a machine screw with 20 threads-per-inch was used for translational movement. This was done to conform to an existing liner housing section of a flow-duct used in previous research work. Section 3.6 below describes the flow-duct facility and its components in detail.

3.5 Experimental Facilities and Instrumentation for Normal Incidence Impedance Measurements

Normal Incidence Impedance Tube

The normal incidence impedance data for the tunable-septum liner described in Section 3.4 was acquired in a commercially available Bruel & Kjaer (B&K) 4206 Impedance Tube. Figure 3.8 shows the standing wave tube used for the present study and its constituent parts. The B&K 4206 impedance tube utilizes the two microphone method of Chung & Blaser³ for determining a material's impedance. It provides impedance data for a range of frequencies simultaneously through broadband sound radiation from the tube's acoustic driver. This feature allows relatively quick determination of input impedance of liner materials compared to a standing wave impedance tube which acquires data at one frequency at a time. A frequency range of 50 Hz to 6400 Hz is possible by configuring the impedance tube with two measurement tube diameters.

Since the impedance tube relies on plane wave impingement of sound onto the test sample, the tube diameter is critical to the frequency range of interest. The B&K 4206 impedance tube has a 3.94-inch diameter tube and a 1.14-inch diameter tube. This ensures plane wave propagation from 50 Hz to 1600 Hz (with the 3.94-inch diameter tube) and from 500 Hz to 6400 Hz (with the 1.14-inch diameter tube).

Data Acquisition and Processing

The B&K 4206 impedance tube is supplied with application software which works in concert with a two-channel signal analyzer and a 486-based computer to automate the data acquisition process. A B&K 2034 Dual Channel Signal Analyzer was used for the signal processing and a WIN 486 PC was used to control data acquisition. The B&K 2034 analyzer provided a broadband signal which was passed through a Cerwin-Vega amplifier before being sent to the speaker in the impedance tube. The microphone signals were input into pre-amp ports on the dual channel analyzer.

3.6 Experimental Facilities and Instrumentation for Flow-Duct Acoustic Measurements

Liner Flow-Duct Facility

Liner testing under grazing flow conditions was performed in a non-anechoically terminated flow-duct. The flow-duct was configured such that sound and flow originated upstream of any liner section placed in the duct. This facility consisted of a high-pressure plenum, a converging duct section, and a constant-area duct section. At some distance along the constant area section, a liner housing section was placed. Upstream of this location, acoustic energy was allowed to enter the duct via two ports on the side. Figure 3.9 shows this facility and its constituent parts. The constant area duct section was rectangular (4.69 inches x 2.00 inches). At a temperature of 72° F, a purely plane wave will propagate up until a frequency of 1450 Hz when the 1ˢᵗ higher mode is cut-on.

The plenum was fed from a larger holding reservoir with a maximum capacity of 300 psi. This was then regulated down to a maximum of 150 psi that was fed to the plenum by a 2-inch diameter pipe. Air in the plenum is acoustically muffled and exits through an 8-inch diameter opening. A square nozzle was attached that had dimensions 4.69 inches x 4.69 inches, thus providing a step-change in area with an area ratio of 2.28. This area then converged to a 4.69 x 2.00 inch rectangular area. This converging nozzle area ratio was 2.34. Thus the plenum to constant-area duct ratio was 5.36. Half-round molding was used to provide a smooth-flow "entrance" for the air into the rectangular converging nozzle.

The acoustic source was provided by two Electro-Voice DH2012 compression drivers. Each driver horn opening was attached to one end of a 6-inch long steel pipe with the other end of the pipe threaded for flush attachment to the side of the flow-duct. The pipe inner diameter was 1.0 inches. The termination of the pipe at the flow-duct wall was fitted with a high porosity (40%) perforate to provide relatively smooth flow over the pipe opening.

The constant area portion of the flow-duct is 38 inches long. An acoustic liner housing section was installed 15 inches downstream of the source section. This section allowed for the long side of the rectangular area to be treated with acoustic liner material over an 11-inch axial distance. For the present study, only one side of the liner housing was used. Fixed flush mounted microphones could be installed approximately 1.5 inches upstream and downstream of the acoustic treatment. Only the upstream location was used in the present study.

Axial Microphone Probe

Figure 3.10 shows the axial microphone probe. Transmission loss data was primarily acquired from a single axially traversing microphone along the centerline of the flow-duct. This microphone was a 1/4-inch B & K 4135 condenser type that was fitted with a B & K UO135 nose cone. A B & K 2633 pre-amplifier was used in conjunction with the microphone. The microphone and the whole assembly was placed in a steel tube. The tube was rigidly fixed in the lateral direction with a fork-like brass support near the front end. Near the rear of the probe, a wooden support was attached that was anchored on a traverse sled. The entire assembly was adjusted so that the center of the microphone was aligned with the centerline of the flow-duct. The probe was free only to move in the upstream and downstream direction of the flow-duct centerline axis.

Source Monitoring Microphone

In addition to the axial probe microphone, a Kulite microphone was used to monitor the acoustic output from one of the two drivers. Monitoring the source in this way allowed for the source conditions to be repeated for different liner configurations. A Kulite model mic-062 LT was placed flush near the acoustic driver in the tube that acts as a conduit for the sound to reach the flow-duct. This microphone was nominally 0.062 inches in diameter and had a protective grid over its diaphragm. It was powered by three 6-Volt lantern batteries to provide an 18-Volt nominal supply voltage. The microphone output was fed directly into an FFT signal analyzer.

Data Acquisition and Processing

All of the B&K microphones were powered by B&K 2084 Power Supplies. The microphone signals were fed into a HP 3667A Multi-Channel Signal Analyzer for FFT analysis. The analyzer was operated from a Windows 95 platform on a Pentium 200 MHz computer. Figure 3.11 shows a schematic of the signal processing paths involved. The FFT analysis was performed with a frequency span of 0 – 6400 Hz with a bandwidth of 4 Hz. Except where noted, 64 averages were used when sampling the microphone signals.

Frequency domain data were saved for each run on the computers hard drive in HP file format. These files were converted to ASCII text format and processed to quantify the sound pressure levels in the duct. The transmission loss of the liner was computed from this raw data for a given liner configuration and grazing flow velocity. This procedure is described in Appendix B.

3.7 Normal Incidence Impedance Results

Experimental Set-Up

The impedance tube (described in Section 3.5) was used without its sample holder to compute the normal incidence impedance of the tunable-septum liner. A rubber gasket, 0.1 inches-thick was attached around the edge of both the large (3.94-inch diameter) and small (1.14-inch diameter) tubes. The liner was then pressed with sufficient force against the gasket to provide an air-tight seal on the surface of the liner. Figure 3.12 shows both the large and small tube test configurations.

Eight septum configurations were chosen that varied the septum porosity from approximately 0 to 19.6%. This porosity was determined from the resulting geometric area of one circle partially covering another circle. Figure 3.13 shows how this area can be analytically determined. Thus, for a given amount of uni-directional translation of one perforate, the resulting open area can be computed. The porosity for the maximum amount of septum open area was determined by counting the open orifice holes in an individual honeycomb cell. An average over several cells yielded approximately 19.6% as a base porosity. Table 3.1 displays the amount of septum translation and the resulting porosity for each configuration.

Table 3.1 Septum translation and resulting porosity

Configuration	Translation, mm [inches]	Porosity
S1	0.00	19.6%
S2	0.79 [0.031]	7.7%
S3	1.00 [0.039]	5.1%
S4	1.19[0.047]	2.8%
S5	1.39 [0.055]	1.0%
S6	1.49 [0.058]	0.4%
S7	1.59 [0.063]	0.0%

The amount of translation was achieved by turning the positioning screw the correct amount of angular degrees determined with a protractor.

Normal Incidence Impedance of Tunable-Septum Liner

The low-frequency results and high-frequency results are shown in Figure 3.14 and Figure 3.15, respectively. These figures show narrow band data but symbols are shown at selected points to distinguish the different septum configurations. The low-frequency results were obtained with the large impedance tube configuration and the high frequency results were obtained with the small impedance tube configuration.

Evidence of the first resonant frequency can be seen in Figure 3.14b where the normalized reactance crosses the zero axis around 1400 Hz. An anti-resonance seems to occur around 500 Hz, which is evident from the locally high value of resistance and rapid change of the reactance from positive to negative. Similarly, Figure 3.15b shows a secondary resonant frequency around 4800 Hz and an anti-resonance varying between 3100 Hz and 3600 Hz.

Shift in Resonant Frequency

Focusing on the normalized reactance and specifically around the resonant frequencies, reveals that a frequency shift of approximately 14% (200 Hz) was observed. This is shown in Figure 3.16a, which is a zoomed view of the portion of Figure 3.14b in the frequency range of 1 – 1.6 kHz. Likewise, a frequency shift of approximately 16% (800 Hz) was observed at the secondary resonant frequency, shown in Figure 3.16b. The maximum mechanical movement required for the full extent of the resonant frequency reduction was one-sixteenth of an inch. When the septum porosity is zero, the liner effectively becomes a single-degree-of-freedom (SDOF) liner and the resonant frequency is governed by the 0.5-inch honeycomb cavity of the first layer as well as the mass reactance of the face sheet.

Figure 3.17a shows the normalized reactance near the frequency range associated with the primary resonance for the maximum septum porosity configuration, S1 and the configuration associated with the largest observed resonance frequency shift, S4. For comparsion, the predicted reactance is included. For configuration S1, the predicted primary frequency appears to be approximately 100 Hz higher than the measured. Below the calculated value of 2.8% porosity, the measured data does not follow the predicted trend shown in Figure 3.4.

Figure 3.17b shows the normalized reactance near the frequency range associated with the secondary resonance for the maximum septum porosity configuration, S1 and the configuration associated with the largest observed resonance frequency shift, S7. Again, the predicted reactance is shown for comparison. The measured data appears to exhibit the predicted trends. However, if the frequency range is zoomed for closer examination as in Figure 3.18, the measured secondary resonance frequency appears to be in agreement with the predicted Helmholtz frequency of a single cavity with perforated opening. The predicted SDOF frequency is approximately 5130 Hz while the maximum septum open area 2DOF configuration has a resonant frequency of approximately 5330 Hz. This raises the question as to whether the expected range of resonant frequency change is closer to 800 Hz as observed in the impedance tube or a smaller 200 Hz as predicted with linear theory. The fact that the measured 1DOF resonant frequency seems to coincide with predicted Helmholtz frequency suggests that the linear prediction is not accounting for the mass and cavity reactance correctly.

In summary, it has been shown that a liner under normal incidence conditions can be tuned by using a septum consisting of two perforates, with one perforate sliding over the other to change the effective porosity. Normal incidence impedance results indicated that a 14% (~200 Hz) shifting in the primary peak absorption frequency and a somewhat large shift 16% (~800 Hz) was observed at the secondary frequency. These results were not predicted by linear impedance modeling where the primary resonance frequency shift was approximately 600 Hz and the secondary resonance frequency was approximately 200 Hz. The overall sound pressure level that the liner was exposed to in these tests was approximately 120 dB. The model's primary assumption is that the acoustic properties are linear and that the orifices are circular. This assumption may break down at much lower porosities and thus a nonlinear effect needs to be accounted for in the model. Furthermore, it is also possible that the mass end correction of these non-circular holes is significantly different than from circular holes.

3.8 Flow-Duct Results

Acoustic data were acquired with the 2DOF liner with movable perforated buried septum installed on one side of the GTRI flow-duct. Several grazing flow velocities and liner septum configurations were tested. A total of four septum configurations were tested and they correspond to the septum porosities shown in Table 3.2.

Table 3.2 Configuration key for estimated porosity of buried septum tested liner

Configuration	Tranlslatonal Movement, mm [inches]	Porosity
I	0.00	19.6%
II	1.19 [0.047]	2.8%
III	1.29 [0.055]	1.0%
IV	1.59 [0.063]	0.25% (Estimated)

Flowfield Characterization

Flow was introduced into the duct to simulate a grazing flowfield across the liner. Nominal centerline mean velocities of 0, 100 ft/s, 150 ft/s, 200 ft/s, and 250 ft/s were chosen for testing and were set by fixing the upstream plenum total pressure. A platinum-plated, tungsten constant-temperature hot-wire was used to characterize the flow profile along the minor axis of the flow-duct 4.125 inches upstream of the liner's leading edge. Figure 3.19 shows the location of the hot-wire measurements relative to the duct and liner geometry. Due to geometry restrictions, the hot-wire could not be placed as close to the top wall of the duct as it was to the bottom wall. The hot-wire placement ranged from 0.18 inches from the top wall and 0.08 inches from the bottom wall. Figure 3.20 shows mean flow profiles upstream of the liner in the flow-duct. Some general observations can be made regarding the flowfield:

1) The flow appears to be not fully-developed. This is evident from the very small change (within measurement error) in the mean velocities in the middle third of the duct height. This implies that the boundary layer growth has not yet merged from the upper and lower walls in the duct.

2) The boundary layer can be described as turbulent based on the velocity behavior near the walls. Since the flow is not fully-developed, it can be treated near the walls like flow over a flat

plate. It has been experimentally established over the years that the behavior of a non-dimensional turbulent velocity profile follows a $1/7^{th}$ power law relationship within the boundary layer[55]. Figure 3.21 shows how this relationship compares with the measured velocity data near the bottom wall. The generally good agreement with the power law suggests that the boundary layer was indeed turbulent.

Finally, the degree to which the flow was turbulent was quantified by measuring the turbulent intensity of the axial component of velocity. Figure 3.21 shows the ratio of the root mean square of the axial fluctuating velocity with the local mean velocity for the four nominal plenum conditions. It is clear that all four velocity conditions exhibit similar turbulent intensities, ranging from 1 % in the middle third of the duct to 9 – 10 % near the walls.

Effect of Tunable-Septum Liner on Transmission Loss

A multi-frequency waveform with a 100 Hz fundamental was input into the flow-duct via two acoustic drivers upstream of the liner and a microphone was traversed along the duct's centerline. Figure 3.22 shows the microphone locations in the duct where acoustic data were acquired. Using the methodology outlined in Appendix B, the transmission loss across the liner was computed. Frequencies from 500 Hz to 2000 Hz were examined. Data was not analyzed below 500 Hz since the liner was not expected to absorb much sound below 500 Hz and the acoustic drivers began to lose performance below this frequency. Although the first cut-on mode (1st non-planar mode) is calculated to be approximately 1430 Hz, the transmission loss calculations were carried out up until 2000 Hz. This was done because the liner had a nominal peak absorption frequency of approximately 1400 Hz and sufficient data was needed to "surround" the peak absorption frequency. The amount of acoustic energy absorbed by the liner can be determined by examining the decomposed incident acoustic wave ahead of the liner leading edge and downstream of the liner trailing edge. Figure 3.23a shows typical spectra of these two incident sound pressure level components for M = 0.0 with the liner in configuration I (a septum porosity of 19.6%). Note that the incident SPL levels are less than 110 dB over the frequency range tested. It is evident that the liner is absorbing a significant amount of energy near and around 1400 Hz. The difference in these spectra is called the transmission loss. The transmission loss is plotted in Figure 3.23b where a positive value is considered a net absorption of acoustic energy.

Figure 3.24 shows the results of the transmission loss analysis as a function of liner configuration for a given grazing flow velocity. For all grazing flow conditions, a shift in peak absorption frequency is observed corresponding to a lower frequency. This shift to a lower frequency is consistent with the impedance tube data. However, the extent of the shift in this case is on the order of 100 Hz, whereas, in the impedance tube, the range for the primary frequency shift was approximately 200 Hz. Figure 3.25 shows only the transmission loss for configuration I (σ_{septum} = 19.6%) and III (σ_{septum} = 1.0 %) in a frequency range near the peak absorption for clarity. The small translational movement has accomplished a shift in frequency and to some extent an increase in the overall absorption magnitude.

The behavior of the tunable-septum liner under increasing grazing-flow velocities is shown more directly in Figure 3.26 Note that for Configuration I (σ_{septum} = 19.6%), the peak absorption frequency shifts to a higher frequency and this trend slow diminished as the septum porosity is

reduced (from Configuration I to IV). With the liner in Configuration IV(σ_{septum} = 0.25%o). only the magnitude of the absorption seems to be affected by the grazing flow. The flow does not have a discernable effect on the peak absorption frequency. Increased flow reduces the amount of absorption for all liner configurations. The trend of decreasing absorption with increasing grazing flow is due to the increased acoustic resistance of the face sheet. This is a well established phenomenon and results in decreased liner attenuation . Recall from Section II. that as the shear layer grows over each orifice act as a way to decrease the effective open area of the orifice. This results in a higher acoustic resistance.

In general, the flow-duct data was consistent with the impedance tube data in that the range of frequency shift (i.e., the tunable frequency range) was smaller for the primary resonance and larger for the secondary resonance. However, the observed tunable frequency ranges were smaller in both cases. It is possible that differences in the construction of the two liners can account for some of this reduction. It is known that the flow-duct liner can not achieve a fully closed septum. A fully closed septum was achieved by removing the second layer altogether and testing the 1st layer in isolation with a simulated hardwall. These results are discussed below.

From the transmission loss data (Figures 3.24 to 3.26) it is evident that for the primary liner resonance that a shift to a new peak absorption frequency can be achieved. Furthermore, with no flow in the duct, the magnitude of the peak absorption is increased and it exhibited a broader frequency at which appreciable absorption took place. The main reason for this is that the liner's normalized resistance is increased until it approaches unity in this frequency range. This increased resistance is due to the buried septum changing its porosity and possibly due to the changing orifice shape. These changes promote higher particle velocities through the orifices. which increase the viscous resistance. This increase in resistance was clearly evident in the impedance tube data (see Figure 3.14).

As the grazing flow was introduced into the duct, the liner still exhibited a shift in frequency. however the extent of the broadened absorption was diminished. Until a mean duct centerline velocity of 150 ft/s was reached, the shifted peak absorption was higher than the baseline liner configuration. Above this velocity, the peak absorption levels are approximately of the same order or less when the septum area is closed. This can be explained as follows. With no grazing flow. the face sheet provides little acoustic resistance and since its geometry is fixed. it will remain the same value while the septum open area is reduced. Hence the buried septum will control the liners resistance. As mentioned, this increased resistance approaches unity and even exceeds it for very small septum porosities. As the face sheet is exposed to grazing flow. the resistance of the face sheet increases. As mentioned earlier, this is a well established phenomenon with perforates and orifices. The result is that the magnitude of the absorption is reduced as the face sheet contribution of the total resistance becomes on the order of and greater than the buried septum's contribution.

It is possible that this effect could be minimized if a more linear face sheet could be employed [i.e., one that is not sensitive to grazing flow], such as a porous layer made of feltmetal or woven screen. However, these types of porous layers also are accompanied by high acoustic resistances. Thus it would be difficult for the septum to be a controlling parameter of the overall resistance.

Figure 3.26 shows another consequence of controlling the buried septum's impedance. With the septum in a maximum open area configuration, i.e., the lowest resistance configuration, the peak absorption frequency shifts to a higher frequency as a function of grazing flow velocity. As the septum's resistance is increased, the sensitivity of this effect is diminished. For example, with the liner in Configurations III (σ_{septum} = 1.0%) and IV (σ_{septum} = 0.25%), there is no observed shift in frequency due to increasing grazing flow. This suggests that the buried septum is also the major contributor to the mass reactance of the liner and indeed when the porosity is small enough it fixes the peak absorption frequency.

Effect of Liner on Insertion Loss

The insertion loss was computed as described in Section 3.3 using data from three microphones located outside of the flow-duct. Figure 3.27 provides an example of a typical insertion loss results. Sound pressure level differences between the rigid wall and a given liner configuration (Figure 3.27a) result in a "loss" due (shown as a positive change in Figure 3.27b) to the liner's presence or "gain" (shown as a negative change). For clarity, a smoothing fit locally weighted, least squares error method smoothing fit was applied to the insertion loss spectra, resulting in Figure 3.27c. The method of smoothing was a locally weighted, least squares error method. All insertion loss plots used the same weighting factor of 5%. This allows for relatively clear identification of peak absorption frequencies. Figure 3.28a -i shows the insertion loss computed from the 60° microphone located two feet from the exit of the flow-duct. For each grazing flow velocity the insertion loss at the lower and higher peak absorption frequencies are shown in the left and right columns, respectively, as a function of liner configuration. In general, both absorption peaks are reduced as a function of decreasing septum porosity. This is consistent with the normal incidence impedance data and the transmission loss data. At the higher frequencies the lower septum porosity both shifts the peak absorption frequency but increases the absorption across a large frequency range.

The insertion loss data reveals consistent trends with liner configuration and grazing flow velocity as was shown with the transmission loss data. The tunable frequency range of the secondary resonance was substantially reduced however, it should be noted the Configuration IV (σ_{septum} = 0.25%) did not represent a true zero septum porosity case that was achieved in the impedance tube liner data. It is clear from Figure 3.29 that having zero porosity in the septum, i.e., creating a 1DOF liner, shifts the frequency to a slightly lower frequency than Configuration IV (σ_{septum} = 0.25%).

Single Layer Liner Results

Due to the construction of the flow-duct tunable-septum liner, Configuration IV did not result in a completely closed or zero porosity buried septum as it did on the liner used for the impedance tube testing. In order to examine the full extent of the tunable nature of this type of liner, only the first half-inch-thick layer was installed in the flow duct and its insertion loss was measured. This was similar to running the 2DOF liner with the buried septum porosity at 0%. Furthermore, the single layer liner was tested with the normal incident impedance tube described in Section 3.5.

76

Insertion loss with no grazing flow of the single 0.5-inch honeycomb layer resulted in the elimination of the primary peak absorption frequency centered around 1400 Hz. The secondary peak absorption frequency centered around 4200 Hz was still present. Figure 3.29 shows the insertion loss from the 60-degree microphone. Note that the first large absorption peak has completely disappeared (see Figure 3.29a). There appears to be another peak centered around 2700 Hz and is addressed below.

The additional local peak absorption centered on 2700 Hz was unexpected. A check was made of this 1st layer liner in the impedance tube to identify if the absorption peak is due to a reactive component or just increased resistance. Figure 3.30 shows the normalized resistance and reactance of the single 0.5-inch honeycomb layer and the 2DOF impedance tube-tested liner with the buried septum at 0% porosity. Figure 3.30b indicates that the normalized reactance of the flow-duct liner and the impedance tube liner with septum in its maximum closed configuration are nearly identical. The value of the reactance that is zero is the resonance frequency. However, it is quite likely that differences in the resistance measured in the 2500 Hz to 4000 Hz range account for the local increase in the liner's absorption shown in the flow-duct in Figure 3.29a. In other words, the resistance of the 0.5-inch honeycomb layer used in the flow-duct liner is close to an optimum value of unity (about 0.8 at 2700 Hz from Figure 3.30a). Thus, for a relatively low reactance this will produce a relatively high absorption.

3.9   Conclusions

The following key conclusions are drawn from the experimental presented in this section:

Normal Incidence Impedance Results

1) The absorption characteristics of a nominal 2DOF resonant-type liner can be controlled to a degree in both peak absorption. This can be accomplished with less than 0.0625 inches (on the order of one orifice diameter) of mechanical movement in the buried septum of the liner.

2) For no grazing flow and for normal incidence, the liner was observed to shift the primary resonance approximately 14% (200 Hz) and the secondary resonance approximately 16% (800 Hz).

3) The small translational change in the buried septum had a strong impact on the normalized resistance and at certain frequencies with near maximum movement the septum resistance increased by an order of magnitude.
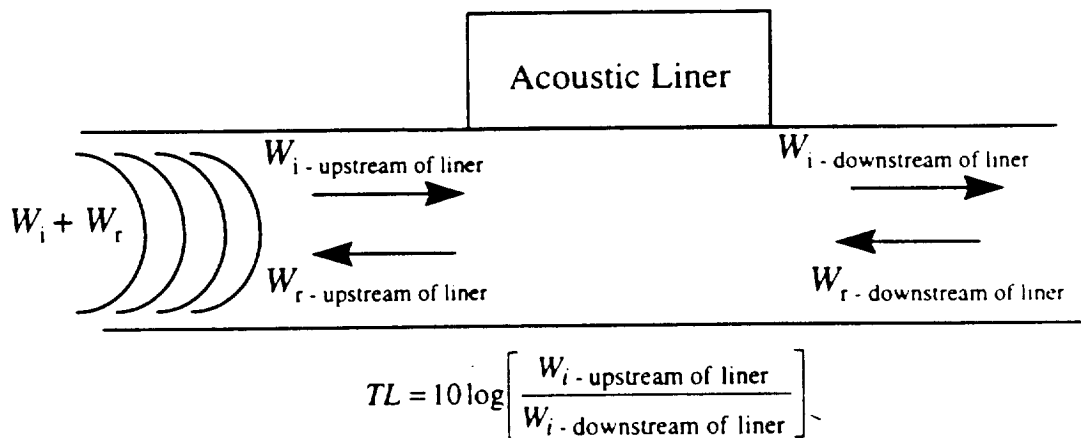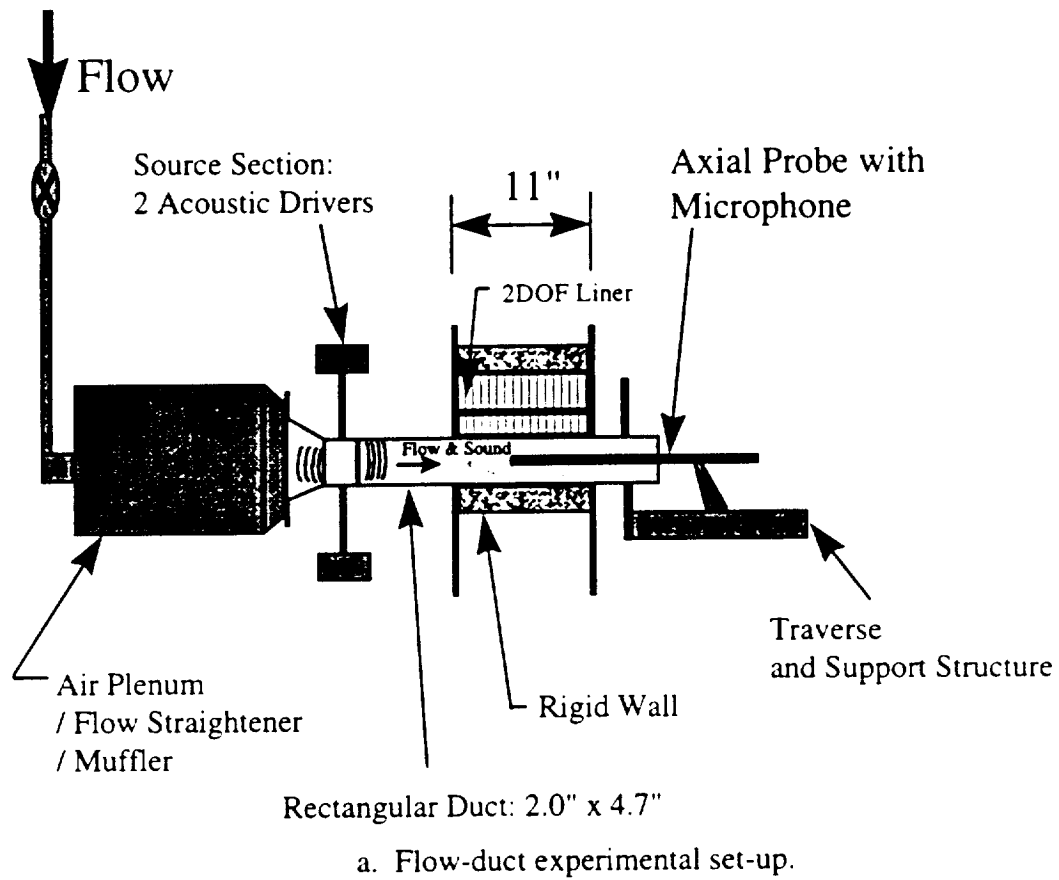
4) Linear impedance modeling predicts a much larger shift in primary absorption frequency, suggesting that even at relatively low sound pressure levels nonlinear effects or orifice shape can be very important.

Flow-Duct Absorption Results

5) Shifting of the peak resonance frequencies was demonstrated in a grazing flow environment with both transmission and insertion loss measurements.

6) Control of the buried septum impedance was able to overcome the increased face sheet impedance due to the grazing flow. This was concluded from the relative insensitivity of the peak absorption frequency as the buried septum porosity was altered.

7) The extent to which the overall magnitude of the absorption can be controlled is directly related to both the mass reactance and the resistance of the buried septum.

How the variable orifice perforate's mass reactance and resistance differ from a standard perforate is examined in the following sections. This needs to be understood to further exploit the tunable liner concept built and tested in this study.

Flow

Source Section:
2 Acoustic Drivers

11"

2DOF Liner

Axial Probe with
Microphone

Flow & Sound

Air Plenum
/ Flow Straightener
/ Muffler

Rigid Wall

Traverse
and Support Structure

Rectangular Duct: 2.0" x 4.7"

a. Flow-duct experimental set-up.

Acoustic Liner

$W_i + W_r$

$W_{i\text{ - upstream of liner}}$

$W_{i\text{ - downstream of liner}}$

$W_{r\text{ - upstream of liner}}$

$W_{r\text{ - downstream of liner}}$

$$TL = 10 \log \left[\frac{W_{i\text{ - upstream of liner}}}{W_{i\text{ - downstream of liner}}} \right]$$

b. Definition of transmission loss

Figure 3.1 Experimental set-up for transmission loss measurments
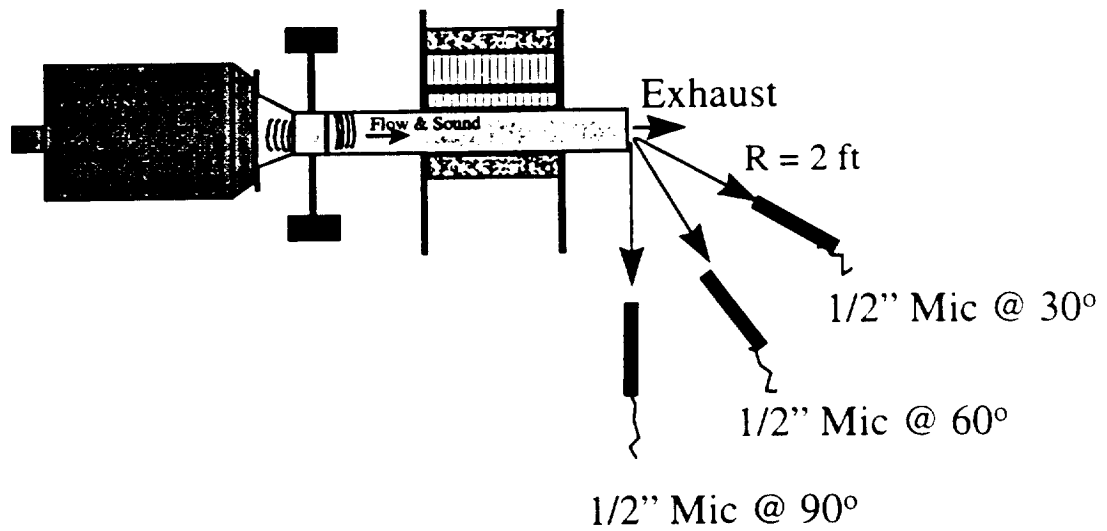
a. Experimental set-up for insertion loss measurements

$$IL = 10 \log \left[\frac{P_{\text{rigid wall}}}{P_{\text{liner}}} \right]$$
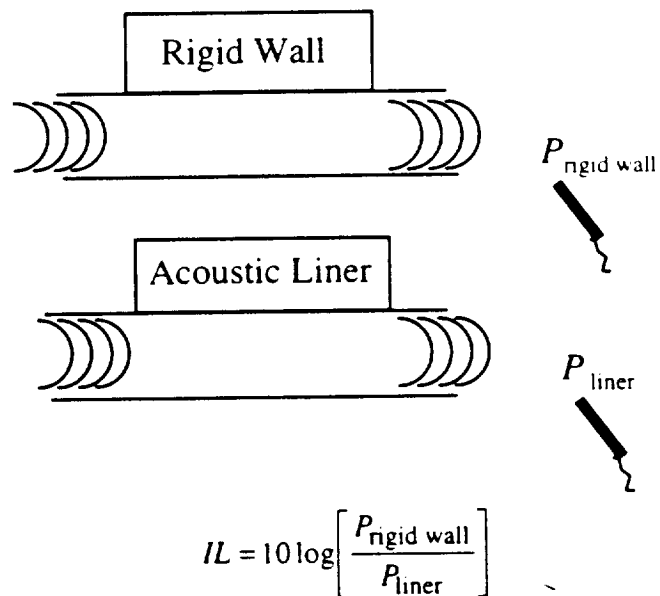
b. Calculation of insertion loss

Figure 3.2 Experimental set-up for insertion loss measurements.
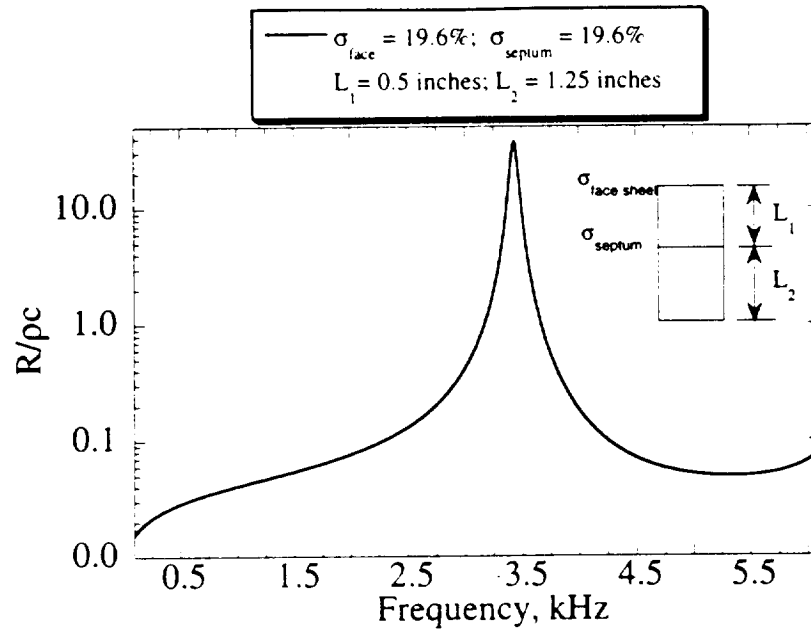
a. Normalized Resistance
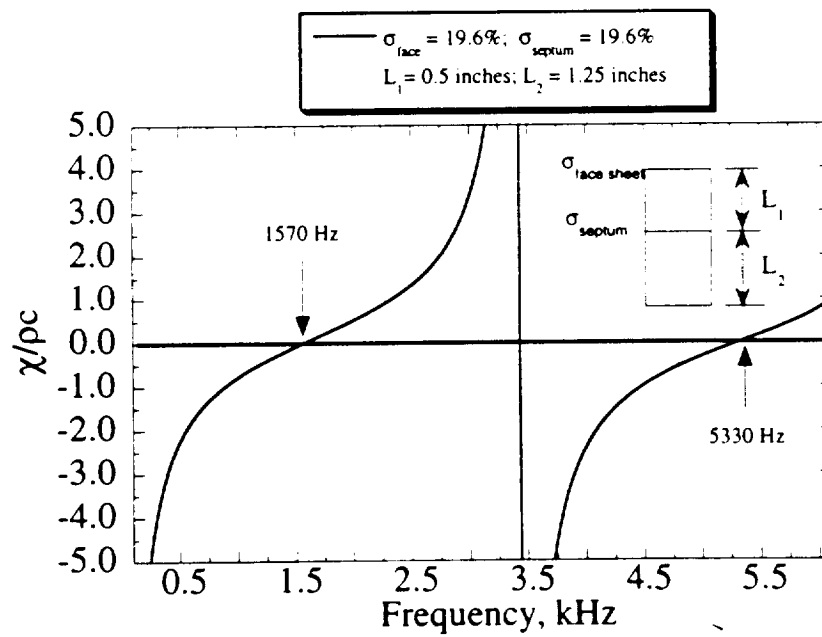
b. Normalized Reactance
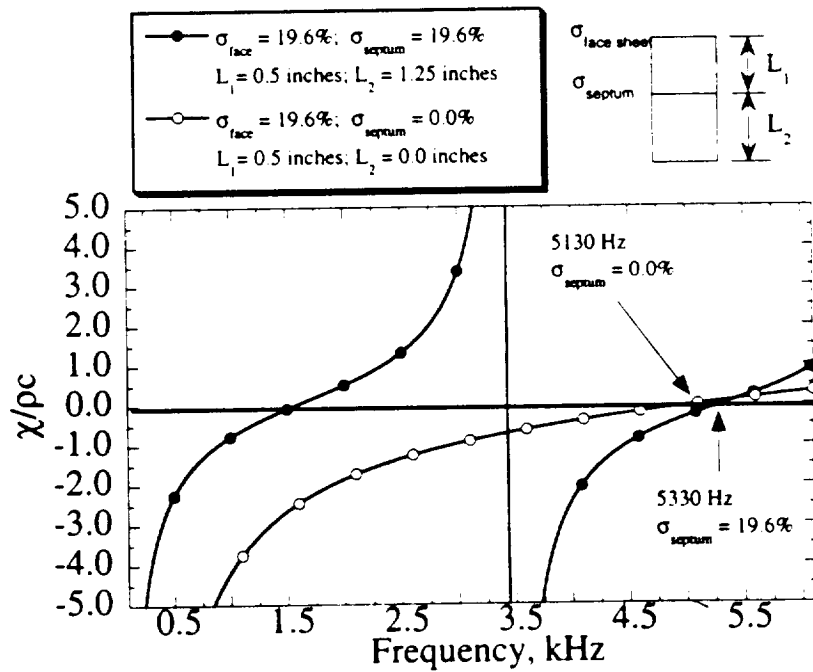
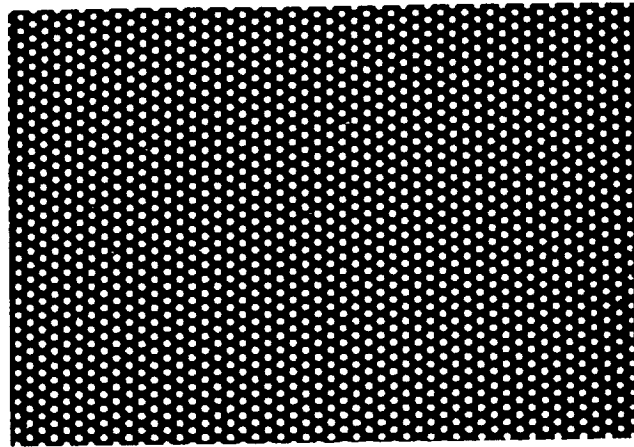Figure 3.3 Prediction of baseline 2DOF liner impedance.
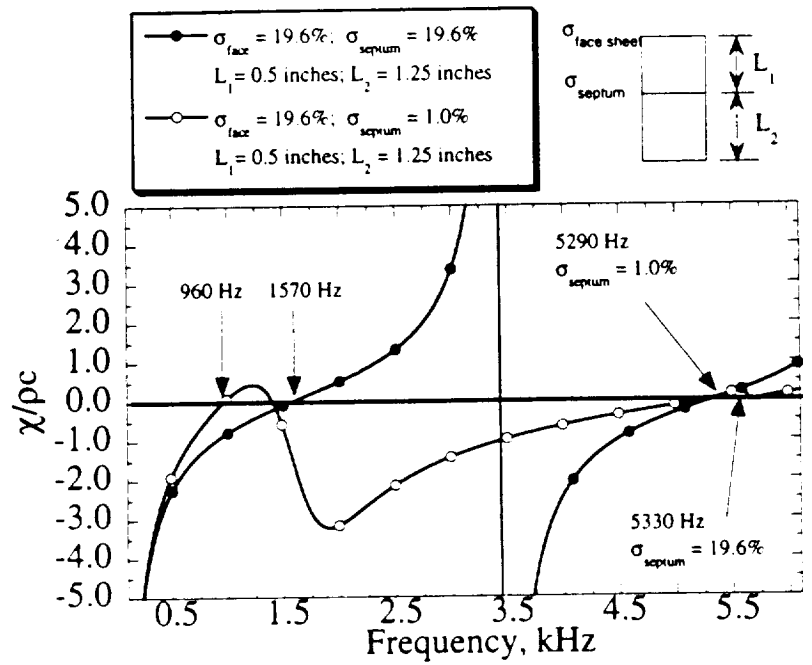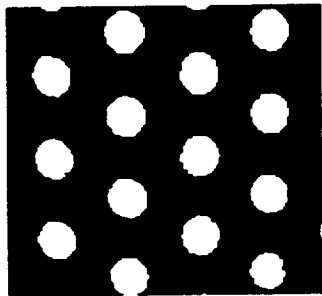
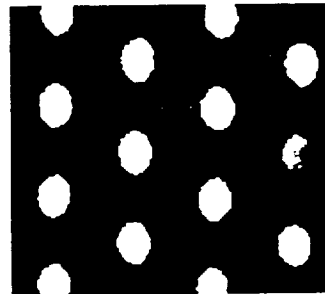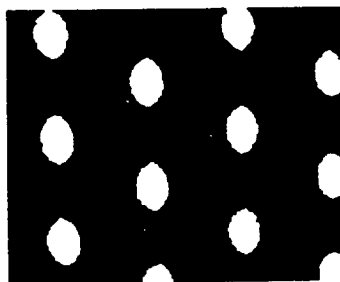Figure 3.4 Prediction of 2DOF liner reactance with two extremes in buried
septum porosity.

Nominal 22.5% perforate with 0.0625-inch diameter
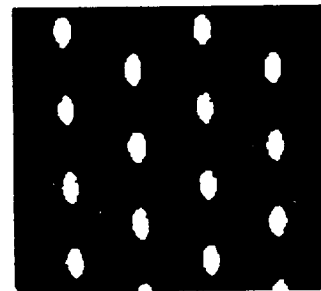holes staggered on 0.125-inch centers

Max Open σ = 22%

~ 1/4 Max Closed

~ 1/2 Max Closed

~ 3/4 Max Closed

Figure 3.5 Perforate orifice size and shape changes with sliding perforate concept.

Septum: Sliding Perforate

Translational
Position Screw

Septum: Fixed Perforate

0.5"
Honeycomb
Layer

1.25"
Honeycomb Layer

Plexiglass "Rigid" Back Wall
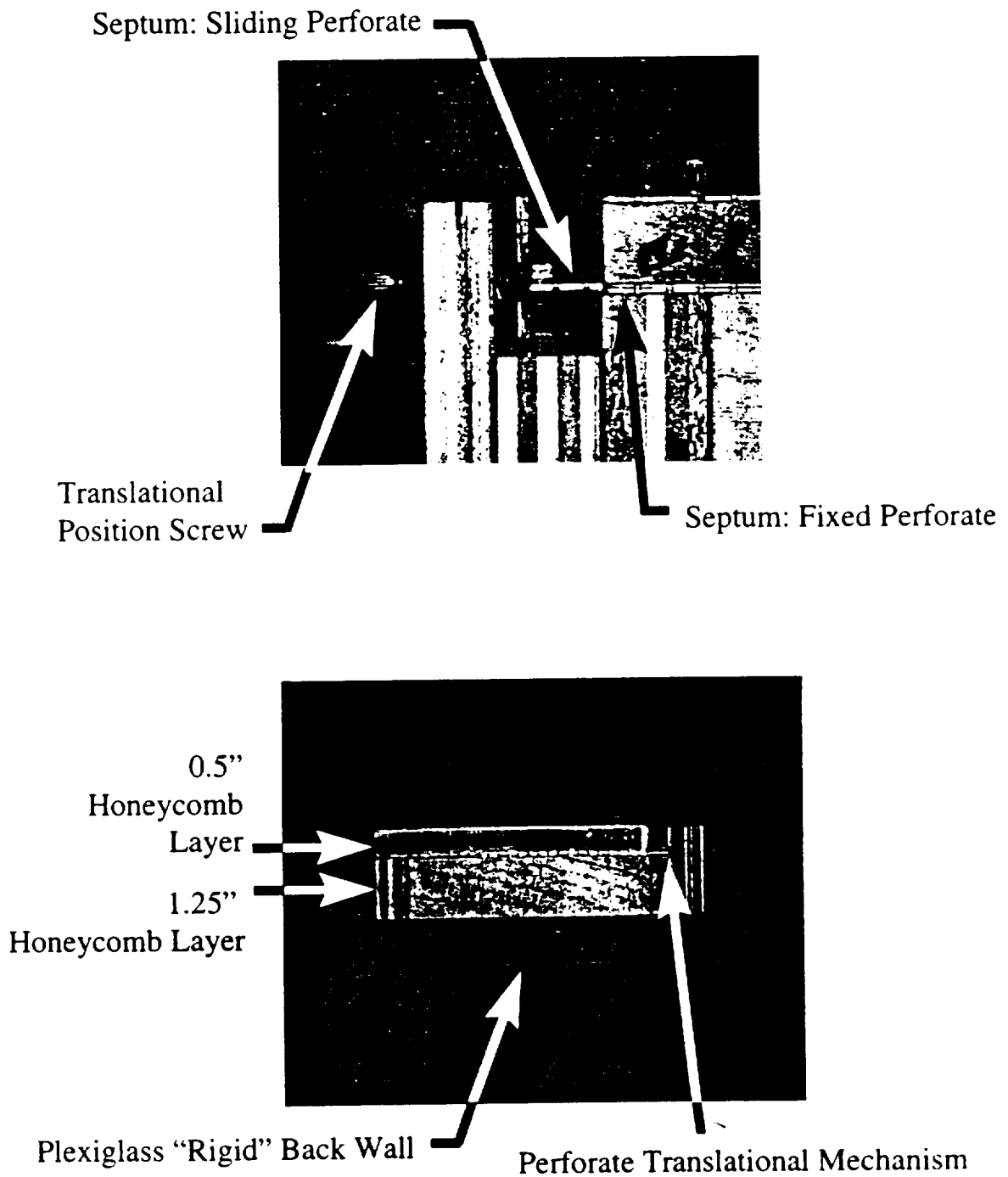
Perforate Translational Mechanism

Figure 3.6 Two-degree-of-freedom liner with variable porostiy buried septum used for flow-duct measurements.
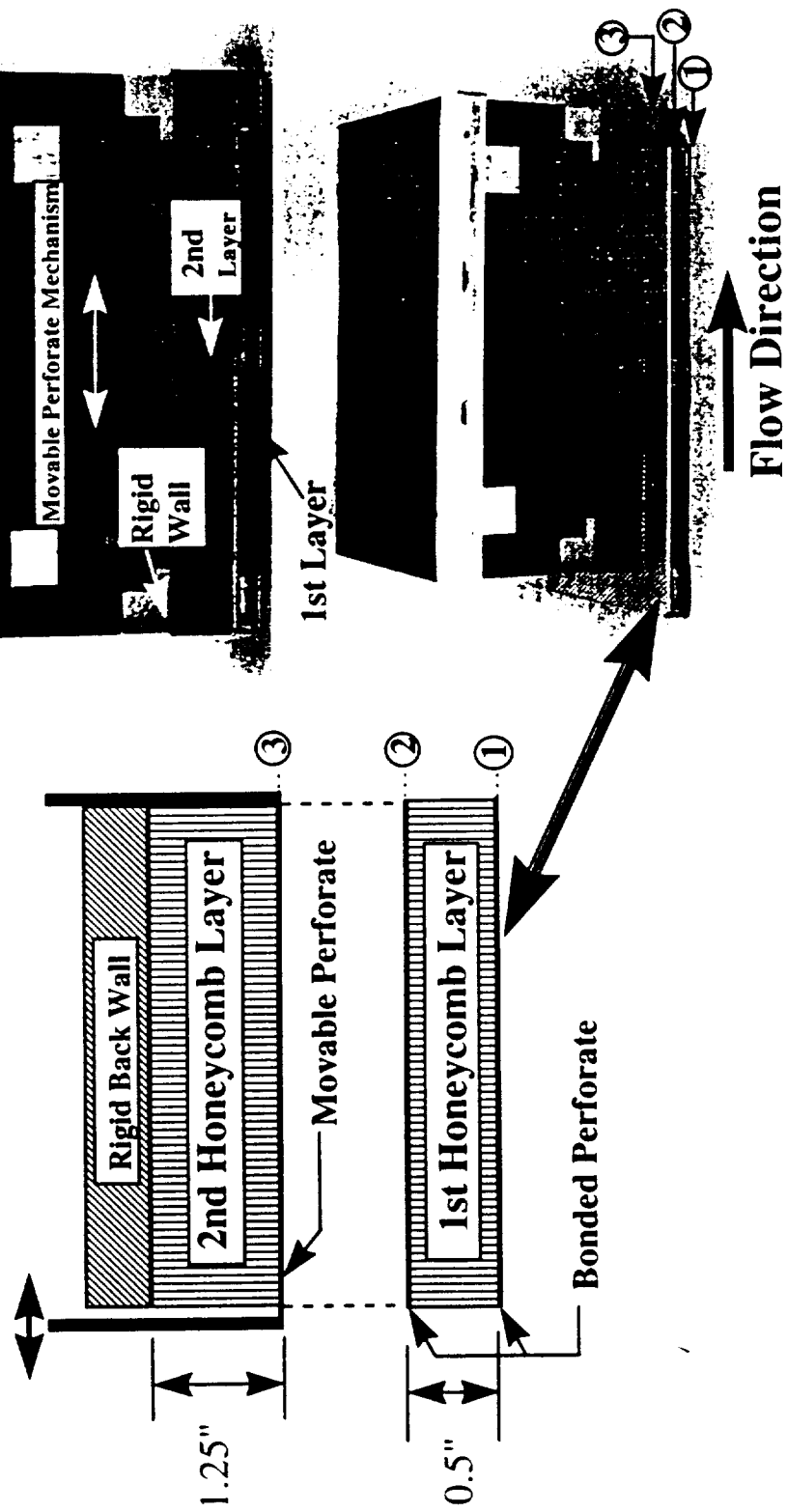
Figure 3.7 Two-degree-of-freedom liner with variable porosity buried septum used for flow-duct measurements.

85
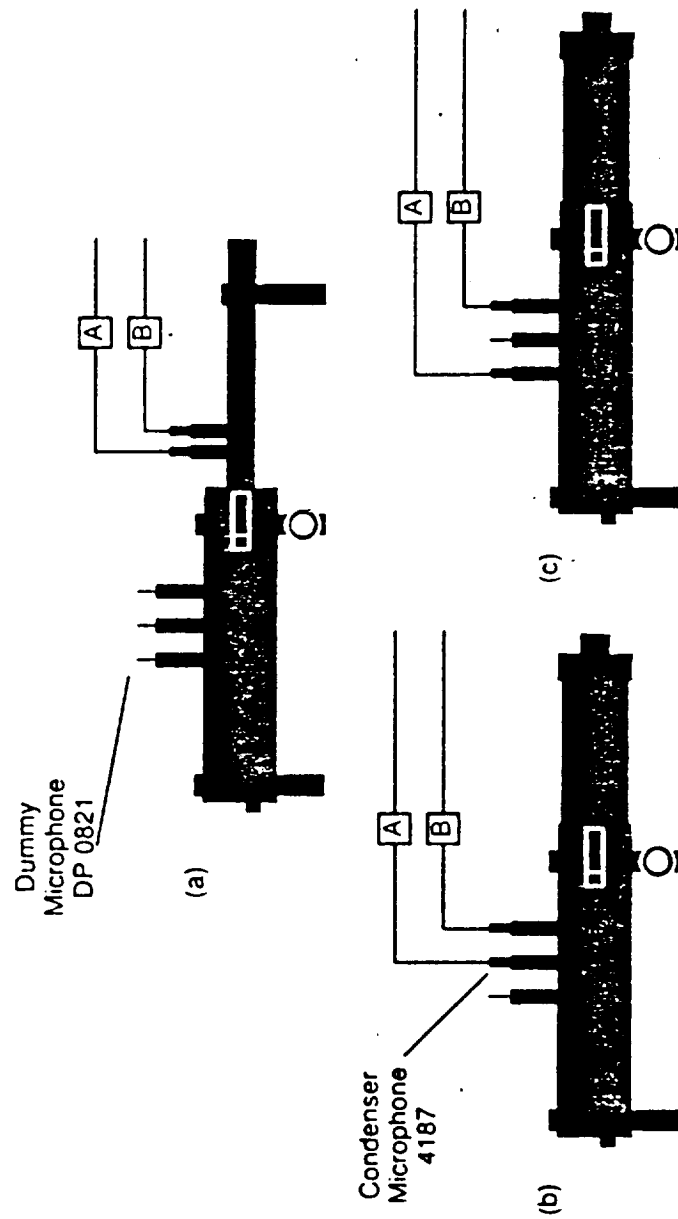
Figure 3.8 Three basic set-up types for the B&K 4206 impedance tube: a) Small tube; b) Large tube - standard; c) Large tube - wide microphone spacing.
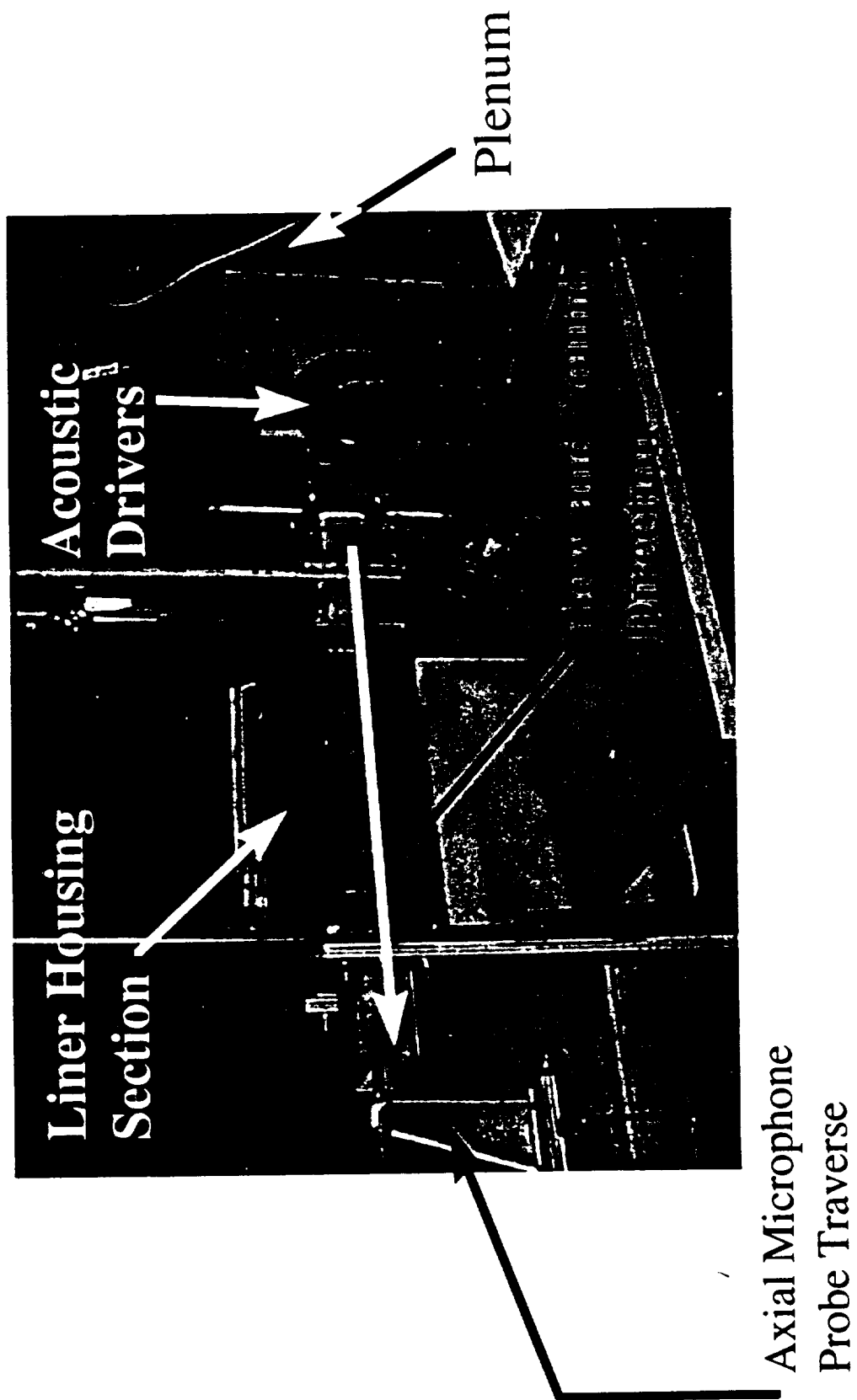
Figure 3.9 Flow-duct facility used for liner transmission loss and insertion loss.
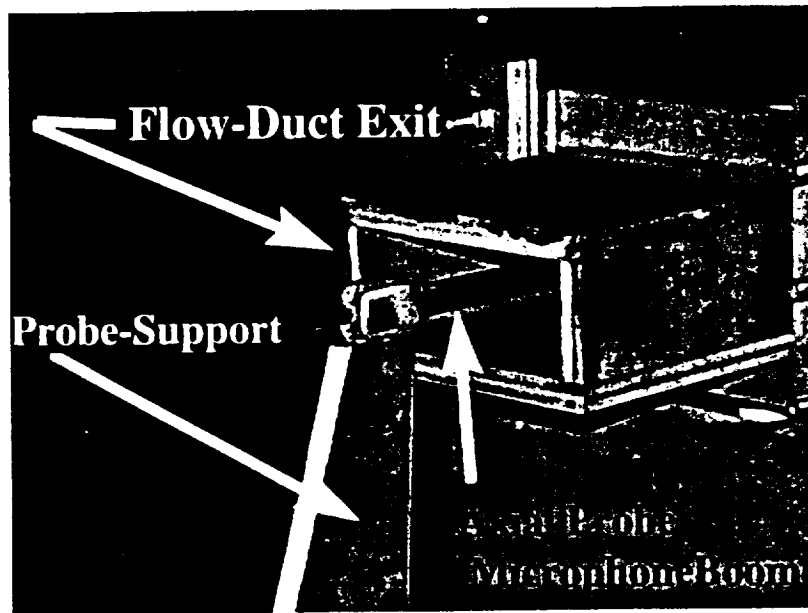
a. Probe-support and microphone boom
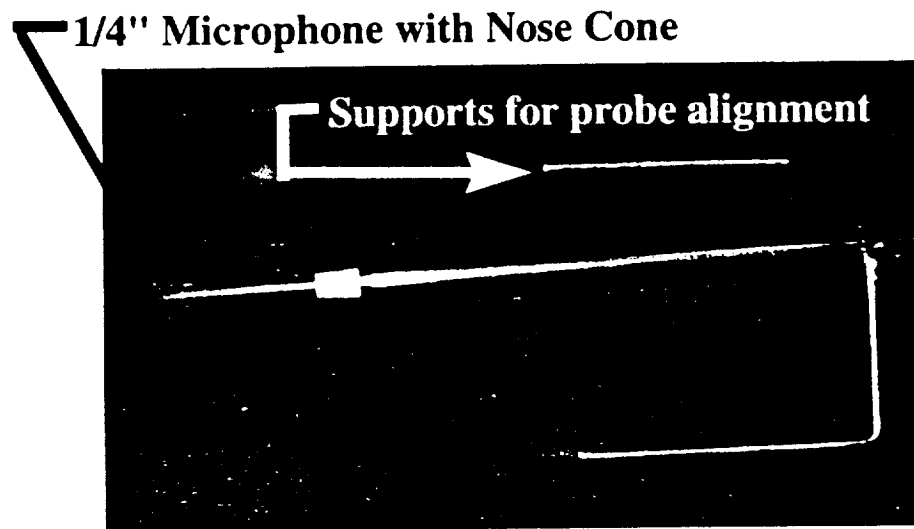
b. Axial probe microthone

Figure 3.10 Axial microphone probe inserted in flow-duct for transmission loss measurements.
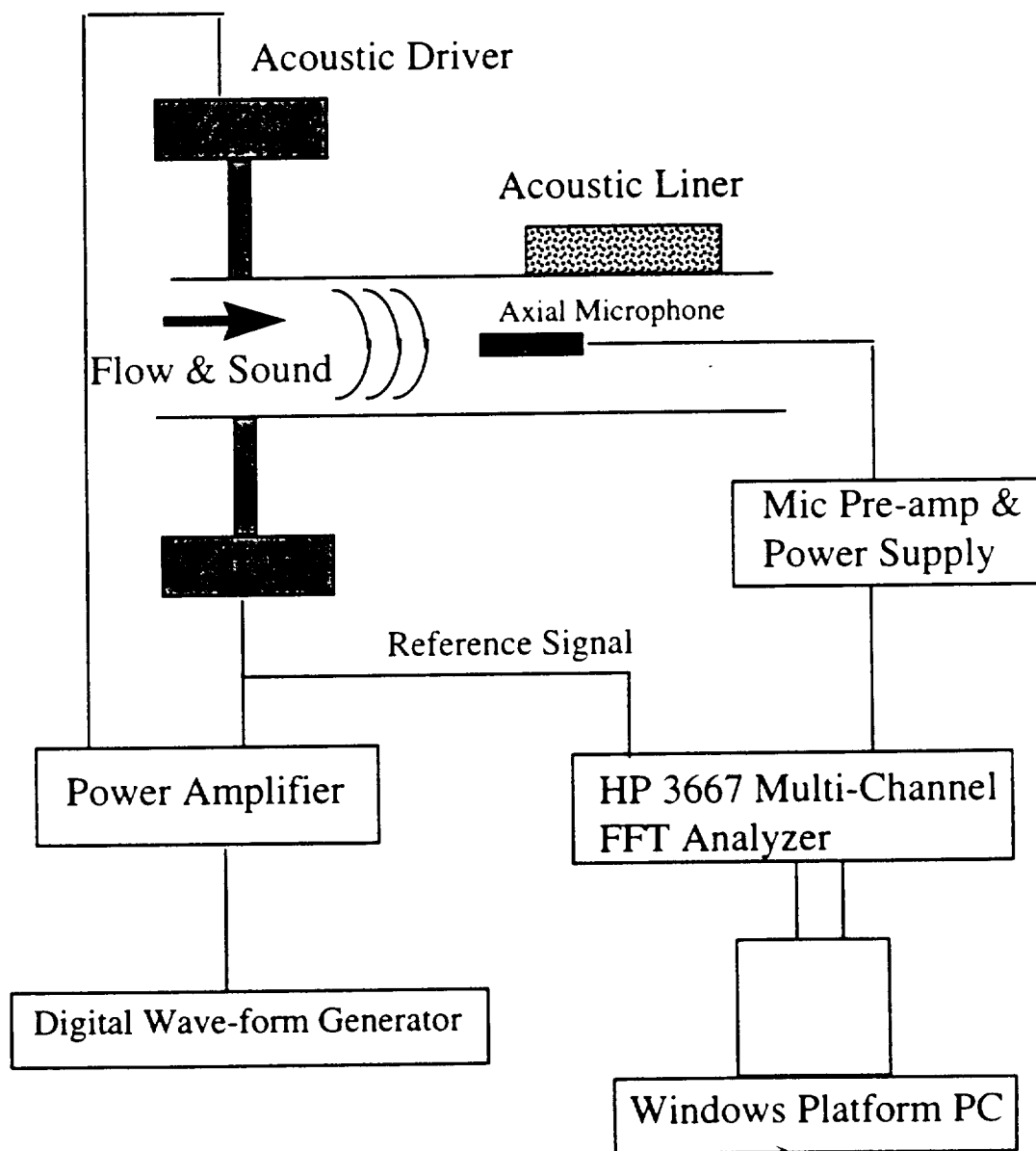
Figure 3.11 Signal processing schematic for flow-duct transmission loss measurements

Impedance Tube

O-Ring

2DOF Liner

Support Jack

a. Large Tube Configuration

Impedance Tube

2DOF Liner

O-Ring
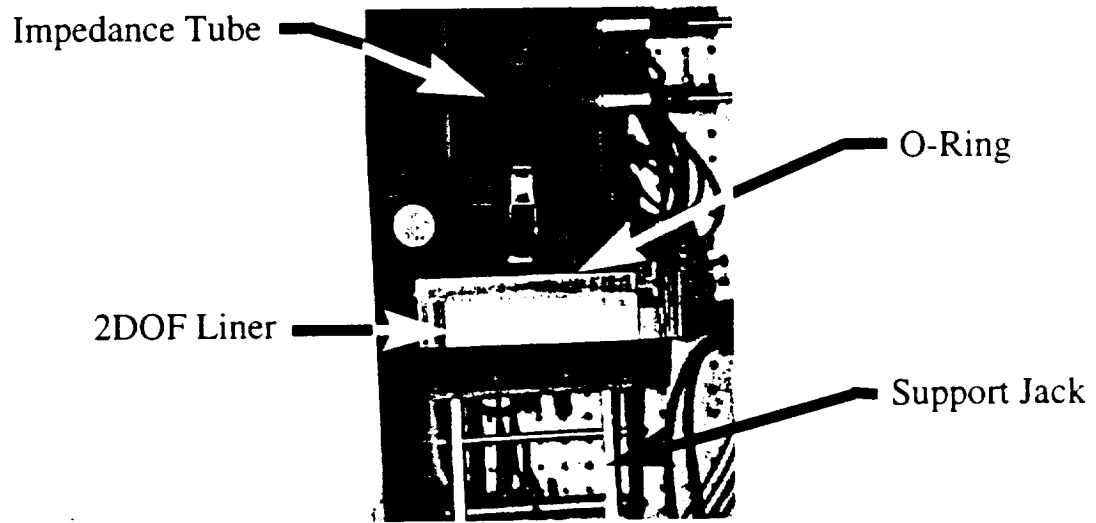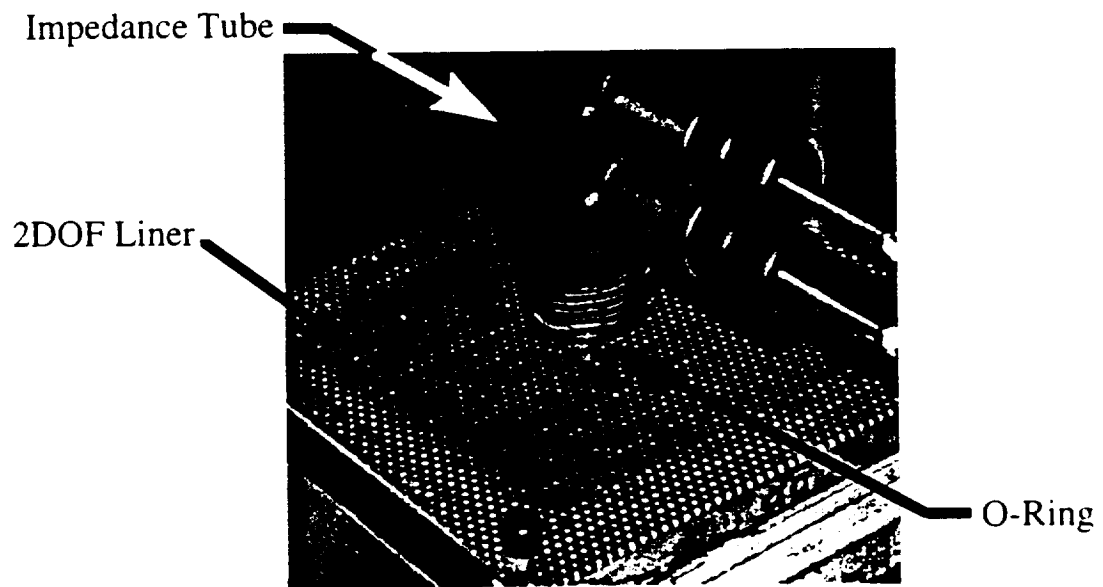
b. Small Tube Configuration

3.12 Impedance tube experimental set-up for normal incidence liner tests.
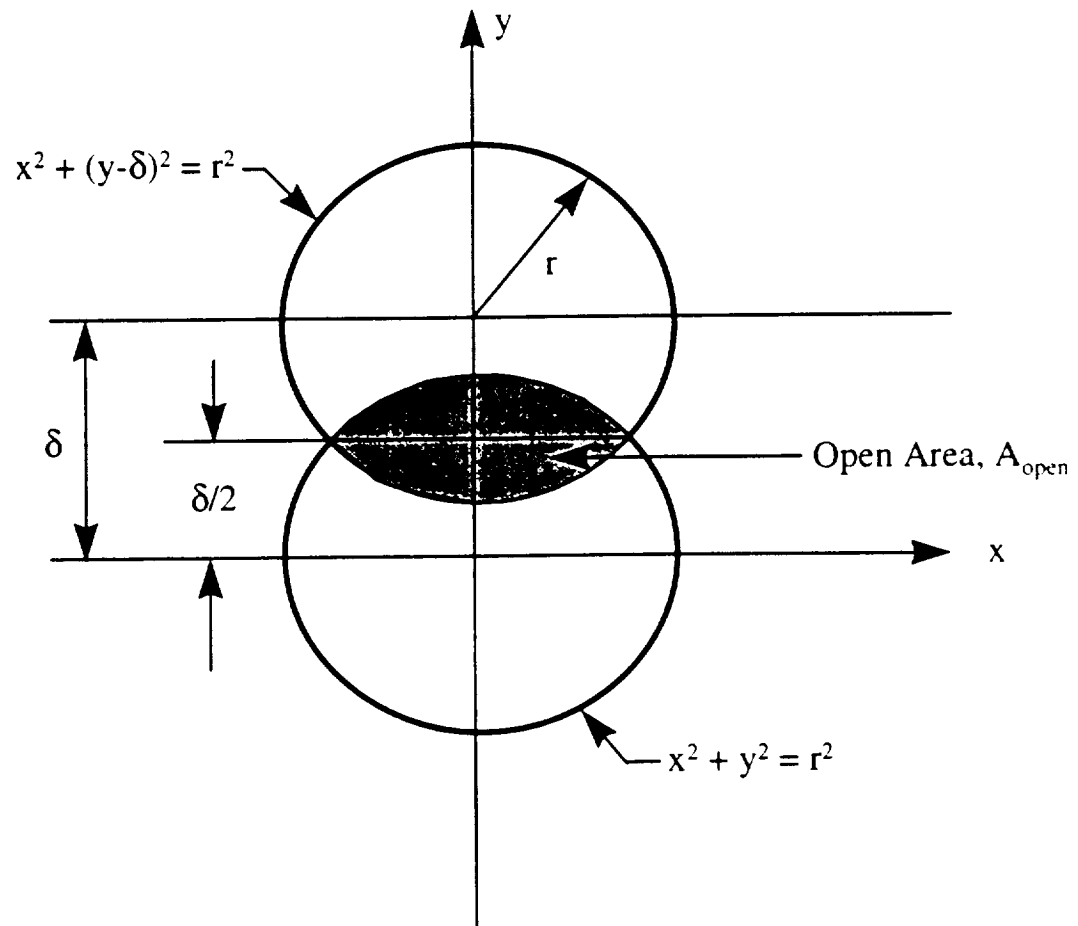
$$A_{open} = 4\int\left\{\sqrt{\left[r^2 - x^2\right]} - \frac{\delta}{2}\right\}dx$$

$$\sigma = \sigma_{\text{full open perforate}}\frac{A_{open}}{A_{\text{full open orifice}}}$$

Figure 3.13 Porosity calculation for orifice shaped resulting from sliding perforate concept.
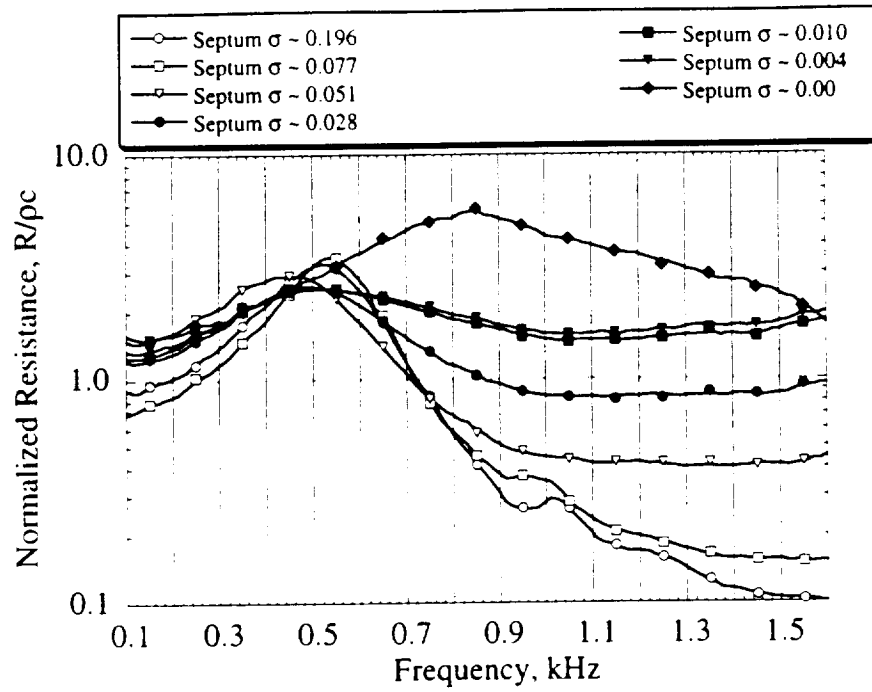
a. Normalized Resistance
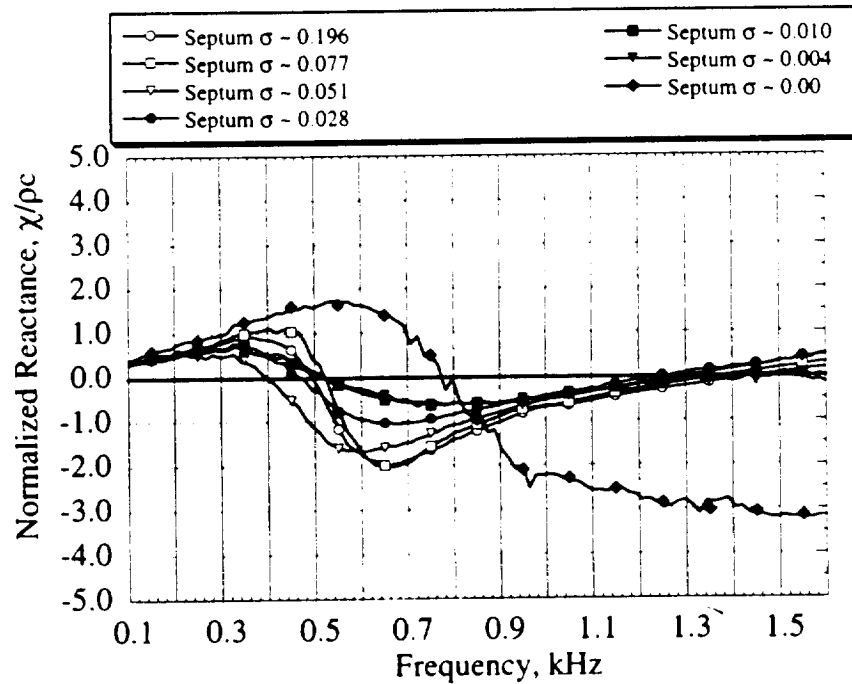
b. Normalized Reactance

Figure 3.14 Measured normal incidence impedance for tunable 2DOF liner as a function of buried septum porosity near primary resonance frequency [Tube dia. = 100 mm; $\Delta f = 2$ Hz; 64 avgs.].
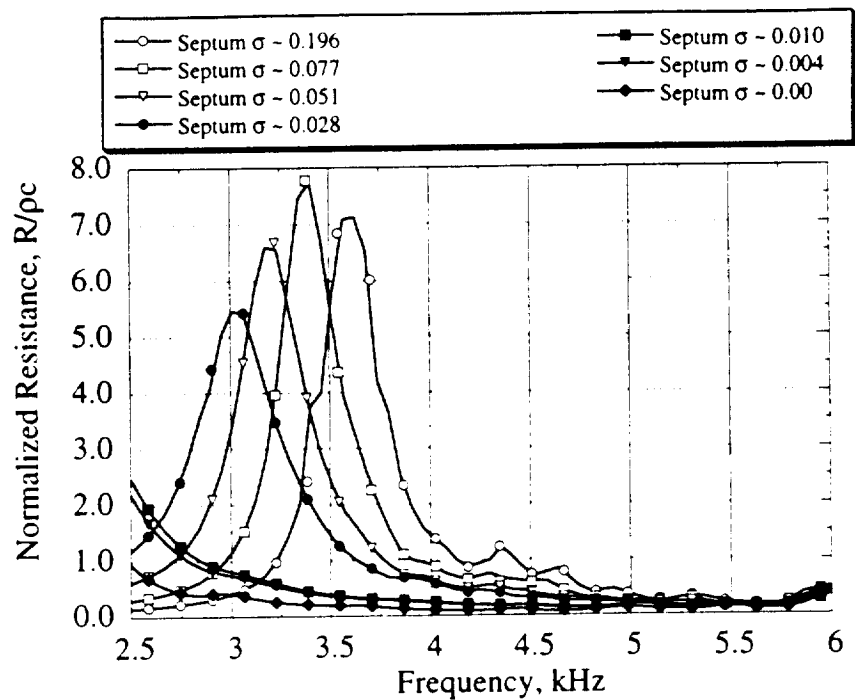
a. Normalized Resistance
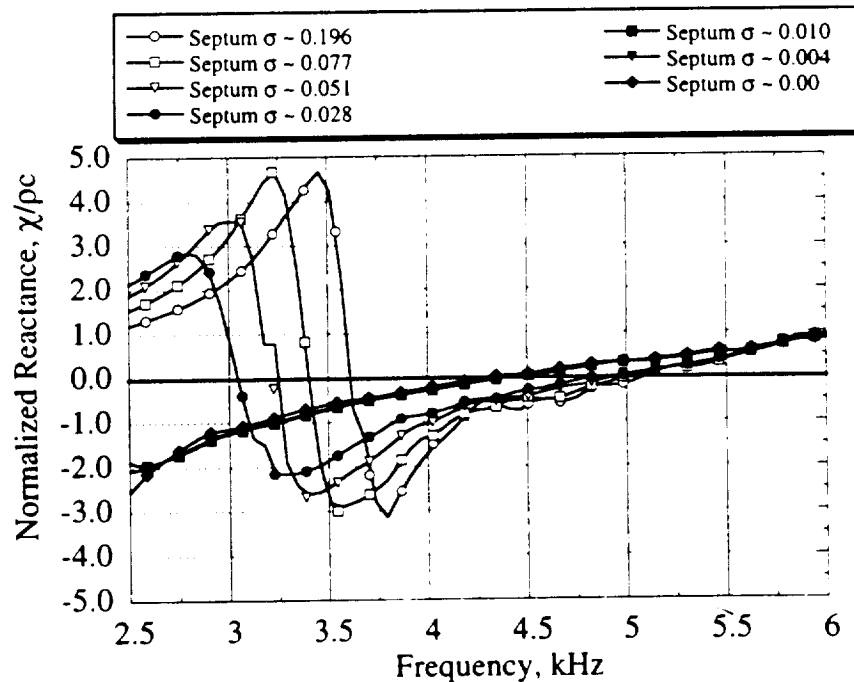
b. Normalized Reactance

Figure 3.15 Measured normal incidence impedance for tunable 2DOF liner as a function of buried septum porosity near secondary resonance frequency [Tube dia. = 29 mm; Δf = 2 Hz; 64 avgs.]
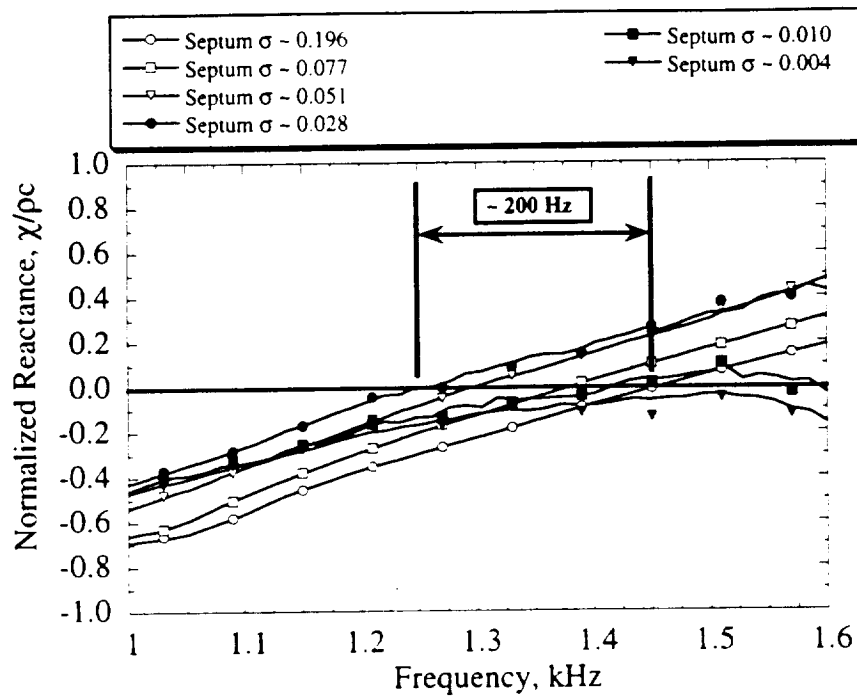
a. Primary Resonance Frequency Range
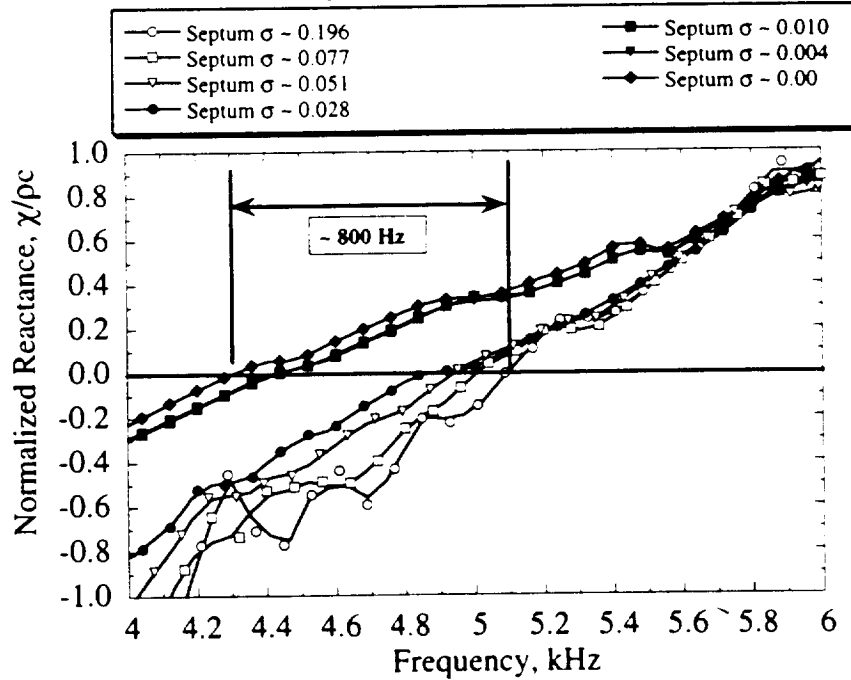
b. Secondary Resonance Frequency Range

Figure 3.16 Measured frequency range of primary and secondary resoance for tunable 2DOF liner.
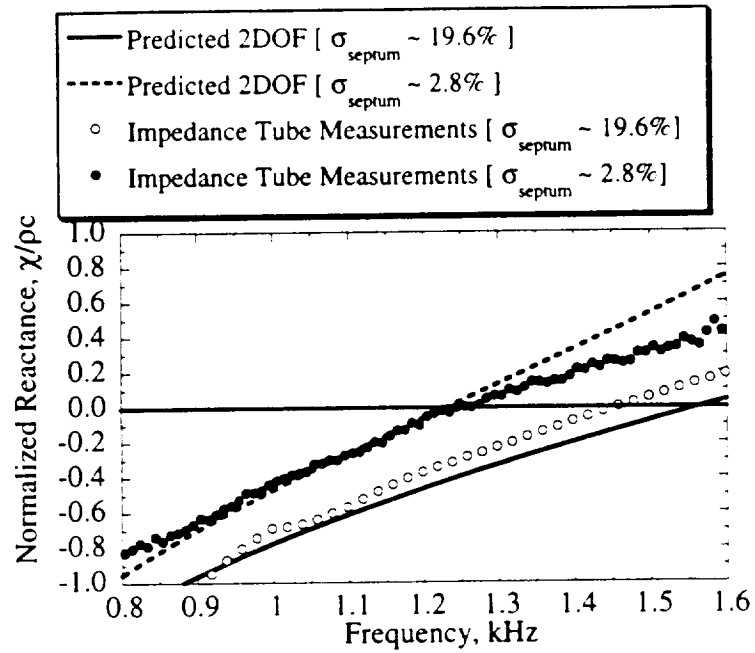
a. Primary resonance frequency
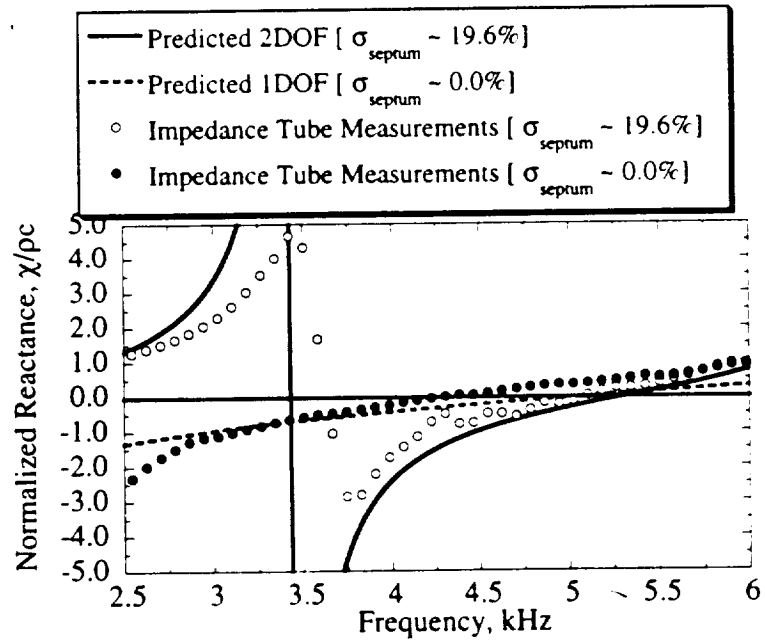
b. Secondary resonance frequency

Figure 3.17 Comparison of measured tunable range with predicted range.
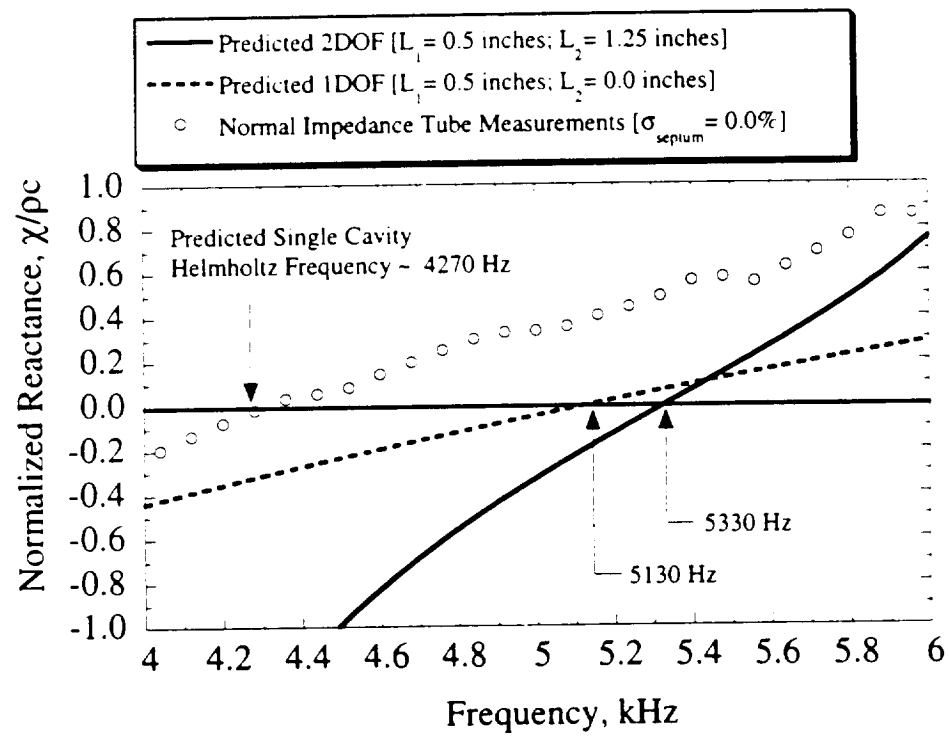
Figure 3.18 Prediction and measurement of 1DOF liner resoant frequency.
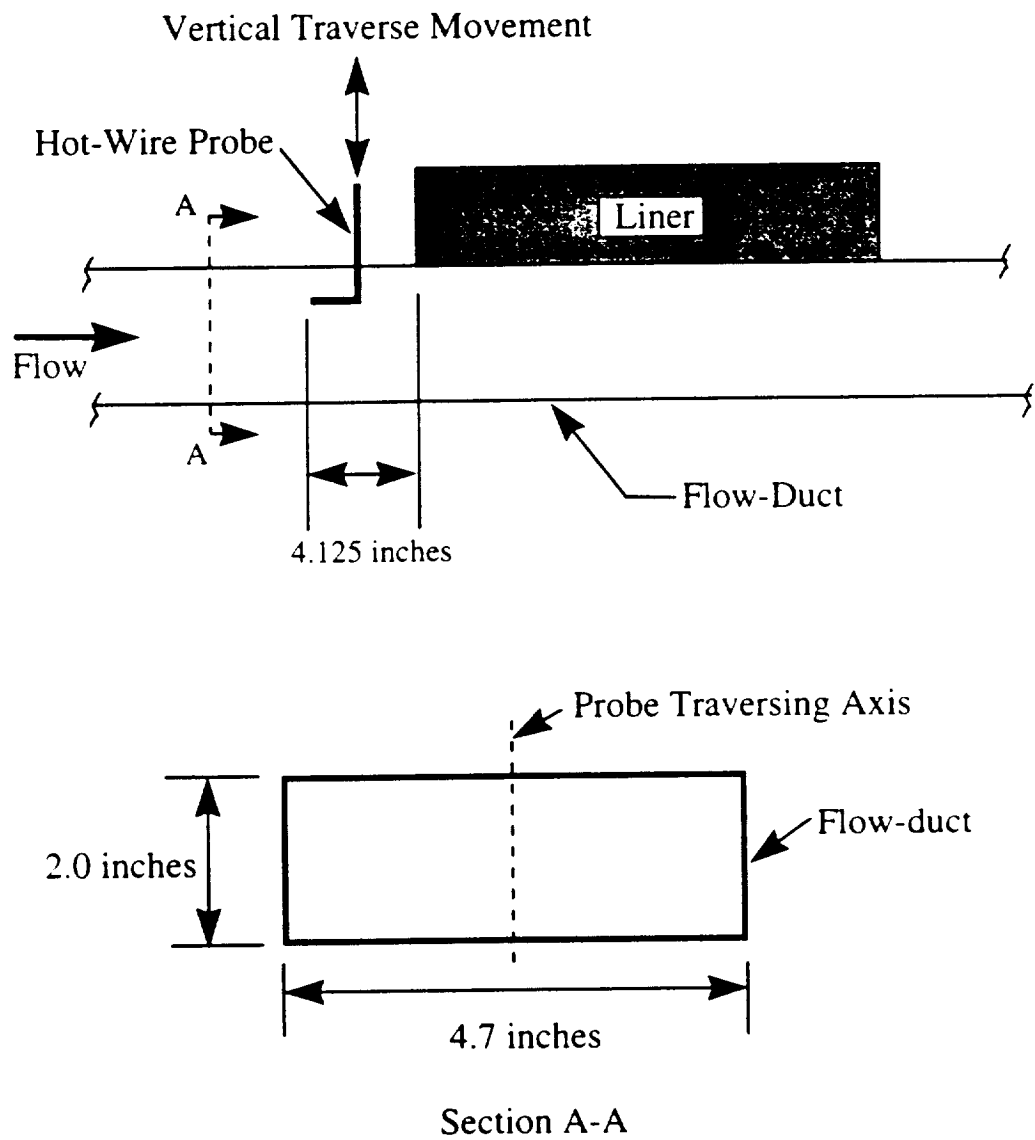
Figure 3.19 Experimental set-up for flow profile measurements in flow-duct.
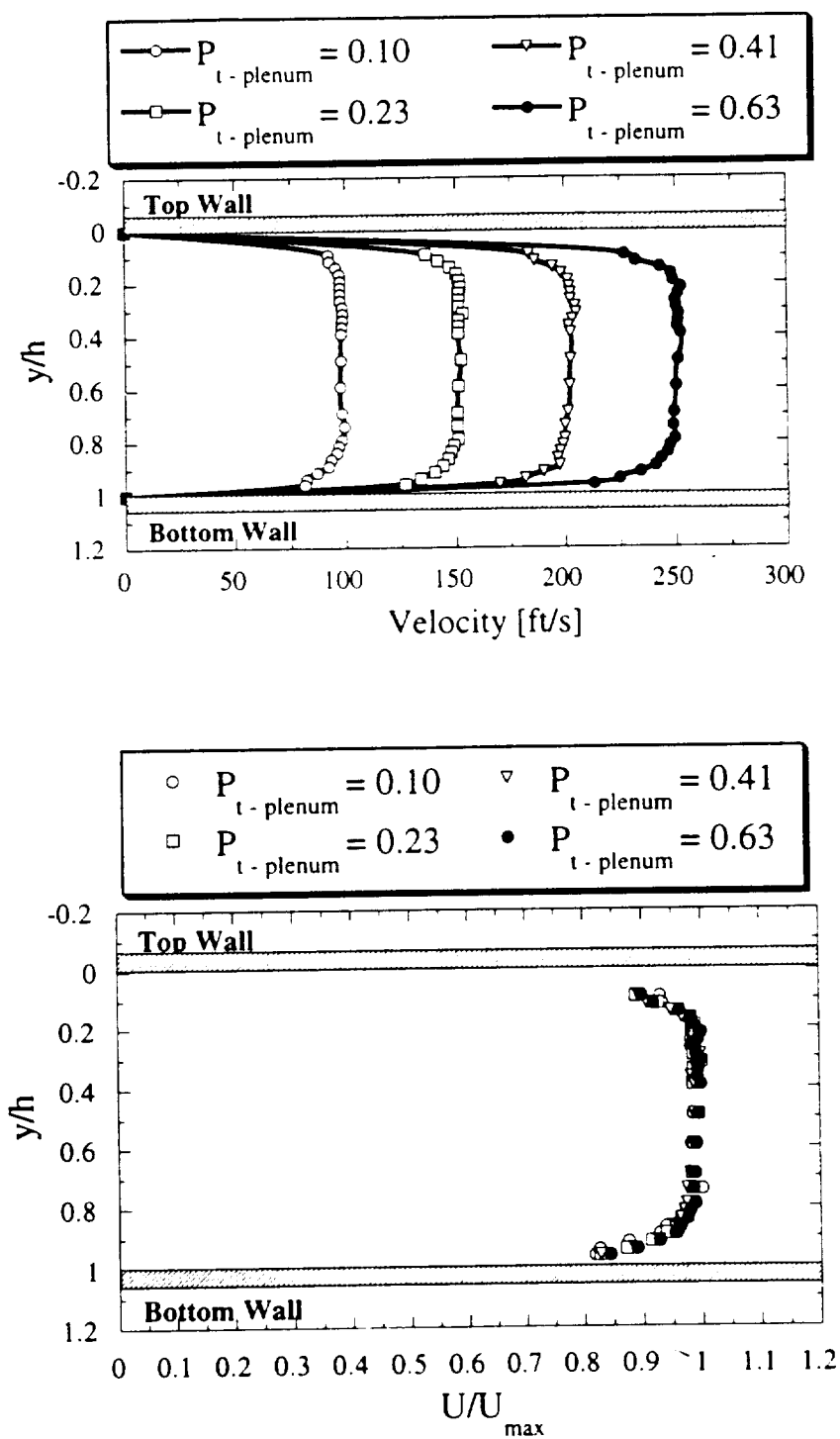
Figure 3.20 Mean velocity profiles of flow approaching acoustic liner in flow-duct.
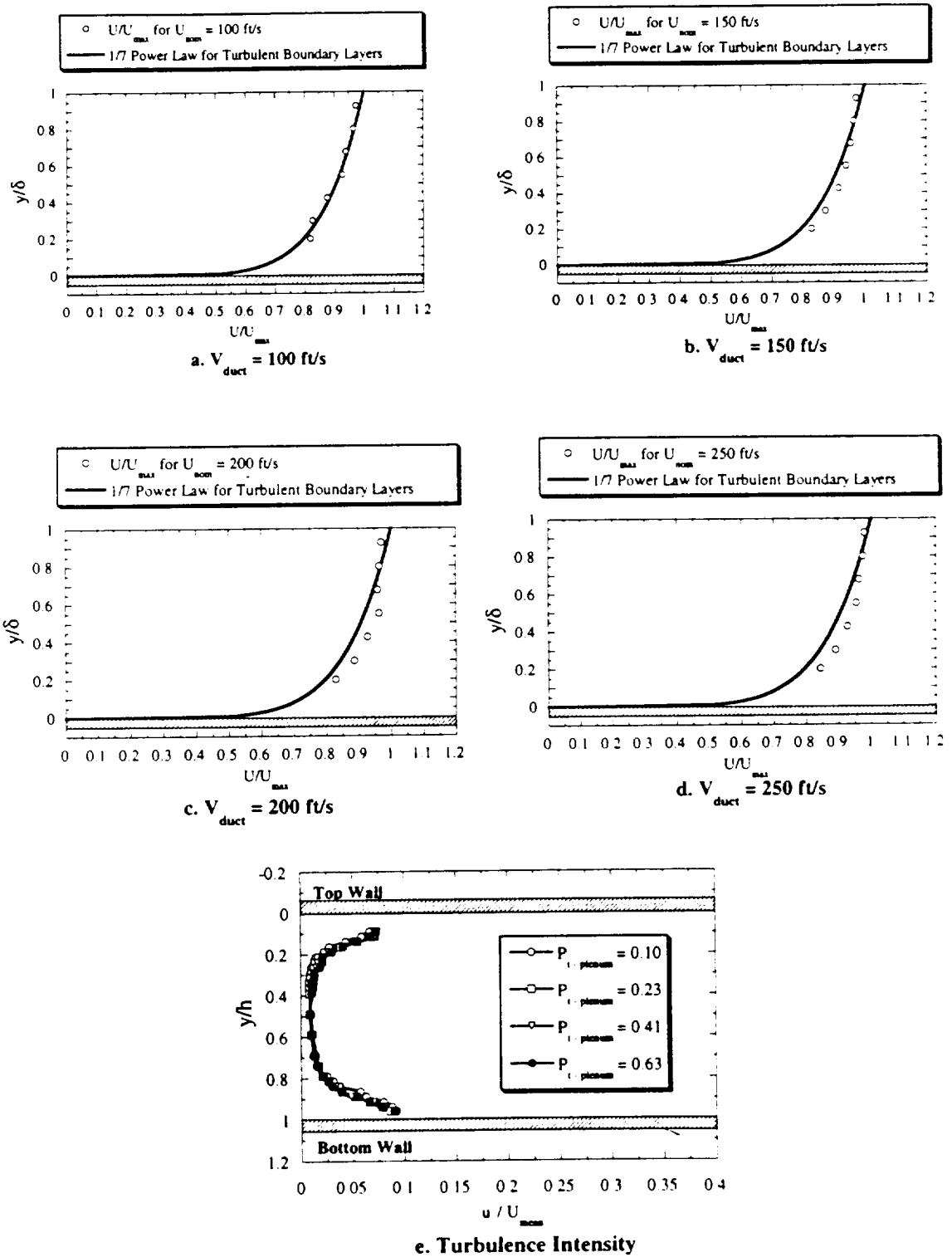
Figure 3.21 Evidence of turbulent flow in boundary layer upstream of liner
in flow-duct.
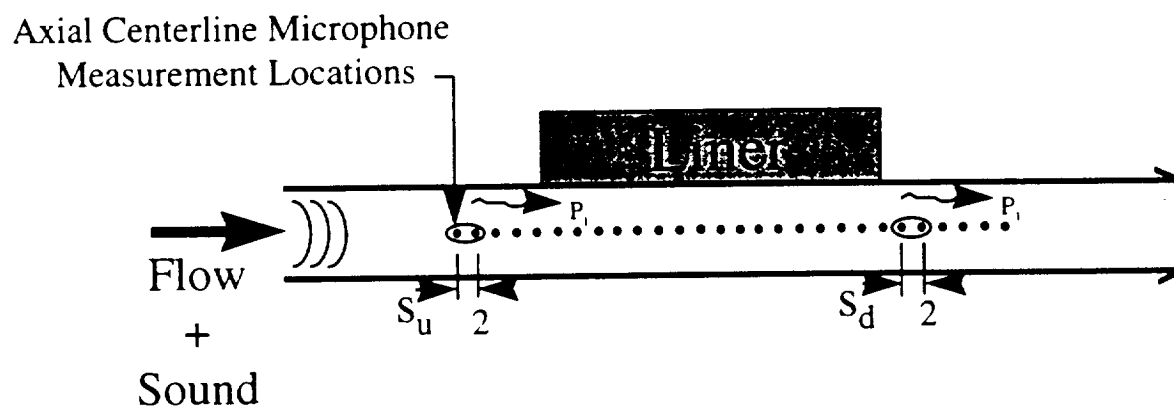
Figure 3.22 Acoustic measurement locations used for transmission loss calculations. Two-Microphone Methodology (TMM).
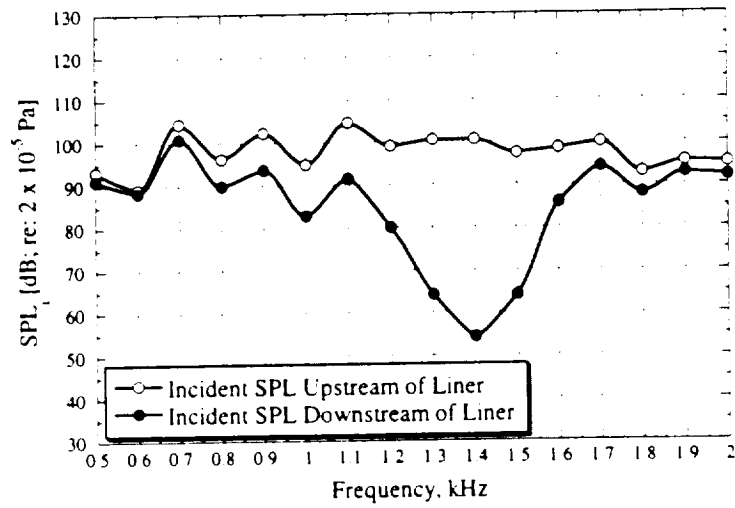
a. Comparison of incident power upstream and downstream
   of a 2DOF resonant liner.
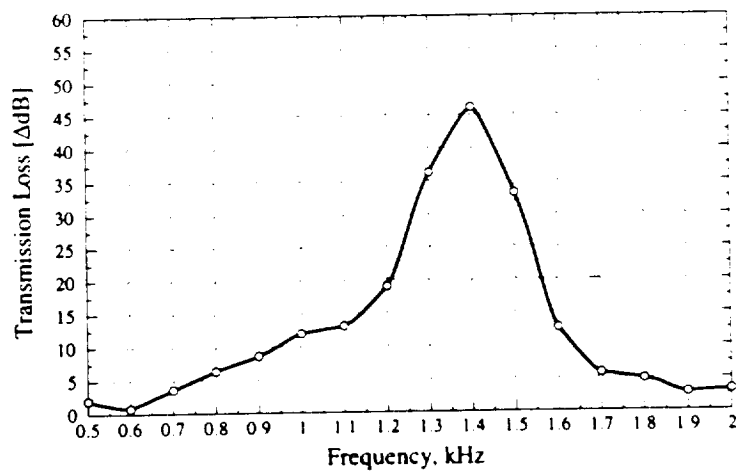
b. Power transmission loss of 2DOF resonant liner

Figure 3.23 Typical transmission loss result for multiple tone input using TMM.
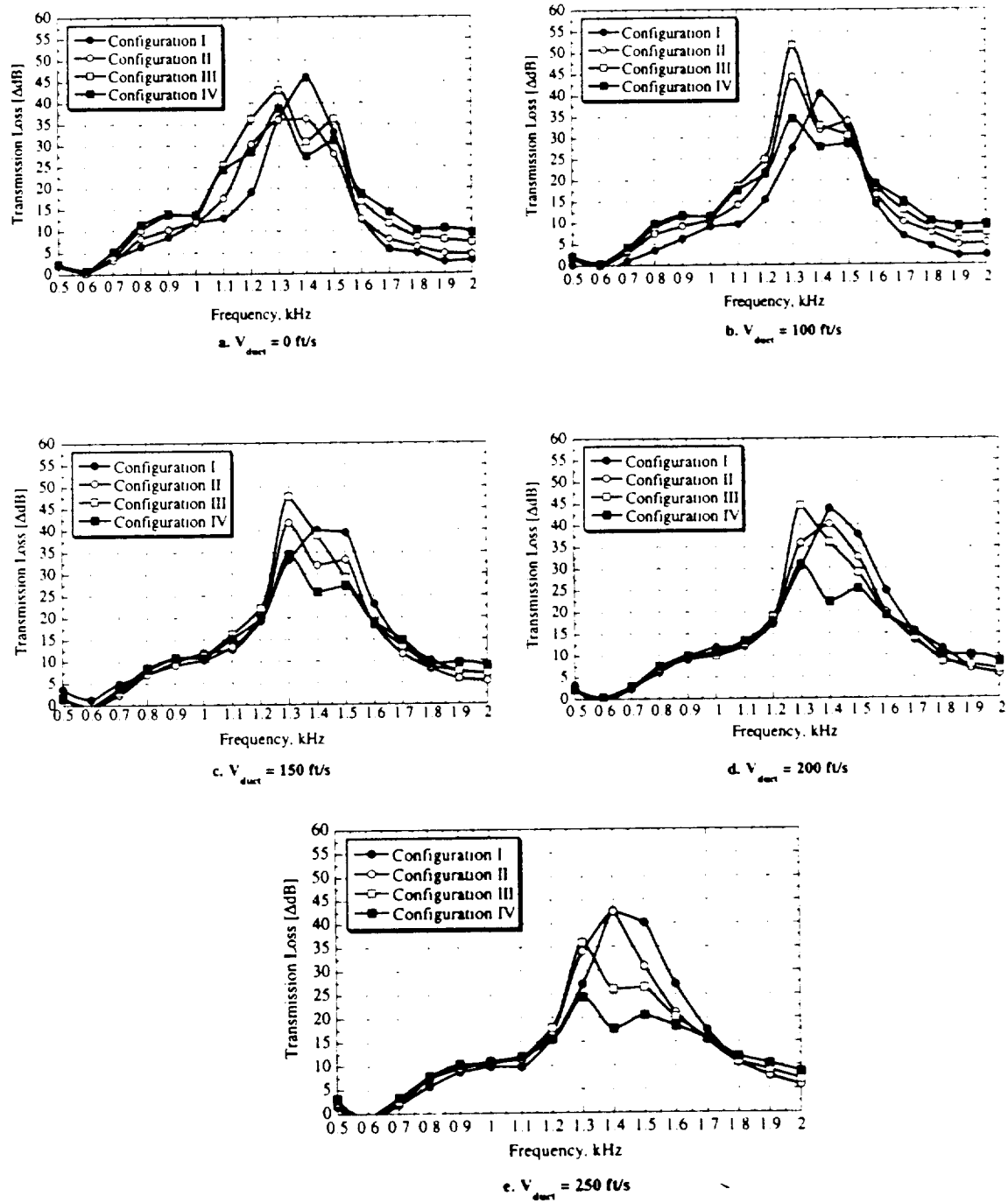
Figure 3.24 Effect of tunable 2DOF liner on flow-duct transmission loss
[Δf = 4 Hz; 64 avgs.].
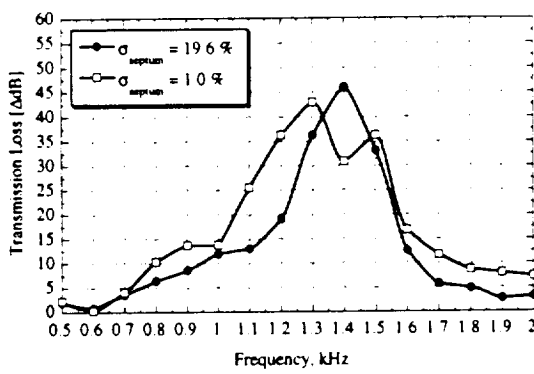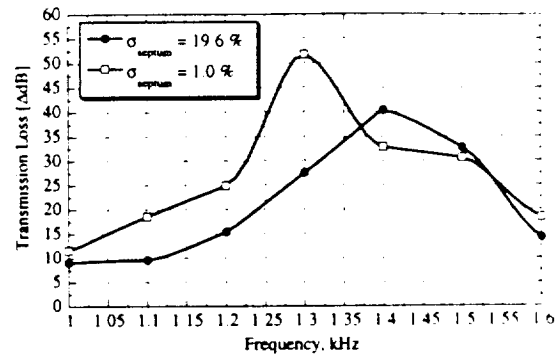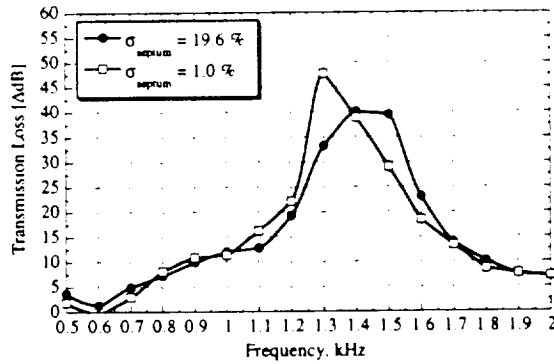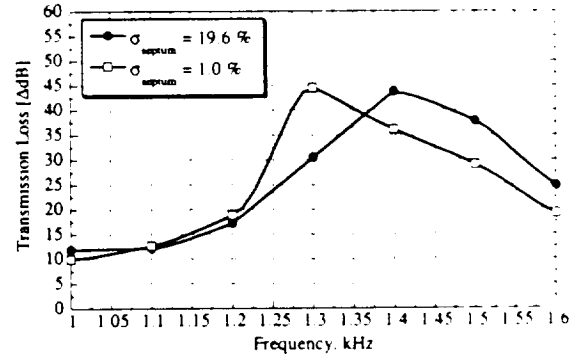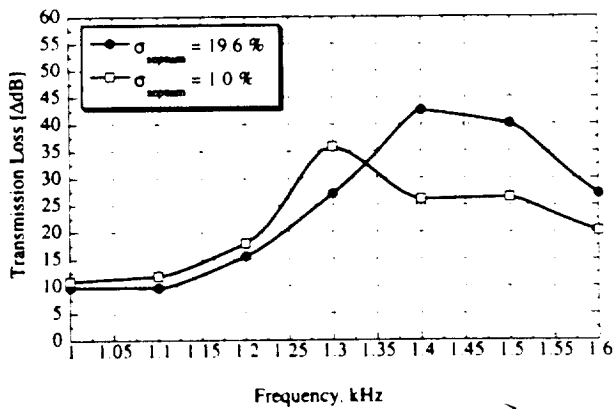
Figure 3.25 Shift in peak absorption frequency for tunable 2DOF liner for
configurations I and III; Transmisson loss [Δf = 4 Hz; 64 avgs.].
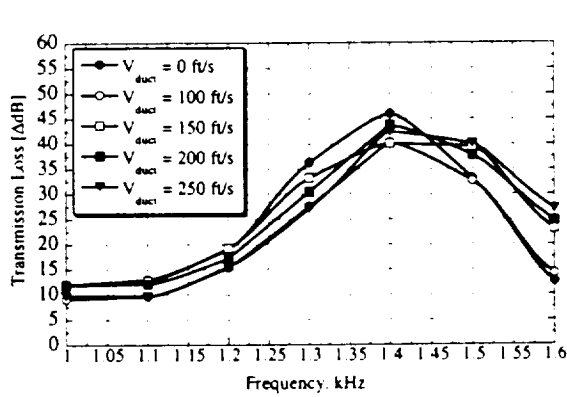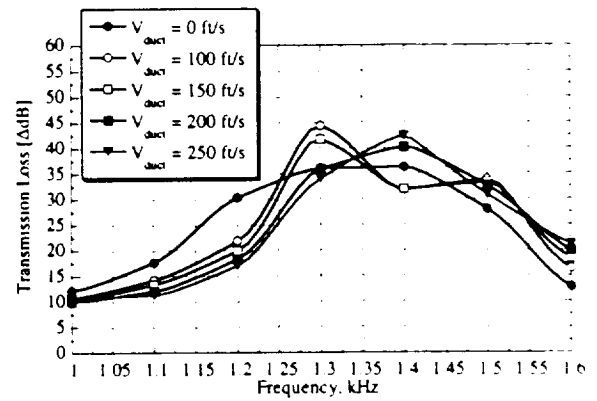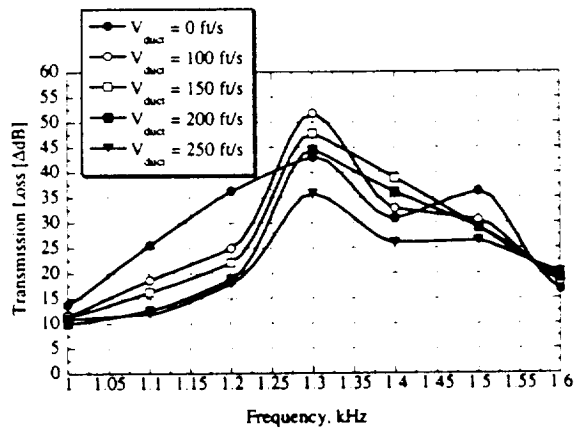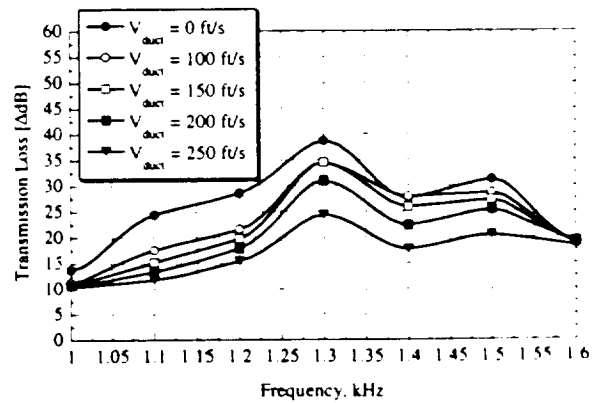
Figure 3.26 Effect of grazing flow on peak absorption frequency: Transmission loss [Δf = 4 Hz; 64 avgs.].
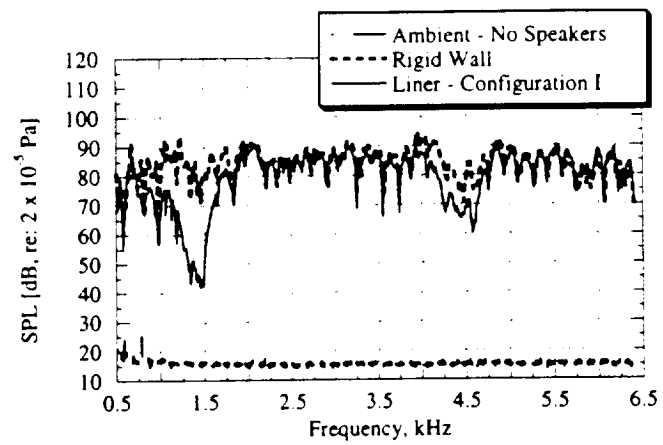
c. Spectra used to compute insertion loss
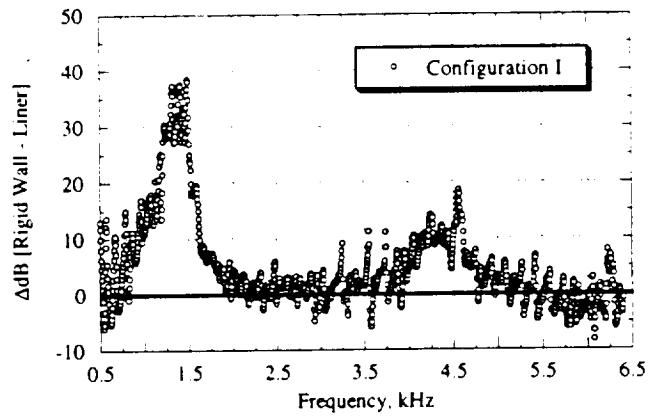
b. Actual Insertion Loss Data
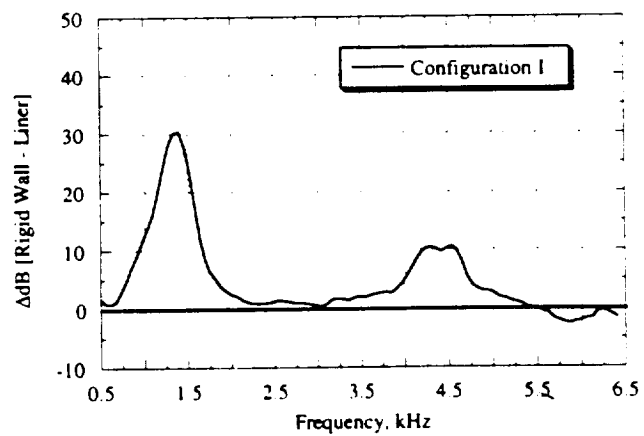
c. Weighted Least Squares Fit of Data

Figure 3.27 Typical data from insertion loss measurements [Δf = 4 Hz; 64 avgs.].

a. 60° Microphone; V = 0 ft/s

b. 60° Microphone; V = 0 ft/s

c. 60° Microphone; V = 100 ft/s

d. 60° Microphone; V = 100 ft/s

e. 60° Microphone; V = 150 ft/s

f. 60° Microphone; V = 150 ft/s
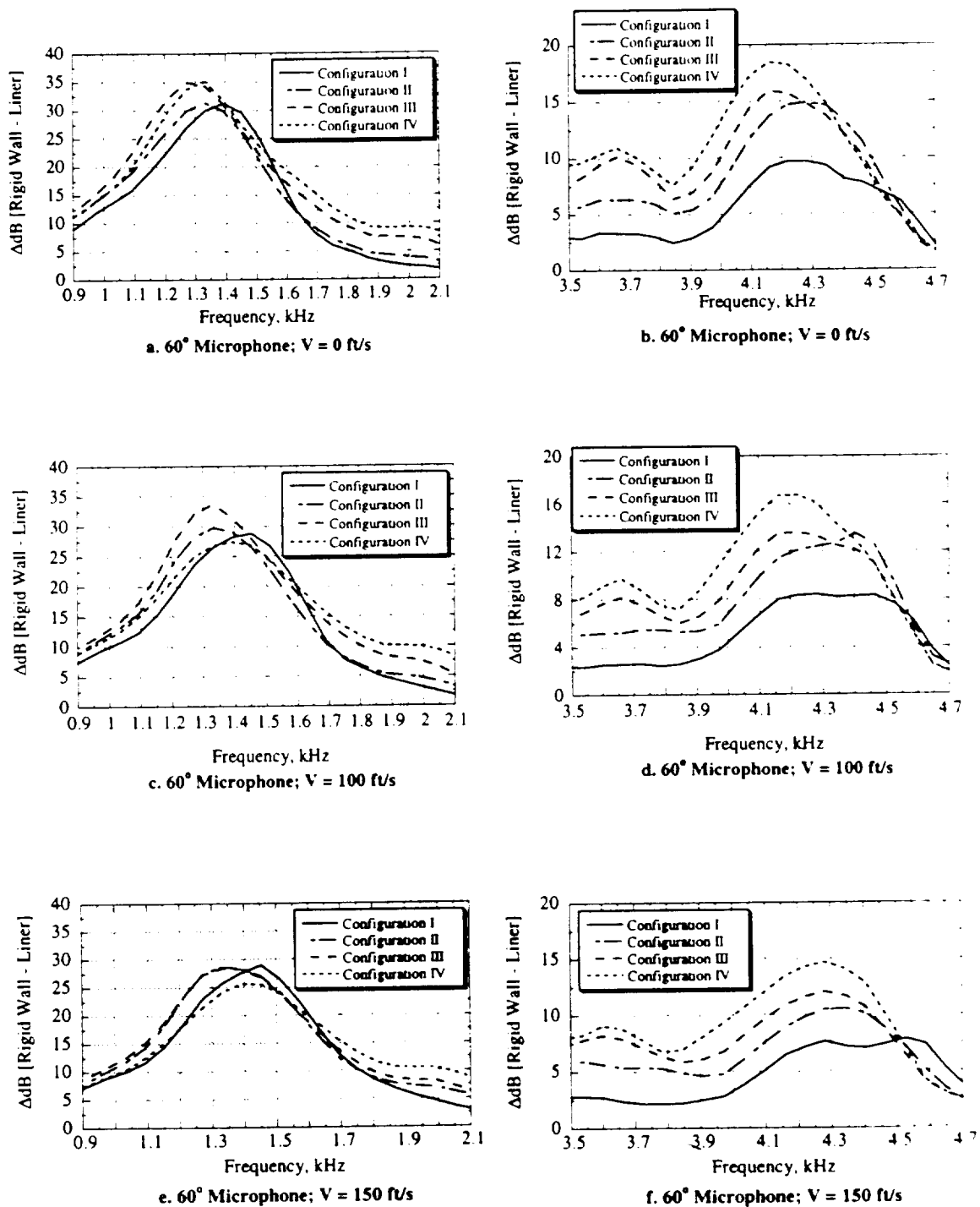
Figure 3.28 Shift in peak absorption frequency for tunable 2DOF liner:
Insertion loss [Δf = 4 Hz; 64 avgs.].

g. 60° Microphone; V = 200 ft/s

h. 60° Microphone; V = 200 ft/s

i. 60° Microphone; V = 250 ft/s

j. 60° Microphone; V = 250 ft/s
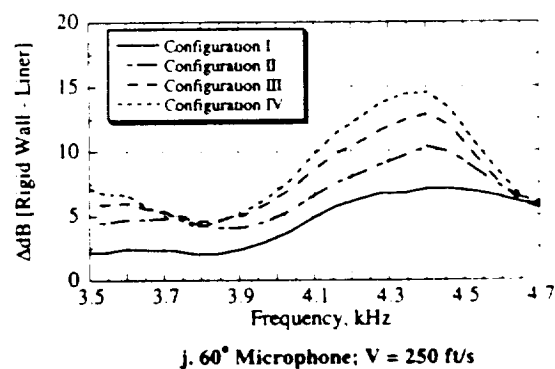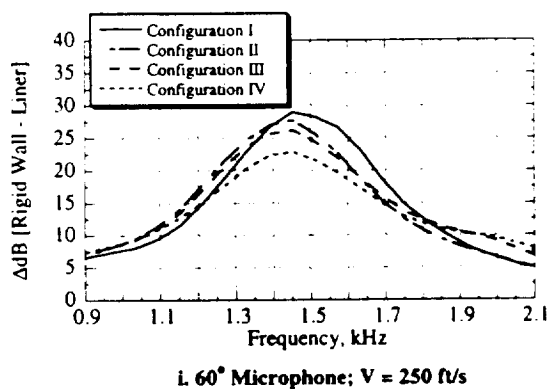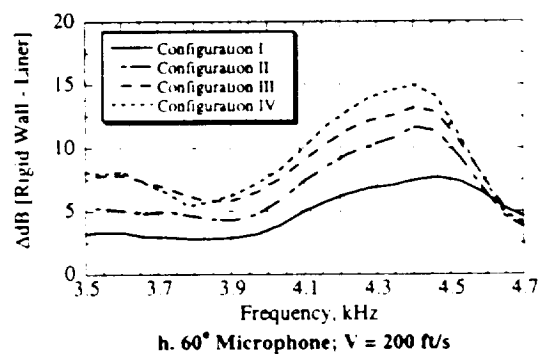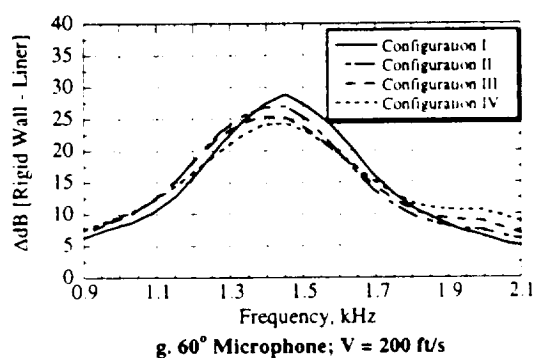
Figure 3.28 Continued.   Shift in peak absorption frequency for tunable 2DOF liner; Insertion loss [Δf = 4 Hz; 64 avgs.].
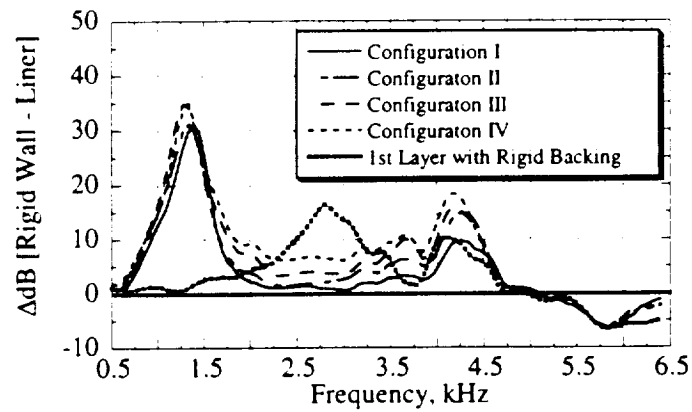
107
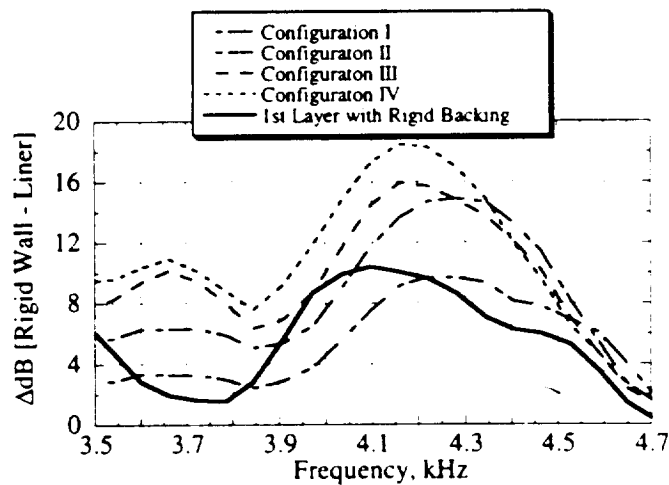
Figure 3.29 Peak absorption frequency shift with simulated maximum septum
open area closure; Insertion loss [Δf = 4 Hz; 64 avgs.].
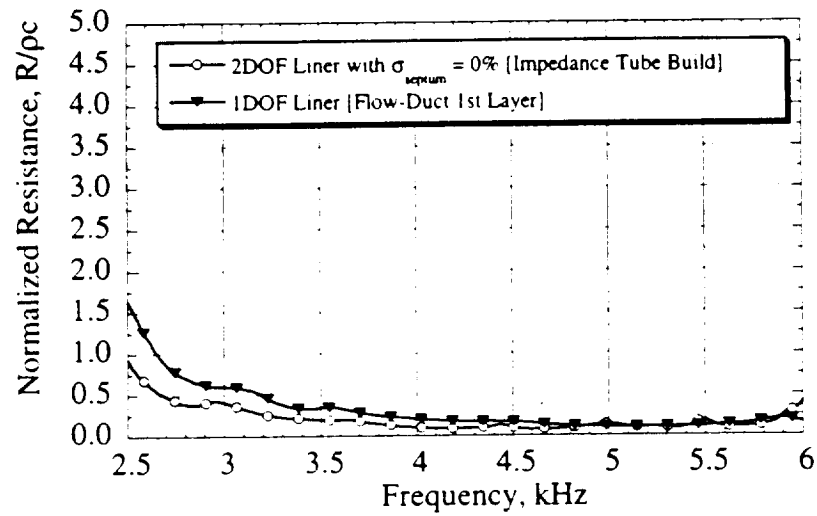
a. Normalized Resistance
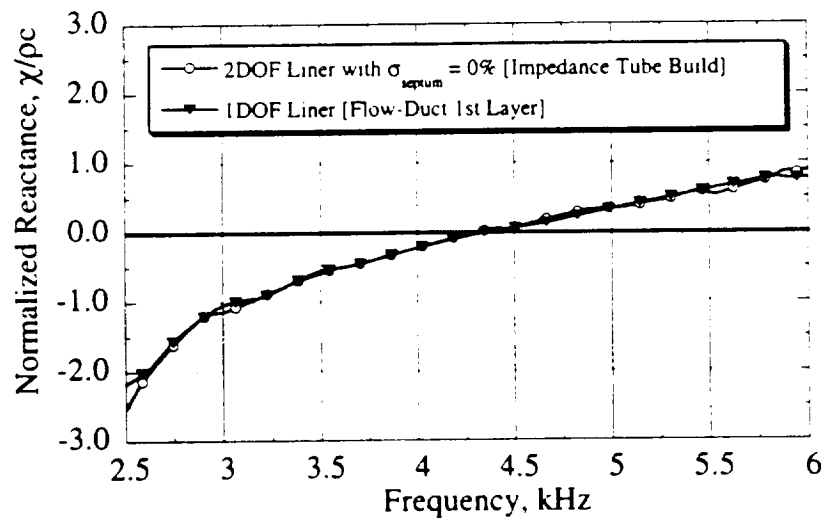
b. Normalized Reactance

Figure 3.30 Comparison between 2DOF liner with septum porosity = 0% and 0.5-inch honeycomb layer from flow-duct liner.

SECTION IV

Acoustic Impedance of a Variable Orifice Perforate

4.1 Introduction

This section examines in more detail the impedance of the variable orifice perforate as an individual acoustic element and as part of a single-degree-of-freedom cavity resonator. The variable orifice perforate concept has the potential for controlling the absorption characteristics of these resonant-type liners with a small amount of mechanical input. In the present section, the degree to which the absorption can be manipulated by the variable orifice perforate is explored using a normal incidence impedance tube and a single cylindrical backing cavity. This is accomplished by creating a variable orifice perforate (VOP) from two off-the-shelf perforates with identical porosities (orifices also have same sizes and shapes). The perforates chosen have orifice dimensions and thickness' that are commonly used in resonant-type acoustic liners. It is understood that the porosity change alone will control the perforate's acoustic impedance. What is left to be seen is how much control of the absorption and resonance frequency can be realized.

Objective

The objective of this section is to evaluate the acoustic impedance of the variable orifice perforate with regard to absorption and resonance frequency control.

Outline of Section

A description of the experimental approach used to measure the normal incidence acoustic impedance for the VOP is followed by a description of the facilities and instrumentation used. Before the results of the experiment are presented, a description of how the mass reactance was computed from the measured data is shown.

4.2 Experimental Approach

When a perforate with a given hole size and spacing and thus, porosity, is allowed to slide over another perforate with identical geometric attributes, it results in a range of orifice patterns. This concept was described earlier in Section I and III. It is obvious that resulting orifice shapes are non-circular. By translating one perforate over the other in one direction, the resulting orifice shapes are "eye" shaped and not random.

Test Article

A variable orifice perforate was created, like the buried septum used in Section III, from two off-the-shelf perforate sheets that had a nominal porosity of 22.5% and a 0.8128 mm (0.032 inch) thickness. The combined thickness was 1.6256 mm (0.064 inches). The orifices were circular with diameters of 1.5875 mm (0.0625 inches) and they were spaced 3.175 mm (0.125 inches) apart on staggered centers. This meant that a maximum of 1.5875 mm of translation of the top perforate would result in complete orifice coverage of the bottom perforate. The baseline configuration for the VOP was a perforate with the same porosity and hole spacing as the single perforate, only the thickness was doubled.

A VOP suitable for testing in an impedance tube was fabricated. Care was taken in cutting the perforates from a large section into pieces that would match identically. In order to ensure only uni-directional translation. a "track" was made for the top perforate to slide uniformly. Figure 4.1 shows the constituent parts of the VOP. Accurate translation was achieved by using a set-screw that had a 32-threads-per-inch pitch. This meant that a full 360-degree turn of the screw would translate the top perforate 0.79375 mm (0.03125 inches) or half of the travel needed to completely cover the orifices.

Impedance Measurements

The acoustic behavior of the VOP was obtained by measuring its impedance in a normal incidence impedance tube. Figure 4.2 shows the general test configuration. The perforate separates the impedance tube from a backing cavity of length L. The measured acoustic impedance is clearly a result of both the impedance of the perforate and the cavity. As mentioned earlier. it is common practice to treat the backing cavity as simple reactive element whose impedance can easily be calculated. Using both broadband and single tone excitation. the VOP was tested in several configurations that corresponded to different perforate porosities and orifice shapes. This allowed for the study of both low and high amplitude behavior of the unique perforate geometries produced by the sliding of one perforate over the another. Figure 4.3 show a typical VOP configuration installed in the impedance tube. It should be noted that as installed in the impedance tube. the VOP had an effective porosity of 23.49%, which is about 1% larger than the nominal value of the whole perforate sheet. The effective porosity was determined by counting the orifices that were encompassed by the impedance tube area. This was done several times and an average porosity was computed. As the top perforate is translated. the resulting porosity can be calculated from geometry. similar to the method described in Section III (see Figure 3.14). Table 4.1 lists the resulting porosities for the configurations tested.

Table 4.1 Porosity configurations tested with the variable porosity perforate.

Perforate Configuration	Translational Movement (mm)	Porosity
T1	0.00	23.49%
T2	0.40	15.72%
T3	0.79	8.99%
T4	1.19	5.97%
T5	1.39	3.32%
T6	1.49	1.20%
T7	1.56	0.43%
T8	1.59	0.00%

Measurement of Acoustic Impedance

The normal incident impedance data were acquired using the so-called *Two-Microphone Method* (TMM) detailed in Appendix A. This method utilizes measured acoustic pressures and phases. Using two microphones mounted flush on the impedance tube wall with some fixed distance between themselves and the end of the tube where a sample is mounted. the incident and reflected acoustic energy can be extracted using a cross-correlation technique.

4.3   Experimental Facilities and Instrumentation

Normal incident impedance testing of the variable geometry perforate was performed in a impedance tube.   A description of this facility along with the instrumentation and data acquisition used in the present experimental study is given below.

Impedance Tube

Figure 4.4 shows the impedance tube and its constituent parts used for the present study. Essentially, it consisted of a tube that has an inner diameter of 29 mm (1.14 in) and can be configured to have several different overall lengths. The inner diameter is such that only plane wave propagation will exist until a frequency of about 6400 Hz. Above this frequency, higher order duct modes can exist along with the plane wave mode. One end of the tube has an acoustic driver attached, while the other end can be configured to have an orifice plate or perforate sandwiched between two flanges while terminating with a cavity of an arbitrary depth. The tube has two flush-mounted microphone ports near the terminating flange in to facilitate the Two-Microphone impedance measurement methodology. Referring to Figure 4.2, microphone A is located 52.83 mm (2.08 inches) upstream of the sample face while microphone B is located approximately 32.82 mm (1.29 inches) from the sample face. The tube is mounted horizontally on wooden supports.

Testing of the VOP consisted of placing the perforate between the two flanges at the impedance tube termination and placing a cavity of the same tube inner dimensions behind the perforate. A malleable graphite gasket, 0.76-mm (0.03-inches) thick, was placed on each flange to prevent sound from escaping the tube. Thus, the test configurations were single-degree-of-freedom resonant-type liners consisting of a perforate covering a cavity.

Instrumentation and Data Acquisition

Acoustic Driver

Acoustic waves in the impedance tube were generated by a JBL Model 2446J acoustic driver in conjunction with a Carvin 1500 power amplifier and an HP 33120A digital function generator. For all frequencies tested, 160 dB re 2 x 10^{-5} Pa tones were easily achieved at Microphone A. The driver-tube arrangement was also able to achieve a nominal overall sound pressure level (OASPL) of about 153 dB at Microphone A with a broadband input signal. Figures 4.5 a and b show typical spectra measured from one of the wall-mounted B&K microphones with broadband excitation and a single tone input to the acoustic driver, respectively.   The broadband measurement shows the expected standing wave induced peaks and valleys across the spectrum. The spectrum for the tone input includes several overtones.   Noise is evident at other frequencies, however, both the overtones and the noise are more than 15 dB lower than the input tone for a cases.

Microphones

Two type of microphones were used for the current testing. Special Bruel & Kjaer (B&K) phase-matched 6.35 mm (0.25-inch) type 4187 microphones were used in conjunction with B&K type 2633 pre-amplifiers. The B&K microphones and pre-amplifier were powered by a battery-powered B&K 2804 power supply. Output from this power supply was fed directly into a FFT

112

analyzer. The B&K microphones were calibrated for amplitude using a B&K 4231 pistonphone which produces a 1 kHz tone at 114 dB in order to provide an absolute baseline sound pressure level. The amplitude and phase response of the B&K 4187 microphone as a function of frequency was determined and documented by the manufacturer of the microphone.

Signal Processing

The microphone signals were fed into a HP 3667A Multi-Channel Signal Analyzer for FFT analysis. The analyzer is operated from a Windows 95 platform on a Pentium 200 MHz computer. Figure 4.6 shows a schematic of the signal processing paths involved. Except where noted, 64 averages were used when sampling the microphone signals. The signal from microphone A (furthest from sample face) was used as the reference for the cross-correlation analysis required by the two microphone impedance technique used here and described in Appendix A.

4.4   Calculation of Perforate Mass Reactance from Measured Data

Recall form Section II that the resonance frequency of a porous layer with a cavity backing can be determined by the cavity dimensions and the reactance of the porous layer. The reactance of the porous layer, in the present case a perforate, is referred to as the *mass reactance*. The expression presented in Section II for the impedance of a cavity-backed perforate is shown below:

$$\frac{Z}{\rho c} = Z_{perf} + Z_{cav}$$

$$= \left[\frac{R}{\rho c} + i\frac{\omega m}{A_o \rho c} \right] - i\sigma \cot(kL)$$

$$= \frac{R}{\rho c} + i\left[\frac{\chi_m}{\rho c} - \sigma \cot(kL) \right] \tag{4.1}$$

The "measured" mass reactance can be determined in the following manner. Adding the quantity cot*(kL)* to the measured total normalized reactance results in the mass reactance of the perforate with porosity, σ:

$$\frac{\chi_m}{\rho c} = \left[\frac{\chi}{\rho c} \right]_{meas} + \sigma \cot(kL) \tag{4.2}$$

The cavity impedance is assumed to be invariant for a given perforate configuration. The frequency at which the total reactance is zero and the normalized resistance is small (determined from impedance tube measurements), is defined as the resonance frequency. For this case, equation 4.2 becomes:

$$\frac{\chi_m}{\sigma \rho c} = \cot(kL) \tag{4.3}$$

In this section. the resonance frequencies discussed will be referred to as 1st, 2nd, 3rd, etc. which correspond to the lowest resonance frequency, increasing to the highest resonance frequency.

Prediction of Mass Reactance

A calculated mass reactance from theoretical considerations was made to compare with the measured data. This predicted mass reactance was computed from the equations developed in section 2.4 from Section II. The mass end correction for a single orifice was estimated using the general expression given by equation 2.51 repeated below for convenience:

$$\delta_m = \frac{\sqrt{\pi A_0}}{\left[1 + \frac{\varepsilon^4}{64} + \frac{\varepsilon^4}{64} + \dots \right]} \qquad (4.4)$$

Where $\varepsilon \equiv$ eccentricity

Accounting for the porosity of the perforate that Ingard established[41], the mass end correction (see Section II) is:

$$\delta_{m-perf} = \delta_m \left(1 - \sqrt{\frac{\sigma}{2}} \right) \qquad (4.5)$$

The shaped formed by the sliding of circular orifices over other circular orifices can be described as "eye" – shaped (see Figure 3.14). It was assumed that this shape can be approximated as an ellipse. Using the computed values of the major and minor axis of the "eye" – shaped orifice. an eccentricity was computed for each of the perforate configurations that were tested. This value was used to compute the mass end correction and thus the mass reactance.

4.5   Results

Broadband Excitation

A broadband signal was input into the impedance tube and the impedance was computed for the configurations listed in Table 4.1. The nominal overall sound pressure level at the microphone nearest the sample face was 153 dB. Figures 4.7, 4.8, and 4.9 show the normal incidence absorption coefficient. normalized resistance and reactance. respectively. over most of the analyzed frequency range.

Recall from Section II that the absorption coefficient measures the amount of incident acoustic energy that is "absorbed" by a material by comparing the incident acoustic wave with the reflected acoustic wave. Figure 4.7 shows that. in general, there are several peaks and several minima in absorption over the measured frequency range. These maxima and minima correspond to the perforate/cavity resonance and anti-resonance frequencies. respectively.

For a tube with no porous covering (i.e.. zero mass reactance). the resonance frequencies can be determined by finding the roots of the cotangent function.

114

$$\cot(kL) = 0 \qquad\qquad (4.6)$$

$$\cot\left(\frac{2\pi f}{c} L\right) = 0$$

$$f = \frac{nc}{4L} = \frac{nc}{\lambda} \qquad n = 1,3,5\ldots\ldots$$

It is evident that for a tube, resonance occurs when the tube length is an odd multiple of the quarter-wavelength associated with incident sound frequency. Alternatively, for multiples of the half-wavelength, anti-resonance occurs. These frequencies will be modified by the impedance of any material placed over the tube. For the backing cavity used for this study, the first several calculated resonance and anti-resonance frequencies based on equation 4.5 are listed in Table 4.2 below.

Table 4.2 Resonance and anti-resonance frequencies for impedance tube backing cavity:
L = 13.2 cm (5.2 inches): T = 22.6 °C (72 F).

Resonance Frequency (Hz)	Anti-Resonance Frequency (Hz)
653	1306
1960	2613
3267	3920
4574	5227
5880	6534

The maxima and minima in the measured absorption coefficient occur close to the frequencies associated with the open tube shown in Table 4.2.

Figure 4.7 shows the general absorption behavior of the variable orifice perforate. A large change in the absorption coefficient is observed as the porosity is decreased. Indeed, there is a significant increase in absorption as the perforate porosity transitions from approximately 6 percent (solid circle symbols) to 1 percent (solid triangular symbols) at the lower resonance frequencies. As the porosity is further reduced below 1 percent, the absorption is significantly reduced which is indicative of a normalized impedance that is significantly different that unity.

For porosities less than 1% and higher than 6%, absorption performance appears to be very poor. Below 1% porosity, the absorption decreases rapidly and exhibits hard wall behavior, namely, a vanishing absorption coefficient. This reduction in absorption corresponds to a rise in normalized resistance which is shown in Figure 4.8. Note the rapid increase in resistance for the last two configurations, that is, the 0.43% and 0% porosity cases. The zero porosity case behaves very nearly like a rigid wall. The "wall" in this case is about 1.57 mm – thick, however. The absorption is nearly zero and the resistance is almost two orders of magnitude higher than that of air. Recall that when the normalized resistance approaches unity and the normalized

reactance vanishes (i.e., when the material impedance matches the wave impedance of air), the absorption coefficient is maximized. The reduction in perforate porosity initially drives the normalized resistance towards unity until it reaches levels over twice the resistance of air. As expected, the perforate porosity controls this resistance and hence the absorption of the perforate/cavity combination in a manner that is inversely proportional to the porosity as predicted by equation 4.1. More than a one order of magnitude increase in the normalized resistance was realized with a mechanical movement of less than 2 mm.

Figure 4.9 shows the normalized reactance for the tested perforate configurations over a large frequency range. The resonance and anti-resonance frequencies are clearly evident. Since resonance frequency has no meaning for the completely closed perforate configuration (porosity = 0%), it is not shown in Figure 4.10. For the configurations tested, the variable orifice perforate shifts the resonance frequency towards a lower frequency as the porosity is decreased. It is also evident that this shift in resonance frequency is larger at higher multiples of the first resonance frequency. It is should be noted that the 0.4% porosity configuration did not exhibit any higher multiple resonance frequencies.

Resonance Frequency Shift

Figure 4.10 shows the normalized reactance and absorption coefficient in the vicinity of the first three resonance frequencies. The three figures on the left hand column show the normalized reactance and the three figures on the right hand column show the absorption coefficient. Since it was shown in Figure 4.9 that the 0.4% porosity configuration did not exhibit multiple resonance frequencies, it was not considered in the data presented in Figure 4.10.

It is clear from Figure 4.10a that the first resonance frequency has shifted by approximately 124 Hz to a lower frequency as the perforate changed porosity from 23.5% to 1.2%. This change in resonance frequency is as easily discernable in the absorption coefficient spectra shown in Figure 4.10b. This is because over the frequency range shown (0.1 kHz to 1.1 kHz), the absorption is relatively broadband in nature. There is a large increase in the absorption of the perforate/cavity combination as the porosity is decreased below 6 %. The is a significant result in that only a mechanical movement of less than 0.2 mm was needed to change the porosity from roughly 6% to 1%. This small translation of one perforate over the other resulted in a very large increase in absorption coefficient. As mentioned earlier, this is due in large part to the increase in resistance from a very low value to a value that is close to the optimum for maximum absorption. It is also possible that the increased resistance has an added component due to the unique orifice shape of the variable orifice perforate. This is addressed in the next section.

At the second resonance frequency, the shift due to reduction in porosity is greater than at the first resonance. Figure 4.10c and 4.10d show the corresponding normalized reactance and absorption coefficient, respectively. A shift of approximately 260 Hz was observed in the resonance frequency. Again, the absorption is significantly enhanced at porosites below 6%. The resonance shift can be seen more clearly in the absorption coefficient shown in Figure 4.10d.

Finally, Figure 4.10e and 4.10f show the normalized reactance and absorption coefficient at the third resonance frequency. A shift of approximately 286 Hz is observed in the resonance frequency. The absorption is not as broadband in this frequency range as in the previous cases;

116

however, the same good absorption is observed at the lower porosities. Table 4.3 lists the shift in resonance frequencies for the first three resonances of the perforate/cavity combination. Figure 4.11 shows the corresponding resonance frequency shifts. The shift is normalized with respect to the maximum porosity configuration. The curves drawn in Figure 4.11 are interpolations of the data represented by the symbols. As a percentage of the baseline resonance, the amount of change in the 2nd and 3rd resonance frequencies is less than the change in the 1st resonance frequency.

Table 4.3 Shift in the first three resonance frequencies for the perforate/cavity resonator. Frequency shift with respect to reference porosity, 23.49%.

Perforate Porosity, %	1st Resonance Frequency	Frequency Shift, Δf	2nd Resonance Frequency	Frequency Shift, Δf	3rd Resonance Frequency	Frequency Shift, Δf
23.49	604 Hz	-	1824 Hz	-	3068 Hz	-
15.75	596 Hz	8 Hz	1812 Hz	12 Hz	3052 Hz	16
8.99	576 Hz	28 Hz	1764 Hz	60 Hz	2984 Hz	84
5.97	568 Hz	36 Hz	1740 Hz	84 Hz	2960 Hz	108
3.32	528 Hz	76 Hz	1648 Hz	176 Hz	2852 Hz	216
1.20	480 Hz	124 Hz	1564 Hz	260 Hz	2782 Hz	286

Comparison with Linear Perforate Model

One way to provide insight into whether or not the non-circular orifices help or hinder the amount of resonance frequency control is to compare the measured results with a standard impedance model used for perforates with round holes. Using the method outlined in Section 4.3, the mass reactance was calculated using the end correction expressed in equations 4.4 and 4.5. This was done for the first resonance frequency. The first resonance frequency was predicted using the first root of equation 4.6 that governs the resonance of a cavity-backed perforate. This equation is repeated below for reference:

$$\omega_{res} - \frac{c}{h}\sigma \cot(\frac{\omega_{res}L}{c}) = 0 \qquad (4.7)$$

It was assumed that the "eye" – shaped orifice shapes were elliptical. For the lowest porosity case considered (1.2% porosity case) the eccentricity was calculated to be approximately 0.97. The model used to predict the mass reactance assumed a linear impedance behavior. That is, the impedance does not change appreciably as a function of sound pressure level on the orifice particle velocity. The linearity assumption may not be as valid because for a given sound pressure level, smaller porosities (i.e., smaller open areas) will have higher orifice velocities. Based on the work of Ingard and Ising[42] if the orifice velocities are much higher than 0.05 m/s then nonlinearity can become important.

Figure 4.12 shows a comparison between the linear model and the measured impedance data for the first resonance frequency as a function of perforate porosity. Figure 4.12a shows the normalized resistance and Figure 4.12b shows the normalized mass reactance. The impedance tube data are computed using equation 4.2. It appears that the resistance is in reasonable agreement with the model. However, the measured mass reactance begins to deviate from the

model as the porosity decreases. The unique "eye" – shaped orifice resulting from overlapping perforate sheets not only creates an elliptical-like shape but also creates a unique "stepped" cross section. It is possible that this stepped geometry could result in a lower mass reactance. This will be examined further in the next section.

Analytically. the elliptic shape itself does not appear to make a large difference when compared to an equivalent circular orifice shape. Table 4.4 compares the predicted mass reactance for circular holes and elliptical holes with the measured reactance. For the smallest porosity shown. the difference between the circular and elliptical prediction is approximately 1.1%.

Table 4.4 Comparison of predicted and measured VOP normalized mass reactance

Porosity. %	Predicted [Circular Orifices]	Predicted [Elliptical Orifices]	Measured
23.49	0.1254	0.1254	0.1293
15.75	0.1782	0.1780	0.1414
8.99	0.2863	0.2853	0.1915
5.97	0.3999	0.3980	0.2110
3.32	0.6276	0.6223	0.2795
1.20	1.2389	1.2255	0.4430

Finally. Figure 4.13 shows a comparison between the predicted and measured first resonance frequency as a function of perforate porosity. The theory under predicts the measured resonance frequencies as the porosity is decreased. At largest porosity. the orifices are exactly circular and the theory predicts the frequency very well (which is consistent with the mass reactance results). Thus. for the lowest porosity shown in Figure 4.13. the predicted resonance frequency is approximately 43% lower than measured. This is a result of the measured reduction in mass reactance for the variable orifice perforate.

Single Tone Excitation

To assess the sensitivity of the variable orifice perforate to large incident sound pressure levels. single tones were input into the impedance tube at frequencies that corresponded to first resonance frequency determined by the broadband data (see Table 4.3). Each perforate configuration was exposed to a single tone at the first resonance frequency. At this frequency. measurements were made at increasing levels. The highest computed incident SPL was approximately 158 dB. It has been established by many researchers[ ] that orifices exposed to ever increasing incident acoustic intensity will exhibit a nonlinear response to the measured impedance. It is suspected that at the low porosities generated by the variable orifice perforate. this nonlinearity will become more evident at lower incident sound pressure levels. This is because for a given sound pressure. continuity forces the velocity in the orifice to be larger for a small area (low porosity) as opposed to a lower velocity with a larger area (higher porosity).

The incident sound pressure levels were computed from the two-microphone impedance measurement technique described in Appendix A. Figure 4.14 shows the normalized resistance as a function of incident sound pressure level and perforate porosity. The curves shown in Figure 4.14 are interpolations of the data points shown. There is no data in-between the symbols

118

shown (this is also true for Figures 4.16 and 4.17). The general increase in resistance with porosity is observed, which at the lower sound pressure levels is consistent with Figure 4.12a. At the highest porosity, the resistance stays almost constant up to 125 dB. Then a rise in resistance occurs above 130 dB, indicating nonlinearity. As the porosity is decreased, the incident sound pressure

level at which the resistance exhibits nonlinearity becomes is lowered. For example, the 3.32 % porosity configuration shows a continual increase in resistance over the levels tested. It is evident that the reduced orifice hole size created by the translating perforate leads to a more nonlinear perforate. The reduced total area of the perforate leads to higher orifice velocities which is due to continuity laws.

Although the orifice velocity was not directly measured, it can be calculated from the knowledge of the incident sound pressure level and the impedance at the perforate itself. If the surface was a rigid wall, the surface acoustic pressure would be theoretically twice the incident acoustic pressure. Since the perforate is not a rigid wall, the pressure at the orifices is modified by the impedance of the perforate. From the formulation given by Guess[ ], the expression for the root-mean-squared orifice velocity is:

$$u_{o-rms} = \frac{2|P_{i-rms}|}{\sigma\rho c \sqrt{\left(\frac{R}{\rho c}+1\right)^2 + \left(\frac{\chi}{\rho c}\right)^2}} \qquad (4.8)$$

Using the tone excitation data at a nominal incident sound pressure level of 106 dB, the calculated orifice velocity is shown in Figure 4.15 as a function of perforate porosity for the tested configurations. This shows the increased velocity for the smaller sized orifices that contributes to the increased resistance.

As outlined in Section II, the increased orifice velocity leads to the formation of quasi-steady jets that have associated viscous losses[ ]. This is the origin of the increased resistance. It is also possible that the noncircular orifice shape may contribute to the perforate's increased nonlinear behavior. This possibility is addressed in the next section.

Figure 4.16 shows the normalized mass reactance as a function of incident sound pressure level and perforate porosity. Again, at the lowest sound pressure level, the trend with porosity is consistent with that shown in Figure 4.12b. As the incident sound level is increased, the mass reactance begins to decrease after a certain acoustic level is reached. For the largest porosity tested, the reduction in mass reactance begins above 135 dB. For the smaller porosities tested, the decrease in mass reactance is evident at the lower sound pressure levels. The nonlinear behavior of the mass reactance is similar to that seen with the resistance in that it is linked to the increased orifice velocity. Ingard[ ] describes the behavior of the nonlinear reactance as a result of the flow within and around the orifice becoming turbulent. That is, the mass reactance stays constant until flow exiting the orifice becomes turbulent. Ingard suggests that the sound waves do not affect the acoustic mass when the quasi-steady jet is laminar. He further suggests that the decrease in mass reactance "can be thought of as a transfer of part of the kinetic mass (kinetic

energy) in the sound field around the aperture into turbulent motion and free boundary flow that breaks away from the aperture."

Figure 4.16 shows some interesting results at the higher sound pressure levels for the lower porosity configurations. The mass reactance begins to rise after a certain level is reached. It is not exactly clear why this happens, however, it is suspected that it is related to the reactance of the backing cavity. Further work is needed to understand this observation and is suggested as on of the items for future work in Section VI. Finally, Figure 4.17 shows the absorption coefficient as a function of sound pressure level and porosity. It is clear that the incident sound pressure level has a major impact on the absorption properties of the perforate/cavity combination. As the normalized resistance approaches unity, the absorption approaches a maximum. For the lowest porosities, it can be seen that this optimal resistance is reached sooner than the higher porosity configurations due to the rapid increase in orifice velocity. As the normalized resistance increases beyond unity, the impedance of the perforate/cavity combination becomes "mis-matched" in relation to the wave impedance of air, thus, the absorption becomes non-optimal.

4.6   Conclusions

This section presented normal incidence impedance data for a variable orifice perforate concept that requires very small mechanical movement to achieve large changes in perforate porosity. By examining the impedance behavior of this perforate in conjunction with a backing cavity, the following observations and conclusions are made:

1) *Control of the perforate's resistance and thus liner absorption can be achieved to a great degree with a small mechanical input.* For movements of less one orifice diameter (2 mm for the present perforate), the absorption characteristics of a perforate-covered cavity can be changed significantly. Normal incidence absorption coefficients are increased not only at the resonance frequencies but also for several hundred Hertz around the resonance frequency. Normalized resistance was increased more that an order of magnitude for the same mechanical movement.

2) *The resonance frequency of a cavity can be controlled by the changing mass reactance of the variable perforate.* A shift in resonance frequency is observed at the first resonance frequency and its multiples. Resonance frequency shifts of 21%, 14%, and 9% were observed for the 1st, 2nd and 3rd resonance frequencies, respectively.

3) *The theoretical linear model over predicts the mass reactance that is measured and under predicts the resonance frequency.* The differences between prediction and measured data cannot be explained. It is possible that a significantly reduced attached mass could explain the lower measured mass reactance. It appears from the analytical prediction that accounting for the elliptical nature of the orifices in the translated configurations does not account for the observed differences. It is possible that nonlinear effects could account for some of the lower measured mass reactance.

4) *It is not clear from the data presented in this section whether the shape of the orifice contributes to the increased resistance at high incident sound pressure levels.* The variable orifice perforate becomes more nonlinear as the porosity is decreased. Nonlinear behavior was

observed to occur near 110 dB for the lowest porosity while occurring near 130 dB for the maximum porosity tested.
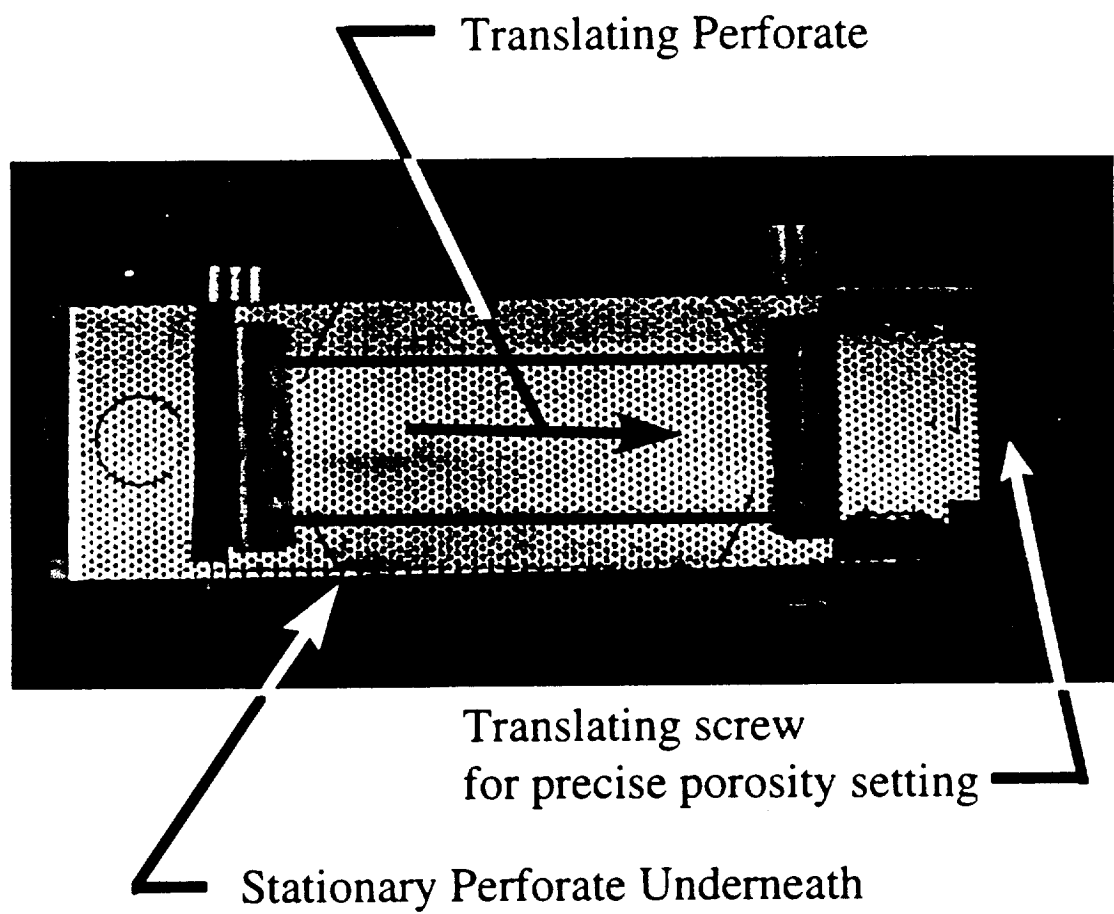
Figure 4.1 Variable orifice perforate test article used in normal incidence impedance tube measurements.
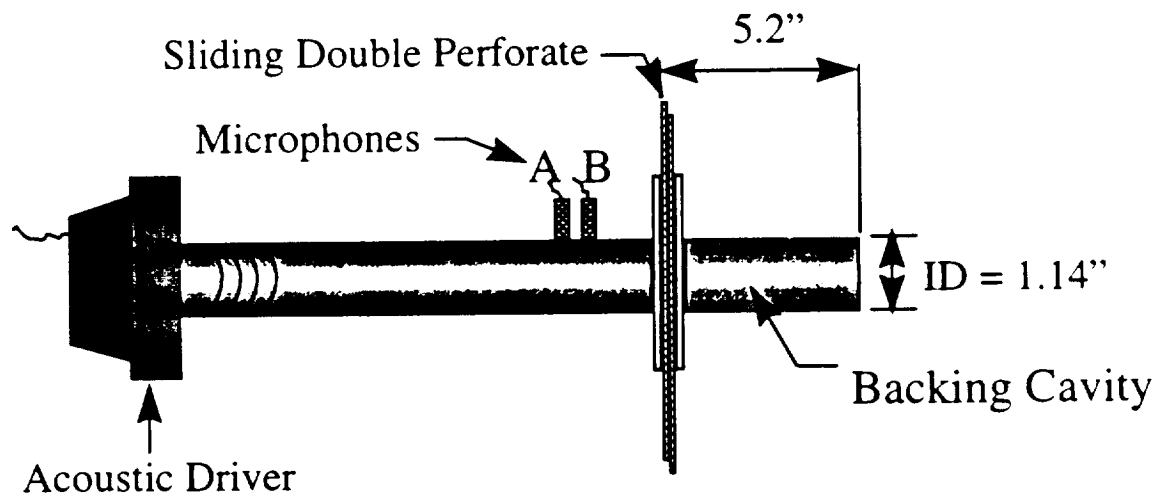
Figure 4.2 Experimental arrangement of normal incidence impedance measurement of variable orifice perforate.
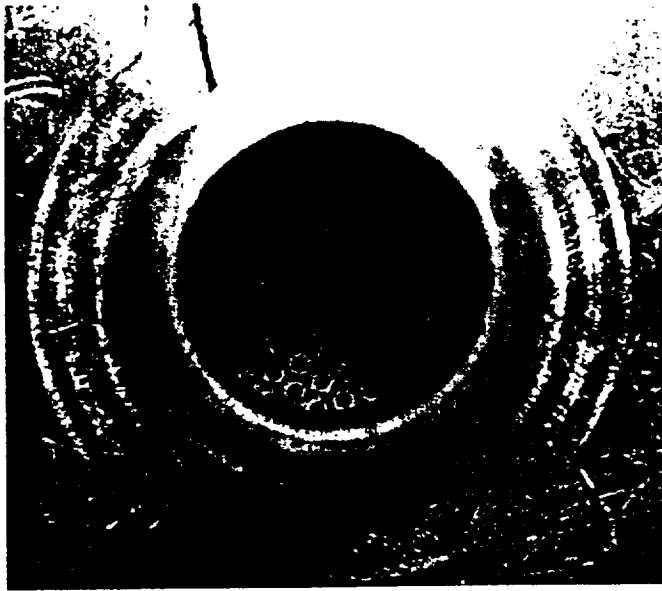
a. Variable Orifice Perforate Installed - Max Porosity
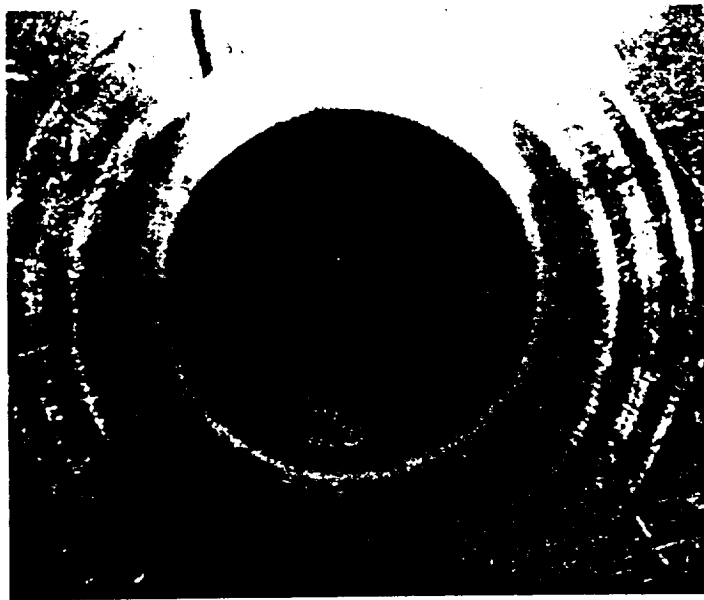
b. Variable Orifice Perforate Installed - Fractional Max Porosity

Figure 4.3 Variable orifice perforate installed in impedance tube.

Flush Mics for
TMM

Sample Holding
Flange

Acoustic
Driver

Standing Wave
Tube

Sample Holder
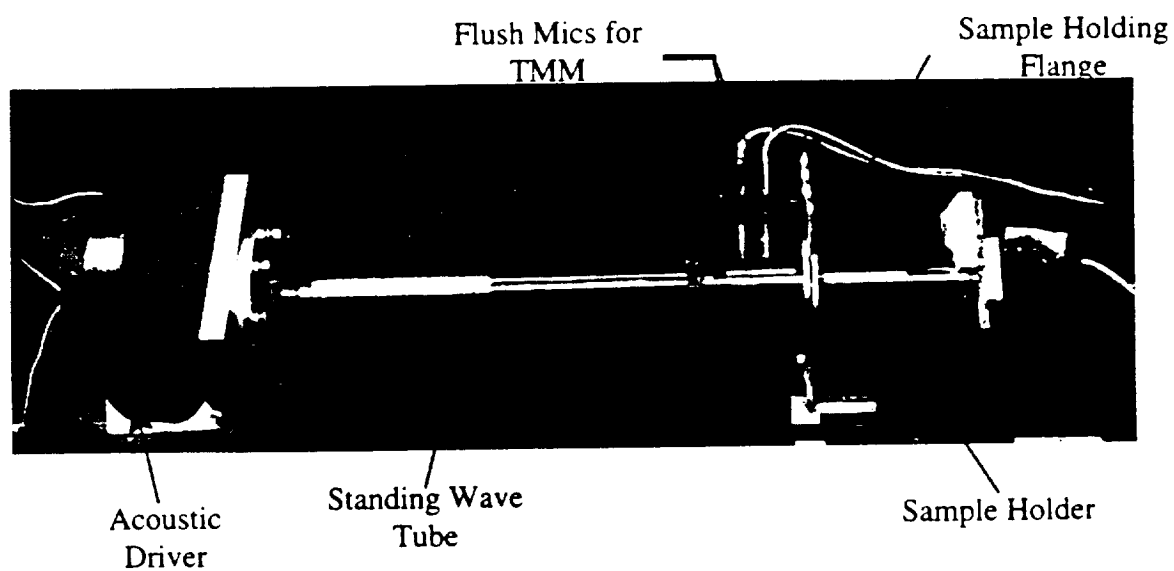
Figure 4.4 Normal incidence impedance tube used for perforate impedance measurements.
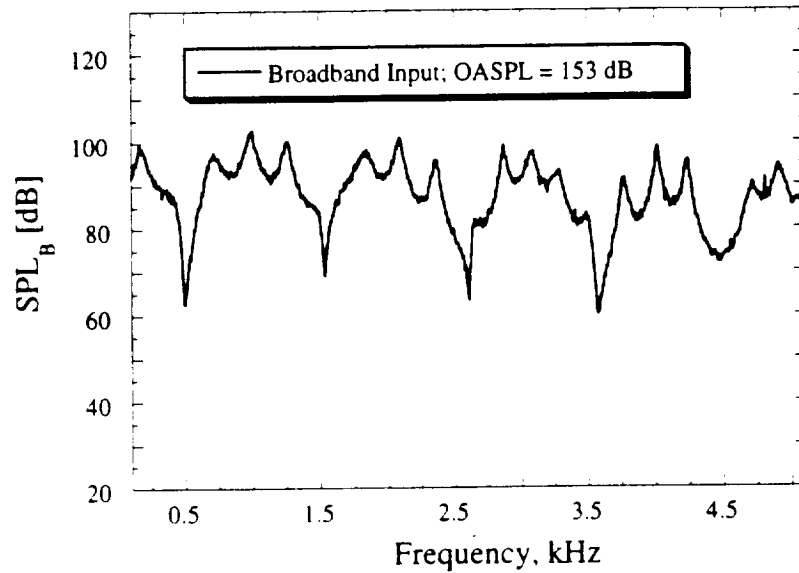
a . Typical microphone response to broadband input.
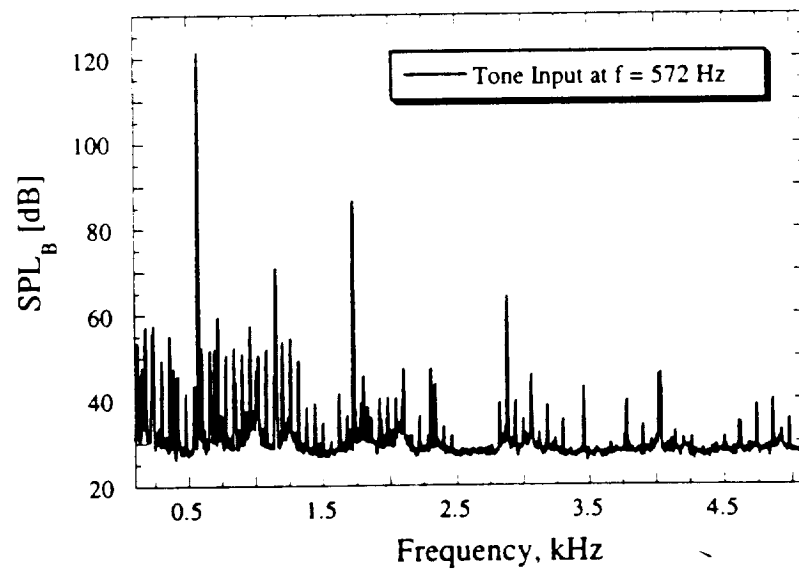
b . Typical microphone resonse to single tone input.

Figure 4.5 Typical broadband and single tone response of impedance tube microphone measurements with variable orifice perforate installed [Δf = 4 Hz; 64 avgs.].

126
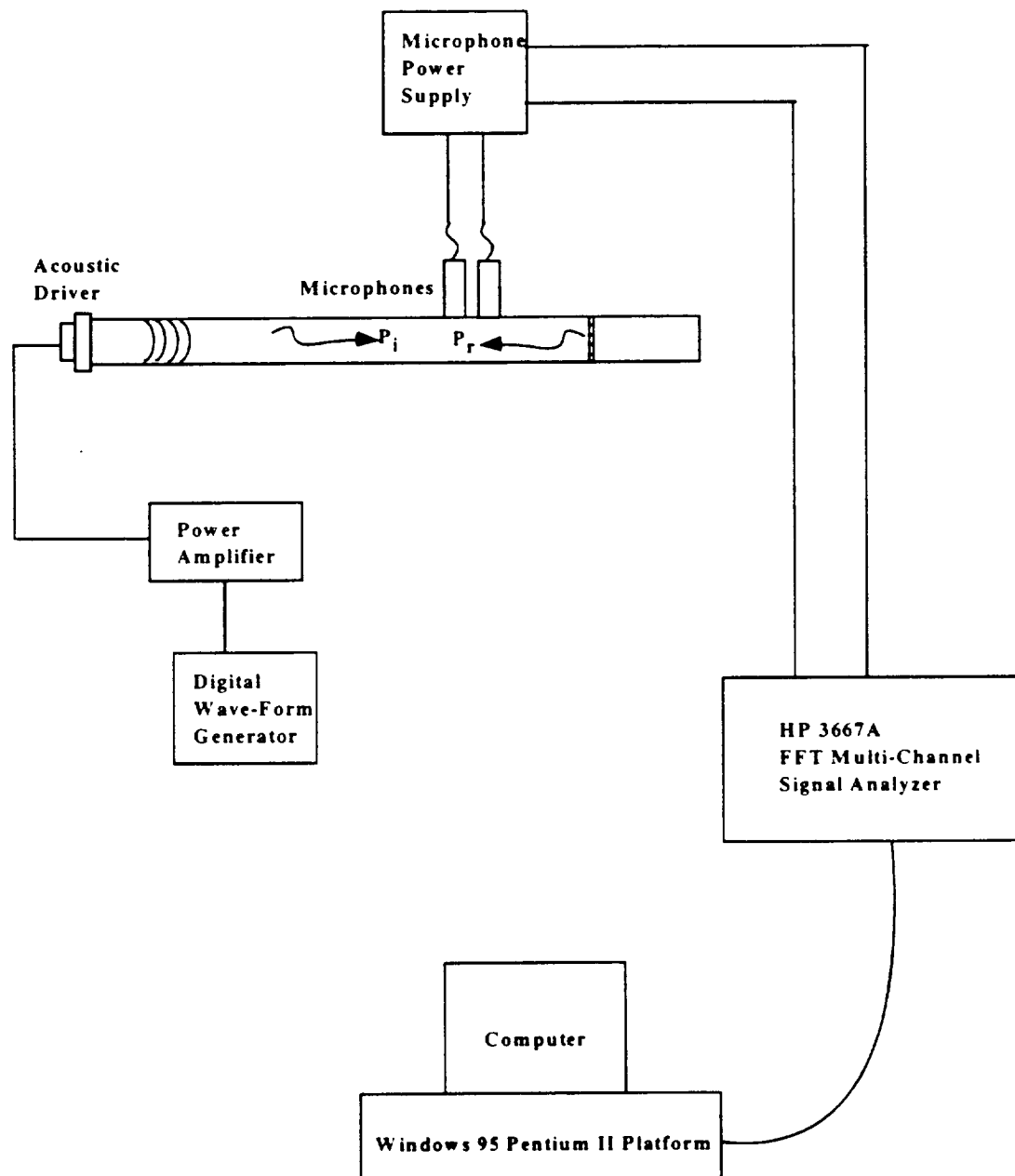
Figure 4.6   Signal processing schematic for impedance tube measruements.
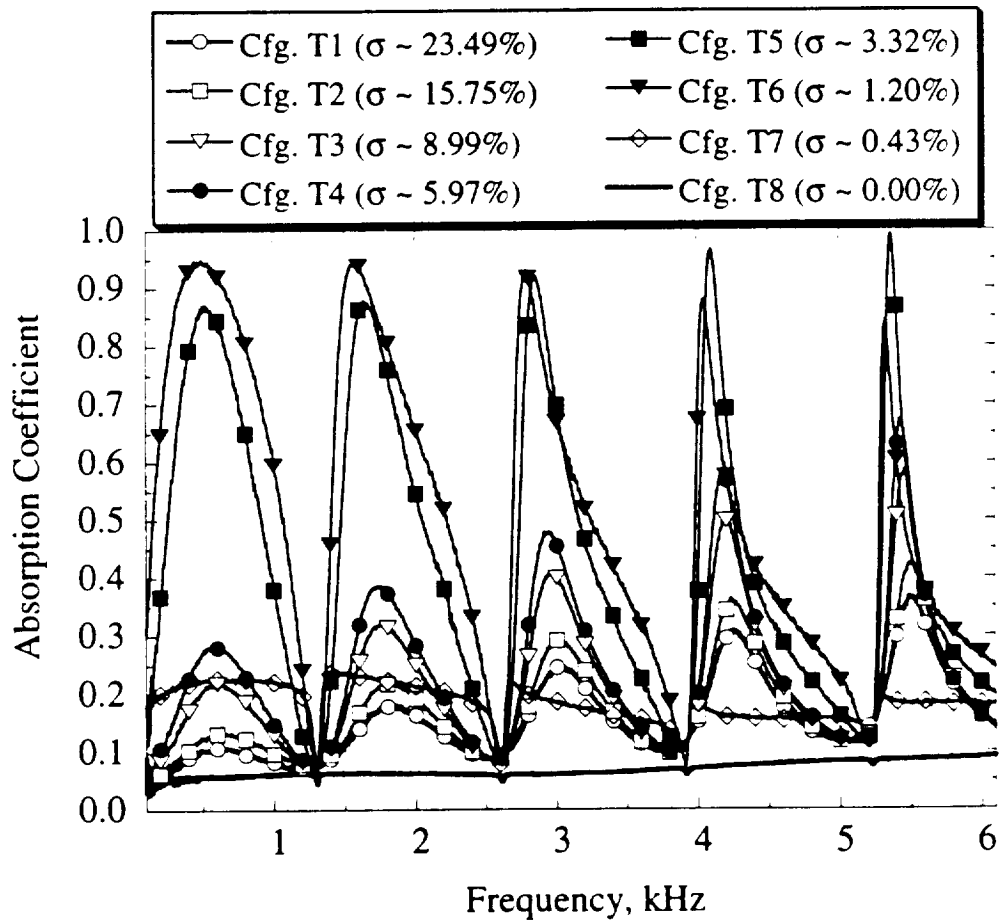
Figure 4.7 Absorption coefficient for tested porosity configurations of the variable orifice perforate [$\Delta f = 4$ Hz; 64 avgs.].
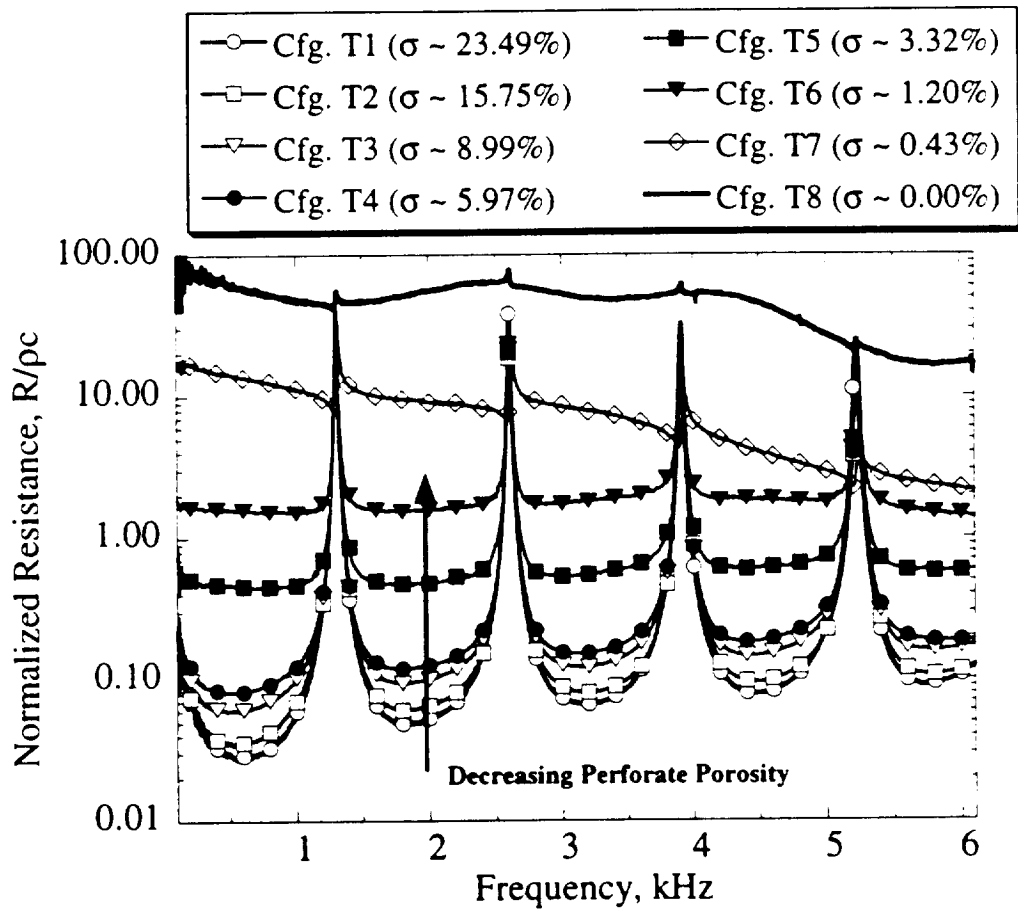
Figure 4.8 Normalized resistance for tested porosity configurations of the variable orifice perforate [Δf = 4 Hz; 64 avgs.].
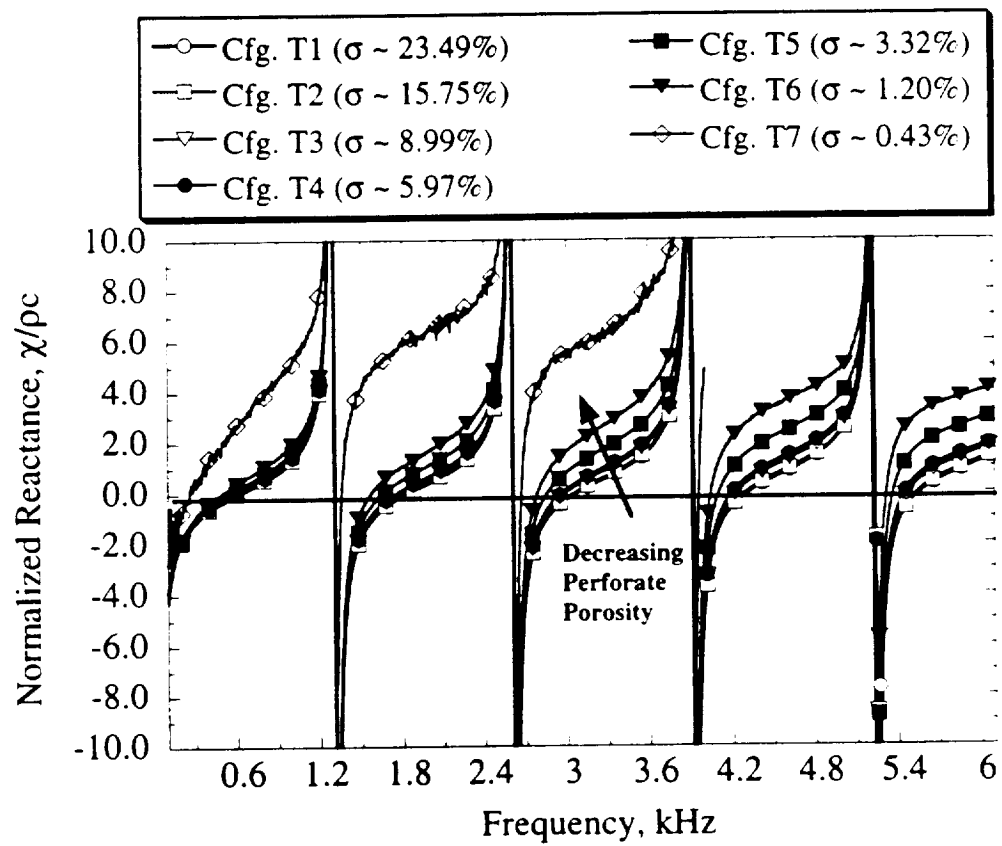
Figure 4.9 Normalized reactance for tested porosity configurations of the variable orifice perforate [Δf = 4 Hz; 64 avgs.].
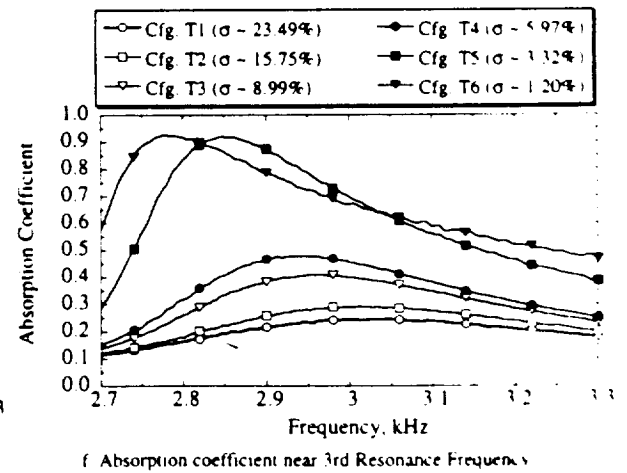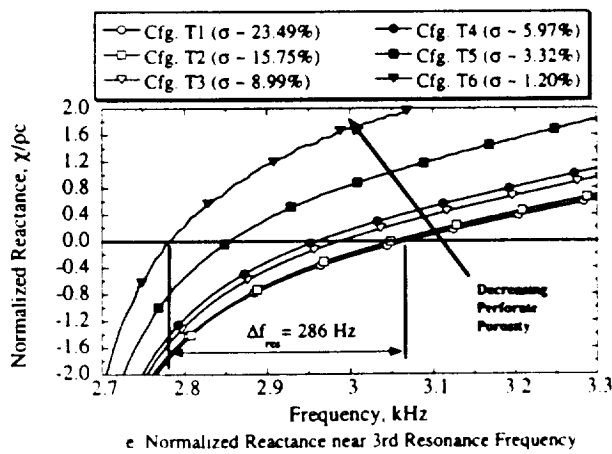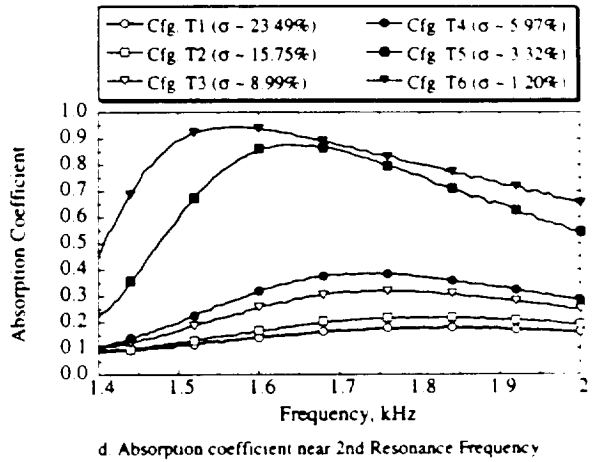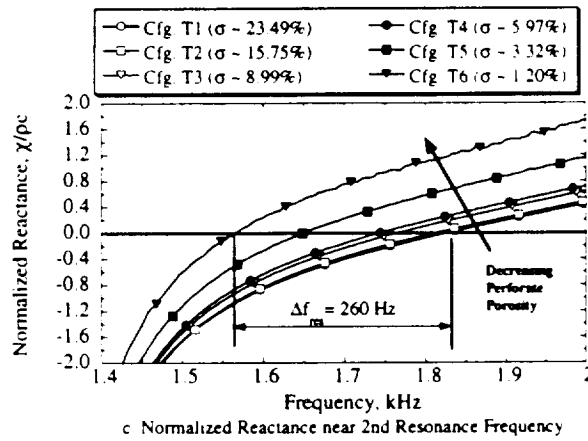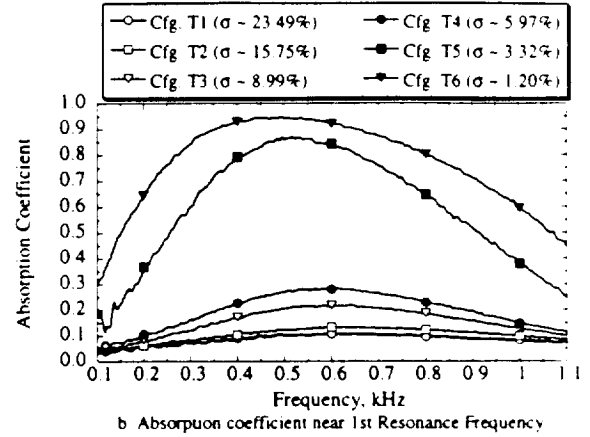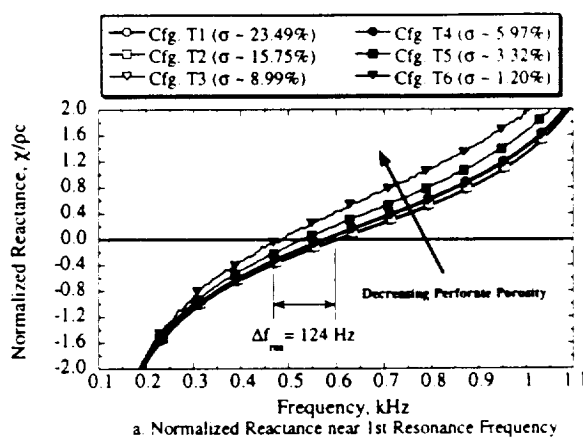
Figure 4.10 Effect of variable orifice perforate on resonance frequency and absorption coefficient.
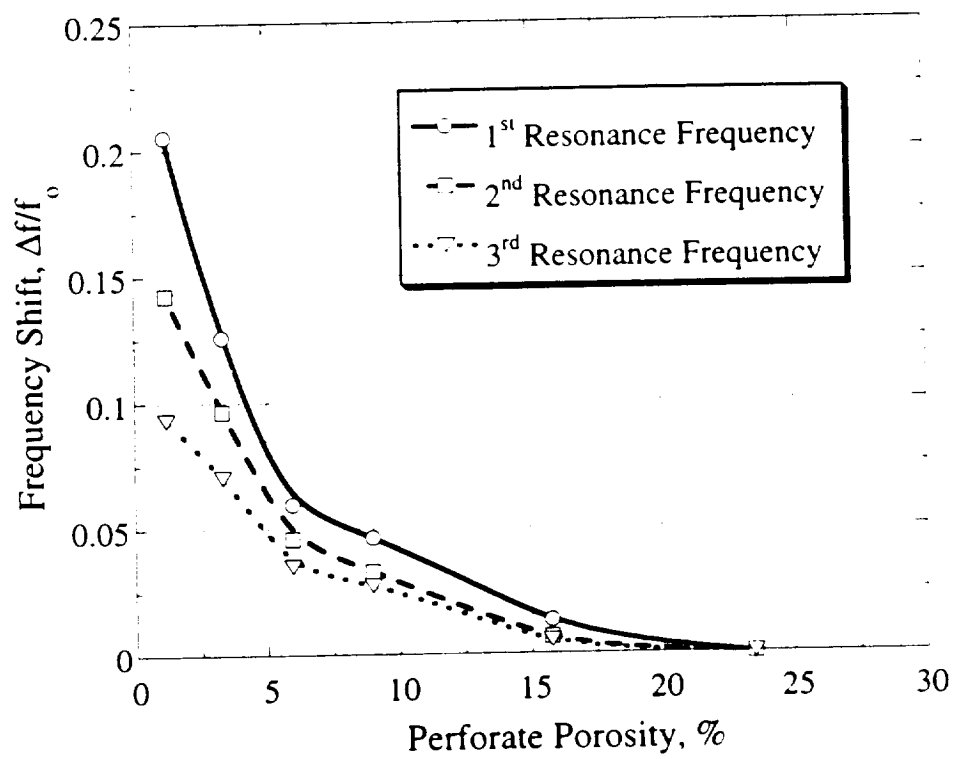
Figure 4.11 Impact of variable porosity on first, second, and third resonance frequencies.
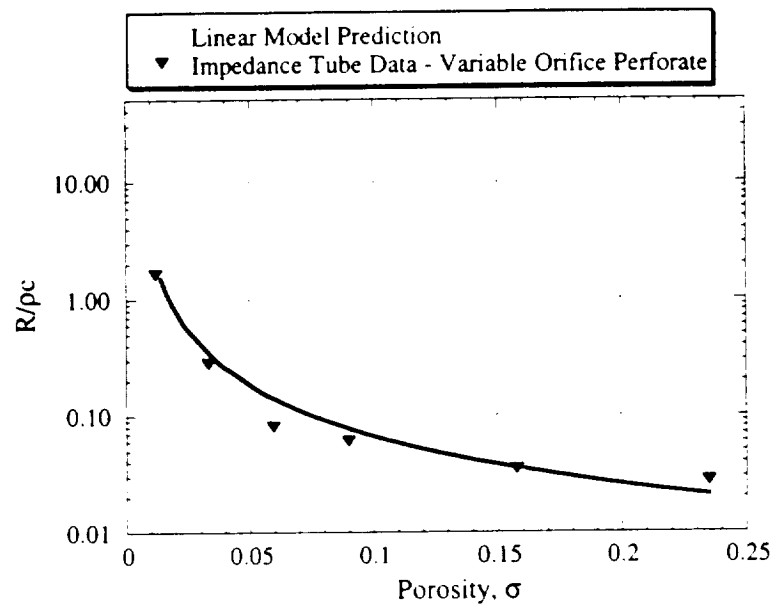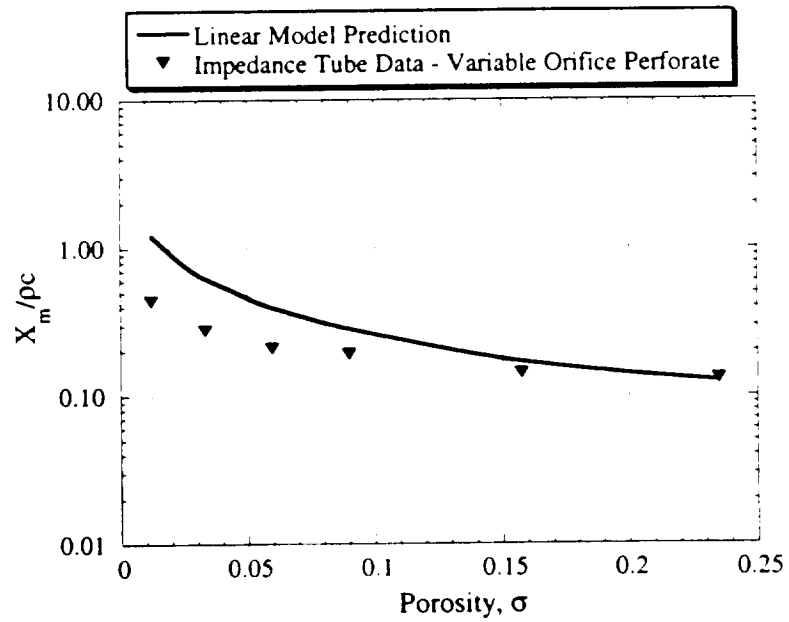
Figure 4.12 Comparison of predicted perforate impedance with measured impedance of variable orifice perforate at first resonance frequency; Broadband input [Δf = 4 Hz; 64 avgs.].
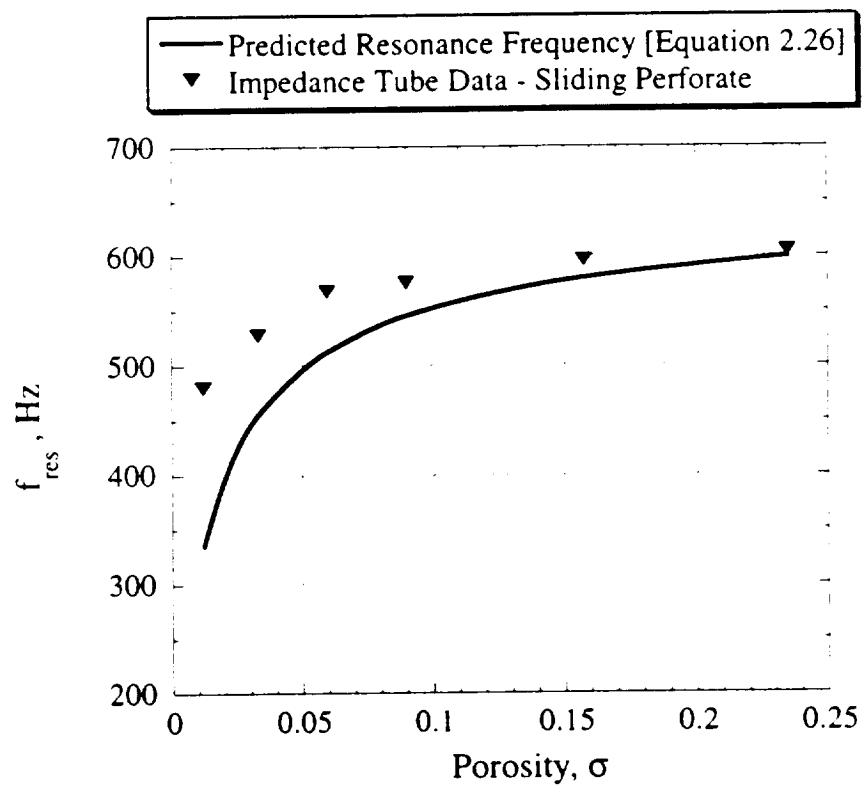
Figure 4.13 Comparison of predicted and measured first resonance frequency.
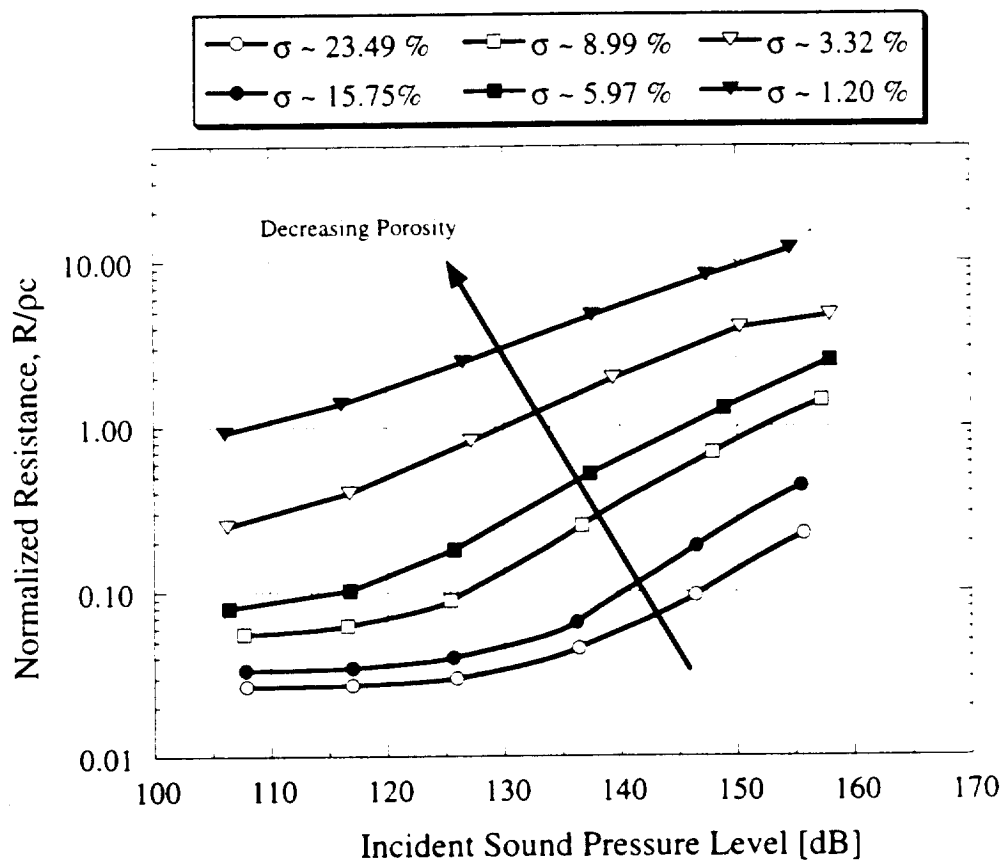
Figure 4.14 Effect of porosity and incident sound pressure level on the
normalized resistance of the variable orifice perforate; Single tone input
[Δf = 4 Hz; 64 avgs.].
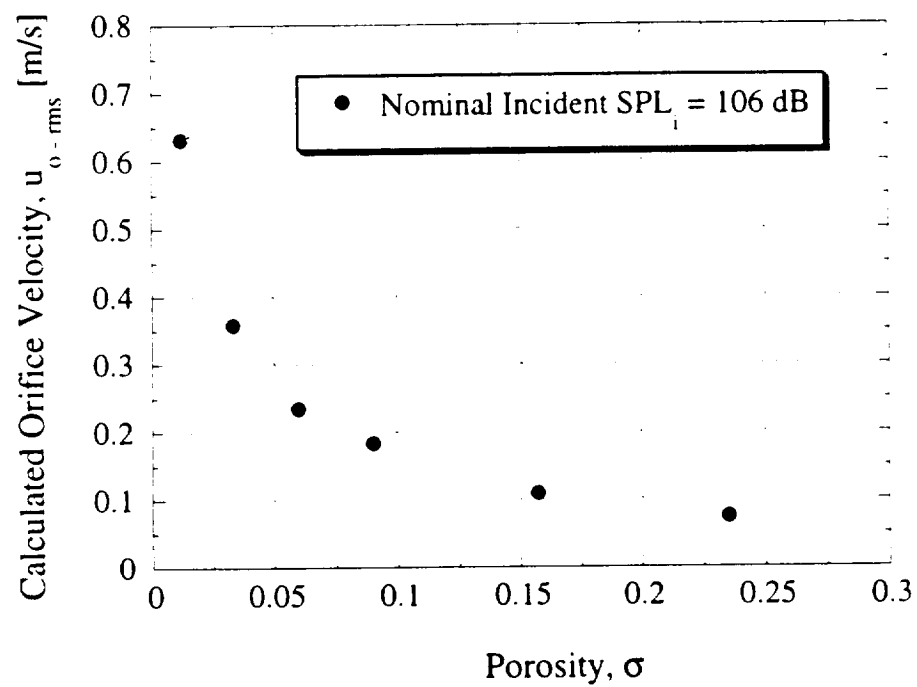
Figure 4.15 Orifice velocity calculated from equation 4.8 as a function of porosity for a nominal incident sound pressure level of 106 dB.
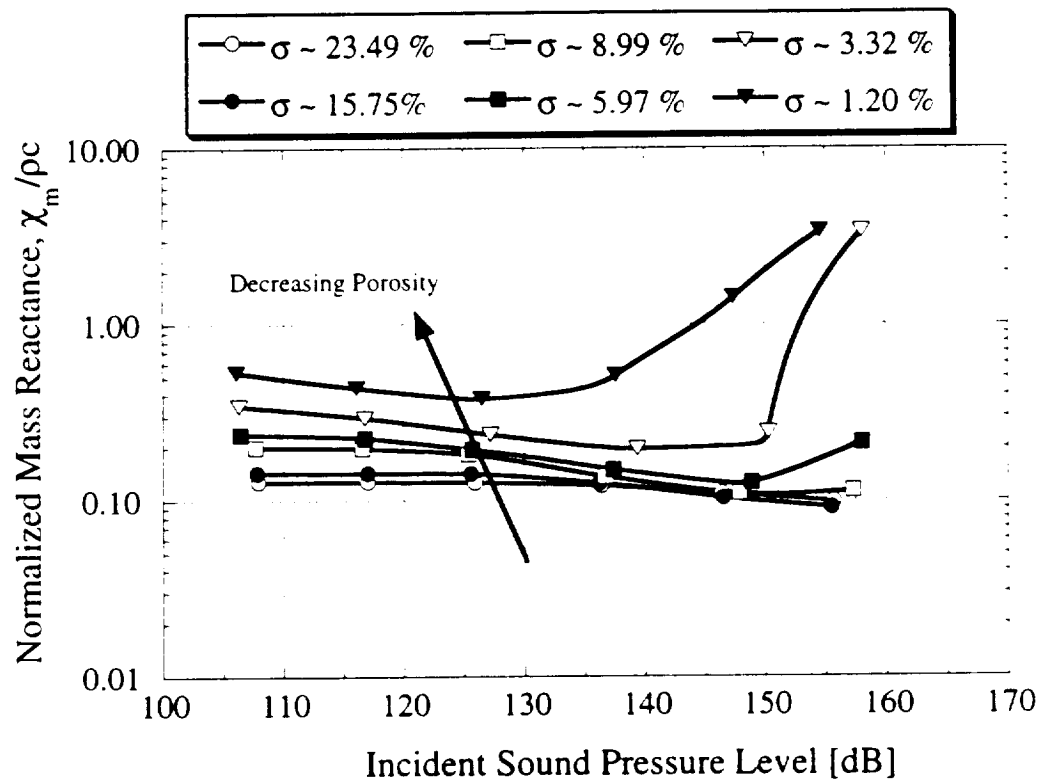
Figure 4.16 Effect of porosity and incident sound pressure level on the normalized mass reactance of the variable orifice perforate; Single tone input [$\Delta f = 4$ Hz; 64 avgs.].
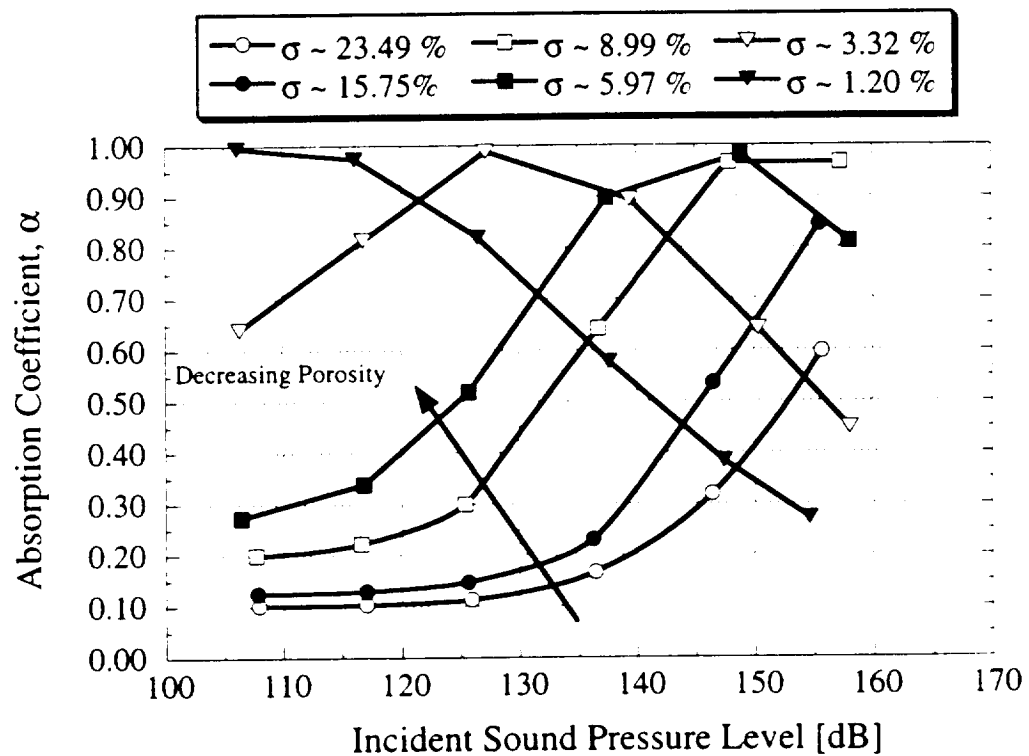
Figure 4.17 Effect of porosity and incident sound pressure level on the absorption coefficient of the variable orifice perforate: Single tone input [Δf = 4 Hz; 64 avgs.].

SECTION V

Effect of Orifice Shape on Acoustic Impedance

5.1   Introduction

In Section III, it was observed that the impedance and hence absorption of an acoustic liner can be controlled through the manipulation of a porous layer's porosity via a variable orifice perforate. Section IV showed that the variable orifice perforate can produce large changes in the perforate impedance with a small mechanical input. It was unclear whether the unique shape of the orifice created by the variable orifice perforate led to the observed lower than expected mass reactance. The present section attempts to quantify how the specific orifice shape that is created by the variable orifice perforate affects the orifice impedance. Furthermore, since there may be other shapes that could be created by the variable orifice concept, selected non-circular orifice shapes were examined as well.

Background

The acoustic impedance of orifices have been examined by many researchers   due in part to the prevalence of orifices as a constituent component of many acoustic liners. Typically, orifices used in such absorbers are circular in shape, and thus most of the impedance models are based on round orifices. A concept for manipulating the porosity of a perforate has been examined in the present study that has an unintended consequence, namely, the creation of a perforate that consists of orifices that can have non-circular shapes.

The acoustic impedance of an orifice can be separated into its resistive and reactive components that roughly correspond to viscous (resistance) and inertial (reactance) properties of the acoustic system. Friction within the orifice is the dominant contributor to the resistance at low sound amplitudes, while the conversion of sound into vorticity at the orifice edges is the dominant contributor to the resistance at high sound amplitudes. At the higher amplitudes, the incident sound produces an oscillatory jet through an orifice. Increased losses in this jet can occur if the vorticity is increased. This follows from well-established findings from the study of steady-flow jets and, in particular, the study of jet mixing enhancement   . The primary component of the reactance of an orifice is the oscillation of air mass within and around the orifice. For orifices where the radius is larger than the thickness, the "attached mass" becomes a dominant contributor to the reactance.

Sliding a perforate consisting of circular orifices over another identical perforate creates orifices that are oval or "eye-shaped" in shape. Moreover, using this sliding method creates a unique orifice cross-section. Figure 5.1 shows a single orifice created by the movement of one circular orifice over an identical orifice. For comparison, a circular orifice is also shown. Note that, for a given orifice open area, the stepped-oval shaped orifice has more air "trapped" within the orifice itself. This excess air resulting from the additional space formed in the region of the step as labeled in Figure 5.1a. It remains to be seen if the so-called "attached mass" that exists just outside of the orifice is different for the stepped-oval shaped orifice as compared to the

standard circular shaped orifice. This attached mass plays a role in determining the resonance frequency of a cavity backing such an orifice and the degree to which it plays a role is examined in this section.

Objective

The primary objective of this section was to determine the effect that a unique orifice. created from two overlapping circular orifices. has on its impedance relative to a circular orifice of equivalent area. A further objective is to determine how selected orifices of different shapes with equivalent area affect the orifice impedance.

Outline of Section

This section presents experimental data for normal incidence impedance measurements for a single orifice backed by a cylindrical cavity. Tests at both high and low incident sound pressure levels are performed. A description of the types of orifices tested and the experimental arrangement is followed by a presentation of the results.

5.2   Description of Orifices Tested

Equal Area Circular Orifice and "Stepped-Oval" Orifice

An orifice created from overlapping two circular orifices of equal diameter will be referred to as a "stepped-oval" orifice for the remainder of this study. The unique cross-section that the stepped-oval orifice possesses (see Figure 5.1) required that it be compared with a circular orifice that was as thick as the two overlapping orifices (h = 1.63 mm) and one that was as thick as one overlapping layer (h = 0.81 mm). Figure 5.2 shows a stepped-oval orifice produced by overlapping two circular orifices along with a single circular orifice with equivalent area. An estimated eccentricity of the stepped-oval orifice was calculated to be 0.77.

Equal Area Orifices for Shape-Effect Tests

Further tests on selected different orifice shapes shown in Figure 5.3. A circular orifice shape of given thickness and area was used as a baseline to compare the acoustic performance of other orifice shapes of equivalent area but different perimeter lengths. A square and triangular-shaped orifices were also fabricated. The triangular shape was equilateral. For a large deviation in orifice perimeter. a star-shaped orifice was made to provide a more unique aperture edge.

Orifice Plate Fabrication

Table 5.1 shows the tested orifices and their pertinent dimensions. The first four orifices listed in Table 5.1 were 6.35 cm (2.5 inches) in diameter and 0.812 mm (0.032 inches) thick each. The thickness of the stepped-oval shaped orifice plate was twice the thickness of the other orifices because it was created by overlapping two round orifice plates. The open area of all of the tested orifices was 0.1935 cm^2 (0.03 inches^2). The orifice plates were fabricated from aluminum sheets using an Electrical Discharge Machining (EDM) process.

Table 5.1 Dimensions for tested orifices. *Twice the thickness of other orifices (1.63 mm)

Orifice Shape	Perimeter, mm (in.)	Hydraulic Diameter, mm (in.)	Thickness, mm (in.)
Round	15.59 (0.61)	4.96 (0.20)	0.81 (0.032)
Square	17.56 (0.69)	4.40 (0.17)	0.81 (0.032)
Triangular	20.06 (0.79)	3.86 (0.15)	0.81 (0.032)
Star	37.82 (1.49)	2.05 (0.81)	0.81 (0.032)
Stepped-Oval*	16.22 (0.64)	4.77 (0.19)	1.63 (0.064)

Note that the oval-shaped orifice falls between the round and the square orifice in terms of its perimeter. However, the thickness of the stepped-oval shaped orifice is greater than the others by a factor of two (see Figure 5.1).

5.3   Summary of Tests Performed and Data Acquired

Experimental Set-up

The orifices were placed at the end of an impedance tube and were backed by a cylindrical cavity of depth, L forming a cavity resonator. Figure 5.4 shows the experimental arrangement with an orifice plate installed in the impedance tube. This experimental arrangement was identical to that presented in Section IV for the normal impedance measurement of the variable orifice perforate. The backing cavity provided a known impedance that could be accounted for when trying to isolate the impedance of the orifice. This approach is identical to that described in Section IV and the expression used to calculate the perforate impedance is repeated here for convenience:

$$\frac{Z}{\rho c} = Z_{perf} + Z_{cav} = \left[\frac{R}{\rho c} + i \frac{X_m}{\rho c} \right] - i\sigma \cot(kL) \qquad (5.1)$$

Broadband noise was used for the stepped-oval and circular orifices impedance tests. For the other orifice shapes both broadband and single tone excitation was used to acquire impedance data.

When the impedance measurements were made with single tone excitation, the frequency chosen was the resonance frequency that was determined from broadband excitation, i.e., when the total normalized reactance was zero. Comparison of measured orifice resistance with analytical models required knowledge of the rms velocity at the center of the orifice. This was measured for selected orifices with a single hot-wire sensor.

Calculation of Mass End Correction from Measured Data

The acoustic mass which occupies the space in and around the orifice can be computed from measured data and its magnitude can be compared as the shape of the orifice is changed. Recall

$$\frac{X_m}{\sigma \rho c} = \frac{\omega m}{A_o \rho c} \qquad (5.2)$$

141

from equation from Section IV that at resonance, the mass reactance can be expressed as:
The left hand side of equation 5.2 is obtained from impedance tube measurements as described in Section IV. It will be carried through in the following equations as a "known" quantity.

The *acoustic mass* can be calculated from:

$$m = \frac{A_o \rho c}{\omega} \left(\frac{\chi_m}{\sigma \rho c} \right) \qquad (5.3)$$

Furthermore, the mass end correction, δ_m, which allows for the attached mass external to the orifice (on both sides) can be expressed in terms of the orifice thickness:

$$m = m_{\text{inside orifice}} + m_{\text{external to orifice}}$$

$$= \rho A_o h + \rho A_o \delta_m = \rho A_o (h + \delta_m) \qquad (5.4)$$

Thus from equation 5.3 and 5.4, the end correction can be calculated:

$$\delta_m = \left[\left(\frac{\chi_m}{\sigma \rho c} \right) \frac{c}{\omega} - h \right] \qquad (5.5)$$

5.4   Experimental Facilities and Instrumentation

Impedance testing was conducted in the same impedance tube described in Section IV, where impedance measurements of the sliding perforate concept was performed. Recall that an impedance tube with an internal diameter of 29 mm was used to measure the acoustic impedance of test sample placed at the tube's termination. The Two-Microphone Method was used to compute the impedance. Similarly, the instrumentation and data acquisition for the experiments here are identical to those used in Section IV. Two phase-matched, Bruel & Kjaer microphones were used to sample sound pressure levels inside the impedance tube. The data were analyzed with a HP 3667A Multi-Channel Signal Analyzer. A frequency span of 0 – 6400 Hz was used with a 4 Hz bandwidth.

Hot-Wire Measurements

A need to measure the orifice velocity directly was fulfilled with a constant temperature hot-wire anemometer. The velocity of the acoustically induced jet was measured in the center of the orifice. For these measurements, a Dantec Streamline system was used in conjunction with a 486 PC platform. This system was the same system used to measure the velocity profiles in the flow-duct work presented in Section III. The hot-wire was calibrated with a Dantec Flow Calibration Unit. This device provided accurately metered flow in which the hot-wire could be immersed. Dantec Software provided automatic control of the flow to the user's specifications for velocities as small as 0.002 m/s.

5.5 Results

Impact of Stepped-Oval Orifice on Impedance

The main impact that the stepped-oval orifice has on the orifice impedance can be stated as follows:

The stepped-oval orifice has a smaller attached mass than an equivalent round orifice.

The end correction in circular orifices is normally independent of the orifice thickness. How it will be affected by the stepped section of the oval orifice shown in Figure 5.1 was not known prior to this study. The stepped-oval orifice impedance was therefore compared with a circular orifice. Under broadband excitation, the impedance of stepped-oval orifice was measured. A single thickness and a double thickness circular orifice was also tested. For descriptive purposes, the round orifice with thickness 0.813 mm will be referred to as the *single round orifice* and the round orifice with twice the thickness will be referred to as the *double round orifice*. Figure 5.5 shows the total normalized reactance in the vicinity of the first resonance frequency for these three orifices. The single round orifice has the highest resonance frequency, as indicated by the zero reactance value. The next lowest resonance frequency is the stepped-oval shaped orifice followed by the double round orifice. Figure 5.6a and 5.6b show the associated normalized resistance and mass reactance of the three orifices, respectively, near the resonance frequencies.

Figure 5.6a indicates that the resistance is not affected significantly by the additional length of the double round orifice or the stepped-oval shape. However, it is clear from Figure 5.6b that the oval shaped orifice doesn't have as much total reactive mass as the double round orifice. It is, however, more than the single round orifice. The additional acoustic mass in the double round orifice due to its increased thickness explains its larger total mass reactance relative to the single round orifice. However, the stepped-oval orifice appears to have some intermediate amount of mass within its stepped geometry.

To better understand the mass reactance of the stepped-oval orifice, the attached acoustic mass and mass end-correction were calculated for each of the round orifices and the stepped-oval orifice using equations 5.3 and 5.5. These results are shown in Figure 5.7a and 5.7b. Since the standard end-correction for a circular orifice is dependent on the orifice radius only, the single and double round orifice should exhibit the same amount of attached mass and thus the same end-correction. This is borne out in Figure 5.6a. and 5.6b. The single and double thickness round orifices have essentially the same end correction at their respective resonance frequency. Using the same thickness as the double round orifice, the corresponding attached mass for the stepped-oval shaped orifice is measurably smaller. If the stepped-oval is assumed to be elliptical, then it has a calculated eccentricity is approximately 0.77. Using the analytical expression for the mass end correction used for elliptical orifices (see equation 4.3), the difference from an equivalent area circular orifice is:

$$\frac{\delta_{m-elliptical}}{\delta_{m-circular}} = 0.987 \qquad (5.6)$$

This suggests that the elliptical shape of the tested stepped-oval orifice does not have a large impact on the attached mass, however, this is only a theoretical result. Flow visualization shown later indicates that the jetting from a stepped-oval orifice is quite different from that from a circular orifice. This may explain the difference observed in the attached mass. A more detailed study of this phenomenon is left for future work.

These results are significant for the application of the variable orifice perforate described and tested in Section IV and as applied in a 2DOF liner in Section III. Since the sliding of one perforate over the other creates unique stepped-shaped orifices in the perforate, the resulting end correction will be smaller than for an equivalent perforate made up of round orifices. The implication of this reduced end correction or attached mass. is a reduction the mass reactance of the perforate. This may explain the over-prediction of mass reactance when using the model based on equivalent round orifices (see Figure 4.13b). This impacts the resonant frequency through equation 5.1 and can limit the extent to which this resonance can be controlled.

Impact of Orifice Shape on Impedance

Since the variable orifice concept present in this study could possibly be modified to produce more convoluted orifice shapes other than an oval or "eye-shaped", selected orifice shapes with equal areas were tested for their normal incidence impedance. The main results can be stated as follows:

At relatively low incident sound amplitudes, orifices with shapes that are significantly different from circular have higher normalized resistance at resonance frequency and are closer to unity compared to a round orifice. They thus have higher absorption.

The normal incidence impedance for the orifice shapes shown in Figure 5.3 was measured with a broadband excitation signal and the normalized resistance and mass reactance are shown in Figure 5.8. The normalized mass reactance (Figure 5.8b) does not appear to be significantly affected by the different shapes. This means that the associated mass end correction for the different shapes tested were not significantly different. Although not tested, an oval shape identical to that of the stepped-oval that was tested but without the stepped areas, would have a perimeter closer circular than the square, triangular, and star-shaped orifice (see Table 5.1). It might be expected that the mass end correction of such a shape would not be significantly different from those different shapes that were tested. This would be consistent with the theoretical result expressed in equation 5.6.

Figure 5.8a shows that for the highly non-circular star-shaped orifice, the normalized resistance is noticeably higher (about 60% higher than the round orifice) in the frequency range near resonance. This result implies that a variable orifice perforate that is made with very non-circular orifices (with highly convoluted perimeters) may provide higher degree of absorption than equivalent circular orifices.

The literature on steady jets indicate that the mixing of non-circular jets is much better than circular jets. It is quite likely that the increased mixing in the near field of the orifice could cause an increase in resistance. Further study is needed to address the detailed mixing of the highly non-circular orifice under acoustic excitation.

To further emphasize the increased resistance and hence absorption of a highly non-circular orifice, the absorption coefficient for the selected orifices is shown in Figure 5.9. Note that the peak absorption corresponds to the resonance frequency (i.e., zero reactance value). Increasing orifice perimeter is accompanied by increasing absorption. The star-shaped orifice has an absorption coefficient that is approximately 40% higher than the equivalent-area round orifice. This can also be explained from the enhanced jet-mixing perspective mentioned above. This mixing translates into a loss of energy that originates from the acoustic energy driving the oscillating mass. Hence, less acoustic energy is reflected back to the source and the absorption coefficient is increased.

Another result can be stated as follows:

At higher incident sound amplitudes, the normalized resistance appears to be independent of the orifice shape.

As discussed in Section II, very large oscillatory velocities in the orifice (produced by high incident amplitudes or very small orifices) have been treated as quasi-steady jets in the literature. As the variable orifice perforate was transitioned to smaller porosities and more non-circular orifice shapes in the work presented in Section IV, it was observed that the standard resistance model based on circular orifices did a reasonable job of predicting the normalized resistance (see Figure 4.13a).

Tests on the selected orifice shapes described above were conducted in the impedance tube using single tones at gradually increasing amplitudes. The frequency of the tone was chosen to be the resonance frequency determined from the broadband data. After the impedance data was acquired, the same acoustic conditions were reproduced and a single hot-wire was placed in the center of the round orifice and the star-shaped orifice to measure a root mean square orifice velocity to correlate with the normalized resistance. Figure 5.10 shows the hot-wire experimental arrangement and Figure 5.11 shows a typical time history of the instantaneous velocity measured for an incident sound pressure level of 110 dB. Only the axial (orifice axis) component of velocity was measured. The hot-wire sampled at 55 kHz and took 1024 samples.

Figure 5.12a shows the normalized resistance of the tested orifices under single tone excitation as a function of the measured orifice velocity. Figure 5.12b shows an expanded plot of the lower amplitude results. In general, the trend is for the resistance to increase in a linear fashion at higher sound pressure levels. At the lower levels, the star-shaped orifice resistance is distinctly higher than that of the other orifice shapes. These lower incident sound pressure level results are consistent with the broadband results shown in Figure 5.8a. At the lowest measured orifice velocity condition (approximately 0.04 m/s), a trend is discernable with increased orifice perimeter. That is, the larger the orifice perimeter, the larger the resistance. However, as the

sound pressure is increased and the orifice velocity is increased above 0.5 m/s, the resistance for all of the shapes tend to collapse on each other.

Figure 5.13 shows the impact that increased sound amplitude has on the absorption coefficient of the orifice/cavity resonator for the two extreme orifice shape cases, namely the round and star-shaped orifice. As with the resistance data presented earlier, the shape of the orifice seems to have an effect on the absorption at the lower orifice velocities while the data tends to merge together at the higher velocities. The absorption rises in conjunction with the movement of the normalized resistance towards its optimum value of unity (see Figure 5.12a). As the resistance increases further the absorption decrease beyond its optimum.

The impact of these results on variable orifice perforate is that the nonlinear orifice impedance models that were outlined in Section II for circular orifices should be adequate to predict the nonlinear impedance for non-circular orifices. Figure 5.14 compares the measured single tone data of the round and star-shaped orifice data with the semi-analytical model outlined in Section II, namely from Melling :

$$
\frac{R}{\rho c} = \text{Real}\left\{\frac{i\omega h_{\text{vis}}}{\left[1 - \frac{2J_1(k_s r_o)}{k_s r_o J_0(k_s r_o)}\right]}\right\} + \frac{0.6}{C_D^2}\left(\frac{1-\sigma^2}{\sigma^2}\right)\frac{u_{o-rms}}{c} \tag{5.7}
$$

A discharge coefficient of 0.55 seems to fit the measured data better than the value of 0.6 which is suggested in the literature . The origin of this value of discharge coefficient is from steady orifice flow metering data. Hersh, et al , fitted experimental data with their theory and educed a C_D. They reported that at amplitudes approaching 170 dB, the discharge coefficients approached a value of 0.4, while at lower amplitudes near 100 dB the value was near 0.7. As the jetting in the orifice diminishes with decreasing sound amplitude, the C_D should approach unity.

5.6   Selected Flow-Visualization of Orifice Jetting

While a detailed study of the energy structure of the jet issuing from different shaped orifices is beyond the scope of this study, some flow visualization was performed on some of the orifices tested in the impedance tube but without the backing cavity. Images of the jetting structure from the orifices were obtained via a Particle Image Velocimetry (PIV) system recently acquired by the Georgia Tech Research Institute Aerospace Laboratory. An acoustic driver was attached to one end of a tube and an orifice plate was attached to the other end. The tube was approximately 20 inches long. The tube was filled with incense smoke and the driver was excited with a single tone input. The laser was pulsed at 15 Hz.

A key finding from the flow visualization was that jetting that issued from the stepped-oval orifice was deflected with respect to the orifice axis. Figure 5.15– 5.17 shows evidence of the orifice jetting for the round, star-shaped, and stepped-oval orifices, respectively, at a moderate sound pressure level. Each figure shows two snapshots at different times. It is immediately

146

evident that the oscillatory jet issuing from the stepped-oval orifice is deflected at some angle from the orifice centerline axis. The pressure difference between recessed space to one side of the orifice which is uniquely created by the overlapping circular orifices and that directly across most likely deflects the jet. Well-defined vortical structures still persist several diameters downstream. It is unknown whether the "vectored" jetting from this orifice contributes to the different attached mass observed in the acoustic measurements. Further work is needed to address this phenomenon better.

5.7   Conclusions

This section presented normal incidence impedance results for orifices of different shapes. but equivalent area. The objective was to discern the impact of the orifice shape on the impedance. The following observations and conclusions were made:

1) The stepped-oval orifice has a smaller attached mass than an equivalent round orifice and has a definite "vectored" oscillatory jet that exists due to he unique stepped orifice cross section as observed with flow-visualization. This possibly contributes to the reduced mass reactance. This impacts the acoustic liner control concept presented in earlier sections because it affects the control of the resonance frequency that can be achieved by sliding one perforate over another. Specifically. it tends to reduce mass reactance of the variable perforate.

2) At relatively low incident sound amplitudes. orifices with shapes that are significantly different from circular have higher normalized resistance (closer to unity) compared to a round orifice leading to higher absorption. This can impact the variable orifice perforate concept if more deviant orifice shapes are produced by another mechanical method.

3) At higher incident sound amplitudes. the normalized resistance appears to be independent of orifice shape. The implication of this result is that existing fluid mechanical models that describe high amplitude orifice impedance are adequate for the description of the variable orifice perforate when exposed to high amplitude sound.

4) The stepped-oval orifice has a definite "vectored" oscillatory jet that exists as a result of the unique overlapping orifice cross-section that the variable orifice perforate concept is based The vectored jetting was observed with flow visualization and could possibly be related to the reduced mass reactance measured in the acoustic tests. Further study is needed to address this phenomenon.

147

Open Area

Excess Air in Step

Excess Air in Step

Section A-A

a. Stepped-Oval Orifice

Open Area

Section B-B
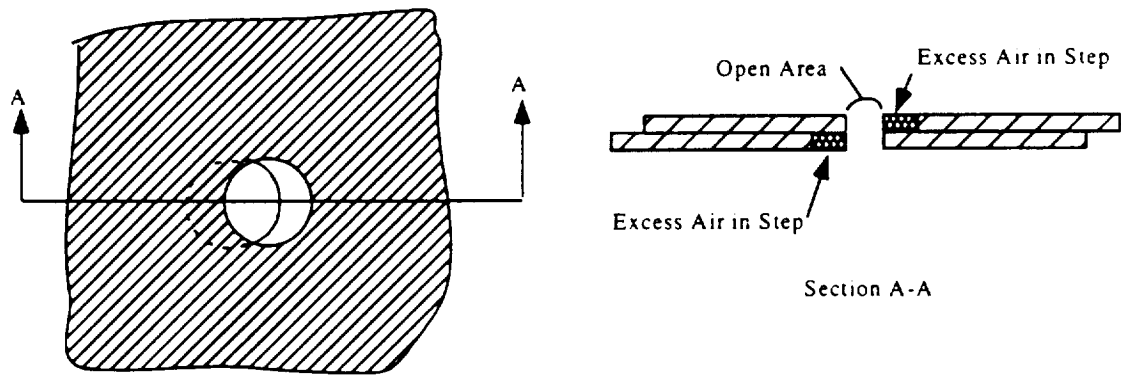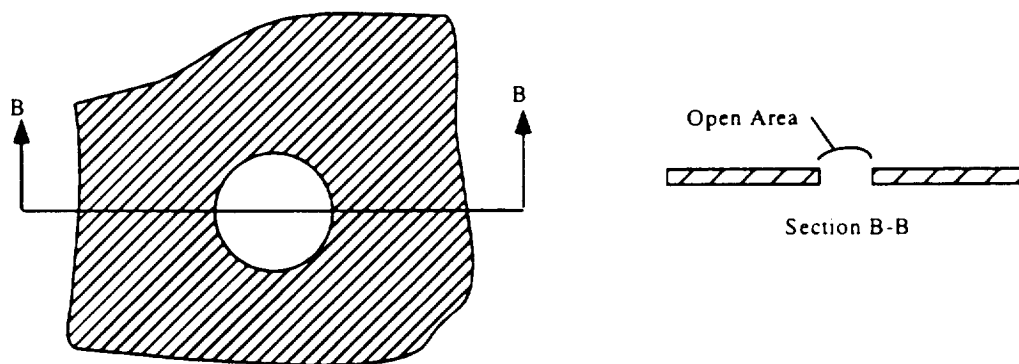
b. Circular Orifice

Figure 5.1 Unique stepped-oval orifice created by overlapping circular orifices
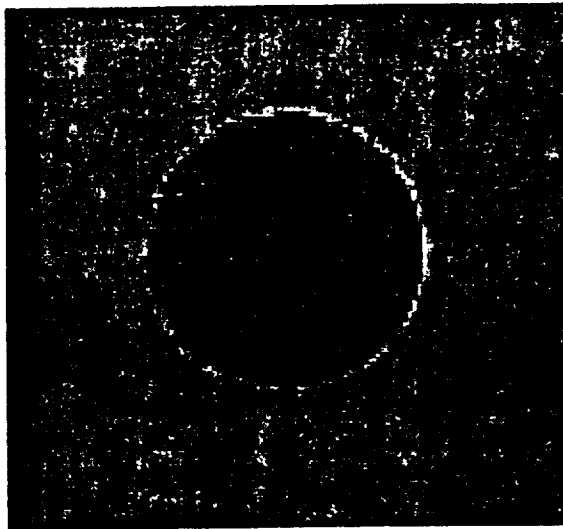
Circular Orifice Plate
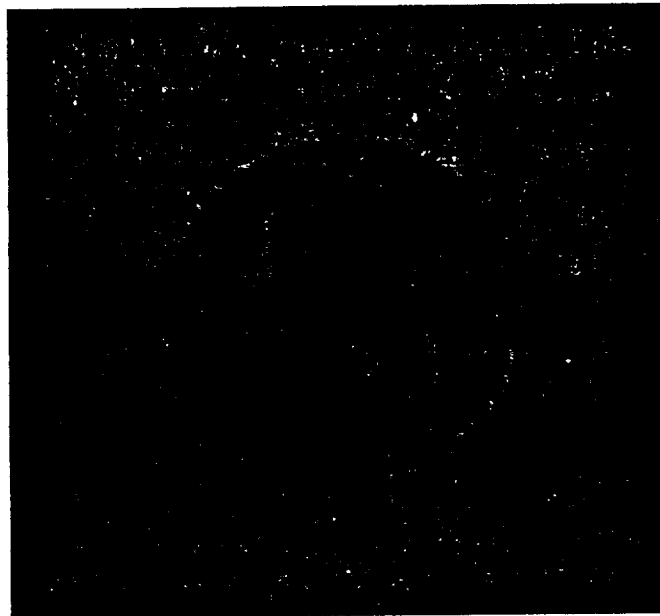
Stepped-Oval Orifice Plate

Figure 5.2 Tested circular orifice and overlapping stepped-oval orifice.
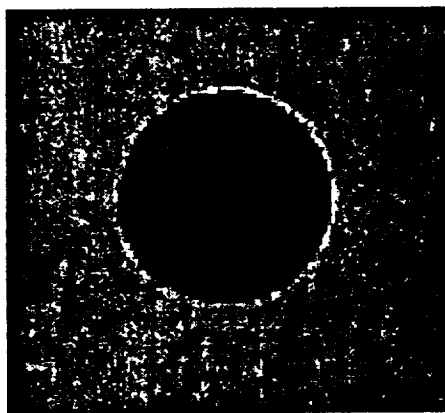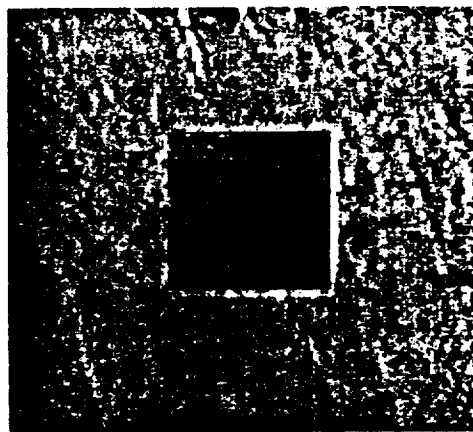
Round   Square
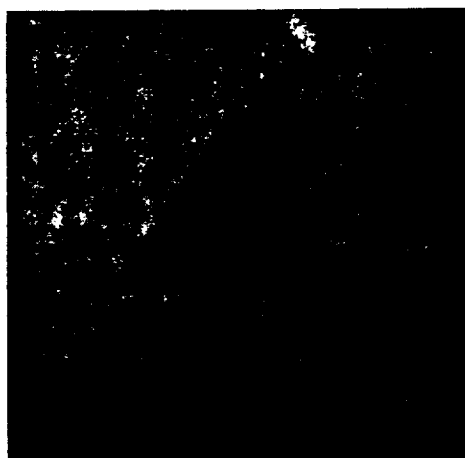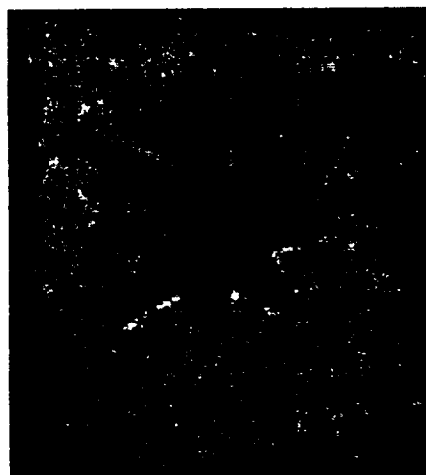
Triangular   Star

Figure 5.3 Orifice shapes tested for impact on impedance; $A_o = 19.36$ mm^2.
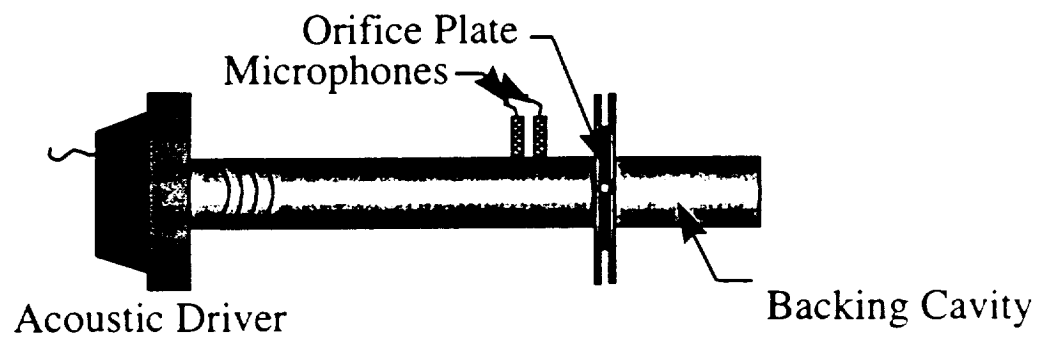
Impedance Tube
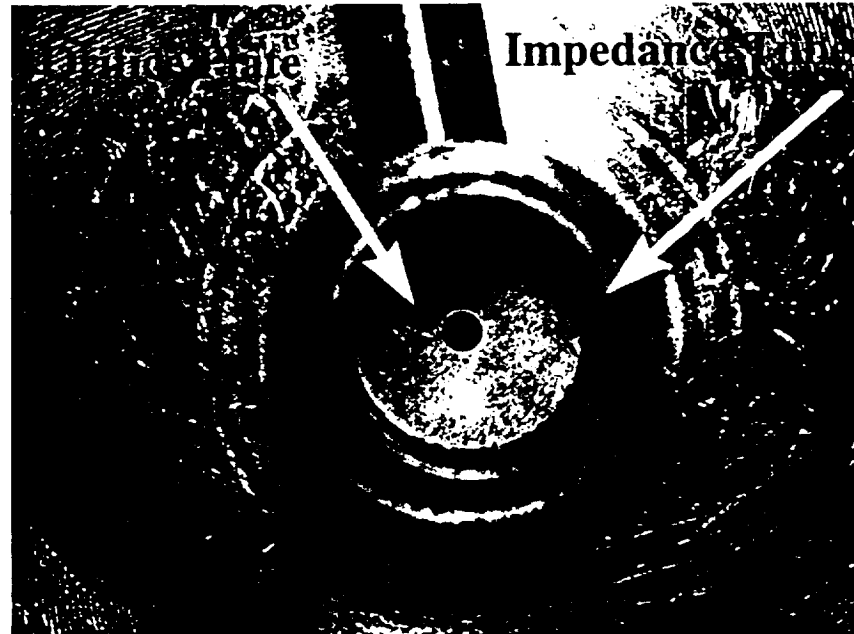
Orifice Plate Installed

Figure 5.4 Impedance tube - single orifice experimental arrangement.
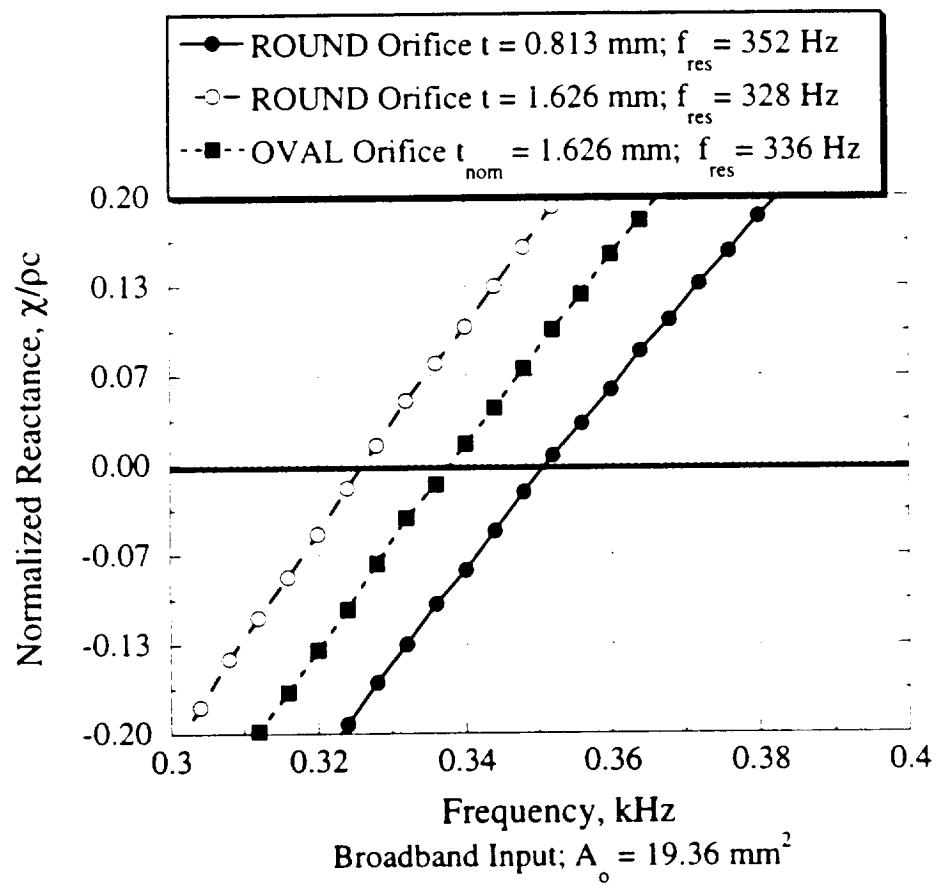
Figure 5.5 Resonance frequency comparison between stepped-oval orifice and circular orifice; Broadband input [OASPL$_i$ = 157 dB; A$_o$ = 19.36 mm^2; Δf = 4 H/. 64 avgs.]
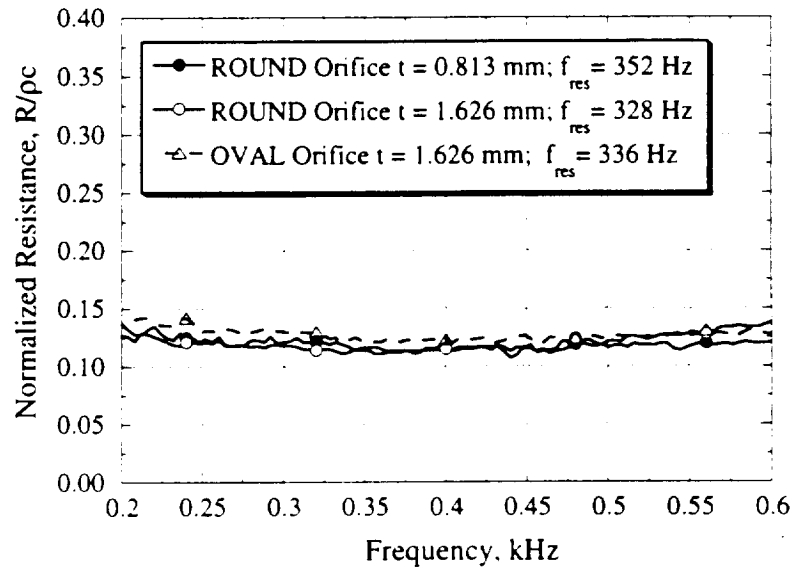
a. Normalized Resistance
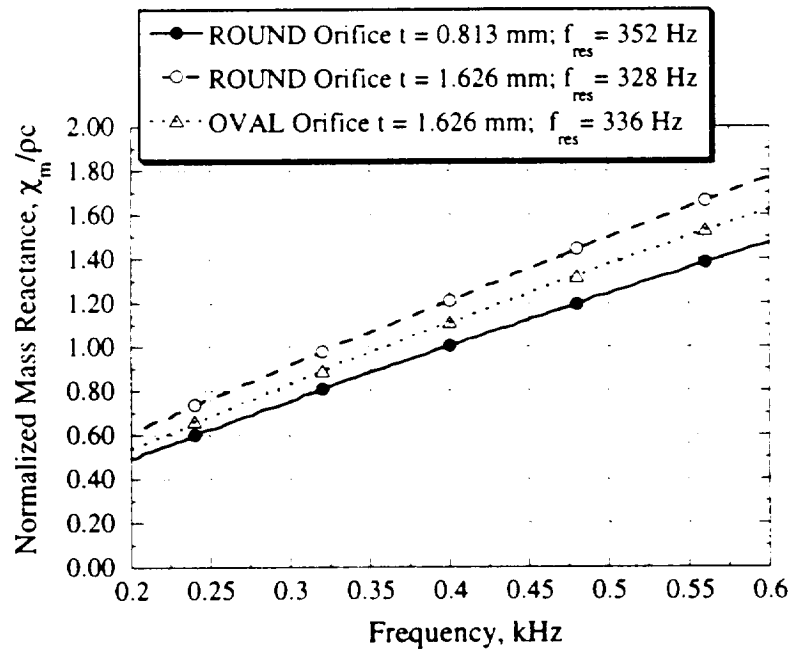
b. Normalized Mass Reactance

Figure 5.6 Impedance comparison between stepped-oval orifice and circular orifice; Broadband input [OASPL$_i$ = 157 dB; A$_o$ = 19.36 mm^2; Δf = 4 Hz; 64 avgs]
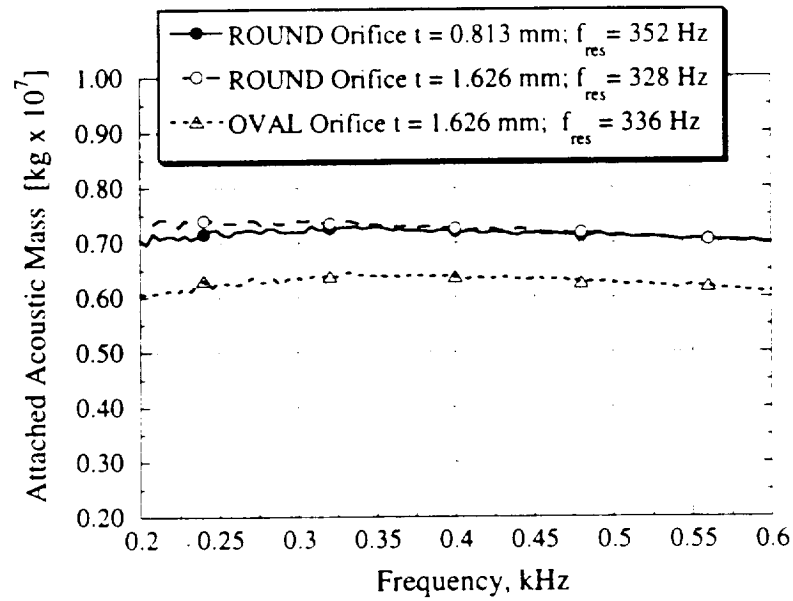
a. Attached Acoustic Mass
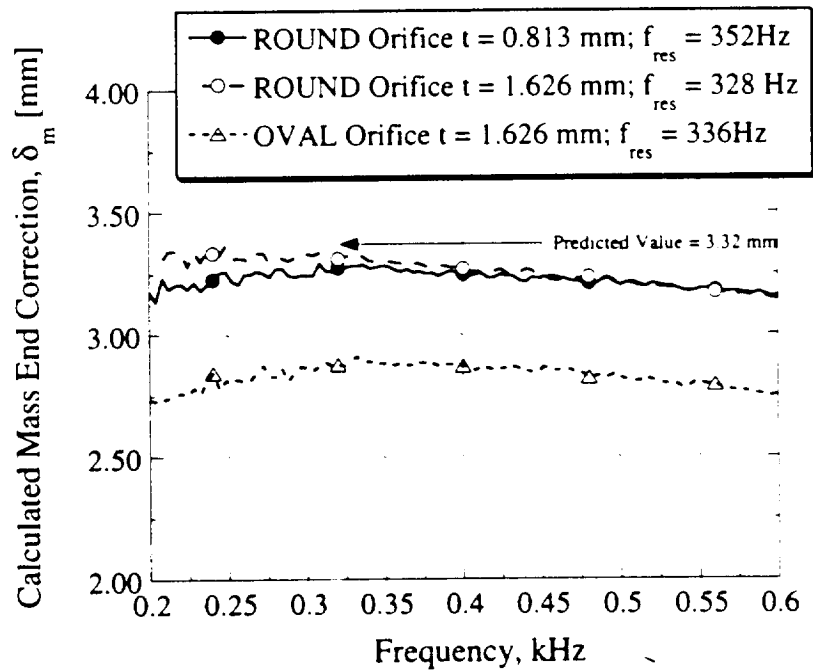
b. End-Correction

Figure 5.7 Attached mass and mass end correction comparison between stepped
-oval orifice and circular orifice; Broadband input [OASPL$_i$ = 157 dB; A$_o$ = 19.36 mm^2.
Δf = 4 Hz; 64 avgs.]
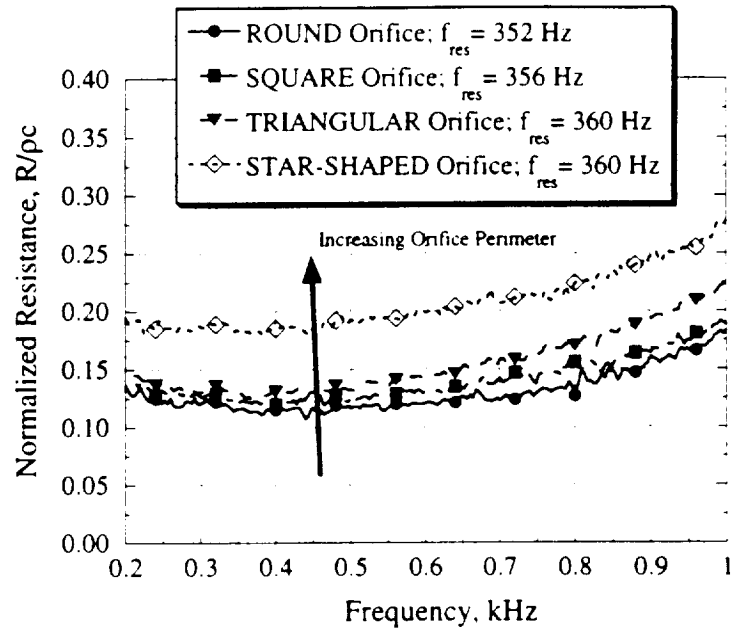
a. Normalized Resistance
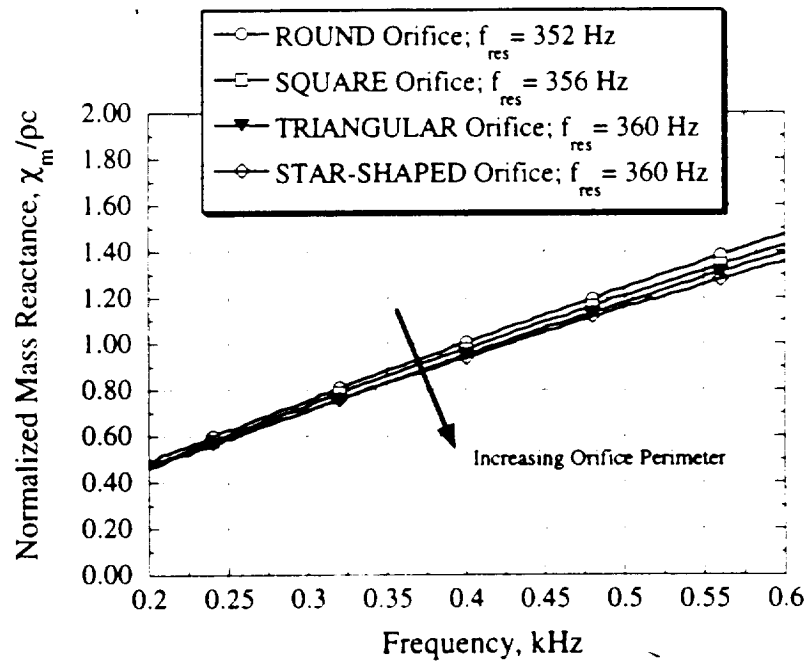
b. Normalized Mass Reactance

Figure 5.8 Effect of orifice shape on normalized orifice impedance; Broadband input [$OASPL_i$ = 157 dB; A_o = 19.36 mm^2; Δf = 4 Hz; 64 avgs.]
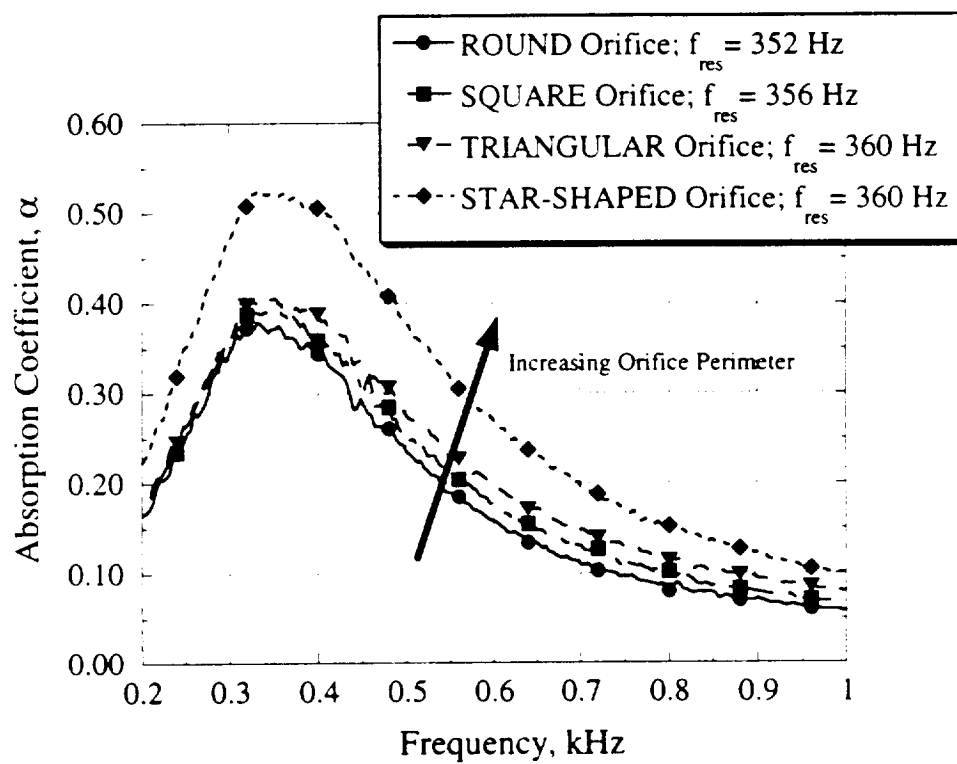
Figure 5.9 Effect of orifice shape on absorption coefficient for cavity-backed orifice.

Broadband input [OASPL$_i$ = 157 dB; A$_o$ = 19.36 mm^2; Δf = 4 Hz; 64 avgs.]
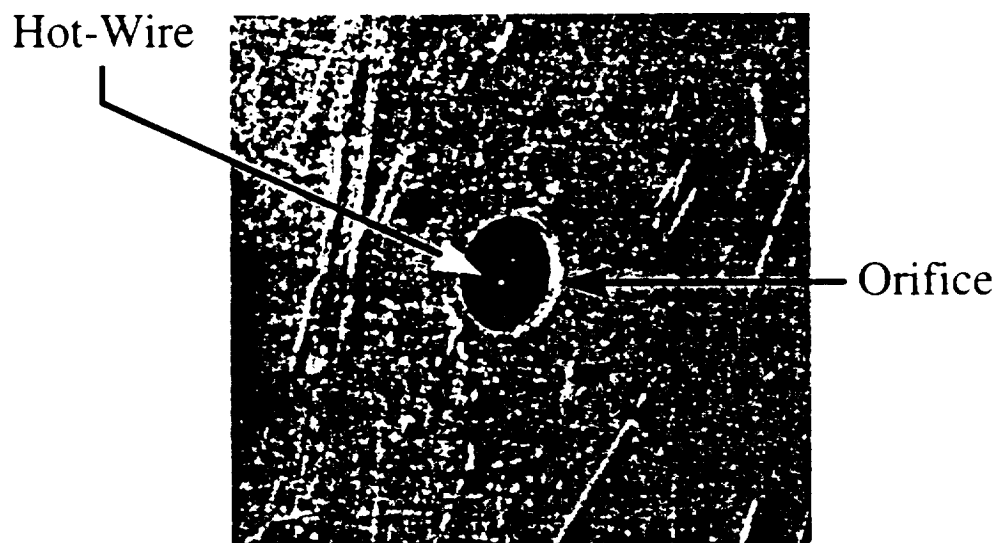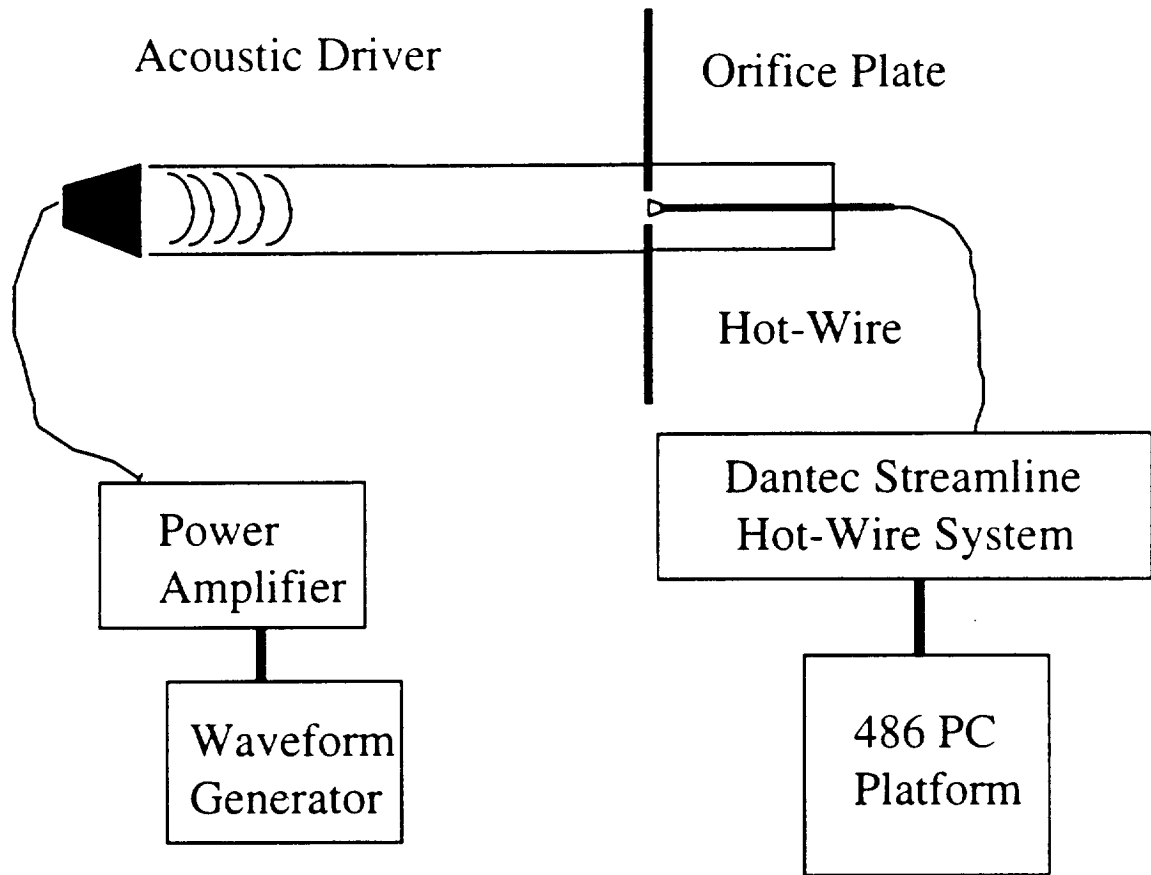
Figure 5.10 Hot-wire/orifice velocity measurement experimental arrangement
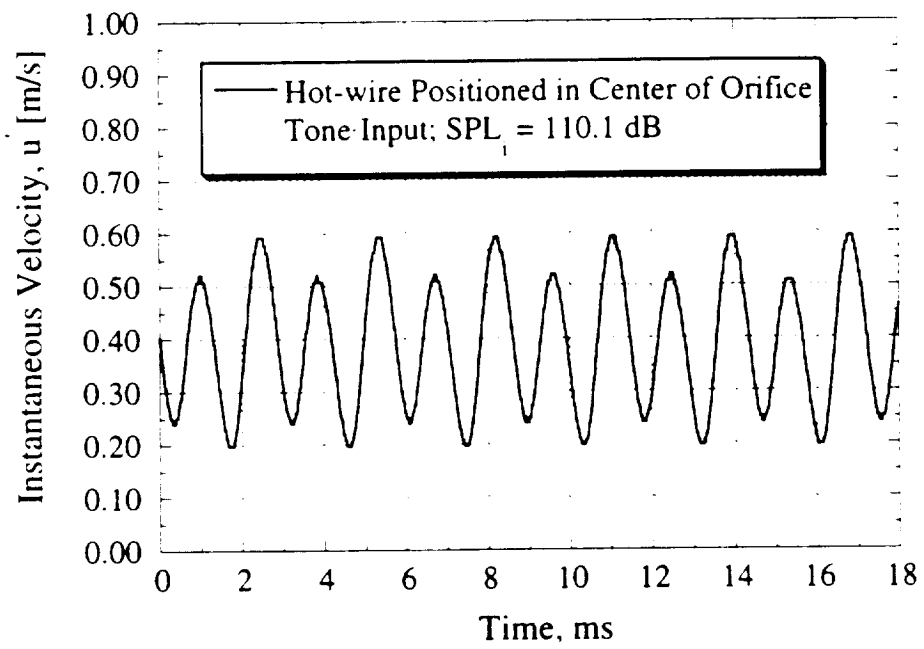
Figure 5.11 Time history of instantaneous velocity measured by hot-wire in center of circular orifice [SPL_i = 110.1 dB: Sampling frequency = 55 kHz: 1024 samples]
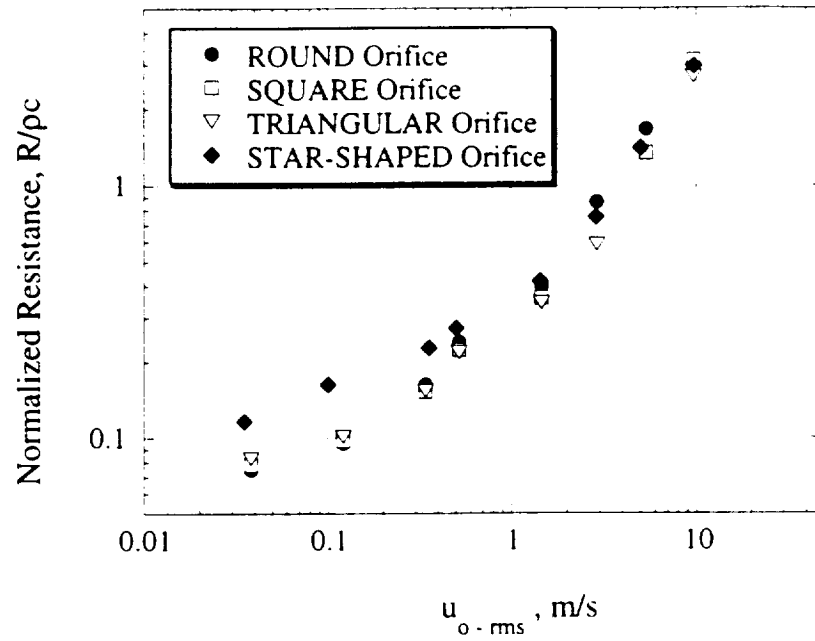
a. Normalized resistance
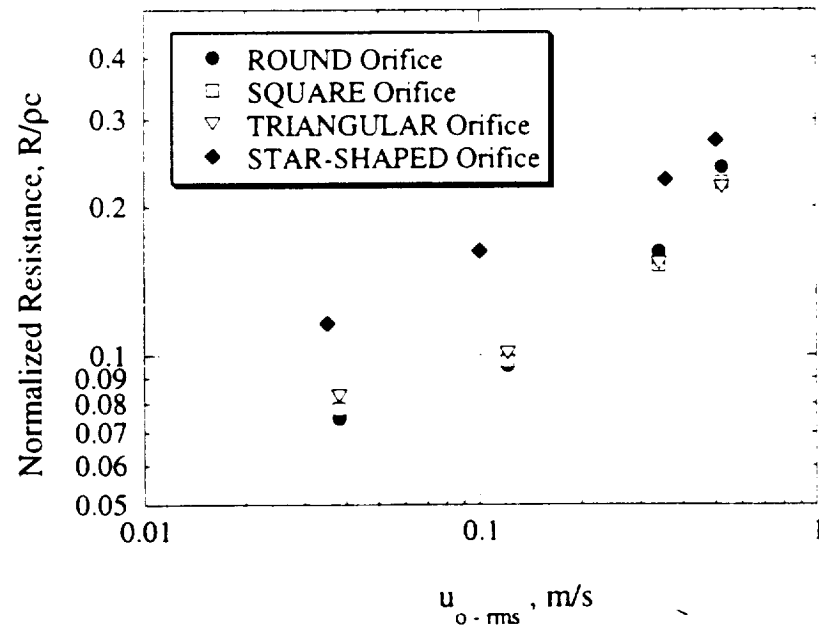
b. Normalized resistance at lower amplitudes

Figure 5.12 Effect of orifice shape on normalized resistance: Single tone input [Δf = 4 Hz; 64 avgs.].

159
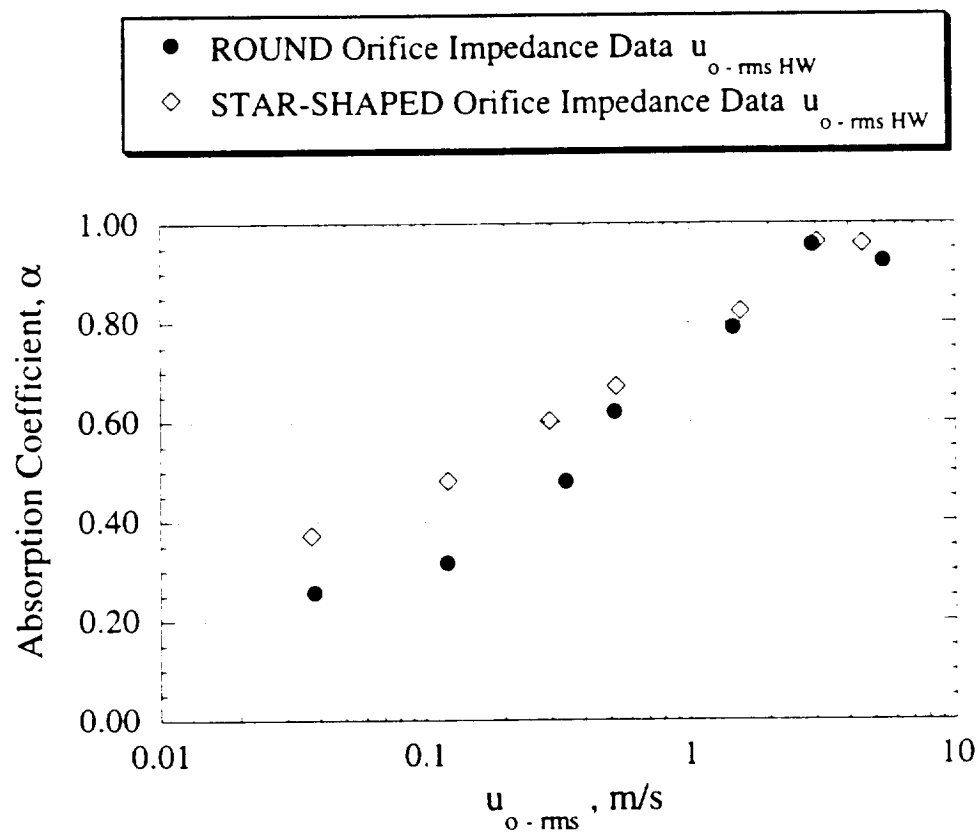
Figure 5.13 Effect on absorption coefficient for extremes in tested orifice shapes:
Single tone input [Δf = 4 Hz; 64 avgs.].
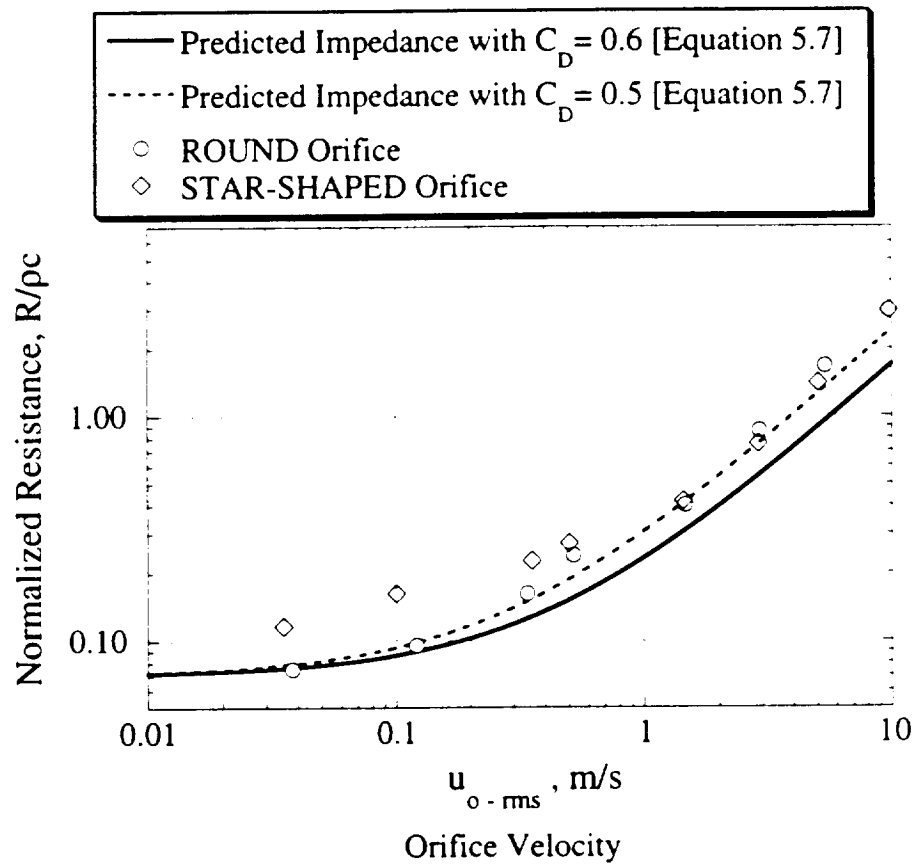
Figure 5.14 Comparison of measured normalized resistance with predicted resistance at high incident sound pressure levels: Single tone input [$\Delta f = 4$ Hz; 64 avgs.].

f = 120 Hz; 0.58 V

f = 120 Hz; 0.58 V
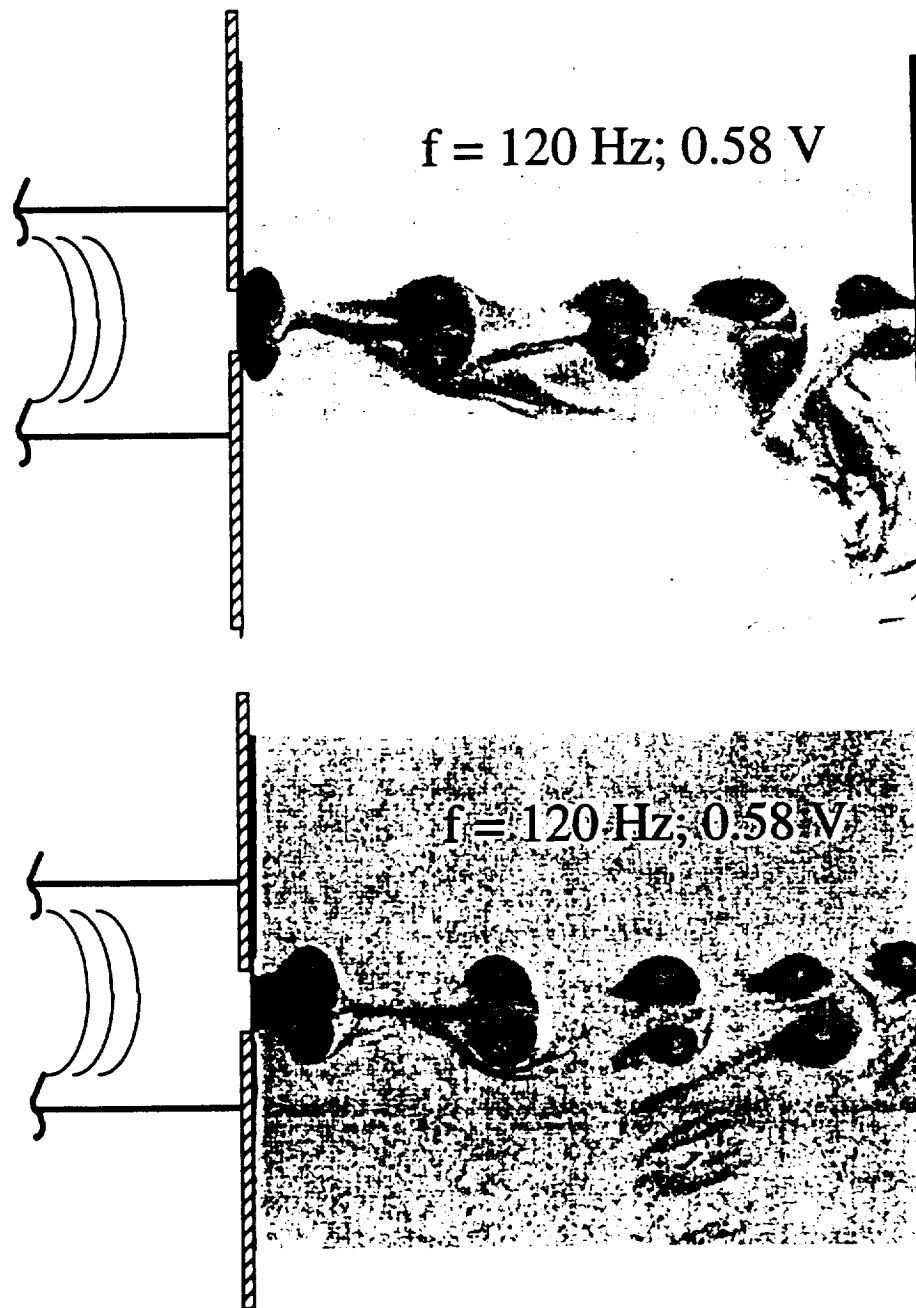
Circular Orifice

Figure 5.15   Flow visualization of orifice "jetting" for circular orifice at moderate sound pressure level using PIV image; Two arbitrary time snapshots shown [f = 120 Hz; Driver voltage = 0.58 V]

f = 120 Hz; 0.58 V

f = 120 Hz; 0.58 V
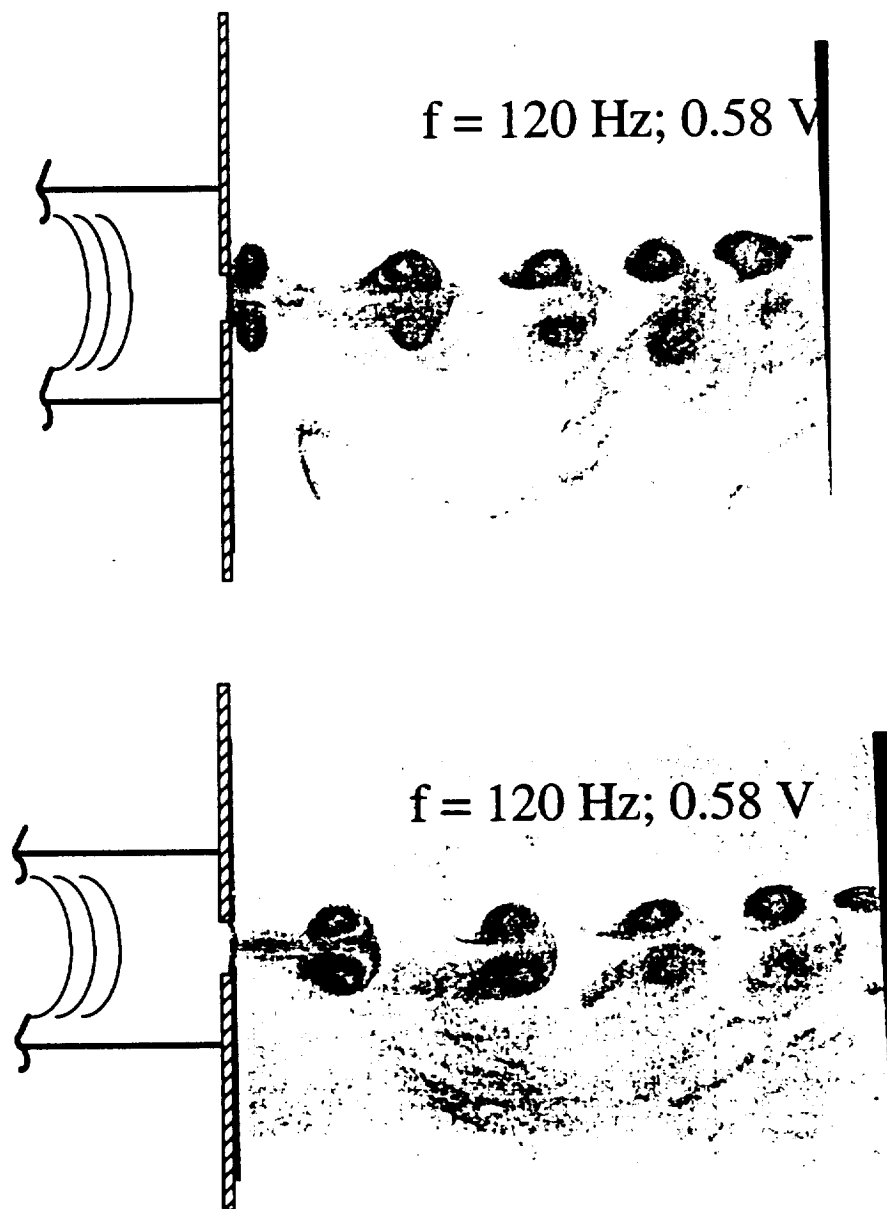
Star-Shaped Orifice

Figure 5.16 Flow visualization of orifice "jetting" for star-shaped orifice at moderate
sound pressure level using PIV image; Two arbitrary time snapshots shown
[f = 120 Hz; Driver voltage = 0.58 V]

f = 120 Hz; 0.58 V

f = 120 Hz; 0.58 V

Stepped Oval Orifice
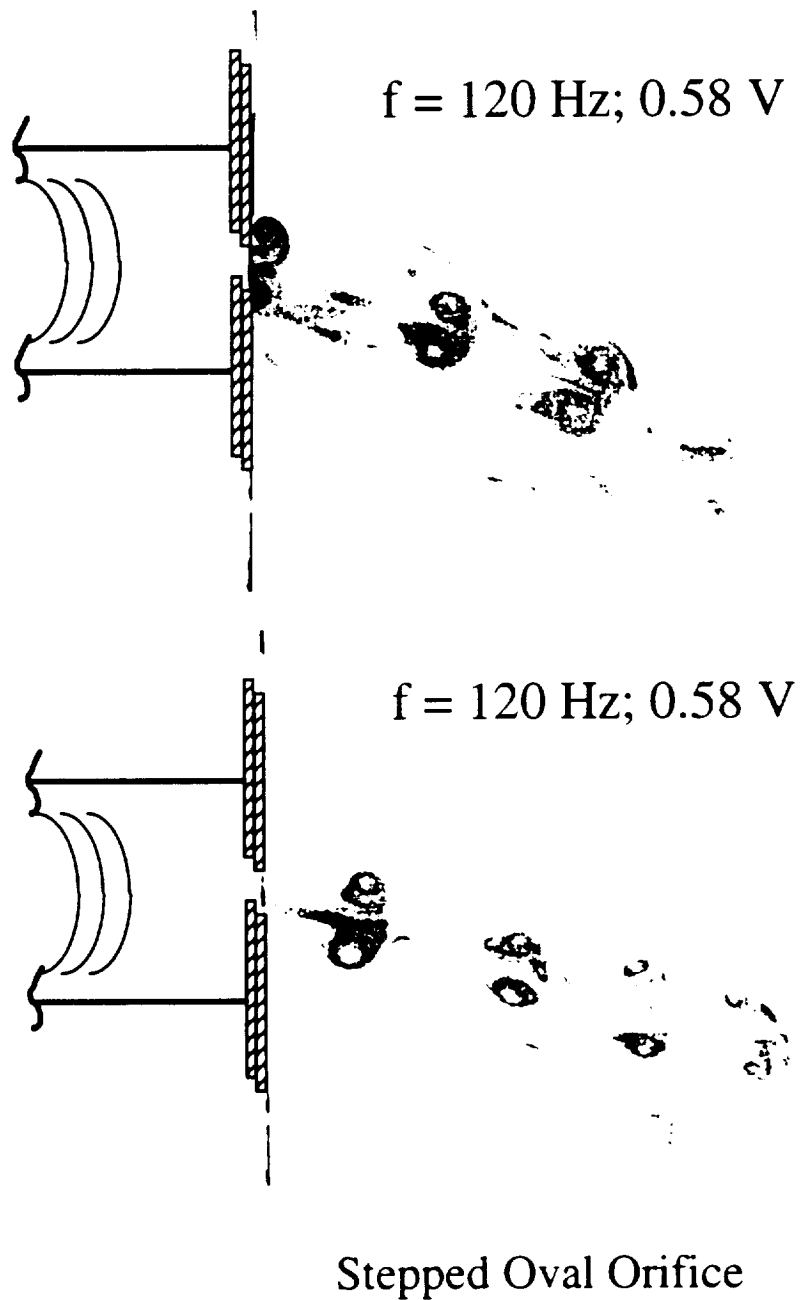
Figure 5.17   Flow visualization of orifice "jetting" for stepped-oval orifice at moderate
sound pressure level using PIV image; Two arbitrary time snapshots shown
[f = 120 Hz; Driver voltage = 0.58 V]

SECTION VI

Summary of Major Findings
and Recommendations of Future Work

6.1   Summary of Major Findings

The present work explored the feasibility of controlling the acoustic impedance of a resonant type acoustic liner. This was accomplished by translating one perforate over another of the same porosity creating a totally new perforate that had an intermediate porosity. This type of adjustable perforate created a variable orifice perforate, whose orifices were non-circular. The degree of translation needed for a porosity change of up to 20% was on the order of one orifice diameter. Larger changes in porosity can be realized by choosing perforates with larger initial porosity but smaller diameter orifices. Two, controllable, two-degree-of-freedom (2DOF) liners were built and tested: one in a normal incidence impedance tube and another in a flow-duct. Furthermore, a variable orifice perforate was constructed for testing in an impedance tube for examination of its low and high incident sound level behavior. Finally, the effect of shape of an orifice was considered by testing orifices of equal area but different edge geometry in an impedance tube.

The key findings of the present work can be summarized as follows:

I)   A more or less conventional 2DOF liner can be fabricated in such a manner as to control its absorption via small mechanical movements (on the order of existing orifice diameters). Both the frequency and magnitude of absorption can be controlled.

II)   Peak absorption frequency and magnitude can be controlled under grazing flow conditions in a flow-duct. Control of the buried septum impedance of the 2DOF liner led to the relative insensitivity of the peak absorption frequency to grazing flow effects on the liner as the septum porosity was decreased.

III)   The unique method of creating a variable orifice perforate resulted in a reduction of attached mass typically associated with circular orifices. This tends to limit the control of the resonance frequency of a perforate backing cavity based acoustic liner.

Details of more specific findings are discussed below:

Normal Incidence Resonance Frequency Control of Tunable 2DOF Liner

165

Using the variable orifice perforate as the buried septum, a two-degree-of-freedom liner was built for testing in a normal incident impedance tube. A range of buried septum porosities were tested and the following conclusions were drawn:

1) For no flow and for normal incidence, the liner was observed to shift the primary resonance frequency approximately 14% (200 Hz) and the secondary resonance approximately 16% (800 Hz).

2) A translational movement of less than one orifice diameter in the buried septum had a strong impact on the normalized resistance. At certain frequencies the septum resistance increased by an order of magnitude. Furthermore, the resistance increase was noticed across a frequency range of several hundred Hertz around the resonance frequency. The increased normalized resistance is due to the reduced septum porosity and the associated increase in septum nonlinearity.

3) A complete closure (i.e., zero porosity) of the buried septum, resulted in the 2DOF liner becoming a 1DOF liner. This has the potential for a large change in the primary resonance frequency of the liner to cover a large source frequency change.

Grazing Flow/Grazing Incidence Sound Absorption of Tunable 2DOF Liner
A variable buried septum 2DOF liner suitable for testing in a flow-duct environment was fabricated. Tests were made on the absorption control it provided in a grazing flow, duct environment. Measurement of both transmission loss and insertion loss were made and the following conclusions were drawn:

1) Transmission loss measurements in the presence of grazing flow revealed that for the tested liner, the primary resonant frequency could be shifted by approximately 100 Hz. This resulted from an approximately 1.5 mm movement of a perforate in the buried septum of the liner.

2) Control of the buried septum impedance was able to overcome the increased face sheet impedance due to the grazing flow. The primary resonance frequency became insensitive to the grazing flow velocity as the buried septum porosity was decreased. This indicates that the buried septum resistance became the controlling resistance for the liner.

3) Insertion loss measurements confirm the shift in primary resonance frequency but also show a shift in the secondary resonance frequency. Furthermore, as the buried septum porosity was reduced, an increase in liner absorption was observed over a broad frequency range indicating increased broadband sound absorption. This is indicative of the increase in broadband resistance demonstrated in the normal impedance measurements.

Normal Incidence Absorption of the Variable Orifice Perforate Concept
The uniqueness of the variable perforate orifice size and shape was tested at low and high incident sound amplitude levels and compared with standard impedance levels. The following conclusions were drawn:

166

1)   Control of a perforate's resistance can be achieved to a great degree with mechanical movements on the order of an orifice diameter. A perforate resistance increase of more than an order of magnitude was observed over a broad frequency range.

2)   The resonance frequency of a cavity covered with a variable orifice perforate can be controlled by changing the mass reactance. The 1st resonance frequency of the tested cavity resonator can be changed by approximately 21% with a mechanical movement of less than an orifice diameter.

3)   The standard linear impedance model over-predicts the mass reactance of the variable orifice perforate, suggesting that the unique orifice construction of the variable orifice perforate partially contributes to a lower mass reactance.

Effect of Orifice Shape on Impedance
In light of the variable orifice perforate impedance data, an examination of the effect of orifice shape and, in particular, the orifice geometry provided by sliding one perforate over another was performed by testing several orifices of different shapes in a normal incidence impedance tube. The following conclusions were drawn:

1)   The unique stepped-oval cross sectional shape of the variable orifice perforate concept results in a smaller attached mass, or end correction, than a round orifice with the same thickness.

2)   At low to moderate sound pressure levels, orifices with shapes that deviate significantly from circular (e.g., star shaped) but with the same area, exhibit increased resistance and hence absorption. A tested cavity-backed star-shaped orifice had an increased peak absorption coefficient by a factor of approximately 1.4 with a perimeter that was almost 2.5 times larger than an equivalent area circular orifice.

3)   At higher incident sound pressure levels, the orifice shape does not significantly alter the impedance.

6.2   Future Research Directions
The present work has led to some unanswered questions that can be the basis for future research.

These are summarized below:

1)   Impact of large scale structures in the oscillatory flow through an orifice on the In-situ impedance measurement technique.
The flow-visualization photographs reveal that large scale structures resulting from the oscillatory flow through the orifice persist for several orifice diameters downstream. At moderate to high incident sound amplitudes, the persistence of the large-scale structure can possibly impinge on the back wall of the cavity, thus affecting the back-wall acoustic measurement which are needed in *in-situ* impedance measurement techniques. The effect of these hydrodynamic fluctuations on the acoustic fluctuations needs to be studied further to examine any erroneous impact on the impedance determination.

2)   High Amplitude Behavior of Orifice Impedance

It was observed in Section IV that at very high incident sound pressure levels (above 145-150 dB). the reactance of the perforate/cavity combination and thus the perforate mass reactance itself began to rise instead of continuing the usually observed trend of reduction. No explanations could be offered for this behavior and needs to be understood.

3)   It was found that the commonly used expression (equation 4.10. repeated below) that computes the orifice velocity via measured impedance. did not match the rms velocities measured by a hot-wire anemometer.

$$u_{o-rms} = \frac{2|P_{i-rms}|}{\sigma\rho c \sqrt{\left(\frac{R}{\rho c}+1\right)^2 + \left(\frac{\chi}{\rho c}\right)^2}}$$ (4.8)

This expression is commonly used for circular orifices. One key assumption in the derivation of this equation is that the propagating acoustic wave is planar and hence the particle velocity across the orifice is also planar. At high incident sound amplitudes. the orifice jetting becomes quite strong and the jet mixing just downstream of the orifice quite likely contributes to the violation of the plane wave assumption. Furthermore. a non-circular orifice shape could create an even more asymmetric velocity profile. thus causing the computed orifice velocity from equation 4.10 to be in error. Further work is needed to derive an expression for the orifice velocity for use in high amplitude cases as well as for orifices that are non-circular.

4)   Use of highly convoluted orifices shapes in conjunction with the variable orifice perforate concept

The present study examined only the stepped-oval shape produced by the sliding two circular orifices over each other. It was also shown that an orifice shape that had a very convoluted shape. like a star. produce higher resistance and absorption in the low to moderate incident sound pressure levels. Further work could concentrate on a variable orifice perforate made up of very different shapes to further improve the absorption characteristics.

5)   Use of the Tunable Liner in conjunction with Bias-flow

The concept of bias-flow as a liner control concept mentioned in Section II requires a nonlinear buried septum to enhance its control. The variable orifice perforate can possibly be used to enhance the bias-flow concept by reducing the amount of steady flow needed through the perforate to control the impedance.

6)   Effect of "Vectored" Jetting on Orifice Impedance

It was observed that the stepped oval orifice produced by overlapping of two circular orifices resulted in an orifice oscillatory flow that was skewed off the orifice centerline. In essence. it appeared to be "vectored" towards the side of the orifice that was recessed. A detailed study on how this affects the radiation impedance of the orifice and thus the attached mass would further help understand the liner absorption control mechanism in the sliding perforate concept examined in this study.

7) *Development of practical implementation of variable orifice perforate in a non-straight wall environment*

It was demonstrated in this work that control of sound absorption can be accomplished by translating one perforate over another perforate over a flat planar surface. In a jet engine (and in many other applications) the perforated sections of a liner are tubular. Translation of one perforate over another would most likely involve rotating a cylindrical perforate inside another cylindrical perforate. A practical and innovative way to implement the mechanical movement of these perforates is needed for applications that do not involve the movement of just planar perforates.

6) *Non-aerospace applications of tunable liner*

While the primary motivation for this work was centered on acoustic liners that are used as part of a jet engine's noise suppression system, there are many other applications where this concept can be applied. Future development of the type of tunable liner described in this work can be pursued in the area of small internal combustion engines that, depending upon their operation, change their firing frequencies. This changes the noise source frequency content and a liner that can change its peak absorption frequency could optimize the noise suppression. Exhaust mufflers for automobiles and motorcycles fall in this category as well. Other applications could be hair dryers, air-conditioning systems and other more common appliances.

References

Section I

1.1   Mangiarotty, R.A. *Acoustic-Lining Concepts and Materials for Engine Ducts* Journal of the Acoustical Society of America Vol. 48, No. 3 (3) 1970.

Section II

2.1   Bechert, D. W. Sound Absorption Caused by Vorticity Shedding, Demonstrated with a Jet Flow Journal of Sound and Vibration, Vol. 70, No. 3, 1980.

2.2   Howe, M. S. *The Dissipation of Sound at an Edge* Journal of Sound and Vibration, Vol. 70, No. 3, 1980.

2.3   Kinsler, L.E., Frey, A.R., et al. *Fundamentals of Acoustics* 3rd Edition, John Wiley & Sons, New York 1982.

2.4   Melling, T. *The Acoustic Impedance of Perforates at Medium and High Sound Pressure Levels* Journal of Sound and Vibration, Vol. 29, No. 1., 1973.

2.5   Guess, A. W. *Calculation of Perforated Plate Liner Parameters from Specified Acoustic Resistance and Reactance* Journal of Sound and Vibration, Vol. 40 No. 1, 1975.

2.6   Maa, Dah-You *Microperforated-Panel Wideband Absorbers* Noise Control Engineering Journal, Vol. 29, No. 3 1987.

2.7   Ingard, U. *Notes on Sound Absorption Technology* Published by U. Ingard, 1994.

2.8   Sivian, L. J. *Acoustic Impedance of Small Orifices* Journal of the Acoustical Society of America, Vol. 7, pg. 94-101, 1935.

2.9   Ingard, U. *On the Theory and Design of Acoustic Resonators* Journal of the Acoustical Society of America, Vol. 25, No. 6, November, 1953.

2.10   Ingard, U. *Notes on Sound Absorption Technology* Published by U. Ingard, 1994.

2.11   Chanaud, R. *Effects of Geometry on the Resonance Frequency of Helmholtz Resonators* Journal of Sound and Vibration, Vol. 178 No. 3, 1994.

2.12   Ingard, U. and Labate, S. *Acoustic Circulation Effects and the Nonlinear Impedance of Orifices* Journal of the Acoustical Society of America, Vol. 22, No. 2, March 1950.

2.13   Ingard, U. and Ising, H. *Acoustic Nonlinearity of an Orifice* Journal of the Acoustical Society of America, Vol. 42, No. 1, 1967.

2.14   Zinn, B. T. *A Theoretical Study of Nonlinear Damping by Helmholtz Resonators* Journal of Sound and Vibration, Vol. 13, No. 3, 1970.

2.15   Hersh, A. and Rogers, T. *Fluid Mechanical Model of the Acoustic Impedance of Small Orifices* AIAA Paper 75-495, Presented at the 2nd Aeroacoustics Conference, Hampton, Virginia March 24-26, 1975.

2.16   Cummings, A. *Acoustic Nonlinearities and Power Losses at Orifices* AIAA Journal, Vol. 22, No. 6, June 1984.

2.17   Salikuddin, M. and Brown, W. H. *Nonlinear Effects in Finite Amplitude Wave Propagation Through Orifice Plate and Perforated Plate Terminations* Journal of Sound and Vibrations, Vol. 139 No. 3, 1990.

2.18   Prasad, M. G. *Acoustical Studies on Louver-Type Orifices* Noise-con 83 Proceedings, 1983.

2.19   Bies, D. and Wilson, O. B. *Acoustic Impedance of a Helmholtz Resonator at Very High Amplitude* Journal of the Acoustical Society of America, Volume 29, No. 6 June, 1957.

2.20   Thurston, G., Hargrove, L. and Cook, B. *Nonlinear Properties of Circular Orifices* Journal of the Acoustical Society of America, Vol. 29, No. 9, September, 1957.

2.21   Bean, H. S. ed. *Fluid Meters – Their Theory and Application* Report of ASME Research Committee on Fluid Meters, 6th edition, 1971.

2.22   Alvi, S.H. *Contraction Coefficient of Pipe Orifices* Proceedings of FLOMEKO 1983, IMEKO Conference on Flow Measurement, Budepest, Hungary Sept. 1983.

2.23   Howe, M. S. *On the Theory of Unsteady High Reynolds Number Flow through a Circular Aperture* Proceedings of the Royal Society of London, A. 366 Great Britain, 1975.

2.24   Salikuddin, M. and Ahuja, K. *Acoustic Power Dissipation on Radiation through Duct Terminations: Experiments* Journal of Sound and Vibration, Vol. 91, 1983.

2.25   Cummings, A. and Eversman, W. *High Amplitude Acoustic Transmission through Duct Terminations: Theory* Journal of Sound and Vibration, Vol. 91, 1983.

2.26   Bolt, R.H., Labate, S. and Ingard, U. *The Acoustic Reactance of Small Circular Orifices* Journal of the Acoustical Society of America Volume 21 No. 2, 1949.

2.27   Hersh, A. and Walker, B. *Acoustic Behavior of Helmholtz Resonators: Part I Nonlinear Model* CEAS/AIAA Paper No. 95-078, , Presented at the 16th Aeroacoustics Conference, Munich, Germany, 1995.

2.28   Meyer, E., Mechel, F. and Kurtze, G. *Experiments on the influence of the Flow on Sound Attenuation in Absorbing Ducts* Journal of the Acoustical Society of America, Vol. 30, No. 3, March 1958.

2.29   Feder, E. and Dean, L. W. *Analytical and Experimental Studies for Predicting Noise Attenuation in Acoustically Treated Ducts for Turbofan Engines* NASA Contractor Report CR-1373 September, 1969.

2.30   Dean, P. D. *An In-Situ Method of Wall Acoustic Impedance Measurement in Flow Ducts* Journal of Sound and Vibration, No. 34 (1), pg 97-130, 1974.

2.31   Baumeister, K. and Rice, E. *Flow Visualization in Long Neck Helmholtz Resonators with Grazing Flow* NASA Technical Memorandum TMX-73400, 1976.

2.32   Rogers, T. and Hersh, A. *The Effect of Grazing Flow on the Steady State Resistance of Square-Edged Orifices* AIAA Paper 75-493   2nd AIAA Aeroacoustics Conference, Hampton, VA, March 24-26, 1975.

2.33   Rao, K., and Munjal, M. *Experimental Evaluation of Impedance of Perforates with Grazing Flow* Journal of Sound and Vibration, Vol. 108, No. 2, 1986.

2.34   Hersh, A. and Walker, B. *Acoustic Behavior of Helmholtz Resonators, Part II: Effects of Grazing Flow* CEAS/AIAA Paper 95-079, Presented at the 16th Aeroacoustics Conference, Munich, Germany, 1995.

2.35   Kraft, R. E. *Theory and Measurement of Acoustic Wave Propagation in Multi-Segmented Rectangular Flow Ducts* PhD Thesis, University of Cincinnati, 1976.

2.36   Jones, M. and Parrott, T. *Enhanced Broadband Absorption for Duct Liners by Means of Spatially Varying Impedances* Proceedings of Noise-Con 93, Williamsburg, VA, May 2-5, 1993.

2.37   Arcas, N. and Parente, C. *Acoustic Liner* United States Patent #5,014,815 May, 14, 1991.

2.38   Wirt, L. S. *Analysis, Testing, and Design of Lined Ducts* Journal of the Acoustical Society of America Vol. 51, Number 5 (Part 1), 1972.

2.39   Shenoda, F. B. *A Multi-Degree of Freedom Acoustic Lining for Noise Suppression in Broad Air Ducts* Sadhand, Vol. 9, Part 4, December, 1986, pp 271-280.

2.40   Shenoda, F.B., Haroun, R. N., and Selim, H. *A Study on a New Silencer Symmetrically Lined with Variable Flow Resistance* Acustica, Vol. 64, 1987.

2.41   Snyder, S. *Sound Attenuating Laminate Installation for Jet Aircraft Engines* United States Patent # 4,947,958, August, 14, 1990.

172

2.42 Marc. F., Denis, T., and Marie-Annick, G. *Actively Enhanced Porous Layers for Free Field Acoustic Absorption* Presented at the Third International Conference on Intelligent Materials (Third European Conference on Smart Structures and Materials), Lyon, France June 3-5, 1996.

2.43 Guicking, D. and Lorenz, E. *An Active Sound Absorber with Porous Plate* Journal of Vibration, Acoustics, Stress, and Reliability in Design, Vol. 106, July, 1984.

2.44 Guicking, D. and Karcher, K. *Active Impedance Control for One-Dimensional Sound* Journal of Vibration, Acoustics, Stress, and Reliability in Design, Vol. 106, July, 1984.

2.45 Green, G. and Feder, E. *Sound Absorption with Variable Acoustic Resistance Means* United States Patent #3,991,849 November, 16, 1975.

2.46 Dean, P. D. & Tester, B. J. *Duct Wall Impedance Control as an Advanced Concept for Acoustic Suppression*, NASA Contractor Rept. CR-134998, Nov. 1975

2.47 Cataldi, P. , Ahuja, K. K., and Gaeta, R. J. NEED TITLE To be published at the 5th CEAS/AIAA Aeroacoustic Conference. Seattle, WA. 1999.

2.48 Harvey, J. *Multi-Layer Acoustic Linings* United States Patent # 4,410,065, October, 18, 1983.

Section III

3.1 Wirt, L. S. *Analysis, Testing, and Design of Lined Ducts* Journal of the Acoustical Society of America Vol. 51, Number 5 (Part 1), 1972.

3.2 Dean, P. D. & Tester, B. J. *Duct Wall Impedance Control as an Advanced Concept for Acoustic Suppression*, NASA Contractor Rept. CR-134998, Nov., 1975

3.3   Jones, M. and Parrott, T. *Enhanced Broadband Absorption for Duct Liners by Means of Spatially Varying Impedance*s Proceedings of Noise-Con 93, Williamsburg, VA. May 2-5, 1993.

3.4 Guicking, D. and Lorenz, E. *An Active Sound Absorber with Porous Plate* Journal of Vibration, Acoustics, Stress, and Reliability in Design, Vol. 106, July, 1984.

3.5   Marc, F., Denis, T., and Marie-Annick, G. *Actively Enhanced Porous Layers for Free Field Acoustic Absorption* Presented at the Third International Conference on Intelligent Materials (Third European Conference on Smart Structures and Materials), Lyon, France June 3-5, 1996.

3.6 Mangiarotty, R. A. *Acoustic Lining Concepts and Materials for Engine Ducts* Journal of the Acoustic Society of America, Volume 48, No. 3 (Part 3) , 1970.

3.7 Nayfeh, A. H., Kaiser, J. E. and Telionis, D. P. *Acoustics of Aircraft Engine-Duct Systems* AIAA Journal, Volume 13, No. 2, February, 1975.

3.8   Vaidya, P. G. and Dean, P. D. *State of the Art of Duct Acoustics* AIAA paper No. 77-1279 presented at the 4th AIAA Aeroacoustics Conference, Atlanta, GA, Oct., 1977.

3.9   Bell, W. A., Daniel, B. R. and Zinn, B. T. *Acoustic Liner Performance in the Presence of a Mean flow and Three-Dimensional Wave Motion* AIAA Paper No. 74-61 presented at the 12th AIAA Aerospace Sciences Meeting, Washington, D.C., January, 1974.

3.10   Chung, J. Y. and Blaser, D. A. *Transfer Function Method of Measuring In-Duct Acoustic Properties: I. Theory* Journal of the Acoustic Society of America, Volume 68, No. 3, Sept., 1980.

3.11   Watson, W.R, Jones, M.G, Tanner, S.E. and Parrott, T.L. *Validation of a Numerical Method or Extracting Liner Impedance* AIAA Journal, Vol. 34, No. 3, March, 1996.

3.12   Motsinger, R. E. and Kraft, R. E.. *Design and Performance of Duct Acoustic Treatment* Aeroacoustics of Flight Vehicles, Section 14, Volume 2; Acoustic Society of America through the American Institute of Physics, NEED DATE.

3.13   Kinsler L., Frey, A., et al. *Fundementals of Acoustics* John Wiley & Sons, 3rd Edition, 1982.

3.14   Ahuja, K. K. and Gaeta, R. J. *A Unique Test Facility to Measure Liner Performance with a Summary of Initial Test Results* NASA Contractor Report: CR-201667, March, 1997.

3.15   Schlicting, H. *Boundary-Layer Theory* 7th Edition; McGraw Hill, New York, 1979.

3.16   Atvars, J. and Mangiarotty, R. A. *Parametric Studies of the Acoustic Behavior of Duct Lining Materials* Journal of the Acoustic Society of America, Volume 48, No. 3 (Part 3), 1970.

3.17   Feder, E. and Dean, L. W. *Analytical and Experimental Studies for Predicting Noise Attenuation in Acoustically Treated Ducts for Turbofan Engines*. NASA Contractor Report, CR-1373; September, 1969.

3.18   Melling, T. *The Acoustic Impedance of Perforates at Medium and High Sound Pressure Levels* Journal of Sound and Vibration, Vol. 29, No. 1., 1973.

Section IV

4.1   Mangiarotty, R.A. *Acoustic-Lining Concepts and Materials for Engine Ducts* Journal of the Acoustical Society of America Vol. 48, No. 3 (3) 1970.

4.2   Nayfeh, A. H. , Kaiser, J.E. and Telionis, D.P *Acoustics of Aircraft Engine-Duct Systems* AIAA Journal, Vol. 13, No. 2, Feb. 1975.

4.3   Vaidya, P.D. and Dean, P.D. *State of the Art of Duct Acoustics* AIAA Paper No. 77-1279, 4th AIAA Aeroacoustics Conference, Atlanta, GA, 1977.

4.4   Zinn, B. T. *A Theoretical Study of Nonlinear Damping by Helmholtz Resonators* Journal of Sound and Vibration, Vol. 13, No. 3, 1970.

4.5   Guess, A. W. *Calculation of Perforated Plate Liner Parameters from Specified Acoustic Resistance and Reactance* Journal of Sound and Vibration, Vol. 40 No. 1, 1975.

4.6   Motsinger, R.E. and Kraft, R.E. *Aeroacoustics of Flight Vehicles - Theory and Practice Volume 2: Noise Control* Section 14: Design and Performance of Duct Acoustic Treatment, Acoustical Society of America, 1991.

4.7   Kinsler, L.E., Frey, A.R., et al. *Fundamentals of Acoustics* 3rd Edition, John Wiley & Sons, New York 1982.

4.8   Ingard, U. *On the Theory and Design of Acoustic Resonators* Journal of the Acoustical Society of America, Vol. 25, No. 6, November, 1953.

4.9   Ingard, U. and Ising, H. *Acoustic Nonlinearity of an Orifice* Journal of the Acoustical Society of America, Vol. 42, No. 1, 1967.

4.10   Sivian, L. J. *Acoustic Impedance of Small Orifices* Journal of the Acoustical Society of America, Vol. 7, pg. 94-101, 1935.

4.11   Ingard, U. and Labate, S. *Acoustic Circulation Effects and the Nonlinear Impedance of Orifices* Journal of the Acoustical Society of America, Vol. 22, No. 2, March 1950.

4.12   Bies, D. and Wilson, O. B. *Acoustic Impedance of a Helmholtz Resonator at Very High Amplitude* Journal of the Acoustical Society of America, Volume 29, No. 6 June, 1957.

4.13   Melling, T. *The Acoustic Impedance of Perforates at Medium and High Sound Pressure Levels* Journal of Sound and Vibration, Vol. 29, No. 1., 1973.

Section V

5.1   Sivian, L. J. *Acoustic Impedance of Small Orifices* Journal of the Acoustical Society of America, Vol. 7, pg. 94-101, 1935.

5.2   Ingard, U. and Labate, S. *Acoustic Circulation Effects and the Nonlinear Impedance of Orifices* Journal of the Acoustical Society of America, Vol. 22, No. 2, March 1950.

5.3   Bies, D. and Wilson, O. B. *Acoustic Impedance of a Helmholtz Resonator at Very High Amplitude* Journal of the Acoustical Society of America, Volume 29, No. 6 June, 1957.

5.4   Ingard, U. and Ising, H. *Acoustic Nonlinearity of an Orifice* Journal of the Acoustical Society of America, Vol. 42, No. 1, 1967.

5.5 Melling, T. *The Acoustic Impedance of Perforates at Medium and High Sound Pressure Levels* Journal of Sound and Vibration. Vol. 29, No. 1., 1973.

5.6 Hersh, A. and Rogers, T. *Fluid Mechanical Model of the Acoustic Impedance of Small Orifices* AIAA Paper 75-495, Presented at the 2nd Aeroacoustics Conference. Hampton. Virginia March 24-26, 1975.

5.7 Lepicovsky, J., Ahuja, K. K., Brown, W. H., and Morris, P. J. *Acoustic Control of Free-Jet Mixing* Journal of Propulsion an Power, Vol. 2, 1986.

5.8 Lepicovsky, J., Ahuja, K. K., Brown, W. H., and Burrin, R. H *An Experimental Study of Tone Excited Jets* Journal of Propulsion an Power, Vol. 2, 1986.

5.9 Cummings, A. *Acoustic Nonlinearities and Power Losses at Orifices* AIAA Journal, Vol. 22, No. 6, June 1984.

5.10 Hersh, A. and Walker, B. *Acoustic Behavior of Helmholtz Resonators: Part I. Nonlinear Model* CEAS/AIAA Paper No. 95-078. Aeroacoustics Conference, 1995.

APPENDIX A

Normal Incidence Impedance Measurement
using a Two-Microphone Methodology

The normal incidence impedance presented in the current work was determined using a technique developed by Chung and Blaser[A1] and employed in the commercially available B&K 4206 impedance tube. The method for determining the normal incidence impedance is summarized in this Appendix.

Figure A.1 shows a normal incidence impedance tube with a sound source on one end and a sample of unknown impedance on the other. Two microphones are placed flush on the side of the tube separated by a distance, s. The first microphone is some distance, l, from the sample face. The impedance at the surface, commonly referred to as the input impedance, is the desired quantity. From this impedance, the absorption coefficient can be determined from equations presented in Chapter II.

The method uses the acoustic pressures from the wall two microphones to determine the complex reflection coefficient. When the tube is driven with a speaker on one end, a standing-wave pattern is set-up in the tube. The acoustic pressure at each point is the summation of the incident and reflected acoustic wave. The transfer function between two acoustic measurements separated by a distance s is defined as:

$$H_{12}(f) = \frac{S_{12}(f)}{S_{11}(f)} \qquad (A.1)$$

where $S_{12}(f)$ is the cross-spectral density between the signals at microphones 1 and 2 and $S_{11}(f)$ is the auto-spectral density of the signal at microphone 1.

From this definition, one can express the transfer functions between microphone 1 and 2, both for the incident and the reflected signals, as

$$H_i(f) = \frac{S_{i,2i}(f)}{S_{i,1i}(f)} \qquad (A2.a)$$

$$H_r(f) = \frac{S_{1r2r}(f)}{S_{1r1r}(f)} \qquad (A.2b)$$

Noting that the complex reflection coefficient at position 1 can be expressed as (see Chung and Blaser)

$$R_{f1}(f) = \frac{S_{1,2r}(f)}{S_{1,1i}(f)} \qquad (A2.c)$$

177

Equations A1 and A2a-c allow us to express the reflection coefficient as

$$R_{fl}(f) = [H_{12}(f) - H_i(f)]/[H_r(f) - H_{12}(f)] \quad (A.3)$$

Plane wave propagation, no mean flow, and no viscous losses,

$$H_i(f) = e^{-jks} \quad (A.4)$$
$$H_r(f) = e^{-jks} \quad (A.5)$$

Where, k, is the wave number and s is the microphone spacing.

Substituting A.4 and A.5 in A.3 yields:

$$R_{fl}(f) = \frac{e^{-iks} - H_{12}(f)}{H_{12}(f) - e^{+iks}} \quad (A.6)$$

This equation refers the phase values with respect to microphone location 1. To determine the reflection coefficient at the termination located a distance l from microphone 1, the reflected signal $P_{1r}(f)$ becomes $P_{1r}(f)e^{-jkl}$ the incident signal has a value of $P_{1i}(f)e^{-jkl}$ and the reflection coefficient at the termination takes the form:

$$R_{fl}(f) = \frac{P_{lr}}{P_{li}} = \frac{P_{1r}e^{+ikl}}{P_{1i}e^{-ikl}} = R_{f1}e^{i2kl} \quad (A.7)$$

$$= \left[\frac{e^{-iks} - H_{12}(f)}{H_{12}(f) - e^{+iks}}\right]e^{i2kl}$$

If the a *mean* flow is present, then the convective effects of the sound propagation are accounted for by recognizing that the incident pressure and reflected acoustic pressure can be expressed as:

$$P_{2i}(f) = P_{1i}(f)e^{-ik_i s} \quad (A.8a)$$

$$P_{2r}(f) = P_{1r}(f)e^{-ik_r s} \quad (A.8b)$$

Where the incident and reflected wave numbers are :

$$k_i = \frac{k}{1+M}; \quad k_r = \frac{k}{1-M} \quad (A.9a,b$$

Carrying through the analysis that led to equation A.7 leads to

178

$$R_{fl}(f) = \left[\frac{e^{-ik_i s} - H_{12}(f)}{H_{12}(f) - e^{+ik_r s}} \right] e^{i(k_r + k_i)l} \qquad (A.10)$$

Finally, for plane wave propagation, the normalized impedance at the sample face can be expressed in terms of the reflection coefficient as:

$$\frac{Z}{\rho c} = \frac{R_{fl}(f) + 1}{R_{fl}(f) - 1} \qquad (A.11)$$

Chung and Blaser expressed equation A.11 in terms of the measured transfer function for no mean flow as:

$$\frac{Z}{\rho c} = i \frac{H_{12}(f)\sin[kl] - \sin[k(l-s)]}{\cos[k(l-s)] - H_{12}(f)\cos[kl]} \qquad (A.12)$$

The acoustic transfer function between 1 and 2 were measured between microphones on the impedance tube walls.
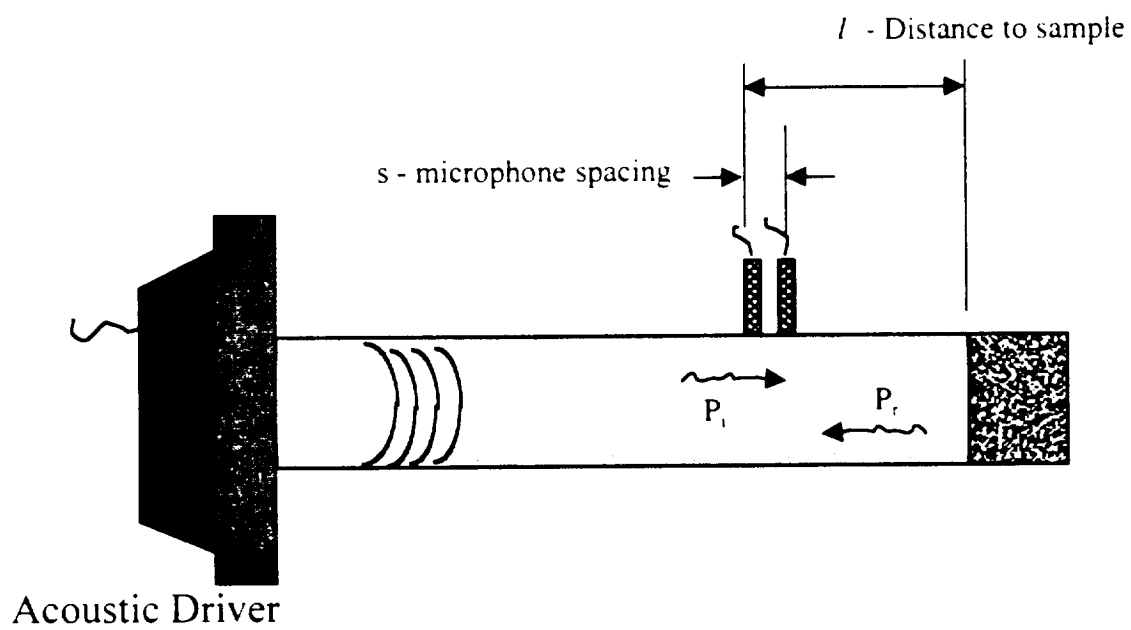
Figure A.1 Two Microphone impedance tube model.

Appendix B

Flow-Duct Transmission Loss Computation
using a Two-Microphone Methodology

Transmission loss is defined in the present work as the amount of acoustic energy that is extracted from an acoustic liner in a duct environment. Specifically, it is defined as the amount of acoustic energy that enters the lined section of the duct, subtracted by the energy that exits the lined section. In decibels, W_l, the transmission loss can be expressed as:

$$TL = 10 \log \left[\frac{W_{i \cdot \text{upstream of liner}}}{W_{i \cdot \text{downstream of liner}}} \right] \qquad (B.1)$$

The subscript, i, refers to the incident energy in the duct. The problem is reduced to the determination of the incident power upstream and downstream of an acoustic liner in a duct. Chung and Blaser[13] developed a technique that relies on the transfer function between acoustic pressures at two locations in a duct to determine the reflection coefficient at another point in the duct. This technique was summarized in Appendix A. With some modifications, the same technique was used in a flow-duct to determine the transmission loss with and without a mean flow present.

Figure B.1 shows the basic arrangement of acoustic measurements needed in a duct with an acoustic element somewhere along the duct wall. In the present study, many measurements were acquired along the duct centerline with a microphone equipped with a nose cone to minimize flow noise picked-up by the microphone. Instead of using two fixed microphones, the same microphone was used at different locations. Furthermore, the needed transfer function was acquired by using the acoustic signal input to the acoustic drivers as reference transfer function at each point. Figure B.2 shows a schematic of the signal processing concept. The equations developed in Appendix A are used in this analysis, using the mean flow expressions for the complex reflection coefficient.

The incident power in the upstream and downstream location can be found from (assuming plane wave propagation):

$$W_i = \frac{P_i A}{\rho c} \qquad (B.2)$$

Chung and Blaser relate the incident acoustic pressure at a point in the duct to the measured acoustic total pressure at the same point with reflection coefficient (or, in effect, the impedance at the point). This is shown below:

$$P_i = \frac{P_t}{|1 + R_{i}|^2} \qquad (B.3)$$

181

Where P_2 is the measured acoustic pressure at the second measurement location (see Figure B.1). So, based on measured acoustic pressures and reflection coefficient based on the transfer function between two points, the incident power can be obtained using equations B.2 and B.3 yielding:

$$W_i = \frac{P_2 A}{\rho c \left| 1 + R_{1,2} \right|^2}$$
(B.6)

Where A is the duct cross-sectional area.

Figure B.1 Application of Two-Microphone Method of transmission loss determination in a flow-duct.
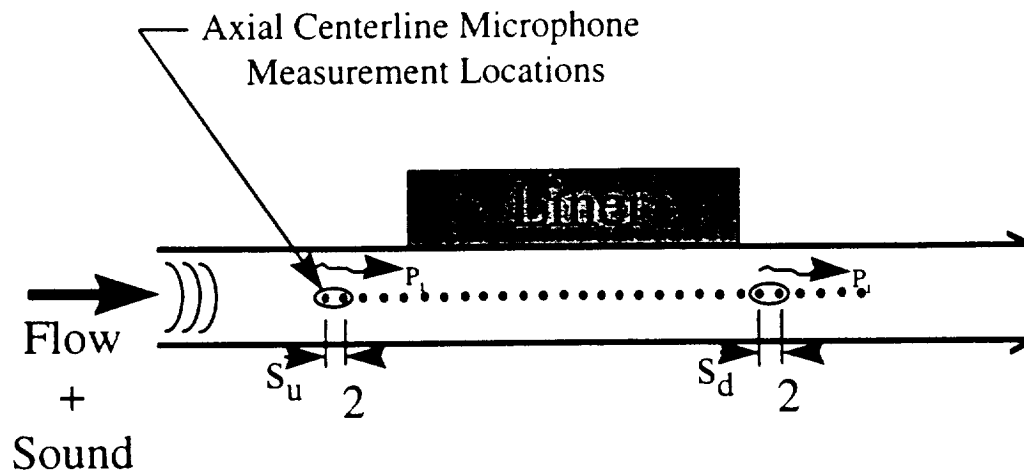
Any combination of 2 mics can be used to find W_i

$$W_i = \frac{S_2 A}{\rho c \left| 1 + R_f \right|^2}$$

$A =$ Cross Sectional Area

$R_f =$ Reflection Coefficient at 2

$S =$ Autopower Spectral Density at 2

Power Transmission Loss

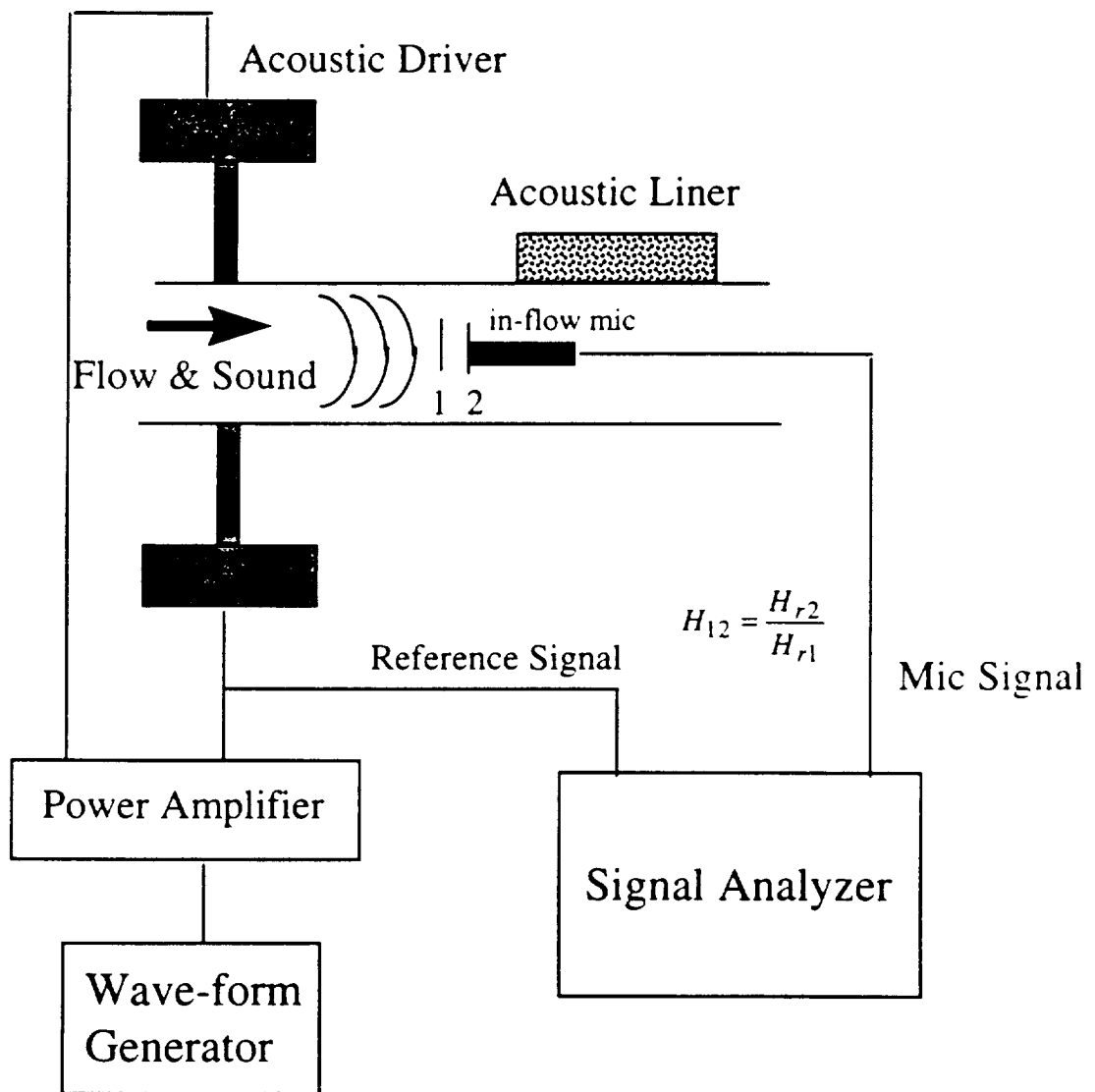$$PWTL = 10 \log \left(\frac{W_{i-upstream}}{W_{i-downstream}} \right)$$

Figure B.2 Signal processing schematic for TMM flow-duct transmission loss analysis

Appendix C

Measurement Uncertainty

C.1   Uncertainty in Acoustic Pressure Measurements

The magnitude of acoustic pressures that were used in the computation of impedance. insertion loss. and transmission loss were measured with condenser type microphones. These microphones were calibrated for a level of 114 dB at 1000 Hz amplitude using a B&K pistonphone. The calibrator was quoted to be accurate within 0.3 dB at a reference condition of 14.45 psi. 20 °C and a relative humidity of 65%. The conditions that the microphones were exposed to during all the tests conduct in this study ranged in ambient pressure from 14.1 to 14.2 psi. in temperature from 22.5 °C to 23.5 °C., and in relative humidity from approximately 53% to 58%. From these differences in the pistonphone reference conditions is was assumed that a standard error of 0.5 dB existed for all microphone pressure measurements. For all acoustic measurements. 64 averages were taken.

C.2   Uncertainty in Normal Incidence Impedance Measurements

The impedance measured in the impedance tube using the methodology summarized in Appendix A. uses equation A.12 reproduced as equation C.1 below:

$$\frac{Z}{\rho c} = i \frac{H_{12} \sin[kl] - \sin[k(l-s)]}{\cos[k(l-s)] - H_{12} \cos[kl]} \qquad (C.1)$$

The uncertainty in each input into equation C.1 is summarized below:

Uncertainty in Measured Distances in the Impedance Tube

The distances l and s. were measured with analog calipers whose divisions were 0.0254 mm (0.001 inches). Assuming that one could accurately read half this division. the measured values of l and s that were used for the impedance tube were 53.594 mm (2.110 inches) and 20.0152 mm (0.788 inches). respectively. Thus the accuracy of these values were thus estimated to be within 0.0127 mm (0.0005 inches). With all else constant in equation C.1. uncertainty in the values of s and l. result in changes in the impedance of less than 0.05%. It was considered that other errors (e.g.. the transfer function) were an order of magnitude greater than this. so the uncertainty in measured distances. s and l. were considered negligible.

Uncertainty in Wave number Calculation

The wave number is a function of the frequency and speed of sound. The frequency was set during all measurements with a digital waveform generator that had a quoted resolution of 5 decimal places. Thus the uncertainty in the frequency input even with a bandwidth of 4 Hz was considered negligible. The speed of sound depends on the square root of the temperature. The thermocouples used to measure the temperature were accurate to within 0.5 °C. This translates

into an uncertainty in the speed of sound of approximately 0.3 m/s for a nominal temperature of 22.6 °C. This uncertainty resulted in less than a 0.1% change in the impedance computed from equation C.1.

Uncertainty in the Estimations of Transfer Function

Estimation of the normalized random error associated with the transfer function measurements were obtained from Bendat and Piersol[1] where a more detailed analysis can be found. Only final results are summarized here. For the magnitude of the transfer function, the normalized random error can be expressed in terms of the coherence function as:

$$\varepsilon\left[\left|\hat{H}_{12}\right|\right] = \frac{\sqrt{1 - \hat{\gamma}_{12}^2}}{\left|\hat{\gamma}_{12}\right|\sqrt{2N}} \qquad (C.2)$$

where $\hat{\gamma}_{12}$ = Estimated Coherence Function

N = Number of Ensemble Averages

Note that the coherence function is also a function of frequency. If the random error in the transfer function above (equation C.2) is relatively small, then the uncertainty in the phase estimate is:

$$\Delta\hat{\phi}_{12} \approx \sin\left(\Delta\hat{\phi}_{12}\right) = \frac{r}{\left|\hat{H}_{12}\right|} \approx \varepsilon\left[\left|\hat{H}_{12}\right|\right] \qquad (C.3)$$

A value of 0.10 or less resulting from equation C.2 was considered relatively small. For a confidence interval of 95%, the uncertainty estimate for the magnitude and phase of the transfer function are:

$$\left|\hat{H}_{12}\right| \pm 2r = \left|\hat{H}_{12}\right|\left\{1 \pm 2\varepsilon\left[\hat{H}_{12}\right]\right\} \qquad (C.4a)$$

$$\hat{\phi}_{12} \pm 2\Delta\hat{\phi}_{12} = \hat{\phi}_{12} \pm 2\varepsilon\left[\hat{H}_{12}\right] \qquad (C.4b)$$

Where r is the radius of a circle in the complex plane that encompasses the true value of the transfer function.

For the normal incidence impedance tube measurements with a single tone input, the estimated coherence function for the tested frequencies were very close to unity. In fact the coherence function at the tested frequencies for the single tone inputs was never below a value of 0.9994. A typical example of uncertainty in the resulting impedance for this level of coherence was computed. For a 95% confidence interval:

$$\Delta\left|H_{12}\right| = \pm 0.0014 \qquad (C.5a$$

$$\Delta\phi_{12} = \pm 0.1013 \text{ degrees} \qquad (C.5b)$$

186

Substituting the worst case uncertainties from equation C.5 in equation C.1 produces an uncertainty of 0.6% in the measured value of normalized resistance and a 2.5% uncertainty in the measured value of reactance.

For broadband input. Figure C.1 shows a typical plot of the coherence function provided by the signal analyzer used in the present study. Except for a few low points, the coherence is very close to unity throughout the spectrum. Using the worst case uncertainties in equation C.1 and using the 95% confidence interval uncertainties defined by equations C.3 - C.5, an estimated error-bound was computed for a typical broadband excitation impedance measurement. Figure C.2 shows these results in a frequency span used in most of the data presented in this study, namely 0.2 kHz to 1.0 kHz. The error bounds for the other frequencies were similar. For the most part, the error estimate in the resistance and reactance is reasonably small compared to the measured values. The larger errors occur where the coherence levels are somewhat lower that 0.95. From Figure C.2b, it is evident that the determination of the resonance frequency (that frequency where the normalized reactance is zero) is not affected by the uncertainty. It is well within the bandwidth of analysis (4 Hz) and is much smaller than the resonance changes observed by the variable orifice perforate presented in the body of this work.

C.3   Uncertainty in Transmission Loss Measurements

Uncertainty in Transmission Loss

The transmission loss measurements relied on the two-microphone method developed to compute normal incidence impedance and described in Appendix B. The impedance measured in a plane in the flow-duct was converted into a reflection coefficient based on expressions developed in Chapter II as:

$$R_I = \frac{Z - 1}{Z + 1}$$

(C.6)

From the reflection coefficient. the incident power was computed from the equation:

$$W_I = \frac{P_2 A}{\rho c \left| 1 + R_{I2} \right|^2}$$

(C.7)

The quantity P_2 is the rms acoustic pressure measured at a point in the plane of interest and R_I is the reflection coefficient in the plane of interest, respectively. The uncertainty in the calculated incident power depends predominantly on the reflection coefficient. As with the impedance measurement discussed previously, the key source of uncertainty is based on the coherence function between the two microphone measurements used to compute the impedance.

In the case of the flow-duct transmission measurements, the flow noise contributed to reduction of the signal-to-noise ratio as well as in coherence level. This was most evident downstream of the acoustic liner because of the lowered speaker noise relative to the flow noise. Figure C.3a and C.3b show coherence levels upstream and downstream of the acoustic liner for mean flow-velocities of 45.7 m/s (150 ft/s) and 76.2 m/s (250 ft/s), respectively. Recall that

several tones at every 100 Hz was the input signal. thus the coherence at frequencies other than those input are meaningless.

Below a duct mean velocity of 45.7 m/s (150 ft/s). almost all coherence levels are above 0.99. For the worst case (i.e.. a mean-flow of 76.2 m/s) the lowest coherence levels are on the order of 0.6 at certain frequencies. Using the 95% confidence level estimates of equation C.4 and using the worst cases in equation C.1. which carried through to equation C.6 and C.7. the uncertainty in the incident power estimation downstream of the liner was maximum at approximately 3.1 dB. Upstream of the liner. due to the high coherence. the uncertainty in the incident power was on the order of 0.5 to 1.0 dB. Thus for the lowest coherence values (below 0.7) the uncertainty in the transmission loss is estimated to be approximately 4 dB.

Uncertainty in Measured Distances in the Flow-Duct

When the distances used in equation A.9 were input for use in determining the transmission loss in the flow-duct. a stepper-motor was used to traverse the microphone locations. The stepper motor used was capable of moving the microphone 200 steps/inch +/- 1 step. This translates into an accuracy of +/- 0.005 inches. This was considered negligible compared to the error due to the transfer function estimates.

C.4 Hot-Wire Calibration and Measurements

The hot-wire anemometer uncertainty was estimated using procedures outlined by Yavuzkurt[C2]. The hot-wire system used for flow-duct and orifice velocity measurements was the Dantec Streamline System that was used with an automated flow calibrator unit which Dantec provided. The flow calibration unit provides a steady. metered. clean flow in which a hot wire can be placed.

A constant temperature. single platinum-plated tungsten wire was used for the measurements. This wire was 1.25 mm in length and 5 micro-meters in diameter. The user can specify the velocity range and the number of points desired to produce a voltage-to-velocity calibration curve. The flow calibration unit has several different test nozzles that provide different known velocity ranges. The range of velocities that can be calibrated are from 0.02 m/s to 345 m s depending on the nozzle chosen. The flow calibration unit specifications indicate that the flow is accurate to within 0.3% of the specified velocity. Therefore the calibration uncertainty is:

$$\frac{\Delta U_{cal}}{U} = 0.003$$

A flow range of 0.02 m/s to 100 m/s was used to calibrate the hot-wire using three different flow nozzles. The 5th order polynominal curve fit was used for the velocity calculation from the calibrated flow data. The curve fit uncertainty is expressed as:

$$\frac{\Delta U_{curve-fit}}{U} = \sqrt{\frac{\sum_{i=1}^{n}\left(\frac{U_{cal} - U_{curve-fit}}{U_{cal}}\right)^2}{n}} \qquad (C.8)$$

188

where n is the number of points used for calibration. For velocities below 0.5 m/s, the curve-fit uncertainty is :

$$\frac{\Delta U_{curve-fit}}{U} \approx 0.0122 \quad (1.22\%) \quad U < 0.5 \text{ m/s}$$

For velocities above 0.5 m/s, the curve-fit uncertainty is:

$$\frac{\Delta U_{curve-fit}}{U} \approx 0.0079 \quad (0.079\%) \quad U > 0.5 \text{ m/s}$$

The total uncertainty in the hot-wire velocity measurement is:

$$\frac{\Delta U_{tot}}{U} = \sqrt{\frac{\Delta U_{cal}^2}{U} + \frac{\Delta U_{curve-fit}^2}{U}}$$

Thus,

$$\frac{\Delta U_{tot}}{U} \approx 0.0126 \quad (1.26\%) \quad U < 0.5 \text{ m/s}$$

$$\frac{\Delta U_{tot}}{U} \approx 0.0085 \quad (0.85\%) \quad U > 0.5 \text{ m/s}$$

Reference C.2 shows that relative errors of the mean and rms components of the instantaneous velocity are equivalent to the relative error in the measured velocity.
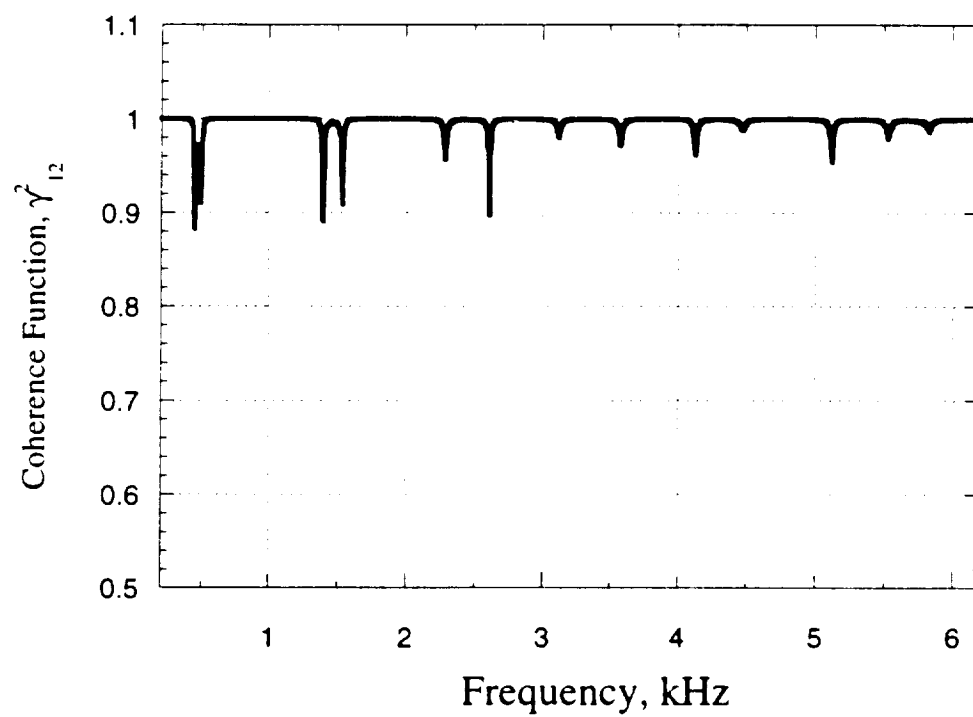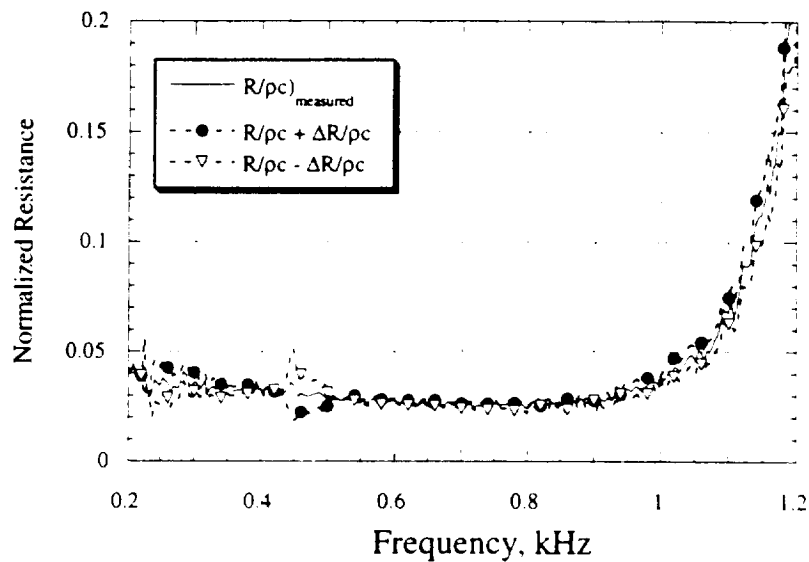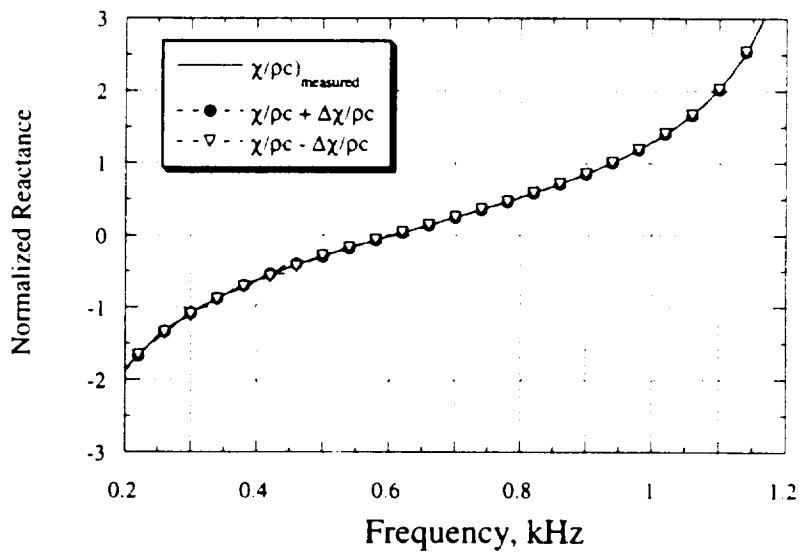
Figure C.1 Typical coherence function spectrum used for impedance determination in impedance tube; Broadband input [Δf = 4 Hz; 64 avgs.].
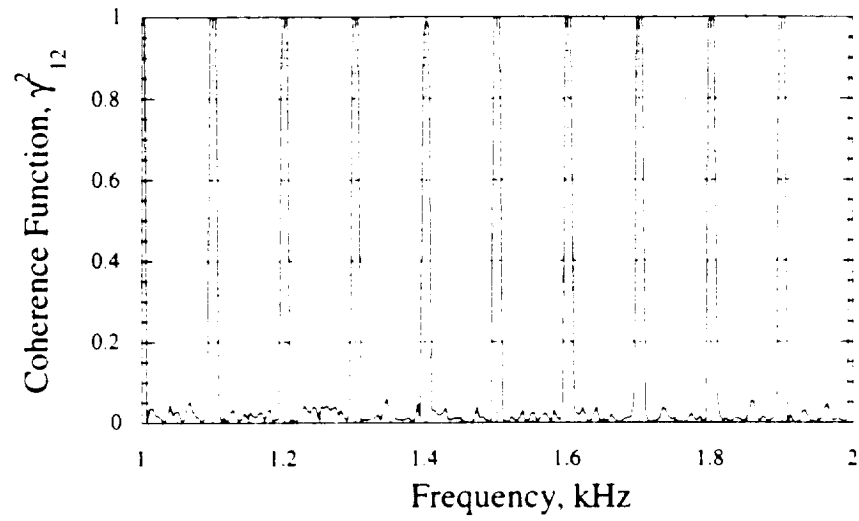
a. Typical "worst case" error bound in Normalized Resistance for broadband signal input into impedance tube.
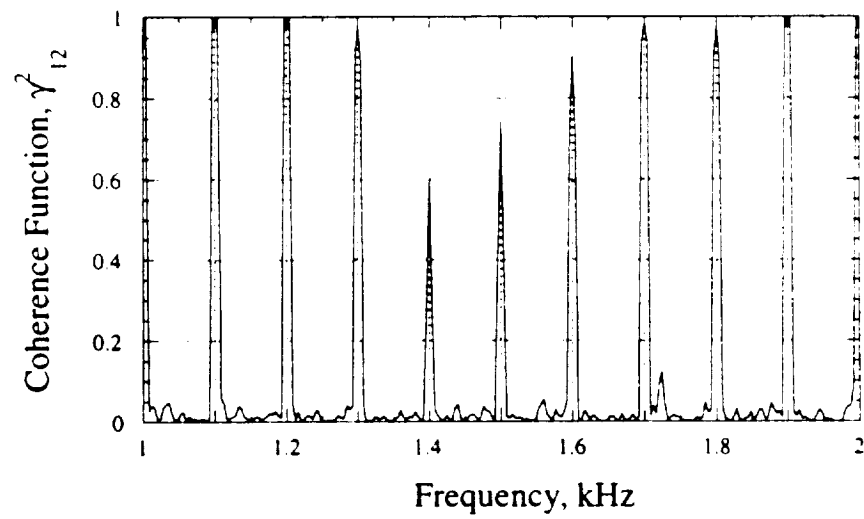

b. Typical "worst case" error bound in Normalized Reactance for broadband signal input into impedance tube.

Figure C.2 Error bound estimate for broadband input into impedance tube.

a. Measurement Location UPSTREAM of liner.

b. Measurement Location DOWNSTREAM of liner.

Figure C.3 Coherence levels for multiple tone input excitation in flow-duct with $V_{mean} = 250$ ft/s; a) Upstream and b) Downstream.